Quantifying CO_2 uptake and biological productivity in the southern hemisphere oceans using atmospheric observations

by

Tilla Margaret Roy

BSc (Hons)

Submitted in fulfillment of the requirements for the Degree of

Doctor of Philosophy

Antarctic CRC and the Institute of Antarctic and Southern Oceans Studies

University of Tasmania

January, 2005

Declaration

This is to certify that the material composing this thesis has never been accepted for any other degree or award in any tertiary institution and, to the best of my knowledge and belief, is solely the work of the author, and contains no material previously published or written by another person, except where due reference is made in the text.

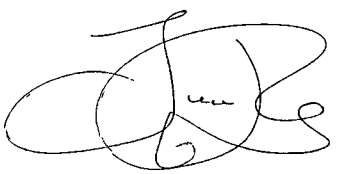

Tilla Roy

Authority of Access

This thesis may be made available for loan and limited copying in accordance with the Copyright Act, 1968.

Tilla Roy

Acknowledgements

First and foremost I would like to thank both of my primary supervisors Richard Matear and Peter Rayner for their excellent support and encouragement; Richard for his great insight and perspectives, and for encouraging me to follow my curiosity and to find my own voice; Peter for continuous inspiration, helping me get off to a solid and exciting start, and for his patience in introducing me to a completely new, and at first, daunting research world.

I would also like to thank my other supervisors Roger Francey for his helpful 'observationalist' angle on the atmospheric inversion work; Bill Budd, for his interest and for encouraging regular meetings in Melbourne in the early part of my thesis, which really allowed me to develop the atmospheric component of my thesis; Tom Trull, for taking me in on at the end of my PhD, for interesting discussions and whipping me through the finish line.

I am also very grateful to my colleagues; Rachel Law, for running the atmospheric transport model especially under such short notice and for her wisdom on things atmospheric; Gareth Wilson, at the HPCCC computer centre for his invaluable expertise which helped me get the code running fast enough that a single model spinup wouldn't see me into the next century; Bronwyn for filling in as a surrogate mother and making sure that as a mere student that the creature comforts and personal maintenance issues weren't neglected. I always had a healthy stationary collection and clean shoes; Simon, for acting as my 'personal secretary' on the final crucial day of printing and handing in my thesis. I would hate to think what could have happened if I was left to my own devices – not to mention the many refreshments along the way.

'Shanks' to the other kids at CSIRO (Ben, Gareth, Perran, Katrina, Beth, Caroline, Soph, Simon, Catia, Andrew, Jaci, Thomas) who made the PhD experience warm and spicy – and of course to the big kids Steve,

George and Trevor who've been a treat to get to know over the years. It's been great to come away with such a great bunch of friends!

And of course I could never thank my Mum, Dad, Bazza and my close friends enough for always being there when I needed support, encouragement and TLC.

I never predicted I'd get so hooked on Tassi. It's been a stunning place to live and write up a PhD. Thanks to all the people who have made it all way too much fun and have made this place my home.

Table of Contents

Abstract

In this thesis, the use of atmospheric observations for quantifying the uptake of CO_2 and biological production in the Southern ocean is explored. For both these processes, ocean observations appear insufficient to accurately quantify their magnitude and variability. It has been proposed that atmospheric observations would provide a better constraint.

In the first section, we use an atmospheric inversion model to combine atmospheric and oceanic observations to investigate the southern hemisphere ocean CO_2 uptake. From sensitivity studies that vary both the initial ocean flux distribution and the atmospheric data used in the inversion, our inversion predicts a total (ocean and land) uptake of 1.65 to 1.90 GtC yr^{-1}. We assess the consistency between the mean southern hemisphere CO_2 ocean uptake predicted by an atmospheric inversion model for the 1991-1997 period and the ocean flux estimate based on observed ΔpCO_2, as in Takahashi *et al.* (2002). In the Takahashi *et al.* (2002) paper the ocean flux estimate is referred to as T99, since the data were first released in 1999. In this study, we adopt the same name for this estimate. The inversion cannot match the large 1.8 GtC yr^{-1} southern extratropical (20°S - 90°S) uptake of the T99 ocean flux estimate without producing either unreasonable land fluxes in the southern mid-latitudes, or increasing the mismatches between observed and simulated atmospheric CO_2 data. The southern extratropical uptake is redistributed between the mid and high latitudes. Our results suggest that the T99 estimate of the Southern Ocean uptake south of 50°S is too large, and we hypothesize that the discrepancy reflects the inadequate representation of winter-time conditions in the T99 estimate.

In the second section, we apply the methods used for estimating biological new production from air-sea oxygen fluxes and atmospheric O_2/N_2 concentrations to a series of model experiments, and evaluate how well simulated new production is retrieved in the southern hemisphere

oceans. The air-sea fluxes of oxygen are simulated using a global biogeochemical ocean circulation model. A series of perturbation experiments are designed to span a feasible range of oceanic circulation and biological productivity scenarios. The atmospheric O_2/N_2 fields are simulated by using the O_2 and N_2 air-sea fluxes, selected from the global ocean biogeochemical model perturbation experiments, taken as a lower bound in a global atmospheric transport model. Estimation of new production using both the oceanic and atmospheric methods is based on the biological seasonal net outgassing (SNO) of oxygen, which is calculated by integrating the biological oxygen flux over the period where the flux is outgassing to the atmosphere. We demonstrate that the large-scale circulation and the disequilbrium-driven fluxes of oxygen produce substantial spatial variability in the *g* (the proportion of photosynthetically produced oxygen outgassed to the atmosphere), which cause the standard oceanic approach for estimating new production to fail. Fortunately, biogeochemical and physical model perturbations only produce small changes to the spatial structure of the *g* (i.e. $\pm$ 0.1), since the spatial distribution of the *g* is largely set by the large-scale ocean circulation. The atmosphere acts to integrate the spatial structure in the air-sea fluxes of oxygen. Therefore, it is possible to use a single *g* when applying the atmospheric approach. If we know the hemispheric *g*, then variability in the biological SNO of atmospheric oxygen primarily reflects variability in new production. Using simulated atmospheric O_2/N_2 concentrations, we show that the magnitude of new production can be retrieved if the *g* and the dilution factor (i.e. the proportion of the atmosphere into which the O_2/N_2 signal is well mixed) are known, given that the atmospheric observing network is large enough to capture the spatial variability in the O_2/N_2 signal.

List of Tables

List of Figures

1. Introduction

The global carbon cycle comprises of four main reservoirs of carbon dioxide - the atmosphere, the terrestrial biosphere, the oceans and the lithosphere. The atmosphere stores ~750 GtC, the terrestrial biosphere stores ~2190 GtC, the surface ocean stores ~1020 GtC and the deep ocean stores as much as ~39 000 GtC. In comparison to the inventory of oceanic carbon, the 7 GtC yr^{-1} emitted into the atmosphere via fossil fuel burning seems very small. Yet this anthropogenic input of atmospheric CO_2 has the potential to drastically change our climate system. Three-dimensional model simulations suggest that a doubling in atmospheric CO_2 concentrations could increase global mean surface air-temperature by 2.1 °C to 4.6 °C (Stocker and Schmittner (1997)). The ocean is by far the largest potential depository of atmospheric carbon dioxide, but the ocean can't absorb all the anthropogenic carbon due to limited air-sea gas exchange and biological production. The rate, at which CO_2 can enter the ocean, is controlled by the efficiency of the solubility and biological pumps of CO_2. Since much of the ocean is vertically stratified, only the surface ocean tends to equilibrate with the atmosphere. The solubility pump is most efficient in regions where surface waters are cold and saline resulting in deep water formation, which subsequently transports CO_2 enriched waters to the deep ocean. The two regions where the solubility pump is most efficient are in the high-latitudes - the North Atlantic and the Southern Ocean. Coupled climate simulations suggest that the solubility pump will become less efficient with climate change due to increased stratification and saturation of the buffering capacity of the oceanic carbonate system.

The biological pump is the other key oceanic process that regulates atmospheric CO_2. Nutrients advected to the surface ocean fuel biological productivity, which results in the formation of biological matter. This biological matter is then passed through the oceanic food web. Some of the biological matter rains out of the surface ocean and remineralises at

depth producing an increasing gradient in dissolved inorganic carbon, which drives a flux of carbon dioxide into the oceans. Given the predicted reduction in the efficiency of the solubility pump, the efficiency of the biological pump needs to increase if the oceanic uptake of CO_2 is to remain unchanged. Again, it is within the high-latitudes where the biological pump can have the greatest potential to influence CO_2 uptake. Much of the high-latitude oceans are described as high nutrient- low chlorophyll regions. The high nutrient levels and low chlorophyll concentrations in these regions indicate that the biological pump is not functioning at its maximum efficiency.

There are significant gaps in our knowledge of the carbon cycle system. Many challenges still lie in trying to find effective ways to estimate the current magnitude and variability of the oceanic processes that control atmospheric CO_2 concentrations – particularly in the Southern hemisphere where climate change has the potential to dramatically change the oceanic uptake of CO_2. The southern hemisphere oceans play a central role in global biogeochemical cycles. But the remoteness of the Southern Ocean has left the region largely undersampled in most hydrographic and biogeochemical tracers relative to all other oceanic regions. We need to identify feasible ways to measure the magnitude and variability of key biogeochemical ocean processes in southern hemisphere oceans. The attraction of atmospheric methods is that the atmosphere mixes the small-scale structure of the air-sea flux of gases. The atmosphere acts as a natural integrator of the air-sea fluxes. Measuring variability in gas concentrations at atmospheric observing stations exploits the integrating property of the atmosphere and potentially provides a more efficient way of measuring air-sea fluxes than trying to estimate fluxes from ocean observations.

Oceanic methods are valuable because they provide both a mechanistic understanding of the processes driving the flux variability and a locally more precise estimate of the flux. But it is virtually impossible to capture the enormous spatial and temporal variability in air-sea gas fluxes across the southern hemisphere oceans by direct sampling. To obtain

large-scale estimates of air-sea exchange from oceanic observations, one needs to resort to measuring fluxes in a small number of regions and extrapolating the flux over the large oceanic zones. In this thesis, I compare atmospheric and oceanic methods applied to determining the magnitude of two fundamental ocean processes in the southern hemisphere – the air-sea exchange of CO_2 and biological new (or export) production.

Carbon dioxide is increasing in the atmosphere primarily due to the burning of fossil fuels. But less than half of the anthropogenic CO_2 emitted remains in the atmosphere. At present, the anthropogenic emissions of CO_2 to the atmosphere are ~ 7 GTC yr^{-1}. Only about half of the emitted CO_2 remains in the atmosphere. The other half is taken up by the oceans and the terrestrial biosphere. To predict the future climate we need to know the future atmospheric CO_2 levels, which requires understanding the roles the ocean and the terrestrial biosphere play in controlling the concentration of CO_2 in the atmosphere. For the ocean, this includes determining the magnitude and spatial distribution of the oceanic CO_2 fluxes. Note that in this study, the CO_2 fluxes refer to the sum of anthropogenic and natural CO_2 fluxes.

An enormous effort has gone into determining the magnitude and distribution of the oceanic CO_2 uptake. There has been a long-standing debate on the relative importance of the oceans and terrestrial biosphere in the uptake of CO_2. From ocean observations, the southern hemisphere oceans have been shown to be an important sink of atmospheric CO_2. However, estimates based on the atmospheric observations, which rely on using atmospheric CO_2 concentrations at observing stations to determine regional uptake, are much smaller.

The atmospheric method for determining CO_2 fluxes involves using the spatial and temporal patterns of atmospheric CO_2 concentrations and knowledge of atmospheric transport to infer the surface CO_2 flux. The process is known as an inversion since it reverses the natural direction of causality. The method has been widely used [Keeling *et al.* (1989); Tans

et al. (1990); Enting *et al.* (1995); Bousquet *et al.* (2000)] and provides an independent check on other integrated estimates of surface fluxes.

Although the sparse data coverage leaves regional flux estimates highly uncertain, atmospheric inversions have yielded some consistent results at hemispheric scales driven primarily by the large-scale interhemispheric gradient in atmospheric CO_2. The interhemispheric gradient is predominantly forced by the asymmetry in fossil fuel combustion (approximately 95% occurs in the northern hemisphere). Early studies noted that the simulated interhemispheric gradient from the spatial distribution of fossil fuel sources was substantially larger than the observed gradient [Tans *et al.* (1990); Law *et al.* (1996)]. Inverse models attempt to reproduce observed CO_2 gradients by inferring surface CO_2 flux distributions. Thus it is not surprising that most inverse studies of CO_2 fluxes have suggested large northern hemisphere sinks (usually over land). Less noted, but nearly as ubiquitous, has been the finding of a corresponding reduction in the southern hemisphere uptake [Keeling *et al.* (1989); Tans *et al.* (1990); Rayner *et al.* (1999)] relative to ocean-derived uptake estimates [Takahashi *et al.* (1997); Metzl *et al.* (1999); Takahashi *et al.* (2002)]. In chapter 2, I will explore the consistency of the ocean and atmospheric estimates of the oceanic uptake of CO_2.

Export production is the process that is responsible for transporting biological matter from the upper ocean to depth, and is defined as the proportion of net production that is transported below the mixed layer to the deeper ocean. There are many reasons why we are interested in trying to quantify and monitor variability in export production. Export production helps maintain the steep vertical gradients in CO_2 between the atmosphere and the deep ocean and lowers the atmospheric CO_2 levels by approximately 200 ppm from an abiotic ocean [*Volk and Hoffert (1985)*]. A stronger biological pump during the last glacial maximum has been postulated to explain the 100 ppm decline in atmospheric CO_2 levels between interglacial and glacial periods [*Kumar and more (1995)*; *Sigman and Boyle (2000)*]. In century-scale climate change scenarios the oceanic uptake of anthropogenic CO_2 in the Southern Ocean is reduced by almost

20% after removing the effect of biological processes [Sarmiento and Le Quéré (1996)]. Export production is also a useful proxy of variability in biological production [Lehodey *et al.* (2003); Loukos *et al.* (2003)]. Climate change simulations predict up to 15% changes in oceanic export production at both regional and global scales by 2100 [Maier-Reimer *et al.* (1996); Matear and Hirst (1999); Bopp *et al.* (2001)].

Although export production is important to regulating atmospheric CO_2, and has the potential to dramatically change the oceanic uptake of carbon with climate change, both the magnitude of the ocean biological response to climate change and the CO_2 feedback of ocean biology on atmospheric CO_2, are highly uncertain. Estimates of the strength of the biological pump in the modern ocean vary widely between 5 to 15 GtC yr^{-1} [*Falkowski et al. (1998)*]. The large uncertainty reflects the poor sampling in space and time of direct measurements of the export of carbon from the upper ocean and the difficulty in extrapolating the local measurements to obtain regional estimates.

Export production is notoriously difficult to observe in the field and validate in models. Modelled export production estimates are frequently assessed using satellite observations [Bopp *et al.* (2001); Palmer and Totterdell (2001)]. But, satellite based estimates of export production could not be reconciled with interior ocean nutrient budgets [Schlitzer (2002b)] in the Southern Ocean. In their study, Southern Ocean export production estimates calculated by the three-dimensional assimilation of tracers, were found to be greater than satellite estimates by a factor of 2 to 5, probably due to the failure of satellites to detect sub-surface chlorophyll maxima, uncertainties in the converting satellite-based primary production estimates to export production and due to the lack of direct export production measurements. Improving our estimates of export production and monitoring how it changes interannually are important to quantifying how biological productivity affects CO_2 uptake.

It is not at all clear how large-scale estimates of export production should be made. Given the large uncertainties associated with measuring and estimating export production, the motivation is to find effective ways

to quantify export production. The biological production of organic matter by photosynthesis and organic remineralisation by bacteria produces and consumes oxygen respectively, which suggests that oxygen may be a useful tracer of the strength of the biological pump. Seasonal variations in oceanic oxygen have long been recognized as a potential tracer of biological productivity in the oceans [Schulenberger and Reid (1981)]. The biological production of organic matter by photosynthesis and organic remineralisation by bacteria produces and consumes oxygen, indicating that oxygen may be a useful tracer of the strength of the biological pump.

Seasonal variations in oxygen are driven by two main processes, which produce an air-sea disequilibrium of oxygen that drives air-sea oxygen fluxes including: I) the biological oxygen flux - due to the combination of photosynthetic production and the remineralisation of biological matter and 2) the thermal oxygen flux, due to the heat flux. Photosynthetic production of biological matter by phytoplankton, which peaks in the spring/summer, releases oxygen into the atmosphere and takes up dissolved nutrient from the water column. The biological matter formed through photosynthesis is passed through the oceanic food web. Some of this biological matter escapes the oceanic food web and falls out of the surface ocean. Bacterial respiration of the biological matter raining into the subsurface ocean, takes up oxygen from the water column and returns nutrients to the water column in dissolved form. When oxygen-depleted subsurface waters are returned to the surface ocean, which occurs more efficiently in the autumn/winter, the air-sea disequilibrium drives an oceanic uptake of oxygen from the atmosphere. The thermal oxygen flux is driven by the heat flux. In winter when sea-surface temperatures are low, the solubility of oxygen increases and atmospheric oxygen is absorbed into the ocean, and vice versa in the spring and summer. Consequently, the thermal and biological fluxes reinforce each other – particularly in the higher latitudes where the seasonal cycle in temperature is most pronounced. Ideally the oxygen variability, used to estimate biological production from oxygen-based methods, needs to be

corrected for the component of the biological oxygen flux driven by the remineralisation of biological matter and for the thermal oxygen flux.

Several attempts have been made to estimate hemispheric new production based on seasonal variations of air-sea gas exchange. Here new production, defined as the proportion of the net primary productivity fuelled by nutrients advected into the euphotic zone, is used as a proxy of export production, since at steady state nutrients must be conserved and new production is equivalent to export production. Keeling and Shertz (1992) used atmospheric O_2/N_2 measurements as a proxy of the seasonal net outgassing of oxygen, *SNO* from the ocean, to calculate the annual new production, *NP*, for the Southern Ocean. Najjar and Keeling (1997) compiled a seasonal surface ocean oxygen dataset and Najjar and Keeling (2000) used it to estimate air-sea fluxes of oxygen and *SNO*. Both atmospheric and oceanic oxygen based approaches for estimating new production rely on estimating *SNO*. The biological seasonal net outgassing of oxygen, SNO_{bio}, was defined by Keeling and Shertz (1992) as the biological oxygen flux, F_{bio}, integrated over the period where the biological oxygen flux is upward. The biological oxygen flux is calculated by subtracting the thermal oxygen flux from the total oxygen flux. The success of the both atmospheric O_2/N_2 and air-sea oxygen flux methods for retrieving new production relies on our ability to estimate the unknown proportion (g) of biologically produced oxygen that is outgassed to the atmosphere (SNO_{bio}) where g is defined as

$$g = \frac{SNO_{bio}}{NP} . \qquad (1)$$

After the initial studies of Keeling and Shertz (1992) atmospheric O_2/N_2 observations have also been used to evaluate biological productivity estimates from global biogeochemical models [Six and Maier-Reimer (1996); Balkanski *et al.* (1999)]. Before we use atmospheric O_2/N_2 to either estimate new production or constrain ocean models, we need to rigorously assess how good a constraint on new production atmospheric O_2/N_2 actually is. Generally, studies using atmospheric O_2/N_2

either to estimate export production or evaluate modelled estimates of export production, separate the total atmospheric O_2/N_2 signal into thermal and biological components. However, they do not treat independently the ventilation and biological effects on the air-sea fluxes of oxygen.

This thesis assesses whether *SNO* from the ocean can be used to estimate new production in the southern hemisphere oceans (90°S to 20°S). We focus on the southern hemisphere for two reasons. Firstly, the Southern Ocean is the region in which modelled estimates of export production deviate most for both present-day and future estimates of export production [Bopp *et al.* (2001)], and where the simulated impact of the ocean biology on anthropogenic CO_2 uptake is greatest [Sarmiento and Le Quéré (1996)]. Also, the largest simulated climate change driven reduction in anthropogenic CO_2 uptake occurs in the Southern Ocean [Maier-Reimer *et al.* (1996); Matear and Hirst (1999)]. Secondly, the Southern Ocean is a particularly attractive place to monitor oceanic oxygen fluxes. Due to the remoteness of the Southern Ocean from major terrestrial sources of O_2 variability the majority of the oxygen variability in the southern hemisphere is driven by O_2 exchange with the ocean. Keeling and Shertz (1992) estimated that almost 90% of the seasonal amplitude in atmospheric oxygen is driven by the ocean. Furthermore, the slow interhemispheric exchange of atmospheric oxygen on seasonal timescales means that seasonal variability of atmospheric O_2 primarily reflects air-sea exchange processes occurring within the southern hemisphere.

Chapter 2 focuses on using atmospheric CO_2 observations to quantify the magnitude and variability of the southern hemisphere oceanic uptake of CO_2 using an atmospheric inversion model. Chapters 3 to 6 focus on providing the relevant information on the model and model experiments for Chapter 7. Chapter 3 briefly describes the global biogeochemical ocean circulation model and the global atmospheric circulation model used for the model experiments. Chapter 4 describes

the suite of biogeochemical and physical circulation perturbation experiments run using the global biogeochemical circulation model. Chapter 6 provides an assessment of the physical circulation and biological new production in the model. The first part of chapter 6 gives a brief assessment of the global circulation for the control experiment and of the southern ocean water masses simulated by the model. In the second part of chapter 6 we assess the range of new production estimates using phosphate. In Chapter 7 methods used for estimating biological new production from air-sea oxygen fluxes are assessed and in chapter 8 atmospheric O_2/N_2 methods used for estimating new production from atmospheric O_2/N_2 concentrations are assessed.

2. Southern Hemisphere Ocean CO_2 uptake: Reconciling atmospheric and oceanic estimates

2.1. Introduction

Historically, ocean CO_2 flux estimates based on the observed CO_2 partial pressure differences between the surface ocean and the atmosphere (ΔpCO_2) [Takahashi *et al.* (1997); Metzl *et al.* (1999)] and global ocean carbon models [Matear and Hirst (1999)] have generally produced larger Southern Ocean CO_2 uptakes than atmospheric inversions [Bousquet *et al.* (1999); Rayner *et al.* (1999)] (Figure 2-1).

Several recent air-sea CO_2 flux estimates for the Southern Ocean [N. Metzl, personal communication; Gloor *et al.* (2003)] give lower oceanic uptakes consistent with atmospheric inversion estimates. Data collected on French OISO cruises during summer and winter in the Indian sector of the austral ocean (January and August 2000) suggest that the Southern ocean is a summer CO_2 sink as generally observed [Metzl *et al.* (1995); Metzl *et al.* (1999); Takahashi *et al.* (2002)] but could be a significant source of CO_2 to the atmosphere during winter. The regional CO_2 flux estimate based on this cruise data was obtained from a one-dimensional biogeochemical model of ΔpCO_2 (N. Metzl, LBCM/IPSL, personal communication). We extrapolate the regional estimate to the full seasonal cycle for the entire Southern Ocean (1b, Figure 2-1). Such an extrapolation may introduce large biases and errors into the estimate, which can only be improved with incorporation of more data. The Gloor *et al.* (2003) estimate (5, Figure 2-1) is based on an ocean inversion method that uses ocean observations of dissolved inorganic carbon (DIC) to infer ocean CO_2 fluxes. The method is limited by the need to prescribe the ocean transport and by the ability to compute the anthropogenic CO_2 concentration (Gruber (1998)) and the atmospherically derived CO_2 concentration [Gruber *et al.* (1996)] from the observed DIC and hydrographic data. The method may introduce biases into the estimate.

For example, biases could be caused by errors in the prescribed ocean transport and errors in the computed anthropogenic CO_2 concentration. Although both these new estimates appear consistent with atmospheric inversion results, at present the potential errors in these estimates have not been quantified and it is premature to claim consistency with the atmospheric inversion results.

Early inverse studies were carried out when much fewer oceanic CO_2 flux estimates were available. The advent of more comprehensive ocean ΔpCO_2 compilations [Takahashi *et al.* (2002)] enables one to combine the independent atmospheric concentration data and oceanic CO_2 flux estimates in an inversion and rigorously compare the oceanic and atmospheric methods for determining fluxes. The southern extratropics is a particularly good region for such as study since the almost complete ocean coverage reduces complications that might arise from terrestrial CO_2 exchange. We use the inversion technique to combine atmospheric data and ocean flux estimates to compare and assess their consistency in the extratropical Southern Ocean, and to obtain an improved estimate of the CO_2 uptake. Considering how critical the Southern Ocean is for CO_2 uptake and how relatively data-poor this region is, it is essential that all the oceanic and atmospheric data are used to estimate the CO_2 fluxes.

2.2. Methods

We use a time-dependent Bayesian synthesis inversion method as described by Rayner *et al.* (1999). The set-up of our calculations follows their paper except for the differences described below. We use a different atmospheric transport model, in our case the CRC-MATCH model used by Law and Rayner (1999) and included in the study of Gurney *et al.* (2002). The influence of errors in atmospheric transport is not explicitly dealt with in this paper, but they have been assessed in a comparison of atmospheric transport models [Gurney *et al.* (2002)]. Gurney *et al.* (2002) find little sensitivity to atmospheric transport and we suspect the same to apply to this study. The inversion of Rayner *et al.* (1999) used uniform source patterns within 26 regions. We have incorporated the geographical distribution of fluxes within the ocean regions (Figure 2-2). This is achieved by fixing the initial source pattern and solving for the offsets, from this distribution, within each ocean region. Hence we can study the effect of different small-scale flux structure on the inversion. The atmospheric data used include the monthly-mean CO_2 concentrations from 65 stations marked in Figure 2-2. The data are a preliminary version of the dataset used by Bousquet *et al.* (2000) and we use data from the period 1980-1997. We also use the O_2/N_2 record from Cape Grim, Tasmania [Langenfelds *et al.* (1999)] to constrain the net global CO_2 uptake by the terrestrial biosphere and the oceans. Unlike Rayner *et al.* (1999) we do not use the $\delta^{13}C$ record from Cape Grim. Given the formulation of the Rayner *et al.* (1999) study, $\delta^{13}C$ was not used to determine the long-term mean net fluxes, so this difference is not significant.

2.3. Results and Discussion

Figure 2-3 shows the zonal mean atmospheric CO_2 gradients estimated from TransCom3 atmospheric transport models using identical terrestrial [Randerson *et al.* (1997)], ocean [Takahashi *et al.* (2002)] and fossil fuel fluxes [Gurney *et al.* (2002)]. All the models overestimate the observed interhemispheric gradient in atmospheric CO_2. The overestimation could be attributed to errors in the fluxes or bias in modelled atmospheric transport and the atmospheric observations.

The effect of atmospheric transport on the southern hemisphere uptake has been tested by Gurney *et al.* (2002). They performed 16 inversions using 16 different transport models. The reduction in the southern hemispheric uptake is one of their most robust findings. Interhemispheric atmospheric transport in each of the 16 models was assessed using tracer SF_6 simulations [Denning *et al.* (1999b)]. They find that even models that underestimate interhemispheric transport produce a reduced southern hemisphere uptake relative to the T99 ocean flux estimate in Takahashi *et al.* (2002), indicating that the gradient mismatch is not due to errors in the modelled interhemispheric exchange rates.

It is important to note that the transport model used in our study, CRC-MATCH, produces a good match to the SF_6 interhemispheric gradient, although the measurements do not allow precise calibration. Our transport model also produces a simulated interhemispheric CO_2 gradient that is within the range of the other transport models and overestimates the gradient by almost 5 ppm (Figure 2-3). It is also worth noting that the simulated gradients in Figure 2-3 are zonal mean concentrations while the atmospheric observing stations are generally located to avoid the large fossil fuel and terrestrial sources. For a better comparison of interhemispheric gradients, we compared the north-south transect of the surface CO_2 concentration averaged between 170°E and 170°W to a transect through the Pacific marine sites. The mismatch was reduced by at most 30% suggesting that sampling bias was not the major

contributor to the gradient mismatch. This comparison also reduces the possibility of overestimating the impact of the (predominantly terrestrial) rectifier effect [Denning *et al.* (1995)].

2.3.1. Control Case

Using the inversion model we calculate monthly flux distributions from 1980 to 1997, which minimise the mismatch between simulated and observed concentrations throughout this period. The T99 ocean flux estimate in Takahashi *et al.* (2002) is used as an initial ocean CO_2 uptake estimate (Figure 2-1). Our predicted flux distribution for the control case where the data constraints are weighted as in Table 2-1, follows the general uptake pattern obtained by previous studies [Ciais *et al.* (1995); Enting *et al.* (1995); Bousquet *et al.* (1999); Rayner *et al.* (1999)]. For the 1980 to 1997 period, the inversion matches the interhemispheric CO_2 gradient, by increasing the total annual mean northern hemisphere uptake (land plus and ocean) from 0.9 to 2.4 GtC yr^{-1}, primarily by increasing the terrestrial biosphere uptake. The inversion also reduces the total southern hemispheric uptake from 1.8 - 1.3 GtC yr^{-1} (Table 2-2).

In the 1980s the southern extratropical uptake was 1.0 GtC yr^{-1} while in the 1990s it increases to 1.8 GtC yr^{-1} (Table 2-2). Most of the increase in the southern extratropical uptake between the 1980s and 1990s in the control case is concentrated over South Africa. In fact the region switches from a source to a sink region, increasing its uptake by 0.7 GtC yr^{-1}. Such a large shift arising from a small continental area of generally low fertility is unlikely. Takahashi *et al.* (2002) provides a monthly mean global ocean flux distribution for 1995. For consistency, we compare the annual mean fluxes of the T99 ocean flux estimate with the annual mean uptake predicted by the inversion for the period 1991-1997 (Table 2-2). Note that for all further comparisons between inversion results and the T99 ocean flux estimate we use only inversion results from the 1990s. At a first glance it would appear that the 1.8 GtC yr^{-1} southern extratropical (18°S – 90°S) uptake in the 1990s is consistent with the T99 estimate (Table 2-2). It is important to be careful when interpreting zonal

uptake estimates from inversions when they contain regions such as South Africa, which are not well observed and therefore tend to produce spurious fluxes.

By reducing the uncertainty on South Africa by a factor of 6 from the control case (South Africa Test Case, Table 2), two thirds of its uptake is shifted to the tropics such that the total mid-latitude uptake is reduced to 1.2 GtC yr^{-1} without changing the local station mismatches. South Africa must be responding to influences outside the southern extratropics. We therefore regard the 1.8 GtC yr^{-1} southern extratropical uptake predicted in the control case as an upperbound value for this region. A total land-ocean uptake larger than the T99 ocean uptake estimate would be difficult to reconcile with the 1990s atmospheric data.

The control case reduces the Southern Ocean uptake south of 50°S relative to the T99 estimate from 0.6 GtC yr^{-1} to 0.3 GtC yr^{-1} (Table 2-2). In the mid-latitudes, it produces a substantial uptake on land at the cost of a reduced ocean uptake. The ocean uptake is reduced from 1.2 GtC yr^{-1} to 0.7 GtC yr^{-1}. Although the ocean is generally better constrained than the land regions within the southern mid-latitudes, the difficulty of defining longitudinal structures of sources from atmospheric inversions makes the separation of the land and ocean uptake much less certain than the combined uptake.

2.3.2. Constrained southern hemisphere cases

To explore the consistency between the spatial distribution of the ocean fluxes and atmospheric inversion estimates we reduce the uncertainty of the T99 oceanic southern extratropical fluxes by a factor of 100 from the control run (Constrained Southern Ocean Case). This forces an increased ocean uptake in the high latitudes of the southern hemisphere and moves the uptake in the mid-latitude southern hemisphere from the land to the ocean.

In the inversion, the atmospheric observations are matched by increasing the land source by 1.8 GtC yr^{-1} over the southern mid-latitudes (18°S–50°S) and by reducing the total southern extratropical uptake to 0.8

GtC yr^{-1} (Table 2-2; Constrained O, Figure 2-4b). This reduction is produced by an unrealistic (1.7 GtC yr^{-1}) source concentrated over temperate South America. South America like South Africa is a region poorly constrained by atmospheric station measurements and consequently has the freedom in the inversion to produce spurious fluxes.

To limit the size of these fluxes we reduced the uncertainty on the southern hemisphere land regions by a factor of 4 from the control case (Constrained Southern Ocean and Land case). In this inversion, the northern hemisphere terrestrial uptake increases by 0.7 GtC yr^{-1} relative to the constrained Southern Ocean inversion, and the uptake in the tropics is reduced. Extra uptake in the northern hemisphere satisfies the interhemispheric gradient, while fluxes in the tropics are reduced to satisfy the atmospheric growth rate (Constrained O+L, Figure 2-4b).

Figure 2-5a shows the normalised mismatches to observations at all southern hemisphere stations for the control case. In our control case the average station mismatch for all stations within the high latitudes is zero, indicating that the inversion succeeds in satisfying the large-scale atmospheric station constraint. Forcing a larger southern extratropical uptake introduces large systematic biases to the southern hemisphere stations (Figure 2-5b). The negative bias in the high-latitudes indicates that the stations require less local uptake. The low-latitude stations become positively biased indicating that they require more local uptake.

Although the magnitude of the total (ocean and land) southern extratropical uptake from the control inversion agrees with the T99 estimate, the ocean uptake is inconsistent. The spatial distribution of the T99 estimate cannot be prescribed in the inversion without producing unrealistic land sources or systematic biases in the southern hemisphere observing stations. The large southern hemisphere uptake as given by Takahashi *et al.* (2002) cannot be reconciled with the atmospheric data, without reallocating the fluxes between the mid- and high-latitudes.

The station bias shown in Figure 2-5b also allows us to assess the contribution of possible systematic observational errors. For the constrained fluxes to be consistent with the atmospheric observations

requires a systematic overestimate of the interhemispheric gradient of 0.5 ppm. Given the relative uniformity of the southern hemisphere atmospheric CO_2 concentrations, and estimates of measurement precision and possible bias (for example, flask storage effects in the annually supplied and retrieved flasks at Antarctic sites) such a large error (0.5 ppm) is unlikely.

2.3.3. Sensitivity studies

Atmospheric inversions use data taken at discrete measuring sites. These measurements can be influenced by local source features. If local sources are very different from large-scale averages these effects can be misleading. To test the sensitivity of the atmospheric inversion to the initial estimates of the ocean fluxes we perform 2 additional inversions using ocean flux estimates from Takahashi *et al.* (1997) and the ocean carbon cycle model from Matear and Hirst (1999). These ocean flux estimates have different geographical patterns from the T99 estimate used in the control case, and a range of Southern Hemisphere ocean uptakes (Table 2-2). Despite differences between the initial zonal uptakes of up to 0.3 GtC yr^{-1} (Table 2-2) the range in the uptakes predicted by the inversions is much lower. The predicted uptakes in the mid-latitudes and high-latitudes lie in the range 1.65 ± 0.1 and 0.25 ± 0.05 GtC yr^{-1} respectively (Table 2-3). The predicted southern hemisphere uptake is not sensitive to either the local geographical pattern or the magnitude of the initial ocean flux estimates.

Despite the inclusion of more data in the T99 ocean flux estimate the inconsistency with the atmosphere inversion has increased. The ocean fluxes from both Takahashi *et al.* (1997) and Matear and Hirst (1999) agree better with the inversion estimates, particularly in the high latitude Southern Ocean where both estimate a 0.3 GtC yr^{-1} CO_2 uptake, identical to our inversion estimate.

The choice of stations in a latitudinal band could also potentially influence the zonal CO_2 uptake. We ran a series of inversion cases where we removed successive southern hemisphere stations from the network.

Although the range in the extratropical southern hemisphere uptakes predicted by this suite of inversions is only ± 0.15 (Table 2-3), the range in the zonal uptake estimates is greater (i.e. ± 0.3 in the mid-latitudes and ± 0.2 in the high-latitudes). The choice of southern hemisphere stations redistributes the uptake between the mid and high latitudes. Although the atmospheric inversion robustly determines the total southern hemisphere uptake the inversion has more difficulty allocating the uptake between the mid and high latitudes.

2.3.4. Seasonality

The comparison of the seasonal variability of the CO_2 fluxes in the Southern Ocean between the T99 ocean flux estimate and the fluxes predicted by the inversion (Figure 2-6), suggests a possible explanation for the higher ocean uptake estimates from ocean observations (Figure 2-1). In the Southern Ocean (south of 50°S), the control inversion predicts a source to the atmosphere in autumn, while for the T99 estimate the ocean is an uptake region throughout the year. Observational evidence supporting a seasonal Southern Ocean source is mounting as more data are acquired [Bousquet *et al.* (2000); N. Metzl, personal communication; B. Tilbrook, personal communication]. The winter observations from the south Indian Ocean (N. Metzl, LBCM/IPSL, personal communication) indicated that the Southern Ocean is a source during winter. Although the new winter observations are only from the Indian Ocean, extrapolating these new observations with a seasonal mixed-layer model produces an estimate that reduces the annual uptake in the Southern Ocean from 0.5 to 0.1 GtC yr^{-1} (Figure 2-1). This demonstrates how under-sampling of the Southern Ocean in winter may cause Takahashi *et al.* (2002) to overestimate the Southern Ocean CO_2 uptake because it contains few winter measurements.

2.4. Summary

Our atmospheric inversion study predicts a total (land and ocean) southern hemisphere CO_2 uptake of 1.65 to 1.90 GtC yr^{-1} for the 1990s (1991-1997) from sensitivity studies that varied both the initial ocean flux distribution and the atmospheric stations used in the inversion. The magnitudes and spatial flux distributions predicted by the inversion in the southern extratropical oceans are inconsistent with the T99 estimate for two reasons. Firstly, although the 1.8 GtC yr^{-1} total (ocean and land) southern hemisphere uptake from the control inversion is the same magnitude as the T99 estimate, the consistency is only achieved by shifting southern extratropical ocean uptake to the land. Constraining the ocean fluxes to the T99 values results in either unrealistic southern hemisphere land sources or unrealistic mismatches between observed and predicted atmospheric CO_2 concentrations at southern hemisphere observing stations. Secondly, the inversion redistributes the uptake between the mid and high latitudes. There is a persistent reduction in the high-latitude Southern Ocean (50°S - 90°S) uptake, which is also one of the most robust findings from Gurney *et al.* (2002). Our results suggest that the T99 estimate for the Southern Ocean uptake south of 50°S is too large. Contrary to the T99 flux estimate our inversion results suggest the high latitude Southern Ocean is a source of CO_2 to the atmosphere in the autumn-winter period. There is mounting observational evidence indicating that the high-latitude Southern Ocean is an atmospheric source during the autumn-winter period [Metzl *et al.* (1999); B. Tilbrook, personal communication]. The recognized undersampling of the Southern Ocean in the T99 winter ocean flux estimate can produce flux estimates that are biased by summer observations and cause an overestimate of the high latitude Southern Ocean CO_2 uptake.

The re-analysis of the T99 flux estimates including the latest winter data could potentially reconcile atmospheric inversion estimates with ocean-based estimates of the Southern Ocean CO_2 uptake. However, to

increase our confidence in both ocean and atmosphere based estimates other approaches must also be pursued. One should i) explore the impact of additional stations and/or improved measurement frequency and precision in southern hemisphere regions which are poorly constrained, ii) divide the Southern Ocean into oceanographically sensible regions in the inversion, iii) apply adjoint methods which allow much greater resolution of the land and ocean regions, iv) combine the ocean inversion approach of Gloor *et al.* (2003) with atmospheric inversions, v) improve regional ocean flux and uncertainty estimates and vi) develop effective ways of integrating sporadic cruise data into the inversions.

2.5. Addendum

The T99 estimate of oceanic CO_2 uptake has been revised since the publication of this study. See the website http://www.ldeo.columbia.edu/res/pi/CO2/carbondioxide/pages/air_sea_flux_rev1.html. The T99 climatology has a systematic error related to the wind speed. Fluxes were overestimated by about 30% due to an oversight related to adjusting the winds to 10 m. The formulation of gas transfer rates is height specific. The regional and global net CO_2 fluxes should be computed using quadratic and cubic formulations, for the wind speed dependence on the gas transfer rate, using wind speeds at 10 m and 0.995 sigma level (about 40 meters above the sea surface) respectively. The T99 estimate mistakenly used winds from the 0.995 sigma level (Takahashi *et al.* (2002)) and the quadratic rather than the cubic gas formulation for the wind speed dependence of gas exchange. These winds averaged about 1 m s^{-1} faster than the 10 m wind. The flux values obtained with these 10 m winds are about 30% less than the values in Takahashi *et al.* (2002). Consequently, atmospheric and oceanic estimates have become more consistent. Interestingly, the revised oceanic estimate gives a smaller Southern Ocean sink, in agreement with the finding in this study, which suggested that the previous oceanic estimate of the Southern ocean sink was too large.

We would not expect the overall conclusions of this study to change significantly if the revised T99 flux estimate were used. Firstly, before the *Takahashi et al. (2002)* T99 estimate became available, this study was conducted using the *Takahashi et al. (1997)* CO_2 flux estimate which had 0.3 GtC yr^{-1} CO_2 uptake in the high latitude southern hemisphere oceans – even lower than 0.35 GtC yr^{-1} from the most recently revised estimate. And, the inconsistency between atmospheric and oceanic estimates was still apparent. Secondly, another experiment was run, but not described in the thesis, where only the high latitude CO_2 uptake was constrained by reducing the uncertainty on the flux south of 50°S by a factor of 100. Even with large predicted CO_2 sources over the Southern hemisphere land regions and decreased predicted CO_2 uptake in the mid-latitudes, the mismatch between observed and predicted CO_2 concentrations in the high-latitude atmospheric observing stations. Thus, even though the revised oceanic estimate of southern hemisphere CO_2 uptake is more consistent with the atmospheric estimate, we would not expect the general conclusions from this study to change, if the revised air-sea fluxes were used as an initial estimate of the southern hemisphere CO_2 uptake in the inversion model.

Note that one of the main conclusions from this chapter was that the T99 estimate of CO_2 uptake in the southern hemisphere was too large. Interestingly, the magnitude of the latest revised observational estimate of CO_2 uptake in the southern hemisphere is indeed half the magnitude of the T99 estimate - in agreement with this conclusion. Thus, the study demonstrates that atmospheric observations can be successfully used to improve oceanic estimates of oceanic CO_2 uptake.

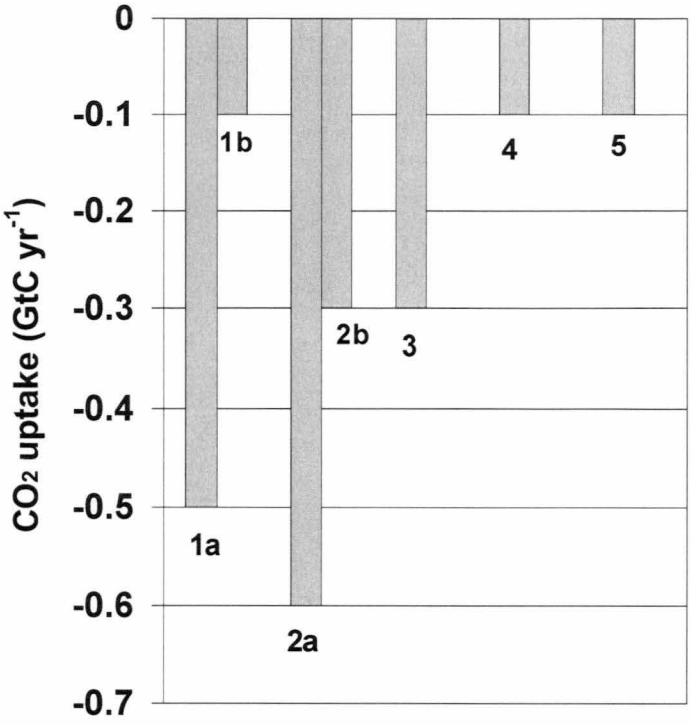

Figure 2-1: Estimates of the Southern Ocean (south of 50°S) CO_2 uptake (GtC yr^{-1}). 1. Regional ocean observations of ΔpCO_2 from (a) Metzl et al. (1999), and (b) N. Metzl, LBCM/IPSL, (personal communication), which includes winter observations; 2. ΔpCO_2 compilations (a) T99 in Takahashi et al. (2002), and (b) Takahashi et al. (1997); 3. Ocean carbon-cycle model of Matear and Hirst (1999); 4. Atmospheric inversion model of Rayner et al. (1999); 5. Ocean inversion model of Gloor et al. (2002).

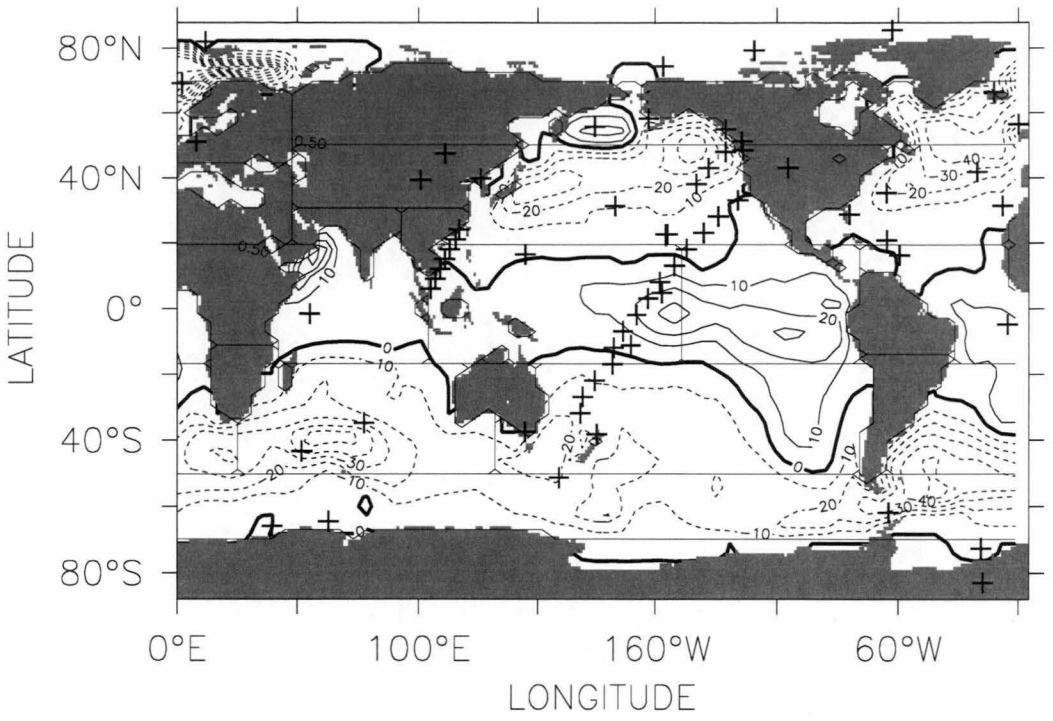

Figure 2-2: Annual mean ocean flux estimate (g m^{-2} yr^{-1}) T99 in Takahashi et al. (2002), which is used as the initial ocean sources in the control inversion. The dashed contour lines denote negative values, which indicate a flux into the ocean (atmospheric sink). The inversion solves for the 26 regions (boxes) and uses atmospheric CO_2 concentrations from the 65 marked atmospheric stations (+).

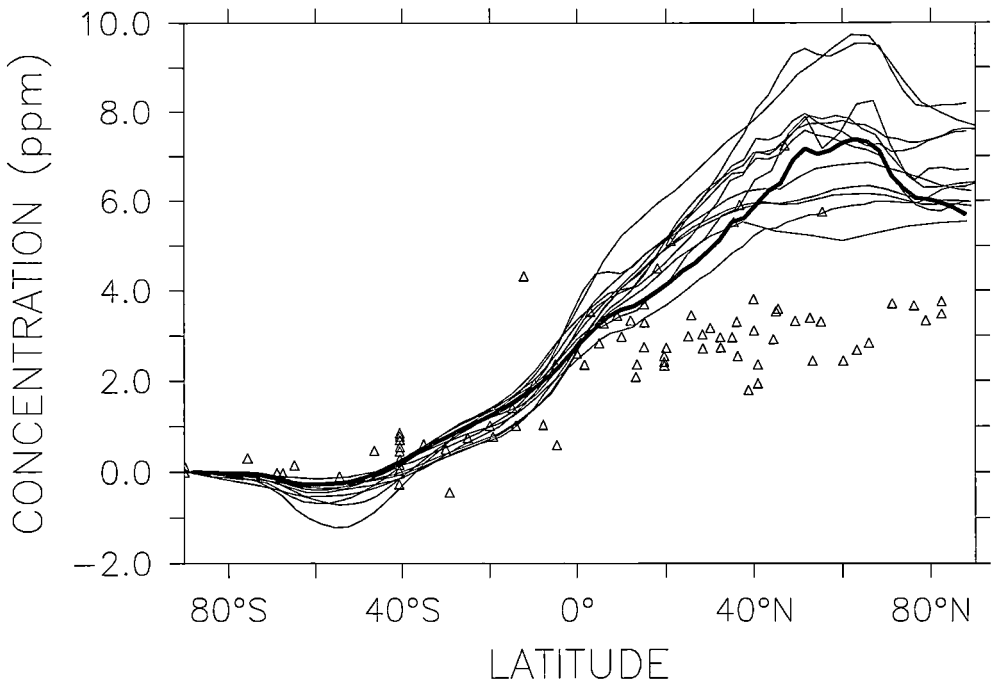

Figure 2-3: The observed (Δ) annual mean atmospheric CO_2 concentrations (ppm) and the simulated (lines) interhemispheric gradients from a range of transport models (Gurney et al., 2002). The simulated gradients were produced from the best estimates of fossil fuel, terrestrial (Randerson et al., 1997) and oceanic (T99 in Takahashi et al., 2002) source fields. The bold line represents the atmospheric transport model, CRC-MATCH, used in our study. *Note:* All data are normalised to the South Pole.

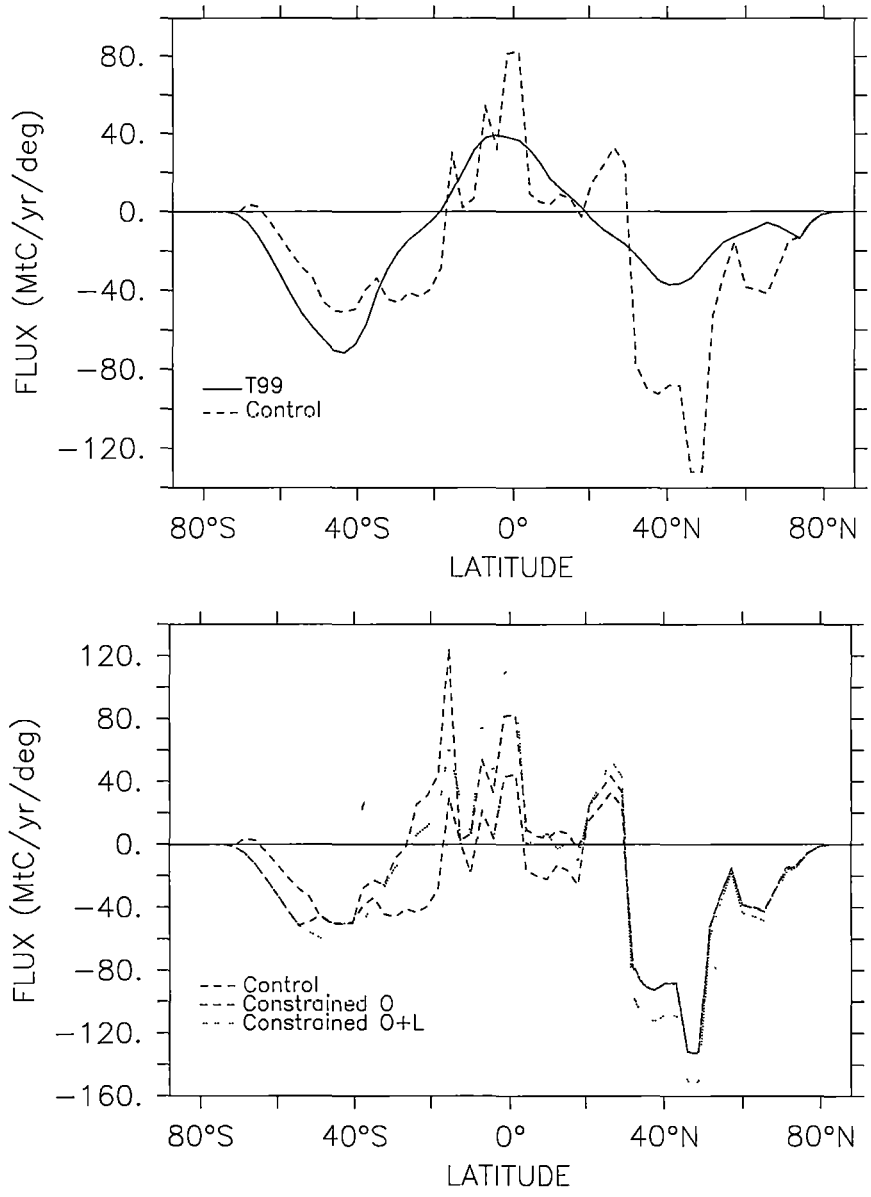

Figure 2-4: The zonal annual mean (1991-1997) CO_2 uptake (MtC yr^{-1} deg^{-1}) for; (a) the T99 ocean flux estimate in Takahashi et al. (2002) used as the initial ocean flux estimate in the control inversion, and the predicted combined land and ocean (total) uptake of the control inversion, and (b) the predicted total uptake of the control, constrained southern extratropical ocean (Constrained O) and constrained southern extratropical ocean and land (Constrained O+L) inversion cases. *Note:* A negative flux denotes uptake of atmospheric CO_2 by the either the land or ocean.

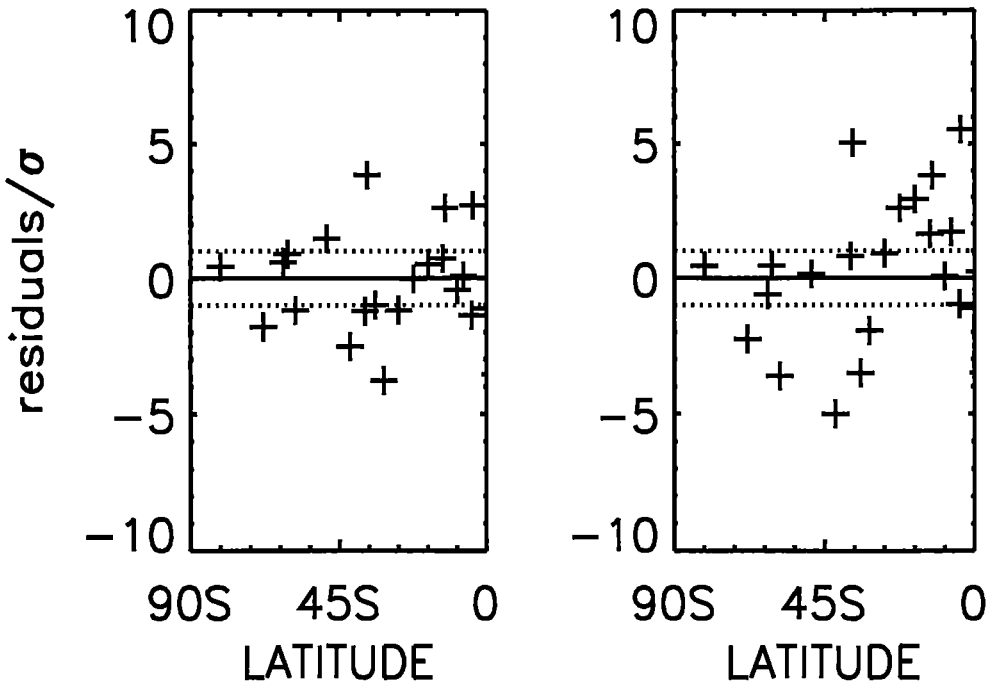

Figure 2-5: Normalised residuals for all southern hemisphere atmospheric CO_2 measuring stations from (a) the control inversion, and (b) the constrained southern ocean and land inversion (Constrained O+L).

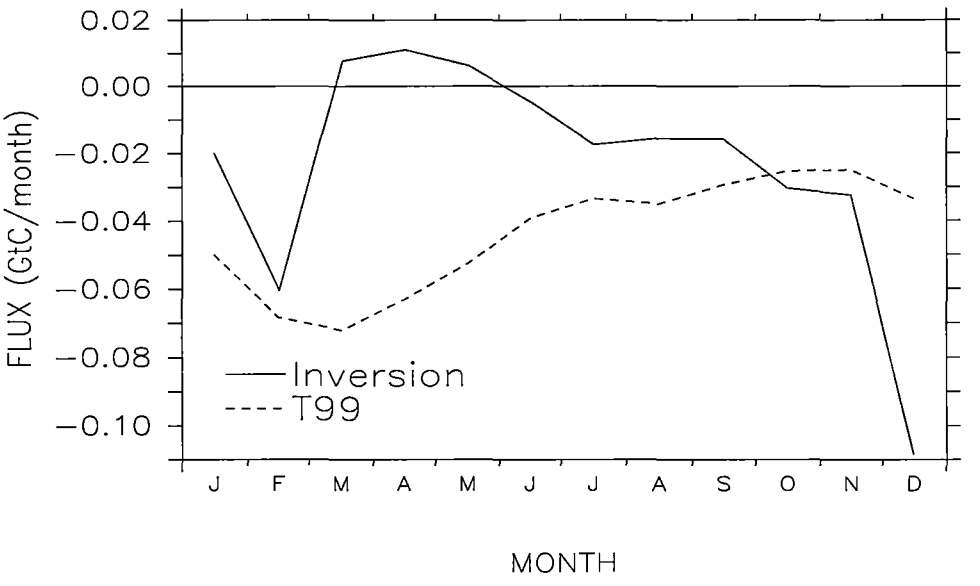

Figure 2-6: Seasonal oceanic CO_2 fluxes (GtC month^{-1}) for the Southern Ocean south of 50°S. The solid line represents the monthly mean fluxes predicted by the inversion for the period 1991-1997. The dashed line represents the T99 ocean flux estimate in Takahashi et al. (2002)

Table 2-1: For the control case, uncertainties given to the initial estimates of sources and to the data constraints.

Sources	
Flux	Standard Deviation
Fossil fuel	**0.3 GtC yr^{-1}**
Northern North Atlantic &	**0.5 GtC yr^{-1}**
Northern North Pacific	
South Pacific	**1.5 GtC yr^{-1}**
Other ocean regions	**1.0 GtC yr^{-1}**
Land regions	**1.2 GtC yr^{-1}**
Data	
Data type	Standard Deviation
CO_2 data	**Range: 0.3 - 5.2 ppm** (Note: The uncertainty is station dependent. See Bousquet et al. (1999) for details.)
O_2/N_2 trend	**0.2 per meg**

Table 2-2: Estimates of ocean CO_2 fluxes and the estimated annual mean southern hemisphere (ocean plus land) CO_2 fluxes (GtC yr^{-1}) from the inversions. The annual mean CO_2 uptakes for the inversions cases marked with an asterisk (*) are calculated for the period 1991-1997. *Note:* A negative flux denotes uptake of atmospheric CO_2.

	Ocean CO_2 Flux (GtC yr^{-1})		Land CO2 Flux (GtC yr^{-1})	Ocean + Land CO_2 Flux (GtC yr^{-1})		
	18°S - 50°S	**50°S - 90°S**		**18°S - 50°S**	**50°S - 90°S**	**Total**
Estimates of the ocean fluxes						
T99 [Takahashi et al., 2002]	**-1.2**	**-0.6**	**0.0**	**-1.2**	**-0.6**	**-1.8**
Takahashi et al., 1997	**-0.9**	**-0.3**	**0.0**	**-0.9**	**-0.3**	**-1.2**
Matear and Hirst, 1999	**-1.0**	**-0.3**	**0.0**	**-1.0**	**-0.3**	**-1.3**
Inversion cases						
Control (1980-1997)	**-1.0**	**-0.1**	**-0.2**	**-1.2**	**-0.1**	**-1.3**
" (1980-1991)	**-1.2**	**0.0**	**0.2**	**-1.0**	**0.0**	**-1.0**
" (1991-1997)	**-0.7**	**-0.3**	**-0.8**	**-1.5**	**-0.3**	**-1.8**
South Africa Test*	**-0.9**	**-0.3**	**-0.3**	**-1.2**	**-0.3**	**-1.5**
Constrained Southern Ocean*	**-1.2**	**-0.6**	**1.0**	**-0.2**	**-0.6**	**-0.8**
Constrained Southern Ocean and Southern Land*	**-1.2**	**-0.6**	**0.4**	**-0.8**	**-0.6**	**-1.4**

Table 2-3: The range of annual mean zonal CO_2 uptakes obtained by the inversion for a series of cases where either the initial estimate of the ocean fluxes is changed or successive southern hemisphere atmospheric stations are removed from the network.

Zonal CO_2 uptake ($GtC\ yr^{-1}$)	Sensitivity studies	
	Initial ocean flux [a]	**Station Network** [b]
18°S - 50°S	**-1.65 ± 0.1**	**-1.4 ± 0.3**
50°S - 90°S	**-0.25 ± 0.05**	**-0.2 ± 0.2**
Total	**-1.9 ± 0.1**	**-1.65 ± 0.15**

[a] The initial ocean uptake estimates used in the inversions are the ocean flux estimates from Takahashi et al. (1997), T99 in Takahashi et al. (2002) and Matear and Hirst (1999).

[b] The range in the fluxes comes from the following cases. In the control inversion the high latitudes (south of 50°S) contain six stations: South Pole (spo), Palmer Station (psa), Macquarie Island (mqa), Syowa Station (syo), Mawson Station (maa) and Halley Bay (hba). The inversion cases are generated by removing the listed stations from the high latitude network; i) all stations except psa, ii) all stations except spo, iii) all stations, iv) spo, v) hba and psa. Two cases are included where the listed stations from the mid-latitude (18°S-50°S) network are removed; vi) all stations and vii) Cape Grim. We also include as the viii) the control case.

3. Model description

In this section we describe the physical and biogeochemical features of the models relevant to section 7 on the Southern ocean biological pump.

3.1. Global ocean general circulation model

The ocean model used in this thesis is a modified version of the Modular Ocean Model (MOM), version 3.1 [http://www.gfdl.noaa.gov/~smg/MOM/web/guide_parent/] from the Geophysical Fluid Dynamics Laboratory (GFDL). The ocean model represents the ocean in CSIRO Mark3 climate model [http://www.dar.csiro.au/publications/gordon_2002a.pdf.]. The ocean model domain is global and includes exchanges from the Baltic, Mediterranean and the Great lakes of North America. The horizontal resolution matches the atmospheric model's T63 grid, for future coupling to the atmosphere in climate simulations. The grid has a constant 1.875 degree resolution in longitude and approximately 0.93 degree resolution in latitude - latitude is defined on a Gaussian grid. The model has 31 vertical levels. The resolution gradually expands from 10 m at the surface to 400 m in the deep ocean. There are 7 levels in the top 100 metres (Table 3-1). The model solves the primitive equations discretized on a staggered Arakawa B grid and uses the 3rd order tracer advection scheme '"quicker" for the tracers.

Mesoscale eddies and convection are parameterised by horizontal and vertical eddy diffusivities and viscosities. The horizontal viscosity A_m is specified as a spatially variable function, $A_m=A_o \cos ø$, where A_o is set to 3 x 10^4 m^2 s^{-1}. A background vertical viscosity of 20 cm^2 s^{-1} is also applied. The idealised form of the advection-diffusion tracer (τ) equation is

$$\tau_t + \nabla \cdot (\mathbf{u}C) = (\kappa_v \tau_z)_z + \rho_z \nabla_n \cdot \left(\frac{\kappa_l}{\rho_z}\right) \nabla_n \tau + Q \,, \qquad (2)$$

where ∇_n is the two dimensional gradient/divergence operator applied along the neutral density surface, ∇ is the three dimensional transport operator for the passive advection of tracers by ocean dynamics, **u** is the 3-dimensional velocity, ρ_z is the density, κ_v and κ_i are the vertical and isopycnal diffusion coefficients and Q represents the source and sinks due to biological process and air-sea exchange (discussed in the ocean biogeochemical model section). The terms for vertical and isopycnal tracer diffusion are on the right hand side of Equation (2). The background vertical diffusivities, κ_v, are calculated following Bryan and Lewis (1979) scheme and vary with depth and according to the relation

$$\kappa_v(z) = \kappa_* + \kappa_r \tan^{-1}\left[\lambda(z - z_*)\right], \quad (3)$$

where κ_* is the vertical diffusion coefficient at reference level z_* (i.e. 2500 m) and κ_r is the range of vertical diffusivities from the surface to ocean floor. The background vertical diffusivities within the top 15 model layers were modified (Figure 3-1, dashed line) to produce a sharper and more realistic thermocline in the equatorial regions. [http://www.dar.csiro.au/publications/gordon_2002a.pdf]. An important and relevant modification made by CSIRO to the physical model is the implementation of the Chen *et al.* (1994) scheme for the wind-driven turbulent mixing of tracers and momentum. The Chen *et al.* (1994) scheme is a hybrid mixing scheme, that combines the Kraus and Turner bulk mixed layer model [Kraus and Turner (1967)] with Price's dynamic instability model [Price *et al.* (1986)]. The hybrid scheme is an improvement over other mixed layer models since it takes into account that the dominant mixing mechanism differs between the high and low latitudes [Godfrey and Schiller (1997)]. The Krauss-Turner model performs better in the high latitudes regions, which experience prolonged positive buoyancy fluxes and strong winds, and local buoyancy forcing dominates the mixing, and entrainment is calculated by an energy balance model that relates the entrainment velocity directly to momentum and buoyancy fluxes at the ocean surface. The Price instability model performs better in equatorial regions where the buoyancy flux is negative

and the winds are light to moderate. The Price model assumes that mixing is dominated by shear instability and convection, and entrainment is calculated by allowing the mixed layer to deepen until the bulk Richardson number exceed a critical value.

The Chen *et al.* (1994) mixing scheme modifies the Bryan and Lewis (1979) vertical diffusivities throughout the water column. In the mixed layer the Chen *et al.* (1994) mixing scheme resets the vertical diffusivities in the mixed layer to very high values (1.0×10^6 cm^2 s^{-1}). Below the mixed layer, the vertical diffusivities due to the effects of Richardson mixing are added to the background Bryan and Lewis diffusivity. Convection is handled implicitly, for numerical stability, by using a large vertical diffusion coefficient between gravitationally unstable model layers, but becomes redundant when the mixing scheme of Chen *et al.* (1994) is implemented.

All horizontal mixing of tracers is along neutral surfaces. No horizontal laplacian diffusion is necessary due to the implementation of the Gent and McWilliams [1990] scheme. Consequently excessive diapycnal mixing in regions of steeply sloping neutral surfaces can be avoided. Instead the more realistic isoneutral mixing scheme of *Redi, 1982* has been implemented, which is a modified version of the Cox (1987) isopycnal tracer diffusion scheme, to mix tracers along isopycnals. This scheme involves rotating the diffusion tensor, using a small angle assumption as recommended by Gent and McWilliams (1990) and Griffies *et al.* (1998), to align the direction of large diffusivity with the neutral surfaces. A constant isoneutral diffusivity, A_I, of 10^7 cm^2 s^{-1} is used, except in regions of steeply sloping neutral surfaces where the diffusivity is reduced via the Gerdes *et al.* (1991) taper to avoid numerical instability.

The Griffies *et al.* (1998) implementations of the adiabatic eddy-induced transport of Gent and McWilliams (1990) uses an isopycnal thickness diffusivity, κ_i, of 10^7 cm^2 s^{-1}. As for the isoneutral diffusivity, the isopycnal thickness diffusivity is reduced according to the Gerdes *et al.* (1991) taper in regions of steeply sloping neutral surfaces.

3.2. Biogeochemical ocean model

A prognostic biogeochemical model was implemented in the ocean global circulation model to determine distributions of oxygen, dissolved inorganic carbon (DIC), and phosphate and alkalinity. The conservation equation for the biogeochemical tracers is similar to the equation for the temperature and salinity (Equation (2)) except for the additional source/sink terms

$$\tau_t = \Gamma(\tau) + \frac{\partial}{\partial z}\left(F_{virt} + F_{gas} + F_{bio}\right), \tag{4}$$

where τ is the biogeochemical tracer (O_2, DIC, phosphate or alkalinity) in units of mmol m^{-3} s^{-1}, Γ is the three dimensional transport operator for the passive advection-diffusion of the biogeochemical tracers by ocean dynamics, F_{virt} is the virtual flux due to tracer concentration changes driven by changes in freshwater fluxes, F_{gas} is the air-sea gas exchange of τ and F_{bio} is the flux due to biological production and consumption of organic mater and calcium carbonate ($CaCO_3$) . All the fluxes are in units of mmol m^{-2} s^{-1}.

The biogeochemical model uses a monthly climatology of the surface fields for a wind forcing, sea ice cover and atmospheric pressure at sea level, $atmP$, provided by IPSL/LSCE and the photosynthetic growth rate from Matear (1995).

3.2.1. Air-sea gas exchange fluxes

The air-sea fluxes for CO_2 are calculated using the relationship

$$F_{gas} = k_w \left(pCO_2 a \times \frac{atmP}{atmP_o} - pCO_2 o \right) \sigma , \tag{5}$$

where k_w is the piston velocity (m s^{-1}); σ is the solubility of CO_2; $atmP$ is the atmospheric pressure at sea level; $atmP_o$ is 1 atm; $pCO_2 o$ is the sea-surface partial pressure of CO_2 and $pCO_2 a$ is the partial pressure of CO_2

in the atmosphere. pCO_2a is maintained at the pre-industrial average concentration of 280 ppm. $\acute{k}_w$ is calculated based on the Wanninkhof (1992) relationship

$$k_W = \left(1 - f_{ice}\right) \times xkw \times \left(\frac{660}{Sc}\right)^{\frac{1}{2}}, \tag{6}$$

where Sc is the Schmidt number of CO_2 in seawater, $Sc\left(CO_2\right)$, using the relationship from Wanninkhof (1992). The wind forcing variable xkw (m s^{-1}), is related to wind speed via the following relation

$$xkw = a_{conv} \times \left(u^2 + v\right), \tag{7}$$

where u is the instantaneous SSMI wind speed, v is the variance of the instantaneous SSMI wind speed and a_{conv} is the piston velocity conversion factor.

The sea-surface partial pressure of is CO_2, pCO_2o, is determined using modelled temperature, salinity, alkalinity and dissolved inorganic carbon (DIC) in the surface model layer according to the CO_2 solubility formulation of *Weiss and Price, 1980* and dissociation constants [http://www.ipsl.jussieu.fr/OCMIP/] based on a full description of the thermodynamic equilibria of dissolved inorganic carbon species in the ocean.

The air-sea flux of oxygen is calculated in the same manner as for CO_2, The solubility of oxygen is calculated using the approach of Garcia and Gordon (1992) and the Schmidt number of oxygen, $Sc\left(O_2\right)$, is calculated following Keeling *et al.* (1998).

3.2.2. Biological fluxes

New production is the proportion of the net primary productivity that is fuelled by nutrients advected into the euphotic zone. Export production is defined as the proportion of net production that is transported below the mixed layer to the deeper ocean. Since at steady state nutrients must be

conserved, in the model new production is equivalent to the export production.

In the euphotic zone the net biological flux of a biogeochemical tracer is given by

$$F_{bio} = rr \times NP \ , \tag{8}$$

where rr is a constant coefficient representing the molar ratio of the tracer to the production of phosphate, based on the Redfield ratio, and NP (or EP), in units of mol m^{-2} yr^{-1}, is new (or export) production. The stoichiometry of the particulate organic matter (POM) is given by the Redfield ratio of L.A. and J.L. (1995)

$$P:C:O_2 = 1:106:-170 \ . \tag{9}$$

Note that nitrate is not been included in the model and phosphate, P, is the limiting nutrient.

The new production, NP (mmol m^{-2} s^{-1}), or equivalently export production, EP, in the euphotic zone is calculated using the relationship;

$$NP(or\,EP) = \sum_{k=1}^{4}\left[\left(\frac{P_k}{P_k + P_o}\right) \times pgr(T) \times phy \times h_k\right] \times \frac{h_e}{\max(h_e, h_{mld})} \times s_{np} \ , \tag{10}$$

where the non-dimensional term $\frac{P_k}{P_k + P_o}$ has the effect of limiting the rate of new production at high phosphate concentrations (Figure 3-2); P_k is the phosphate concentration in the k^{th} model layer (mmol m^{-3}); P_o is the half saturation constant set at 0.1 mmol m^{-3} and provides a lower productivity limit for the rate of production in nutrient poor waters; $pgr(T)$ (s^{-1}) is the phytoplankton growth rate which varies with the amount of incoming solar radiation averaged over a day and as a function of the solar angle; phy (mmol m^{-3}) is the phytoplankton concentration expressed as phosphate concentration and is set to a constant value of 0.1 mmol m^{-3}; the $\frac{h_e}{\max(h_e, h_{mld})}$ term is a mixed layer adjustment to the

photosynthetic growth rate; h_{mld}, is mixed layer depth; h_k is the thickness of the kth model layer; h_e is the depth of the euphotic layer and is set to the 4th model layer (i.e. h_e is set to ~50 m) and s_{np} is a dimensionless new/export scaling factor adjusted to improve the match between simulated and observed annual mean phosphate concentrations of Conkright *et al.* (2002).

The temperature-dependent photosynthetic growth rate, $pgr(T)$ (s^{-1}), was obtained by taking the monthly mean of the photosynthetic growth rate from Matear (1995). Refer to this reference for details. Note that $pgr(T)$ is approximated by

$$pgr(T) \simeq pgr(T_{mean})\left(a + b(T) + c(T)^2 + d(T)^3\right). \quad (11)$$

Note that, the Southern ocean has been argued to be a high nutrient low chlorophyll region due to the inhibition of phytoplankton growth from iron limitation. In the model, iron is not explicitly modelled but the HNLC regions are mimicked by the limitations imposed on the photosynthetic growth rates by low sea-surface temperatures and by the $\frac{P_k}{P_k + P_o}$ term. This term has the effect of limiting new production in regions of high phosphate concentrations (such as within the Southern Ocean).

The total particulate organic carbon, *POC*, flux from the euphotic layer (i.e. *NP* from Equation (10)) is exported to depth according to the power law relationship of Martin *et al.* (1987)

$$F_{POC}(z) = NP\left(\frac{z}{z_{POC}}\right)^{-b}, \quad (12)$$

where $F_{POC}(z)$ (mmol m^{-2} s^{-1}) is the amount of the total flux reaching the depth level z, the exponent b is the set to 0.9, z_{POC} is the compensation depth (the bottom of the 6th model layer at ~90m). The compensation depth is the depth at which remineralisation equals primary production.

Note: $\left(\frac{z}{z_{POC}}\right)$ is set to 1 above z_{POC} except in waters shallower than the compensation depth where the organic matter is remineralised throughout the water column to conserve phosphate in the model.

The flux of particulate inorganic matter, *PIC*, reaching each depth, $F_{PIC}(z)$ (mmol m^{-2} s^{-1}), is prescribed by the following equation

$$F_{PIC}(z) = 0.8 \times NP \times e^{-\left(\frac{z}{3500}\right)} . \quad (13)$$

Following Yamanaka and Tajika (1996), the *PIC* export was set to 8% of the *POC* export. In the model, the remineralisation of both *POC* and *PIC*, $R_{POC/PIC}(z)$ (mmol m^{-3}), occurs instantaneously according to

$$R_{POC/PIC}(k) = \frac{1}{dz(k)} \int F_{POC/PIC}(k-1) - F_{POC/PIC}(k)\,dt \quad (14)$$

where $F_{POC/PIC}(k)$ is the flux of either *POC* or *PIC* to the k^{th} model layer and $dz(z)$ is the depth of the k^{th} model layer. The *POC* and *PIC* that reaches the bottom is remineralised in the bottom model layer. The remineralisation of *POC* occurs under anoxic conditions and is important in the eastern equatorial Pacific and the Gulf of Guinea. In these regions, *POC* is remineralised by denitrification. This is allowed in the model according to Equation (12) even in the absence of dissolved oxygen. If dissolved oxygen becomes negative during one time iteration, the oxygen concentration is reset to zero and the remineralisation reflects denitrification.

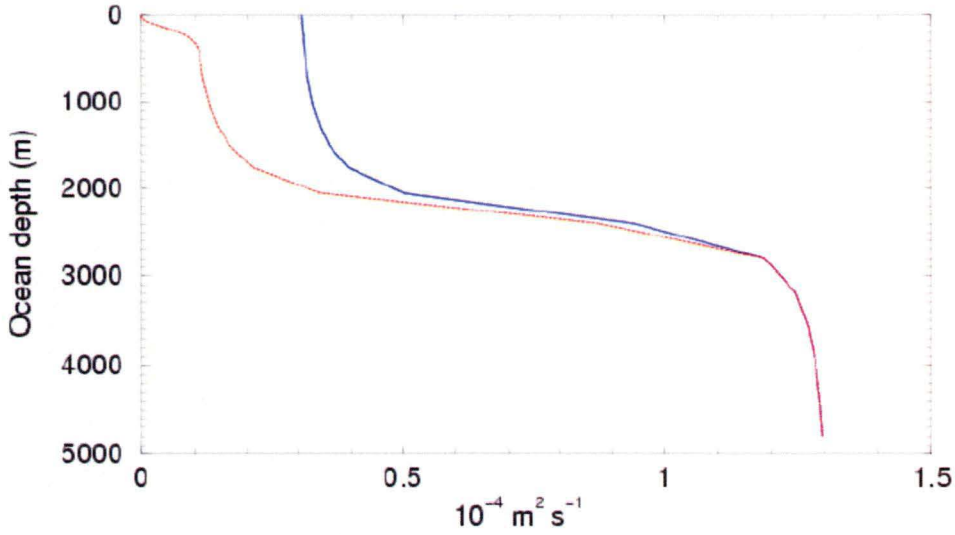

Figure 3-1: Vertical diffusivities as a function of depth. The control case (red line) uses the modified profile of vertical diffusivities from Bryan and Lewis (1979). The standard profile of vertical diffusivities from Bryan and Lewis (1979) (blue line) is used in the perturbation experiment test 15.

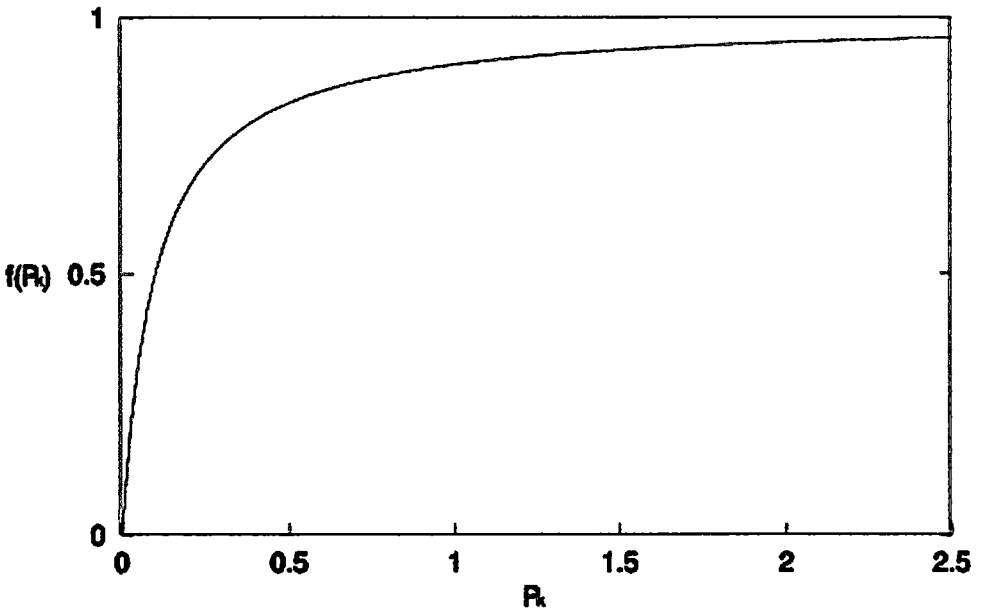

Figure 3-2: The macronutrient saturation curve. The function $f(P_k)=\frac{P_k}{P_k+P_o}$ is the component of the new production equation (Equation (10)), which produces new production rate limitation at high phosphate concentrations.

Table 3-1: Depth coordinates of the global biogeochemical ocean model.

Model level (k)	Depth of layer (*m*)	Layer thickness (*m*)
1	5.00	10.00
2	15.00	11.62
3	28.25	13.51
4	42.02	15.71
5	59.66	18.26
6	78.54	21.22
7	102.11	24.67
8	127.88	28.68
9	159.47	33.34
10	194.56	38.75
11	236.97	45.04
12	284.65	52.36
13	341.69	60.87
14	406.38	70.75
15	483.19	82.24
16	570.87	95.83
17	674.86	111.45
18	793.76	129.61
19	934.08	150.73
20	1095.21	175.29
21	1284.65	203.85
22	1502.91	237.06
23	1758.77	275.69
24	2054.29	320.61
25	2400.00	372.85
26	2800.00	400.00
27	3200.00	400.00
28	3600.00	400.00
29	4000.00	400.00
30	4400.00	400.00
31	4800.00	400.00

4. Perturbation experiments

In this section, the biogeochemical and physical circulation experiments designed for section 7 and 8 are described. In sections 7 and 8 we use a global biogeochemical ocean model, to assess whether the observational techniques currently used to estimate new production, from seasonal oxygen variability, actually work. We know that both the variability in the magnitude of new production, and in the physical circulation and the biogeochemical properties of the ocean, changes the seasonal variability of oxygen fluxes. The perturbation experiments were designed to span a feasible range of new production, remineralisation and physical circulation scenarios. By applying the observational techniques to the simulated seasonal oxygen fluxes from each of these experiments, we can determine whether we can expect the techniques to be effective, given the range of possible physical circulation, new production and biogeochemical states of the ocean. If the oxygen fluxes are more sensitive to the remineralisation and circulation perturbations than the new production perturbation, we may conclude that the technique is not effective in the southern hemisphere oceans.

We distinguish between the new production, biogeochemical formulation and physical circulation experiments. The new production experiments were designed specifically to perturb the magnitude of new production in the southern hemisphere oceans, while the biogeochemical formulation experiments change the distribution of nutrients within the water column without significantly changing the magnitude of new production. The physical circulation in the new production and biogeochemical formulation experiments the oceanic circulation is identical. To determine the effect of the physical circulation on oxygen fluxes, the physical circulation experiments were designed to change the properties that would be expected to change the supply of nutrients to the

ocean surface, and thus the oxygen concentrations at the ocean surface, without changing the magnitude of new production.

The model was initialised with the annual mean temperature and salinity fields of Conkright *et al.* (2002), and global mean concentrations were used for the biogeochemical tracers (i.e. oxygen 200 mmol m^{-3}; DIC 2000 mmol m^{-3}; phosphate 2.238 mmol m^{-3} and alkalinity 2428.1 mmol m^{-3}). To produce the restart file the model was run to quasi-steady state for approximately 2500 years without any changes to the model formulation. All the new production and remineralisation perturbation experiments were initialised from a common restart file. The tracer equation was integrated with a time step of 0.5 days. All the biogeochemical experiments were run for 500 years. Although the ocean has not reached equilibrium below the surface ocean, the response over 500 years gives a good indication of the potential signature of export production on the tracer distributions. The physical perturbation experiments were run to quasi-equilibrium for different time periods listed in Table 4-3.

4.1. New production perturbation experiments

The new production experiments were designed to perturb the magnitude and distribution of new production in the southern hemisphere oceans without changing the ocean circulation. The perturbations are summarised in Table 4.1. Firstly, we run two cases with different new production scaling factors (Equation (10)). In the first case (test 4), we double the new production scaling factor (i.e. $s_{np} = 0.05$) and in the second (test 5), we halve the scaling factor (i.e. $s_{np} = 0.0125$). The magnitudes of southern hemisphere new production from these perturbations lie within the range of estimates from satellites, sediment traps, Fe fertilisation experiments and global biogeochemical ocean circulation models. Estimates of primary production in the Southern Ocean, based on satellite ocean colour data, vary by a factor of two interannually [Moore *et al.* (1999)]. A doubling in primary productivity was observed during the artificial iron release experiment, SOIREE [Boyd *et*

al. (2000)]. Particle fluxes from deep sediment trap moorings in Southern Ocean vary by more than a factor of 2 interannually [Honjo *et al.* (2000); Tom Trull (personal communication)]. The new production experiments vary by as much as a factor of 4. Note that since in the model new production and export production are equivalent, the two processes are discussed.

Second, we perturb the magnitude of southern hemisphere new production by changing the temperature dependence of biological productivity (Equation (11)). The influence of temperature on new production is uncertain. We remove the dependence of biological productivity on temperature by fixing the temperature in the temperature-dependent growth rate curve of Eppley (1972) (Figure 4-1) to the global modelled annual mean temperature (i.e. 18°C) (Table 4.1- test 1). The effect is to increase new production in the waters lower than 18°C and slightly decrease new production in higher temperature waters. Ecosystem based approaches to determining export production disagree on the influence of temperature on export production. Laws *et al.* (2000), based on data from 11 sites, showed a strong correlation between the *f*-ratio and temperature, suggesting that lower temperatures decrease the growth rates of heterotrophic bacteria. Consequently more organic matter escapes the euphotic zone before remineralising (i.e. higher export production). Conversely, higher temperatures increase the growth rates of heterotrophic bacteria and more particulate organic matter is remineralised within the euphotic zone (i.e. lower export production). Moore *et al.* (2002a) found little export variability with temperature, using a global intermediate complexity ecosystem model [Moore *et al.* (2002b)]. They suggest this discrepancy may be due to an observational bias towards choosing high export sites in the Southern Ocean, and to mixing and detrainment processes not accounted for, in the Laws *et al.* (2000) study. In cold waters the export ratio in the Laws *et al.* (2000) study is almost 3 times the ratio of Moore *et al.* (2002a) [see Figure 13 in Moore *et al.* (2002a)]. The sensitivity test (test 1) produces a similar change (i.e. by a factor of > 2) in export/new production relative to the control. The

sensitivity test mimics the correlation of export with temperature from Laws *et al.* (2000), while the control case exhibits no explicit dependence of export production on temperature similar to Moore *et al.* (2002a).

To further perturb the magnitude of new production in the Southern Ocean, another experiment is run (Table 4-1 - test 2), where in addition to changing the temperature dependence of new production the scaling factor is doubled as in test 4. This perturbation produces an almost 4-fold increase in new production in the southern hemisphere oceans.

4.2. Biogeochemical formulation experiments

This set of experiments was designed i) to perturb the parameterisation of key biogeochemical processes, particularly those expected to have a significant effect on the supply of nutrients to the surface ocean, and ii) to span the range of uncertainty for a selection of key model parameters.

One of the key uncertainties in modelling oceanic nutrient cycles is the remineralisation of organic and inorganic matter in the water column. Two cases are run to span a range of possible remineralisation profiles. The exponent, *b*, from Equation (12) determines the shape of the remineralisation profile (Figure 4-2), altering the depth at which particulate organic matter remineralises in the water column. In the first experiment (Table 4-3 - test 6), the remineralisation profile is deepened by halving the value of the exponent, *b*, in the remineralisation function, from the control experiment (i.e. $b = 0.45$, Figure 4-2). In the second experiment (Table 4-3 - test 7), the exponent is doubled (i.e. $b = 1.8$, Figure 4-2), resulting in a shallower remineralisation profile. Schlitzer (2002a) demonstrated that to match hydrographic and nutrient observational constraints in the Southern Ocean, organic matter must be remineralised shallower in the water column (i.e. $b = 1.08$) than what is predicted using the standard remineralisation exponent of Martin *et al.* (1987) (i.e. $b = 0.89$). In some regions, Schlitzer (2002a) estimated *b* to be greater than 2. Observation-based estimates of the flux of particulate matter to depth also suggest spatial and temporal variations in the remineralisation exponent. One

school of thought argues that deeper remineralisation profiles occur as a result of short circuiting the food web and particle aggregation, while another school of thought argues for repackaging of smaller particles by the food web into larger, faster sinking particles. Francois *et al.* (2002) found that the exponent of the power function must vary spatially between 0.7 and 1.2 to provide a reasonable estimate of the particle flux to the deep-sea. They suggest that transfer of particulate organic matter to depth in the Southern Ocean is less efficient than in the lower latitudes. In the tropics, POC is not processed as extensively by the food-web before being exported out of the mixed layer, and is therefore remineralised more efficiently at shallower depths. Algorithms used to estimate the particle flux into the mesopelagic ocean (200 to 1000 m) diverge widely, and sufficient observations do not exist to test the algorithms. The remineralisation profiles chosen for the perturbation experiments represent extremes and the profiles produce a wide range of particle fluxes within the mesopelagic regions of the ocean. Berelson (2001) estimates the exponent from four JGOFS cruises using particle flux from deep and mid-depth sediment traps and found that the exponents vary spatially within the Southern Ocean from 0.5 to 2.

Another uncertainty in the remineralisation of biological matter is the depth at which remineralisation equals primary production, known as the compensation depth, z_{poc} (Equation (12)). Below the compensation depth remineralisation produces a net increase in dissolved nutrients. In the control experiment the compensation depth is set to the depth of the 6th model layer (i.e. $z_{poc} \approx 90\,\mathrm{m}$, Equation (12)). We run a perturbation experiment with a shallower compensation depth (Table 4-3 - test 8). In test 8, the compensation depth is set to the depth of the 5th model layer (i.e. $z_{poc} \approx 69\,\mathrm{m}$, Equation (12)).

Another process that can alter the distribution of dissolved nutrients in the surface ocean is the depth of the euphotic zone, the depth over which biological productivity occurs. In the control experiment, the euphotic zone is set to the depth of the 4th model layer (i.e. h_e = 50 m,

Equation (10)). We run a perturbation experiment with a deeper euphotic zone (i.e. Table 4-3 - test 13, h_e = 69 m).

4.3. Physical circulation perturbation experiments

Like with the biogeochemical parameters there is considerable flexibility in the parameter values of the physical model. The sensitivity tests were designed to systematically perturb both parameters and model formulations that change features of the oceanic circulation known to influence the supply of nutrients to the surface ocean, which include the meridional overturning, lateral advection, vertical stratification, mixed layer evolution and mesoscale effects. While an effort was made to perturb each of these processes, it is difficult to treat these processes independently since changing one process inadvertently influences other oceanic features.

How to parameterise mesoscale processes and vertical diffusivities in global circulation models remains an unresolved issue. Commonly used isopycnal thickness diffusivities range from 0.3 x 10^7 cm^2 s^{-1} to 2.0 x 10^7 cm^2 s^{-1}. In the control case, we use an intermediate value of this parameter (i.e. κ_l = 1.0 x 10^7 cm^2 s^{-1}). It has been common to set the isopycnal thickness and along isoneutral diffusivities, κ and A_l, to the same value. More recent theoretical work suggests setting the isopycnal thickness diffusivity to 1/3 or 1/4 that of the along isoneutral diffusivity (http://www.gfdl.noaa.gov/~smg/MOM/web/guide_parent/). With increased model resolution, the magnitude of the eddy diffusivity parameter can be reduced [Trevor McDougall, personal communication].

Two experiments were designed to test the influence of changing the isopycnal thickness diffusivity via the scaling coefficient, κ_l (Equation (2)). In one experiment (i.e. test 11, Table 4-3) the isopycnal thickness coefficient is halved (i.e. κ_l = 0.5 x 10^7 cm^2 s^{-1}, Equation (2)). Decreasing κ_l increases North Atlantic Deep Water (NADW) formation and increases convective instabilities in the North Atlantic and Southern Ocean. In the other experiment (i.e. test 12, Table 4-3) the isopycnal diffusivity

parameter is doubled (i.e. $\kappa_i = 0.5 \times 10^7$ cm^2 s^{-1}, Equation (2)). It has been argued that the κ_i should reflect the high values found in boundary currents and the Southern ocean (Visbeck *et al.* (1997)) rather than the lower values of subtropical gyres. In the Southern Ocean the isopycnals slope steeply, increasing the tendency to produce baroclinic instabilities and the highest eddy transport occurs. Increasing κ_i increased the overturning in the Northern Hemisphere and reduced convection along the Antarctic continent due to the stabilising effect from the diffusion of isopycnal thickness, which flattens the isopycnals. Increasing κ_i also increases the northward flow of cold and fresh surface waters, which are swept over warmer saltier waters reducing convection in regions of the Southern Ocean.

Next we test the effect of reducing the surface stratification in the model by changing the vertical diffusivity profile. The vertical diffusivity profile of Bryan and Lewis (1979) is the most commonly used profile in global ocean circulation models. The control case is run with a *modified* Bryan and Lewis (1979) profile. In this profile (Figure 3-1), vertical diffusivities are reduced through the top ~2000 m of the ocean to produce a sharper thermocline for improved simulations of tropical interannual variability in the coupled CSIRO climate model. We run an experiment where we change the vertical diffusivities by replacing the vertical diffusivity profile with the standard profile of Bryan and Lewis (1979). The vertical diffusivity increases from 0.3 cm^2 s^{-1} at the ocean surface to 1.3 cm^2 s^{-1} at the ocean bottom according to Equation (2).

The influence of convection is tested by replacing the vertical mixing scheme of Chen *et al.* (1994) (test 9) by implicitly vertically mixing model layers that are gravitationally unstable. The vertical mixing homogenises tracers throughout the water column. Replacing the vertical mixing scheme of Chen *et al.* (1994) essentially eliminates wind-driven vertical mixing. The only way deep mixed layers form is through overturning due to static instability.

We run an experiment that essentially perturbs the heat and freshwater fluxes. In the model the surface fluxes for the tracers, *T*, heat

and freshwater, $F(T)$, are calculated by restoring to Conkright *et al.* (2002) using a Newtonian damping according to

$$F(T) = \frac{dz_1}{\gamma}(T - T^*), \tag{15}$$

where γ (s) is a time constant; dz_1(m) is the thickness of the surface model layer; T is the tracer concentration in the top model layer and T^* is the prescribed tracer field of Conkright *et al.* (2002). It is often argued that relaxing surface temperature and salinity values to a climatology is a form of data assimilation since in general these tracers are better known than the surface heat and freshwater fluxes. In the control case, temperature is relaxed back to the climatology of 6-day time scale (i.e. $\gamma(T) = 6 \times 86400\,\mathrm{s}^{-1}$, Equation (15)). In the perturbation experiment (test 18), we use a relaxation time scale of 30 days.

Two final experiments (test 19) were designed specifically to increase mixed layer depths in the Southern ocean. Two changes were made to the control experiment. As for test 18, $\gamma(T) = 6 \times 86400$ s^{-1}. In addition, the isopycnal thickness diffusivity was reduced to 0.3 cm^2 s^{-1}. Mixed layers are increased throughout the high-latitude oceans, particularly in the Subantarctic zone of the Southern ocean. The physical circulation in test 20 is identical to test 19, but new production is increased by quadrupling the new production scaling factor (i.e. $s_{np} = 0.1$, Table 4-3).

All cases are initialised from the same restart file as for the biogeochemical perturbation experiments, except for test 18, test 19 and test 20. The physical circulation experiments were run for different time periods ranging between 1300 and 2800 years, and are listed in Table 4-3. Ideally we would like all models to be run for longer and equivalent amounts of time, but the large computing expense limits the run times. Only small changes in the seasonal anomalies of the biogeochemical tracer concentrations occur with longer integrations times.

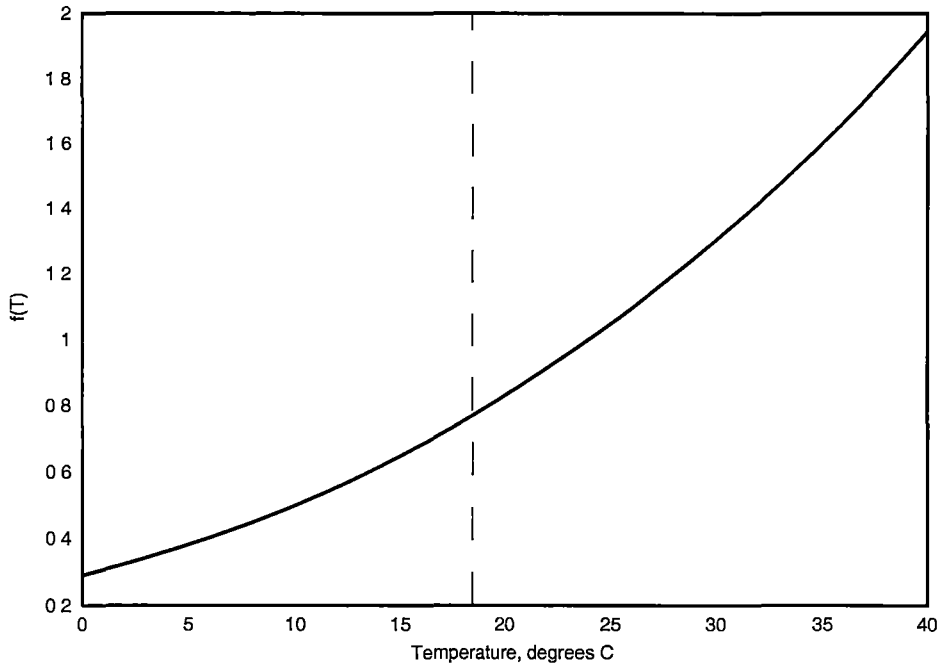

Figure 4-1: The maximum temperature-dependent growth rate curve from Eppley (1972)

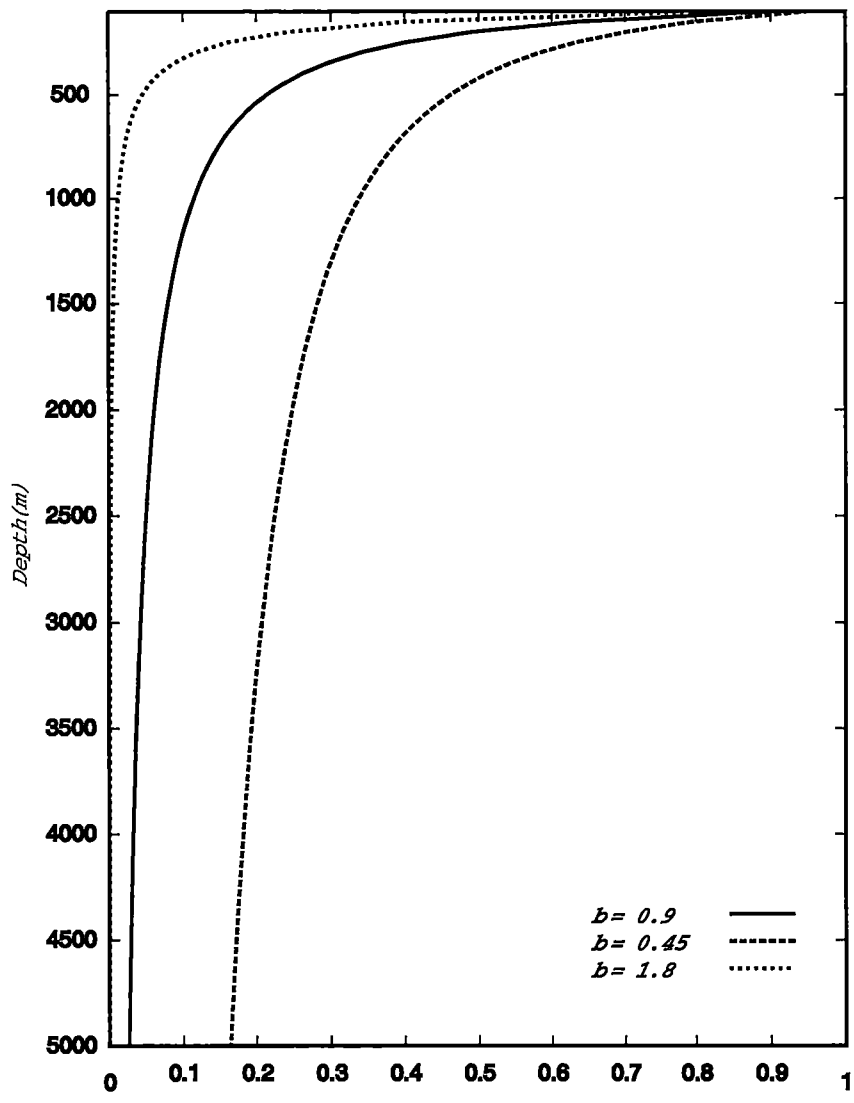

Figure 4-2: Flux profiles of Martin *et al.* (1987) (Equation (12)) with different values of the exponent, *b*.

Table 4-1: A summary of the new production perturbation experiments. Each perturbation experiment was run for 500 years from the same physical and biogeochemical initial conditions. The initial biogeochemical and physical circulation fields had been run to quasi-equilibrium.

Experiment	Perturbation description	
1	Remove temperature dependency of productivity	T=18°C (Equation (11))
2	Increase new production scaling factor Remove temperature dependency of productivity	s_{np} = 0.05 (Equation (10)) T=18°C (Equation (11))
4	Increase new production scaling factor	s_{np} = 0.05 (Equation (10))
5	Decrease new production scaling factor	s_{np} = 0.0125 (Equation (10))
17	Reduce export production scaling factor in the Southern Ocean only	s_{np} = 0.05 (Equation (10))
22	No biological productivity in Southern hemisphere oceans	s_{np}= 0 between 20°S and 90°S (Equation (10))
23	No biological productivity in the global oceans	s_{np}= 0 throughout the global ocean (Equation (10))

Table 4-2: A summary of the biogeochemical formulation perturbation experiments. Each perturbation experiment was run for 500 years from the same physical and biogeochemical initial conditions. The initial biogeochemical and physical circulation fields had been run to quasi-equilibrium.

Experiment	Perturbation description	
6	Shallower remineralisation profile	b = 0.45 (Equation (12))
7	Deeper remineralisation profile	b = 1.8 (Equation (12))
8	Shallower compensation depth	z_{poc} = 69m (Equation (12))
13	Deeper euphotic zone depth	$\sum_{k=1}^{5}$ in place of $\sum_{k=1}^{4}$ (i.e. h_e = 69 m) (Equation (10))

Table 4-3: A summary of the physical circulation perturbation experiments.

Experiment no.	Integration Time (years)	Experiment description
9	5679	Constvmix vertical mixing scheme used in place of the mixing scheme of Chen *et al.* (1994).
11	2428	Decreased isopycnal thickness diffusivity, $\kappa_i = 0.5 \times 10^7$ cm^2 s^{-1}
12	1252	Increased isopycnal thickness diffusivity $\kappa_i = 2.0 \times 10^7$ cm^2 s^{-1}
15	1761	Increased vertical diffusivities, κ_v, in the top ~2000m of the ocean. (Figure 3-1). Vertical diffusivity profile of Bryan and Lewis (1979)
18	1862	Decreased temperature relaxation time scale $\gamma = 6 \times 86400$ s^{-1}
19		Decreased temperature relaxation time scale $\gamma = 6 \times 86400$ s^{-1} $\kappa_i = 0.3 \times 10^7$ cm^2 s^{-1}
20		Decreased temperature time scale and increased new production scaling factor (Equation (10)). $\gamma = 6 \times 86400$ s^{-1} (Equation(15)) $\kappa_i = 0.3 \times 10^7$ cm^2 s^{-1} $s_{np} = 0.1$

Note: In the control case the temperature and salinity relaxation time scales are set to 6 and 30 days respectively. The eddy diffusivity thickness coefficient and κ_i, is set to 1.0×10^7 cm^2 s^{-1}.

5. Modelled new production estimates

In this section, we describe how and why the perturbation experiments alter the magnitude and spatial distributions of new production. The assessment of whether the new production is similar to what is observed in the real ocean is discussed in section 6.

Since in section 7, we test how well the modelled new production fields in the southern hemisphere oceans are retrieved using atmospheric and oceanic oxygen tracers, it is important that we produce a range of experiments with different magnitudes of new production, particularly inside the southern hemisphere oceans. Oxygen concentrations in the southern hemisphere depend on changes in new production outside as well as inside the southern hemisphere oceans, so we also briefly present the global distribution of new production. Also, to tease apart the effects of the circulation and new production on the air-sea fluxes of oxygen in the southern hemisphere oceans (section 7), we would like to produce a series of experiments where the new production magnitudes are changed without altering the circulation and a series of experiments where the ocean circulation is changed without changing the distribution of new production.

5.1. Globally integrated new production

The global annual mean new production in the control case is 4.5 GtC yr^{-1} (Table 5.1). The global annual mean new production from the biogeochemical perturbation experiments ranges between 3.3 GtC yr^{-1} and 5.9 GtC yr^{-1} (Table 5.1). This range is small considering the relatively extreme changes made to the biogeochemical parameterisations. Even the biogeochemical perturbation experiment with the highest new production of 5.9 GtC yr^{-1} (test 7, Table 5.1) is on the lower end of the range predicted by other similar models [Maier-Reimer *et al.* (1996); Gnanadesikan *et al.* (2002); *Najjar et al. (2003)*]. Globally dissolved organic matter only accounts for about 10 to 20% of export production

[Hansell and Carlson (1998)]. Thus, including dissolved organic matter would only partly explain the low export production in the model. The only way the magnitude of new production can be increased significantly is by changing the physical circulation [Gnanadesikan *et al.* (2002)]. The set of biogeochemical perturbation experiments shows that global new production is most sensitive to the remineralisation length scale in the equatorial regions. Dramatic changes to the scaling factor and the temperature dependence of new production are required to produce a similar response.

Shallowing the remineralisation profile (test 7) increases global new production by 1.4 GtC yr^{-1}, while deepening the remineralisation profile (test 6) reduces the production by 1.2 GtC yr^{-1} (Table 5.1). Shallowing the compensation depth (test 8) has a similar effect to shallowing the remineralisation profile, increasing new production by 0.8 GtC yr^{-1}. In the model, the magnitude of global new production is very sensitive to the rate at which nutrients are resupplied to the euphotic zone within the equatorial regions. New production throughout the tropics is limited by the rate of vertical nutrient resupply, while the rate of nutrient resupply in high latitudes has very little influence on the magnitude of new production because nutrient concentrations throughout much of the high latitudes are high, so the nutrient dependent term in the new production equation is effectively saturated (i.e. $\frac{P_k}{P_k + P_o} \approx 1$, Equation (10)). Physically, the rate of nutrient supply to the equatorial regions is increased by increasing the vertical diffusivities in top ~2000 m (Figure 3-1, test 15), increasing global new production to 7.1 GtC yr^{-1} (60%) due to increases in new production in the equatorial regions (Figure 5-1a). Increasing the vertical diffusitivies reduces the surface stratification and increases the rate of upwelling, and simultaneously the rate of nutrient supply. The rate of nutrient resupply in the equatorial regions is increased biogeochemically by either shallowing the remineralisation profile (test 6), or the compensation depth (test 8). Increasing the nutrient supply increases the concentration of nutrients in the waters upwelled into the

euphotic zone. Lengthening the remineralisation profile results in less nutrient remineralisation shallower in the water column. The upwelled water is less rich in nutrients resulting in a reduction in the new production throughout the equatorial regions (Figure 5-1b).

Unreasonable changes to the scaling factor and the temperature dependence of new production would be required to produce a similar shift in global new production. The new production scaling factor does not scale global new production effectively. Doubling the scaling factor (test 4) increases new production by only 11%, while halving the scaling factor (test 5) reduces new production by only 2%. Although, doubling the scaling factor effectively doubles new production in the high latitudes, new production in the equatorial regions is reduced (Figure 5-1c). To interpret these responses it helps to look at the spatial distributions of new production for the experiments. The spatial distributions of new production for the control case and the new production, biogeochemical and physical perturbation experiments are shown in Figure 5-2, Figure 5-3, Figure 5-4 and Figure 5-5 respectively. The reduction in equatorial new production produced from increasing the new production scaling factor is probably due to two effects. Firstly, increasing new production in the southern hemisphere oceans exports nutrients out of southern ocean waters that resupply nutrients to the tropics [Sarmiento *et al.* (2004)]. Secondly, from comparing the spatial distribution of new production in the control case (Figure 5-2) with the distribution produced by increasing the scaling factor (Figure 5-3b,c), shows that increasing the scaling factor concentrates new production close to the west coast upwelling regions of the equatorial regions causing a trapping of nutrients at depth below the thermocline.

New production is also increased by 0.7 GtC yr^{-1} if the temperature dependence of productivity is removed (test 1). The remaining biogeochemical perturbation experiments have very little influence on the global annual mean new production, changing new production by no more than ± 0.1 GtC yr^{-1}.

Note that we do not discuss the Northern hemisphere in much detail since the northern and southern high latitudes show similar proportional changes to the perturbation experiments and are less relevant to our studies, which focus primarily on the southern hemisphere. Also, the new production from the high northern latitudes contributes much less to the global total. So, even a doubling of new production in the northern hemisphere does not affect the global number significantly.

5.2. Equatorial new production perturbation responses

As previously discussed, new production in the equatorial regions is most sensitive to the remineralisation profile (test 6 and test 7) and compensation depth (test 8 – Table 5.1, Figure 5-1b). Shallowing the remineralisation profile (test 7) results in an almost 50 % (0.8 GtC yr^{-1}) increase in equatorial new production. But the largest increase (1.9 GtC yr^{-1}) occurs in the experiment with increased vertical diffusivity in the top ~ 2000m of the ocean (test 15 – Table 4.3). Increasing the vertical diffusivities reduces the surface stratification through the tropics, which increases the supply of nutrients to the region.

The new production scaling factor (test 4 and test 5) has little influence on the magnitude of equatorial new production (i.e. ± 0.3 GtC yr^{-1}, Table 5.1). The scaling factor changes the distribution of new production (Figure 5-3), but only slightly changes the magnitude of new production in the region (Figure 5-1c) since the total amount of nutrients supplied to and utilised within the region does not change with scaling. The region over which the new production extends depends on how efficiently the nutrients are utilised. By reducing the scaling factor, new production in the equatorial pacific decreases in the east and increases in the west. More of the nutrients supplied to the ocean surface in the upwelling regions escape export production and are advected zonally to the western side of the ocean basins and meridionally towards the subtropical gyres. Increasing the scaling factor concentrates new production closer to the regions of strong upwelling regions. New

production is ultimately limited by the supply of nutrients into the region, which does not change much with new production scaling factor perturbations.

Note that the only physical perturbation experiment that also has a different distribution of new production outside the southern hemisphere ocean is the experiment run with increased vertical diffusivities (Figure 5-1c).

5.3. Southern hemisphere new production responses

The response of new production to the perturbation experiments in the Southern Ocean is more intuitive than in the equatorial regions. Since nutrient concentrations are high, new production scales directly with changes to the new production scaling factor (i.e. test 4 and test 5 in Table 2, Figure 4). Doubling the scaling factor doubles new production. Any changes to the remineralisation scheme (test 6, test 7 and test 8) have no effect since productivity is already nutrient saturated (i.e. $\frac{P_k}{P_k + P_o} \approx 1$, Equation (10)) and changes to the nutrient supply have little impact. Removing the dependence of productivity on temperature (test 1) increases new production relative to the control case.

In the high latitude oceans the new production scaling factor (test 2, test 4 and test 5) and the temperature dependency of production (test 1) have the greatest impact on new production (Figure 5-1c). Removing the dependence of the photosynthetic growth rate on temperature (test 1) prevents the inhibition of biological production in the high latitudes where temperatures are much less than 18°C (Figure 4-1). Consequently, the new production in the high latitudes is increased.

The new production experiments provide a range of distributions (Figure 5-1c) and magnitudes of southern hemisphere (15°S – 90°S) new production (i.e. 1.7 to 3.8 GtC yr^{-1}, Table 5.1). Each of the new production experiments has the same physical circulation. The physical perturbation experiments provide a suite of runs with virtually identical magnitudes and

distributions of new production in the southern hemisphere (Figure 5-1a) but with different physical circulation.

Table 5-1: Zonal and global new production estimates (GtC yr^{-1}) for the control and perturbation experiments. The biogeochemical perturbation experiments are marked by a * and the physical perturbation experiments are marked by a $^{\#}$. The air-sea fluxes experiments listed in bold were also run in an atmospheric transport model.

Zonal New Production	90°N-66°N	66°N -50°N	50°N -15°N	15°N-15°S	15°S -50°S	50°S -90°S	Global total
Control	0.06	0.19	0.65	1.7	1.5	0.45	4.5
1*	0.10	0.30	0.67	1.5	1.6	1.0	5.2
2*	0.11	0.41	0.51	1.0	1.8	2.0	5.8
4*	0.09	0.32	0.59	1.4	1.8	0.89	5.1
5*	0.04	0.10	0.86	1.9	1.3	0.23	4.4
6*	0.05	0.17	0.43	1.0	1.2	0.45	3.3
7*	0.07	0.20	0.89	2.5	1.7	0.45	5.9
8*	0.06	0.19	0.79	2.2	1.4	0.7	5.3
9$^{\#}$	0.06	0.18	0.51	1.7	1.4	0.55	4.4
11$^{\#}$	0.06	0.19	0.77	1.8	1.7	0.45	5.0
12$^{\#}$	0.05	0.18	0.47	1.5	1.2	0.45	3.9
13*	0.07	0.21	0.73	1.9	1.6	0.55	5.0
15$^{\#}$	0.06	0.22	0.96	3.6	1.6	0.66	7.1
18$^{\#}$	0.06	0.22	0.53	1.8	1.2	0.67	4.5
19$^{\#}$	0.06	0.38	0.75	2.1	1.4	0.67	5.3

a)

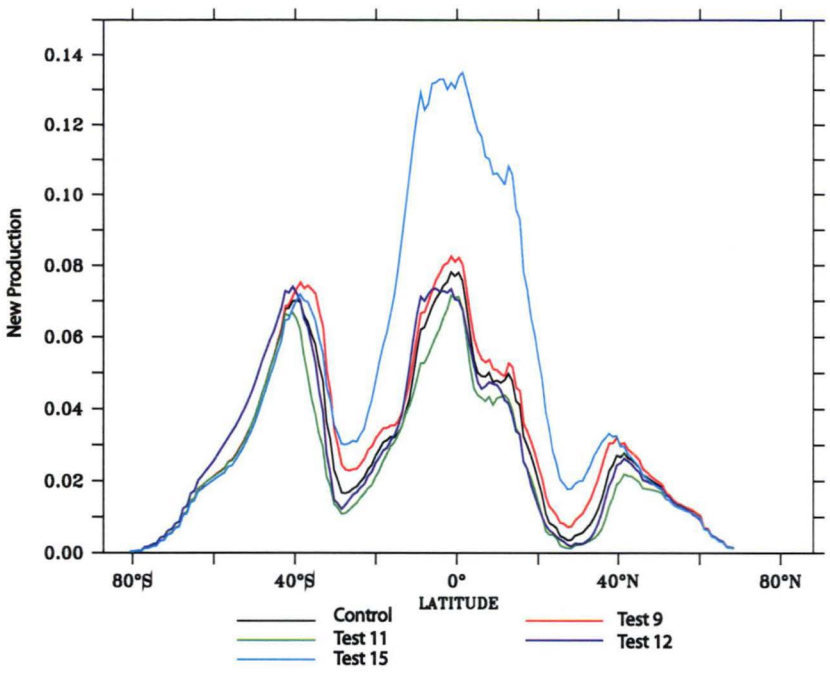
New Production
0.14
0.12
0.10
0.08
0.06
0.04
0.02
0.00
80°S
40°S
0°
40°N
80°N
LATITUDE
Control
Test 11
Test 15
Test 9
Test 12

b)

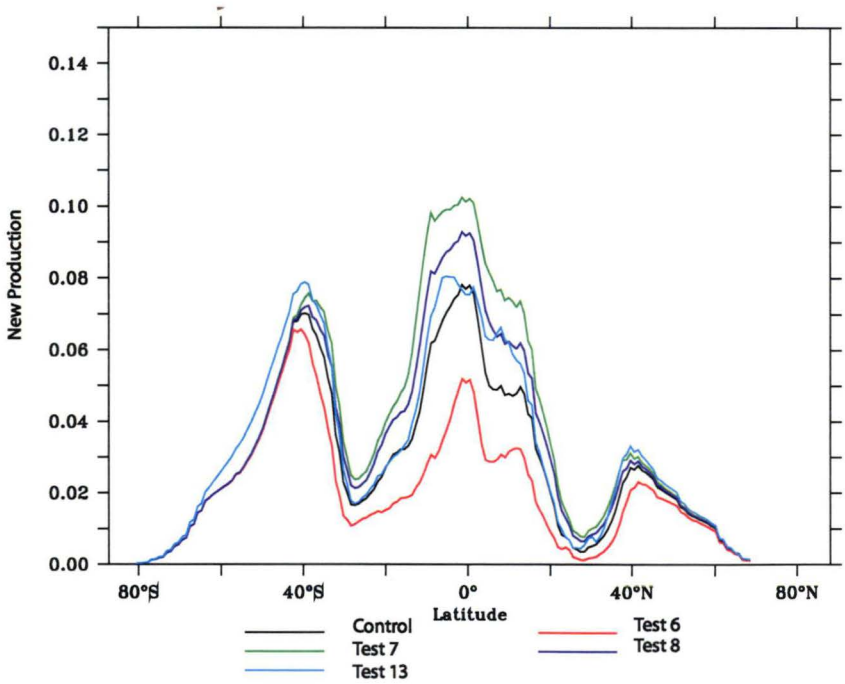
New Production
0.14
0.12
0.10
0.08
0.06
0.04
0.02
0.00
80°S
40°S
0°
40°N
80°N
Latitude
Control
Test 7
Test 13
Test 6
Test 8

c)

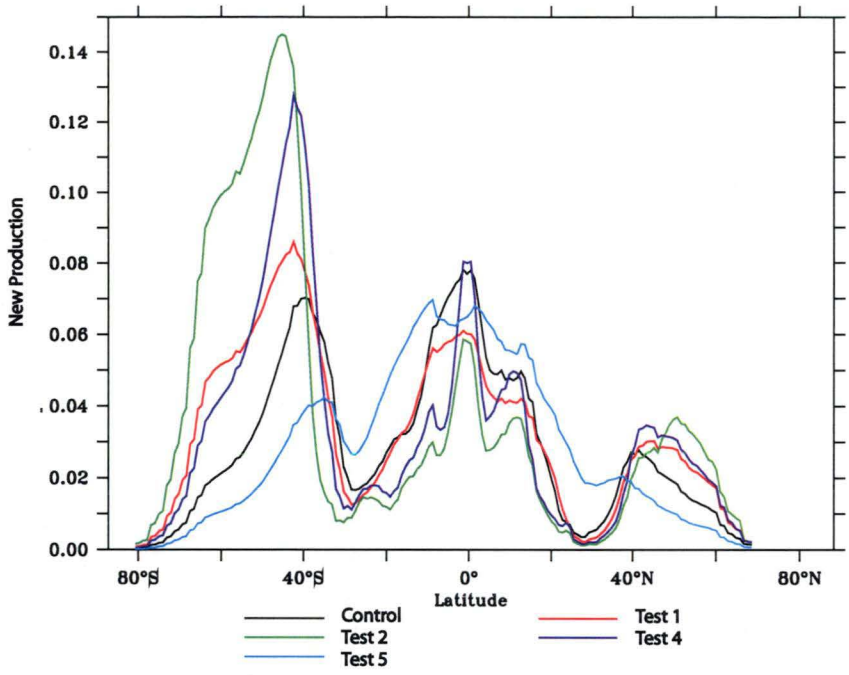

Figure 5-1: Zonally integrated new production (GtC deg^{-1} yr^{-1}) for the perturbation experiments – a) physical circulation perturbation experiments (Table 4.3), b) biogeochemical formulation perturbation experiments (Table 4.2) and c) new production perturbation experiments (Table 4.1).

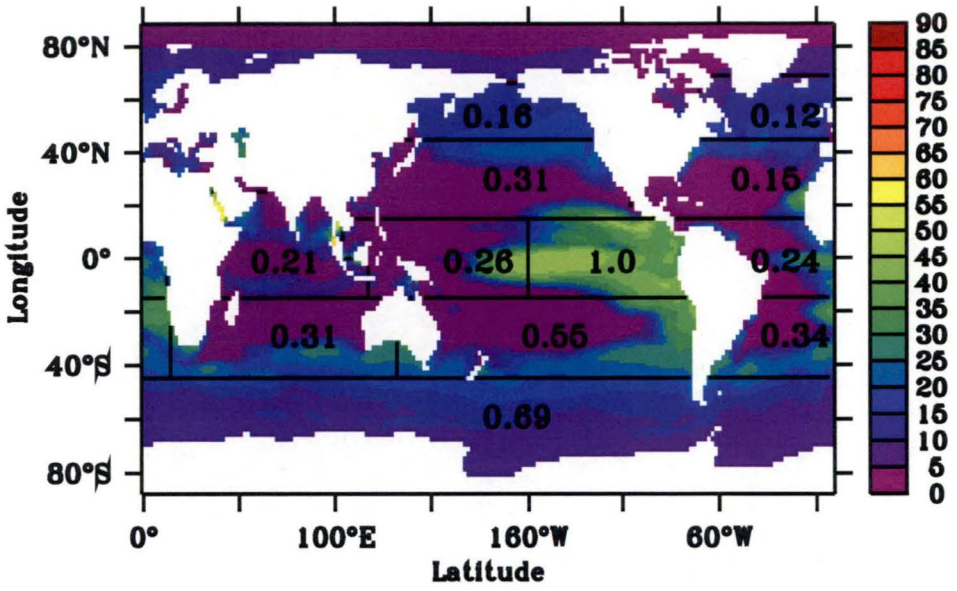

Figure 5-2: Distribution of new production for the control case (gC m^{-2} yr^{-1}). The total regional new production estimates (GtC yr^{-1}) are listed inside the marked regions.

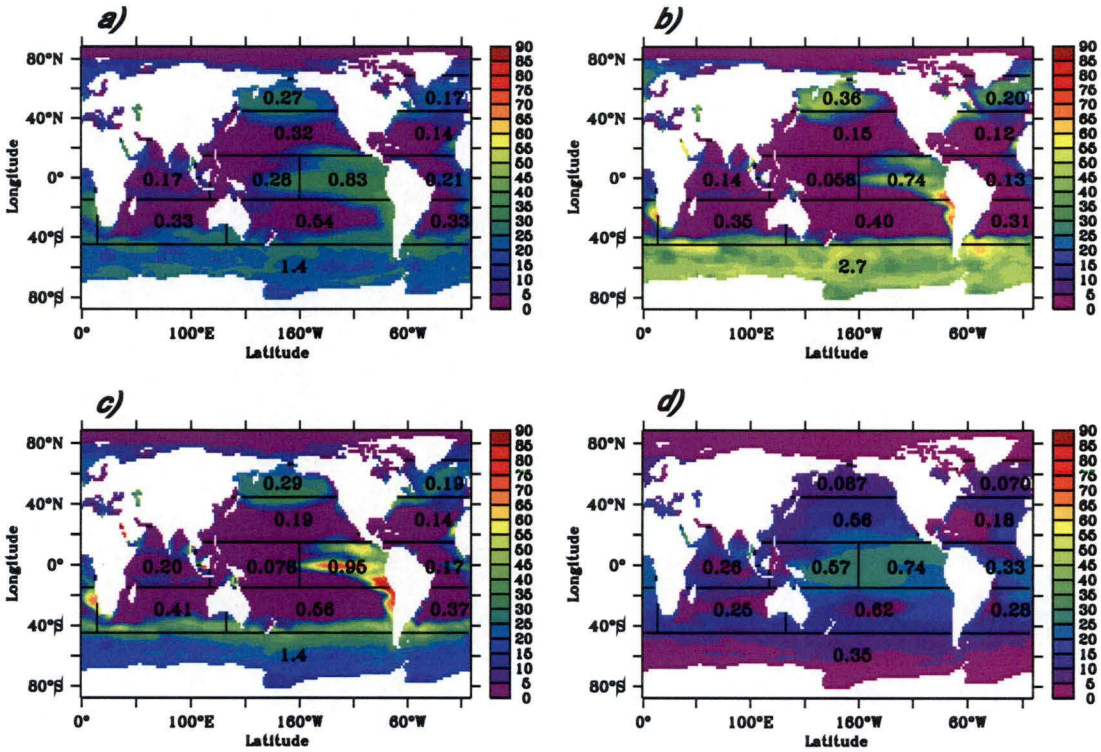

Figure 5-3: Distributions of new production for the new production perturbation experiments a) test 1, b) test 2, c) test 4 and d) test 5. The total regional new production estimates (GtC yr^{-1}) are listed inside the marked regions.

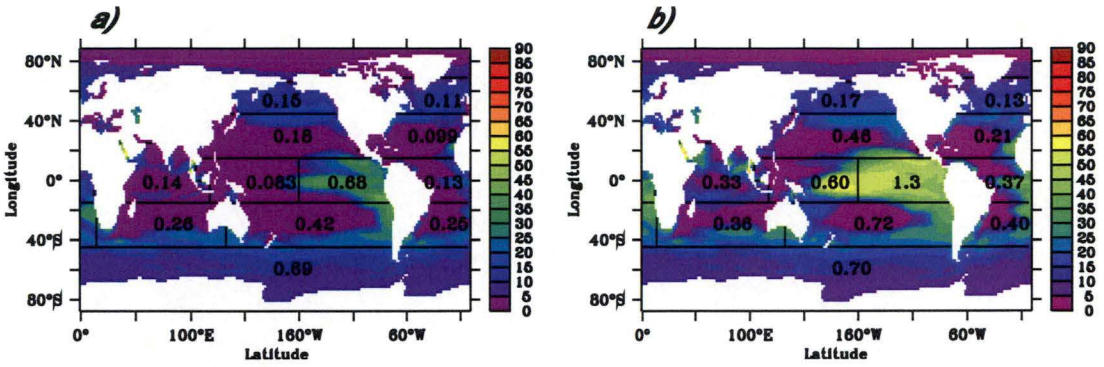

Figure 5-4: Distributions of new production for the biogeochemical formulation perturbation experiments for a) test 6 and b) test 7. The total regional new production estimates (GtC yr^{-1}) are listed inside the marked regions. Note that only the experiments with markedly different distributions of new production from the control are shown.

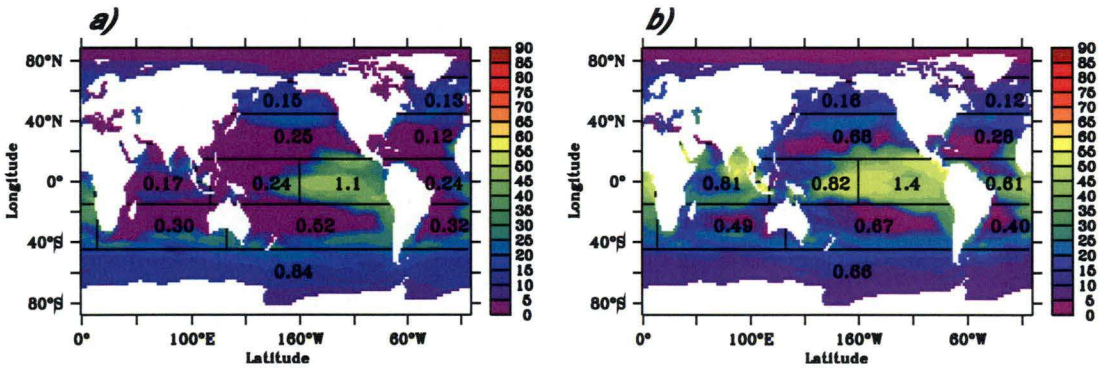

Figure 5-5: Distribution of new production for the physical circulation perturbation experiments a) test 9 and b) test 15. The total regional new production estimates (GtC yr^{-1}) are listed inside the marked regions. Note that only the experiments with markedly different distributions of new production from the control are shown.

6. Model Assessment

By running a series of perturbation experiments we intend to span a range of new/export scenarios that appear plausible given the observations available to assess new production. Using this approach defining the "best" solution is not critical. However, we would like to have some confidence that Southern Ocean water masses and frontal regions of the Southern Ocean are reasonably captured so that the simulated perturbations do resemble those we may expect to see in the real ocean.

We also want to develop some confidence that the model realistically simulates both the magnitude and spatial distribution of new production. Since both the distribution and the magnitude of new production are poorly determined from observations, we use biogeochemical tracer fields to assess the modelled new production. To assess the modelled new production we use phosphate since this is the only biogeochemical tracer in the model that is influenced by new production and does not have an air-sea exchange source term.

6.1. The ocean circulation

Here we describe several key features of the physical ocean circulation in the control experiment, particularly those known to be important for the supply of nutrients to the surface ocean including meridional overturning, vertical convection and ocean stratification. We also compare modelled and observed zonal tracer sections to determine how well Southern Ocean water masses are represented in the model.

6.1.1. Barotropic and meridional overturning streamfunction

Some key features of the Southern Ocean circulation are captured by the barotropic and meridional overturning streamfunctions. The mean barotropic stream function is shown in Figure 6-1. The maximum transport through the Drake passage is 128 Sv and compares well to the transport

suggested by observations (130 ± 13 Sv) [Whitworth *et al.* (1982); Whitworth (1983)]

The meridional overturning supplies nutrients to the surface ocean on decadal to century timescales. The Southern Ocean meridional overturning is driven partly by the large-scale wind forcing and buoyancy forcing along the coast of Antarctica. The modelled meridional overturning streamfunction is shown in Figure 6-2. Both the resolved Eulerian and eddy-induced transport velocities are used to calculate the total meridional overturning streamfunction. Like many models that use the Gent and McWilliams (1990) scheme [England and Hirst (1997); Gnanadesikan *et al.* (2002); Large *et al.* (1997)], the direct Antarctic cell (centred near 70°S and 1000 m) is considerably weaker (3 Sv) than observations (i.e. 14 Sv - Orsi *et al.* (2002)). The Deacon cell is strong with a maximum of 34 Sv (centred near 50°S at 150m). Incorporating the Gent and McWilliams (1990) scheme, has been argued to weaken the Deacon cell because the Eulerian transport almost cancels the eddy induced transport [Danabasoglu *et al.* (1994); England and Hirst (1997); Large *et al.* (1997)]. Figure 6-3 shows the Eulerian (Figure 6-3a.) and the eddy-induced (Figure 6-3b) components of the streamfunction. Here we see that the eddy-induced transports are not strong enough to completely cancel the Eulerian transport. There is no physical rationale for the Eulerian and eddy-induced transports to cancel. The large Deacon cell is an artefact created by integrating velocities on depth coordinates [Doos and Webb (1994); Hirst *et al.* (1996)]. The physical nature of the Deacon cell is more faithfully represented on neutral density surfaces, where the Deacon cell is significantly diminished.

The meridional overturning circulation in the Northern hemisphere is dominated by the formation of North Atlantic Deep Water (Figure 6-4). The maximum (13 Sv) of the North Atlantic Deep Water formation is centred close to 45°N, which agrees well with observational estimates (15 Sv, Schmitz (1995)). Approximately 10 Sv of the North Atlantic Deep water cross the equator, with about 3 Sv upwelling in the Northern hemisphere.

6.1.2. *Convection and mixed layer depths*

Convective mixing is an extremely efficient way to mix nutrients through the water column, and can homogenise the properties of unstable water columns in less than a day.

To compare modelled mixed layer depths to observations we need to use a diagnostic mixed layer depth. The choice of temperature or density-based criterion used has a large influence on the magnitude of the diagnosed mixed layer depth Kara *et al.* (2000). Figure 6-5a shows the modelled maximum seasonal mixed layer depths calculated using a density gradient criterion of 0.05 kg m^{-3} from the sea-surface. The model produces deep (~ 400 m) mixed layers particularly within high wind regimes areas within the Southern ocean. Deep convection (> 500 m) is confined to the North Atlantic and small regions along the Antarctic coast, particularly the Ross and Weddell gyres. The observed [Conkright *et al.* (2002)] mixed layer depths using the same criterion (Figure 6-5b) are generally shallower throughout the Southern Ocean, particularly in regions of deep convection along the Antarctic coast. The mixed layers based on the climatology of Conkright *et al.* (2002) may be too shallow because of a summer sampling bias.

A closer inspection of the property sections in winter when mixed layers are at their maximum, demonstrates that properties such as temperature and salinity are not well mixed throughout the diagnostic mixed layer depth. Using this density criterion only provides a proxy of the mixed layer depth and overestimates the modelled mixed layer depth. Using a common density gradient criterion of 0.125 kg m^{-3} would further increase the overestimate of the modelled mixed layer depth.

6.1.3. *Vertical velocities and ocean stratification*

Two further physical properties that enhance the degree of upwelling, and the subsequent supply of nutrients to the surface ocean are the vertical velocity and the vertical density gradient. The annual mean vertical velocities at 50 m depth are shown in Figure 6-6, where positive vertical velocities indicate upwelling oceanic regions. The

oligotrophic regions are defined as regions with negative vertical velocities (i.e. downwelling) and phosphate concentrations that are lower than the half saturation constant (i.e. P_o = 0.1 mmol m^{-3}, Equation (10)). The oligotrophic regions are contoured in Figure 6-6, demonstrating the extent to which incomplete biological utilisation of nutrients leads to the advection of nutrients away from upwelling regions.

The vertical density gradient is important for controlling the distribution and depth of convection. Figure 6-7a, b and c shows the simulated global annual mean depth profiles of temperature, salinity and density respectively. Figure 6-8 shows the same set of profiles for the observational climatologies of Conkright *et al.* (2002). The thermocline waters are too cold and salty, while the deeper waters are too warm and fresh. The model-data differences are reduced with depth. Consequently, the density-compensating effects of temperature and salinity produce good model-data agreement below 1000 m in the density profile, but surface waters of the model are more stratified than the observations. In the Southern Ocean (40°S - 90°S), ocean temperatures are too low relative to observations [Conkright *et al.* (2002)] (Figure 6-8a) and too high throughout the water column. Modelled salinity is to low at the surface and too high below the thermocline (Figure 6-8b). Here the density-compensating effects produce fairly good model-data agreement throughout the water column (Figure 6-8c).

6.1.4. The seasonality of the hydrographic properties in the Southern Ocean.

Figure 6-9a, Figure 6-10a and Figure 6-11a show the simulated annual cycle of zonally averaged temperature, salinity and mixed layer depth over the southern hemisphere oceans south of 20°S. Figures Figure 6-9b and Figure 6-10b show the difference between the simulated and observed [Conkright *et al.* (2002)] annual cycle of zonally averaged temperature and salinity respectively. Figure 6-11 shows the annual cycle of mixed layer depths diagnosed from the observation-based climatology of Conkright *et al.* (2002). Simulated sea-surface temperatures deviate

from observations by ± 0.7°C. Simulated sea-surface salinity deviates by ± 0.2 psu. The model generally produces sea-surface temperatures and salinities that are higher than Conkright *et al.* (2002) during periods when mixed layer depths are deeper. This is expected because simulated subsurface ocean temperatures and salinities are higher than Conkright *et al.* (2002). During autumn/winter - when convective events occur more frequently and mixed layers are deeper - more of this subsurface water is brought to the sea-surface. The simulated mixed layer depths are shallower than the observations almost year round, except between 60°S and 75°S in the late winter time, where the model is deeper than the observations by up to 100 m. Between 35°S and 65°S the mixed layers in the model are shallower by as much as 450 m, even in the spring/summer period. Thus, generally we would expect that simulated photosynthetic growth rates would be less light-limited in the model than in the real ocean, particularly north of 60°S in the spring/summer period, where mixed layer depths are shallower than the euphotic zone.

6.1.5. Southern Ocean fronts, zones and water masses

To have confidence in the tracer responses we observe in response to both the physical and biogeochemical perturbation experiments, we would ideally like the water mass and frontal structure in the southern hemisphere oceans to be well represented in the model. The purpose of this section is to locate the key Southern Ocean zones, fronts and water masses and determine how well they are represented in the model. We will focus the analysis along 144°E - the approximate route of the WOCE SR3 transect. Viewing property sections provides a better indication of how well fronts are represented in the model, because the frontal positions in the Southern Ocean, and therefore also the water masses, meander both longitudinally and with time. Zonal averaging of hydrographic properties and tracers in the Southern Ocean smears the frontal and water mass positions and properties. Furthermore the SR3 WOCE transect crosses all the major Antarctic front and zones, and

physical [Rintoul and Bullister (1999); Rintoul and Trull (2001)], chemical [Lourey and Trull (2001); McNeil *et al.* (2001); Trull *et al.* (2001)] and biological [Marchant *et al.* (1987); Odate and Fukuchi (1995); Wright *et al.* (1996)] properties have been studied intensively on both seasonal and interannual scales. Thus, we can use the SR3 line to tailor perturbation experiments and capture the magnitudes and variability expected in the southern hemisphere oceans.

The eastward flowing Antarctic circumpolar current (ACC) consists of a series of fronts, characterised by enhanced lateral gradients in hydrodynamic properties. The major fronts coincide with the cores of the ACC and are responsible for the bulk of the transport. The fronts bound relatively slow moving water masses with comparatively uniform water properties. Moving southwards, the major oceanic zones and fronts are: the Subtropical front (STF), the Subantarctic zone (SAZ), the Subantarctic front (SAF), the Polar frontal zone (PFZ), the Polar front and the Antarctic zone (AZ). The region of the Antarctic zone that is covered seasonally by sea ice, is defined as the Seasonal ice zone (SIZ) (Figure 6-12).

Many criteria are used to locate fronts and oceanic zones, including geostrophic velocities, horizontal surface and subsurface gradients in hydrodynamic properties, prominent features in the temperature and salinity distributions, and the relative location of water masses. We use a combination of these criteria from direct observations along the transect [Rintoul and Bullister (1999); Lourey and Trull (2001); Rintoul and Trull (2001)] to locate the equivalent modelled water masses, zones and fronts along the 144°E transect. We compare the modelled water masses to the observational climatology of Conkright *et al.* (2002). The main water masses and fronts can be identified from a comparison of the modelled and observed zonal sections of temperature (Figure 6-12) and salinity (Figure 6-13) at 144°E.

First we locate the key water masses and compare the properties of the water masses to observations [Conkright *et al.* (2002)]. The properties of the subantarctic mode water (SAMW) compare well to observations. In both the model (Figure 6-12a) and observations (Figure

6-12b) the SAMW is represented by the layer quasi-homogenous in temperature between the depths of approximately 100-300m north of 48°S. Although the depth of the mixed layer in this region agrees fairly well with the observational climatology of Conkright *et al.* (2002) (Figure 6-11), direct observations show this layer to be as deep as 600 m [Rintoul and Trull (2001)]. The model does not produce mixed layers this deep within in the SAZ.

The model successfully forms Antarctic intermediate water (AAIW) and is clearly identified by a tongue of low salinity water that subducts near the Subantarctic front (SAF) to a depth of approximately 1000 m (Figure 6-13a). Modelled AAIW is slightly fresher than observed (Figure 6-13b). The fresh (33.9 psu) surface waters centred at 56°S in both the model and observations is the Antarctic surface water (AASW). Lower Circumpolar Deep Water (LCDW) in the model is characterised by a salinity maximum encircled by the 34.75 psu contour line (Figure 6-13a). Observed LCDW (Figure 6-13b) is slightly fresher than in the model. Upper Circumpolar Deep Water (UCDW) lies between the AAIW and the LCDW. In the model, the UCDW is located by the subsurface temperature maximum (i.e. 2°C isotherm between 56°S and 60°S), that lies below the temperature minimum layer (Figure 6-12a) and compares well with observations (Figure 6-12b).

Now we locate the key fronts and zones in the model and compare them with observations. The Southern Ocean fronts from direct observations are much sharper than both observed climatological and modelled fronts, which is typical for coarser resolution models and observations. The Subantarctic zone (SAZ) lies between the Subtropical front and the Subantarctic front. In the model, the SAZ lies north of the Subantarctic front between 52°S and 42°S. The deepest winter mixed layers in the Southern Ocean are formed in this region, ultimately leading to the formation of SAMW and AAIW. As observed [Rintoul and Trull (2001)], the deepest mixed layers along 144°E are found in this region in the model (Figure 6-5).

The observed Subantarctic front (SAF) is the main jet of the ACC south of Australia and separates warm, salty subtropical waters in the North from cold and fresh subpolar waters. The front is deep-reaching and produces strong gradients in hydrographical properties throughout the water column. The modelled SAF produces an almost 5°C drop in temperature at 200 m depth between 50°S and 54°S. The centre of the modelled SAF is defined as the maximum zonal velocity along the SR3 line (i.e. 13 cm s^{-1}) at approximately 52°S. The observed PFZ along the WOCE SR3 transect lies between the SAF and the northern branch of the Polar front N-PF. Both the observed and modelled PFZ are very narrow along the SR3 transect. In the model, the PFZ lies between 52°S and 54.5°S. Zonal velocities throughout this region are high (i.e. > 11cm s^{-1}).

The Polar front is composed of two branches at several places in the Southern Ocean, including south of Australia. The northern polar front is commonly located by northernmost extent of the temperature minimum water (less than 2°C) at 200 m depth. In both the model (Figure 6-12a) and the observational climatology (Figure 6-12b) the 2°C minimum lies at about 54°S, but is shallower than 200 m in both. This subsurface temperature minimum is a remnant of the deep winter mixed layers and disappears altogether north of the N-PF. In the model, the shallower temperature minimum throughout this region suggests that the modelled winter mixed layers are too shallow. In the model, the core of the PF-S is defined by the 2^{nd} zonal velocity maximum (6 cm s^{-1}) along the WOCE SR3 transect, and is located at 60°S. The location of the S-PF, based on the zonal velocity, agrees fairly well with other definitions based on temperature criteria such as the southernmost extent of water higher than 2.2°C at the subsurface temperature maximum (i.e. >59°S) [Rintoul and Bullister (1999)], and an increase in the depth of temperature minimum layer.

The Antarctic zone (AAZ) lies south of the PF-N. Both UCDW and LCDW upwell within the Antarctic zone, where Ekman transport is divergent. In the model, south of the N-PF vertical velocities switch to

positive values (Figure 6-6). The subsurface temperature minimum layer, characteristic of the AZ, is captured well by the model (Figure 6-12b) and compares well with observations (Figure 6-12b). The Antarctic zone is split into 2 zones by the Southern polar front S-PF. In the model, we call the region between the N-PF and the S-PF the N-AZ and the region south of the S-PF the S-AZ. Winter mixed layer depths in the N-AZ reach 120 m, while the S-AZ mixed layer depths are very shallow (60 m). Zonal velocities in the N-AZ are considerably higher (i.e. > 6 cm s^{-1} and <12 cm s^{-1}) than in the S-AZ (i.e. < 6 cm s^{-1}). The Seasonal ice zone (SIZ) is the region south of 62°S, which is seasonally covered by sea ice. Here, the mixed layers (100 m) are deepest in September, several months later than in the N-AZ (Figure 6-14). Compared with Conkright *et al.* (2002) (Figure 6-12b), sea surface temperatures are too low at the surface and too high at depth (Figure 6-12a), reflecting the low AABW formation rates in the model.

Most of the key water masses and fronts in the model compare well to observations [Conkright *et al.* (2002)]. A significant shortcoming is the fact that the modelled mixed layer depths in the SAZ are too shallow.

6.2. New production

Here we very compare modelled export production to other model and observational estimates globally, regionally and locally. Then using phosphate as a proxy of new production, we assess how well new production is simulated in the new production perturbation experiments and show that the suite of experiments captures the likely range of new production magnitudes expected in the real southern hemisphere oceans. Note that the purpose of this perturbation experiments is not to produce the 'best' model experiment, but be confident that the model experiments capture the range of likely new production magnitudes in the southern hemisphere oceans.

6.2.1. *Simulated new production*

The range of global new production estimates simulated by the global biogeochemical model used in this study (3.3 – 5.9 GtC yr^{-1}), lies at the lower end of the range simulated from similar biogeochemical global ocean circulation models [Najjar *et al.* (2003)] and are much lower than estimates based on atmospheric O_2/N_2 and satellite chlorophyll (Table 6-1). The simulated new production estimates are much closer to estimates based on the seasonal variability of phosphate and oxygen and at least half of the estimate from Schlitzer (2002b) estimated from a 3D assimilation of biogeochemical tracers (Table 6-1).

Southern hemisphere new production (20°S - 90°S) in the model used in this study ranges between 1.7 and 3.8 GtC yr^{-1}, and new production in the high latitudes (50°S – 90°S) ranges between 0.23 and 2.0 GtC yr^{-1}. These estimates lie within the range from other global biogeochemical ocean models and observational studies (Table 6-2). For example, Schlitzer (2002b) estimated 3 GTC yr^{-1} export production south of 30°S, and a 1 GTC yr^{-1} south of 50°S, by assimilating tracers into a 3D model. MacCready and Quay (2001) estimated a 2.0 +/- 1.7 GtC yr^{-1} export of carbon south of 40°S and a 0.+/- 1.2 GtC yr^{-1} south of 50°S. Louanchi and Najjar (2000) estimated a 1.1 GtC yr^{-1} south of 40°S and a 0.4 GtC yr^{-1} in the southern subtropical gyres (i.e. between 15°S and 40°S). based on the seasonal variability of phosphate in the top 100 m and a C:P ratio of 106 (Table 6-3).

Direct estimates of new production are considered locally precise but highly uncertain when extrapolated over large regions. Yet, a comparison of local estimates in the southern hemisphere oceans, using a different techniques (Table 6-3), shows that estimates within a particular zone, or even at the same location vary widely (eg. 3.33 – 19.98 gC m^{-2} yr^{-1} in the SAZ).

Figure 6-15 shows the export production along the SR3 line for a selection of the new production perturbation experiments. In the control

case, annual export production in the AZ is approximately 0.83 molC m^{-2} yr^{-1}, and ranges between 0.83 and 1.25 molC m^{-2} yr^{-1} in the PFZ, and between 1.25 and 2.08 molC m^{-2} yr^{-1} in the SAZ. Doubling the export scaling factor (test 4) doubles export production in the PFZ, but does not completely double export production in the SAZ due to the onset of macronutrient limitation. Removing the dependence of export production on temperature and doubling the scaling factor (test 2), increases export production throughout the Southern Ocean to between 3.75 and 4.58 molC m^{-2} yr^{-1} dropping rapidly north of 44°S driven by extreme macronutrient limitation. The export production estimates in the PFZ and SAZ from doubling the scaling factor (test 4) are similar (1.4 and 3.4 molC m^{-2} yr^{-1} in the PFZ and SAZ respectively) to those of Lourey and Trull (2001) determined using a nutrient depletion method (

Table 6-2). But estimates from all the tests are lower than the estimates of Wang *et al.* (2001) calculated using a 1-D biophysical model of both the PFZ and SAZ and the observation-based estimates of Metzl *et al.* (1999) in the Indian SAZ.

The new production perturbation experiments give a range of new/export production estimates in the Southern ocean, which are comparable or slightly less than what is derived from observations.

6.2.2. Phosphate

The main features of the observed [*Conkright et al. (2002)*] spatial distribution of phosphate (Figure 6-16b) are well reproduced by the control experiment (Figure 6-16a). But, modelled phosphate concentrations are too high through much of the Southern Ocean.

The average surface phosphate concentration, in the high latitude southern hemisphere oceans, for the control experiment is 1.7 mmol m^{-3}, which is 0.2 mmol m^{-3} higher than observed. Increasing new production (test 1, Figure 6-17) reduces surface phosphate concentrations to 1.5 mmol m^{-3}. Further increases in new production (test 4, test 1) produce surface phosphate concentrations that are lower than Conkright *et al.* (2002) (Figure 6-17). Therefore, based on surface phosphate a new

production scaling factor, s_{np}, between 0.05 and 0.1 would be appropriate. Using annual mean phosphate as a proxy of new production alone has its limitations. Physical processes can also substantially alter the spatial distribution and the concentrations throughout the ocean. Figure 6-18 shows phosphate concentrations for two selected new physical circulation experiments (test 9, test 15, Table 4-3). These two experiments have the quite similar new production magnitudes in the southern hemisphere oceans (Table 5-1), yet phosphate concentrations are reduced by between 0.2 and 0.3 mmol m^{-3}. Much larger increases in new production, produced via the new production experiments produce similar reductions in surface phosphate concentrations (Figure 6-17, test 1, test 4). The relationship between annual mean surface phosphate concentrations in the southern hemisphere oceans and new production are often not so intuitive, because changing the physical circulation changes nutrient concentrations throughout the global ocean - not just locally. Surface nutrient concentrations are a function of surface utilisation and resupply. Nutrient resupply is a function of the rate of local upwelling and subsurface nutrient concentrations. So, even though the vertical diffusivities are increased in test 15, subsurface nutrient concentrations in the southern hemisphere are much lower due to large-scale changes in new production outside the southern hemisphere oceans (not shown). Consequently nutrient supply to the southern hemisphere is lower than in the control case, despite the enhanced vertical diffusivites throughout the region.

In the Southern Ocean, phosphate concentrations at all depths throughout the water column are too low in the control case (test 0) when compared to observations (Figure 6-20). Increasing new production in the Southern Ocean relative to the control case (test 1 and test 4) improves the phosphate distributions at depth (Figure 6-21a, c). But larger increases in new production (test 2) result in phosphate concentrations that are too high at depth and too low at the surface (Figure 6-21b). Reducing the compensation depth (test 8, not shown) has a negligible

effect on Southern Ocean phosphate concentrations at depth. The simulated nutrient distribution is very sensitive to the depth at which nutrients are remineralised. Although the annual mean new production in the Southern Ocean is insensitive to the remineralisation profile (Figure 5-4), changing the remineralisation profile dramatically alters nutrient distributions at depth (Figure 6-22). Counter-intuitively, shallowing the remineralisation profile (test 7) decreases phosphate concentrations throughout the top 2000 m of the Southern Ocean. This may reflect that when nutrients are remineralised shallower in the water column, a greater proportion of the nutrients upwelled in the southern hemisphere ocean is advected northwards, and out of the region, by Ekman transport. Deepening the remineralisation profile (test 6) increases phosphate concentrations in the same region by trapping nutrients at depth, and improves the match to observed phosphate concentrations.

In the northern high latitudes, the phosphate concentrations throughout the water column between 50 cm and 3500 m are generally too low by as much as 0.25 mmol m^{-3} in all of the sensitivity tests (Figure 6-20, Figure 6-21). In the top 700 m the concentrations are much too low. Only reducing the scaling factor (test 5) produces a relative increase in phosphate in the upper 700 m. Note that in the southern high latitudes, reducing the scaling factor (test 5) results in a decrease in phosphate concentrations throughout the same depths.

No one set of parameters and biogeochemical formulations produce a phosphate distribution that agrees completely with observed phosphate concentrations throughout the southern hemisphere oceans, but the range of experiments encapsulates the observations.

Summarising the most relevant features for our purposes, increasing new production (test 1, test 4) produces a better match with observed concentrations in the Southern Ocean and reducing the new production scaling factor (test 5) produces a better match with observed concentrations throughout the rest of the oceans. The modelled phosphate concentrations in the Southern Ocean, from test 1, closely

resemble the observed phosphate concentrations of Conkright *et al.* (2002), both at depth and in the surface ocean. We can be quite confident that the suite of new production perturbation experiments spans a substantial range of the new production scenarios we might expect to observe in the true southern hemisphere oceans.

Figure 6-23a shows the zonally averaged annual cycle of phosphate (mmol m^{-3}) for the control experiment. Figure 6-23b shows the difference between the zonally averaged annual cycle of phosphate concentrations from the control experiment and the observational climatology of Conkright *et al.* (2002). Phosphate concentrations in the control experiment are too high throughout all of the southern hemisphere oceans and for virtually all months. The modelled seasonal amplitude of phosphate concentrations is less than observed by 0.2 - 0.4 mmol m^{-3}, suggesting that new production may be on the low side in the control case. This does not unequivocally indicate that new production in the model is too low, because surface concentrations reflect the complex interplay of the physical supply of nutrients to the sea surface and nutrient utilisation by the oceanic food web. But, doubling new production in the southern hemisphere oceans by removing the temperature inhibition of new production in the high-latitudes (test 1), produces a better agreement between modelled and observational climatology of phosphate concentrations (Figure 6-23c). Also, the magnitude of the seasonal amplitude of the annual cycle of phosphate concentrations is closer to the observational climatology.

The annual mean new production in perturbation experiment test 2 is approximately double that of test 1, and annual mean new production in the experiment, test 5, is approximately half that of the control experiment. Thus, given that new production has been observed to vary by a factor of two in the southern hemisphere oceans, the control experiment, test 1 and test 2 should bracket the range of observed new production magnitudes.

6.3. The annual cycle of oxygen

Figure 6-24a and b show the zonally averaged annual cycle of oxygen concentrations in the southern hemisphere oceans, for the control model experiment, and for the difference between the control experiment and the observational climatology of Conkright *et al.* (2002), respectively. The seasonal amplitudes of the annual cycle of oxygen concentrations, north of 60°S, are less than the observational climatology of Conkright *et al.* (2002) by between 10 and 15 mmol m^{-3}. The simulated oxygen and oxygen concentrations are up to 40 mmol m^{-3} higher around the Antarctic coast (i.e. ~ 70°S). Confidence in both the simulated and observed climatological oxygen concentrations around the Antarctic coast is limited, due to the lack of a fully integrated sea-ice model and the lack of seasonal oxygen measurements. The study of Boyer *et al.* (1999) shows a map of the statistical significance of the winter minus summer difference for 5-degree squares at the surface and 100 m depth across the globe. Virtually in all the waters surrounding the Antarctic coast, and throughout much of the Southern ocean, there is no statistical significance because of the lack oxygen observations in either or both winter and summer.

Assuming that the observation-based climatology of oxygen concentrations are correct, the high simulated oxygen concentrations in the high-latitudes may be due to the oxygen content of the upwelled subsurface waters being to high, due to colder sea-surface temperatures than observed, or due to the inability for oxygen to escape the surface due to the presence of sea-ice. In this region, the annual cycle of the simulated oxygen concentrations (Figure 6-24b) is always higher than the observations, while the simulated temperatures are only cooler in the summertime (Figure 6-9b), so sea-surface temperature are not likely to be entirely responsible for the high oxygen concentrations. But, simulated subsurface oxygen concentrations are slightly higher than observations, down to depths greater than 1000 m, in this region. Also, the oxygen concentrations are much higher (~ 40 mmol m^{-3}) in a localised region

confined to the top 50 -100 m (not shown). Oxygen concentrations are high here due to a combination of the fact that the oxygen concentrations in the upwelled surface are too high relative to observations and that oxygen is unable to escape due to the presence of sea ice. Figure 6-25 show the zonally averaged fraction of the sea-surface that is covered by sea-ice. The high oxygen concentrations observed in the model (Figure 6-24b) occur in regions covered by sea ice.

The annual cycle of the zonally averaged oxygen fluxes in the control experiment is compared to the oxygen fluxes of Garcia and Keeling (2001) based on a climatology of oxygen observations. Figure 6-26 show the zonally averaged annual cycle of oxygen for the control model experiment for the air-sea oxygen flux climatology of Garcia and Keeling (2001). The oxygen fluxes based on observations and the model are broadly consistent, with oxygen outgassing (shown in red) occurring in both hemispheres during the spring/summer, and ingassing occurring during the autumn/winter. In spring/summer both increasing temperatures and photosynthesis both produce an oxygen outgassing. As sea-surface temperatures increase, oxygen becomes less soluble and outgases to the atmosphere. The increasing sea-surface temperatures also enhance biological productivity in the oceans. Photosynthesis produces oxygen that subsequently outgases to the atmosphere.

In the southern hemisphere, the amplitude of the simulated oxygen fluxes is less than the observations (35 mol m^{-2} yr^{-1}, relative to 45 mol m^{-2} yr^{-1} in the observations), primarily due to less outgassing, in the model, during spring/summer. Since the seasonal amplitude of modelled sea-surface temperatures is similar to observations (and assuming the observational climatology is correct), the lower outgassing in the model could be due to an underestimate of simulated biological productivity. New production needs to be approximately quadrupled throughout the southern hemisphere oceans to reproduce the maximum seasonal outgassing in the observations (Figure 6-26c). In the model, the maximum ingassing in the wintertime occurs further south (~ 60 °S) compared to the observations (~ 45°S) and may reflect that the fact the mixed layer depths

are too low or that biological production is too high in the Subantarctic zone (~ 45°S). In the high-latitude oceans around the Antarctic continent, the model produces a strong ingassing during the winter period, which occurs in the regions of deep wintertime convection (Figure 6-11a) and oxygen poor subsurface waters are rapidly ventilated. Again since observational coverage throughout the high latitudes is extremely poor – particularly in the wintertime - we would not expect highly localised deep convective events to be well captured by the observations.

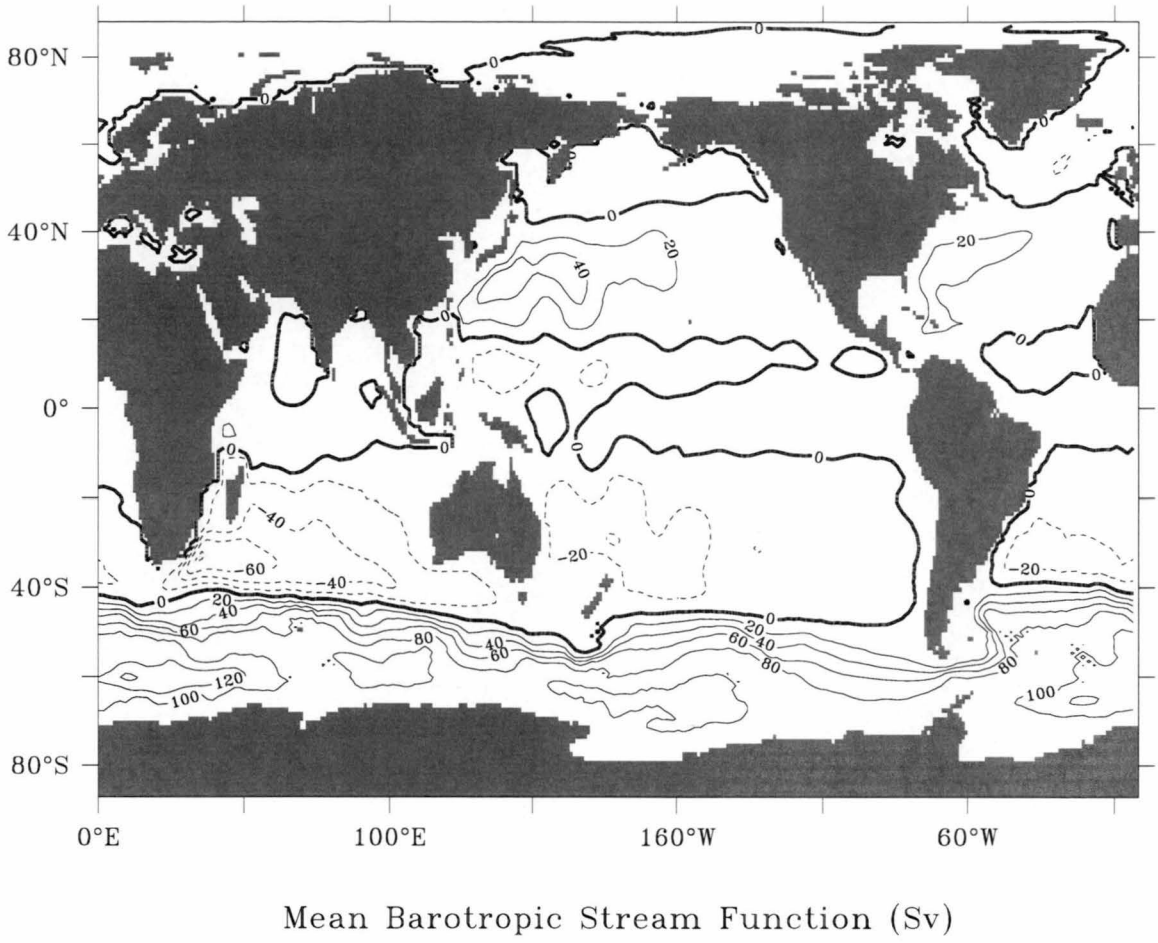

Figure 6-1: The mean barotropic streamfunction (Sv) for the control experiment.

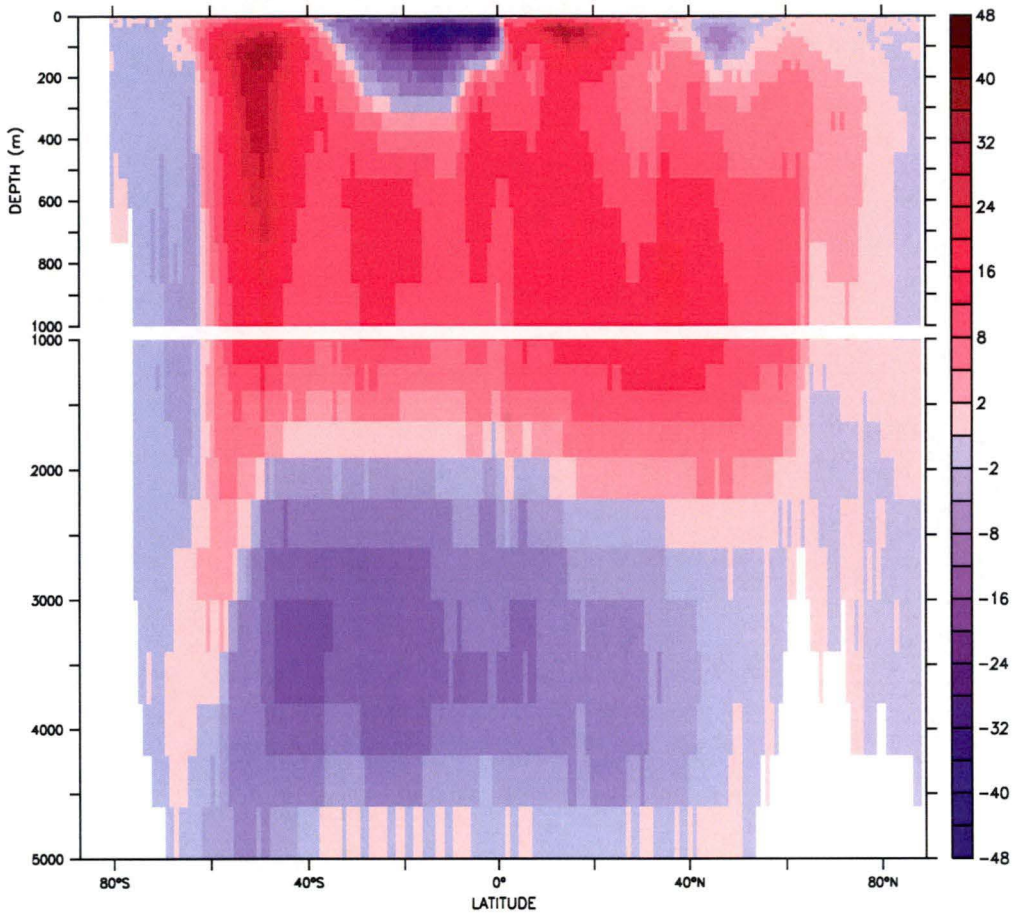

Figure 6-2: The total meridional overturning streamfunction (Sv) for the control experiment.

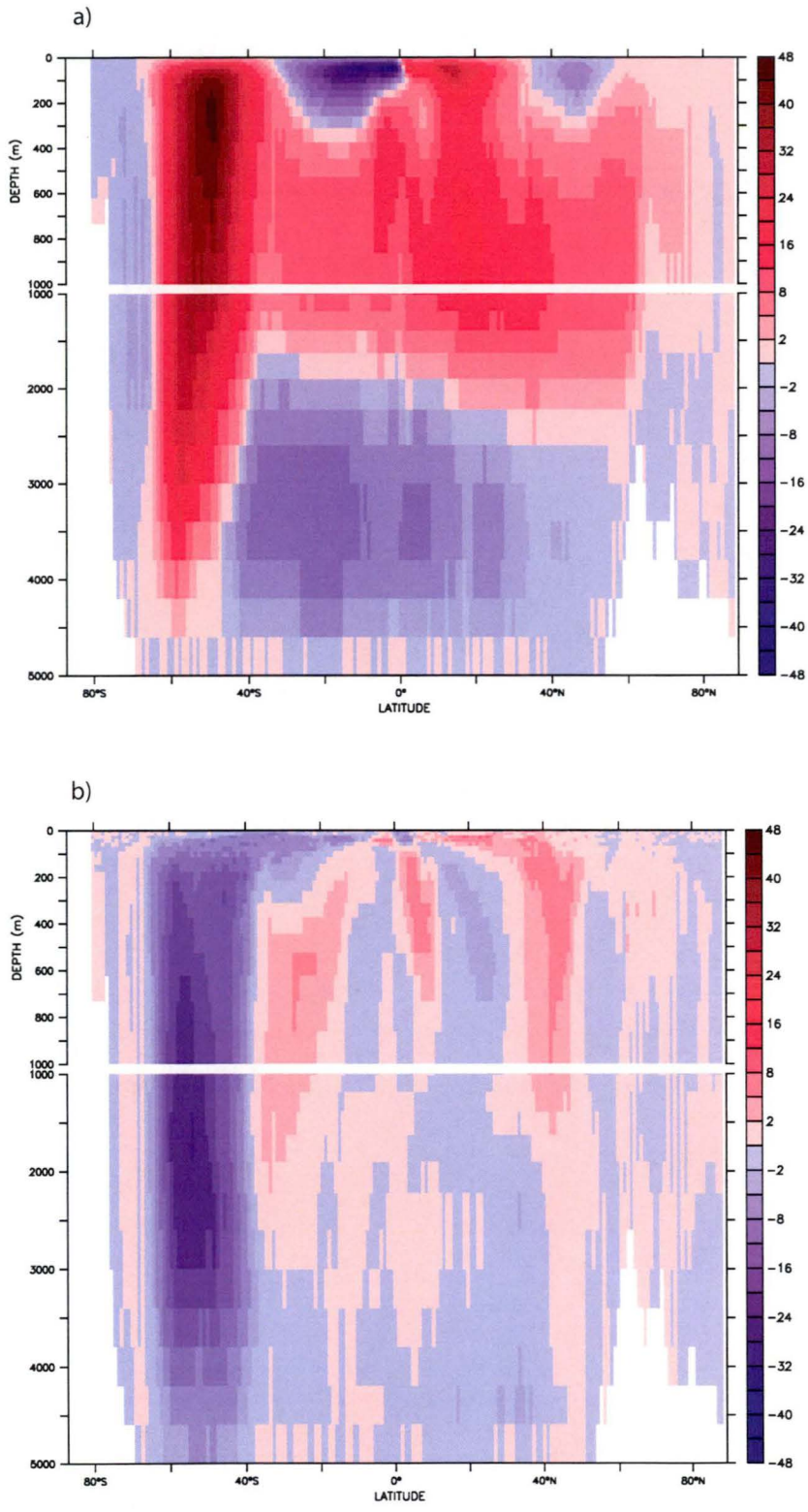

Figure 6-3: Components of the global meridional overturning streamfunction (Sv), The a) Eulerian and b) eddy-induced transport for the control experiment.

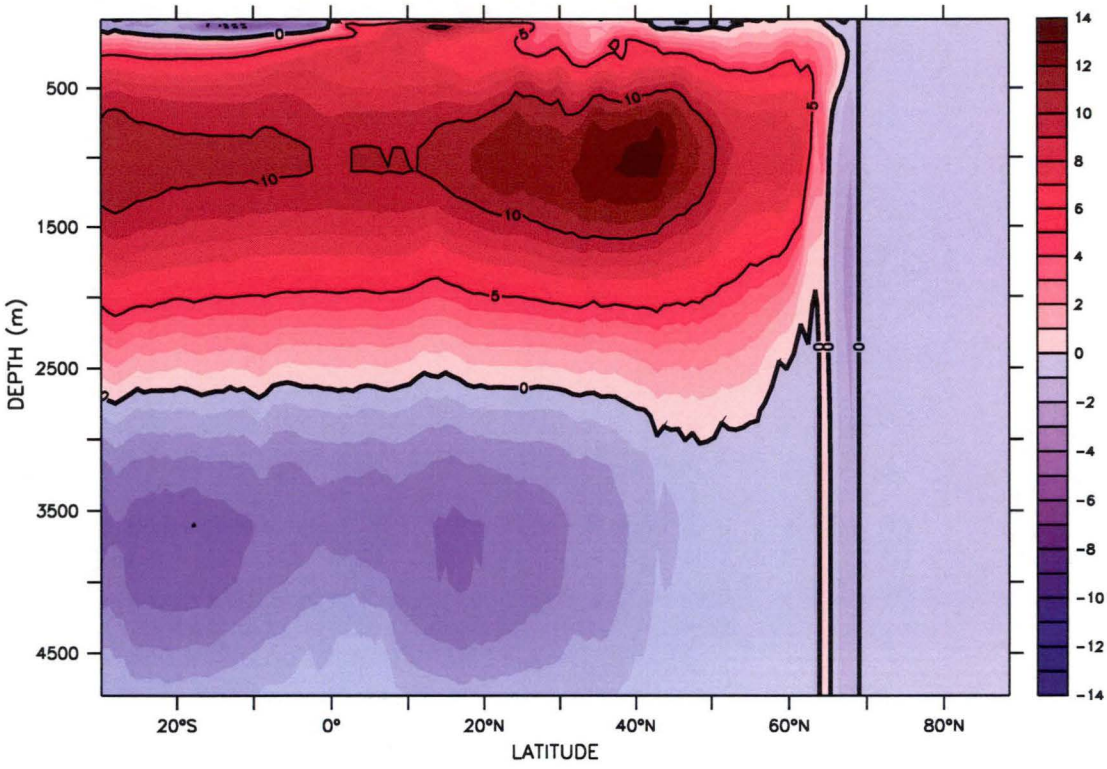

Figure 6-4: The North Atlantic overturning streamfunction (Sv) for the control experiment.

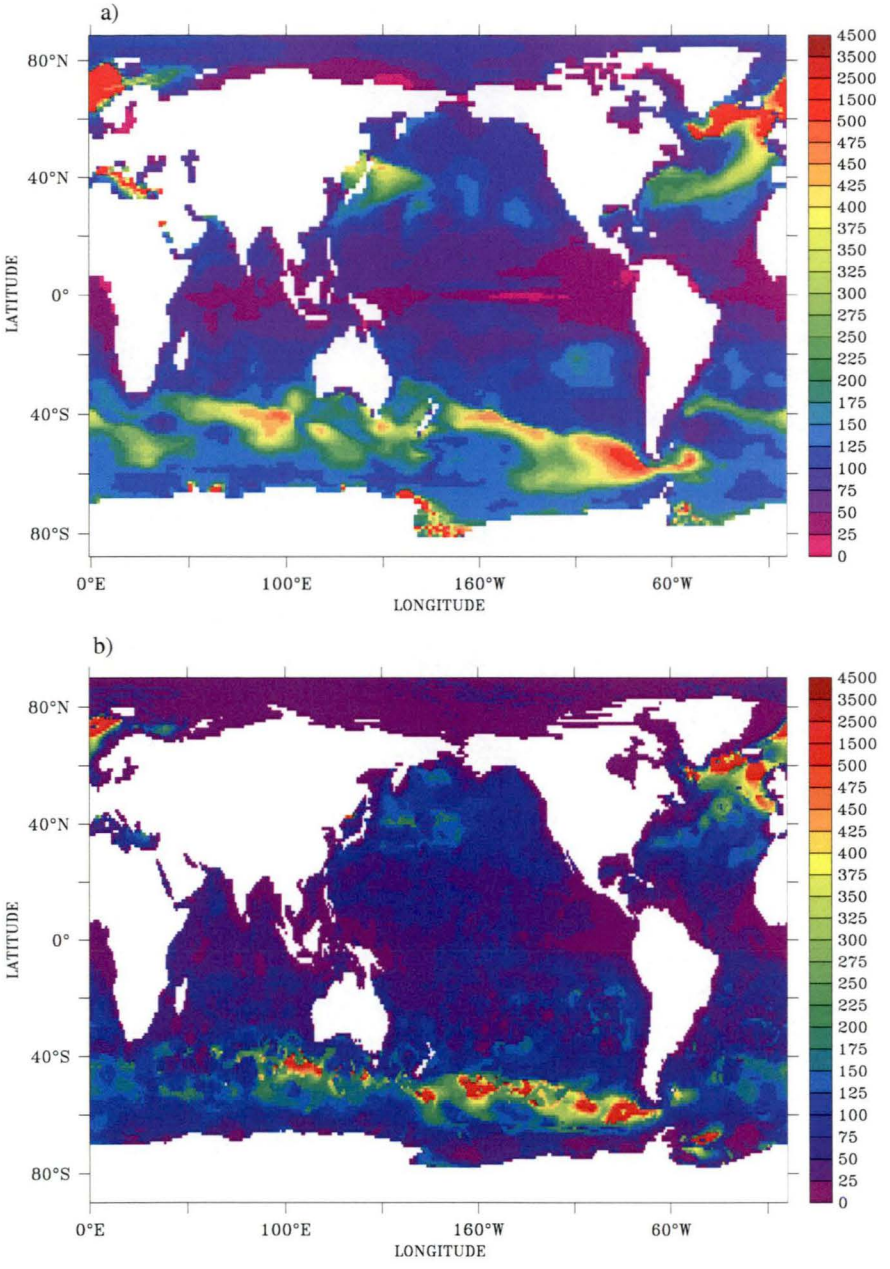

Figure 6-5: Maximum seasonal mixed layer depth (m) determined using a density gradient criterion of 0.05 kg m^{-3} for a) the control case and b) Conkright *et al.* (2002).

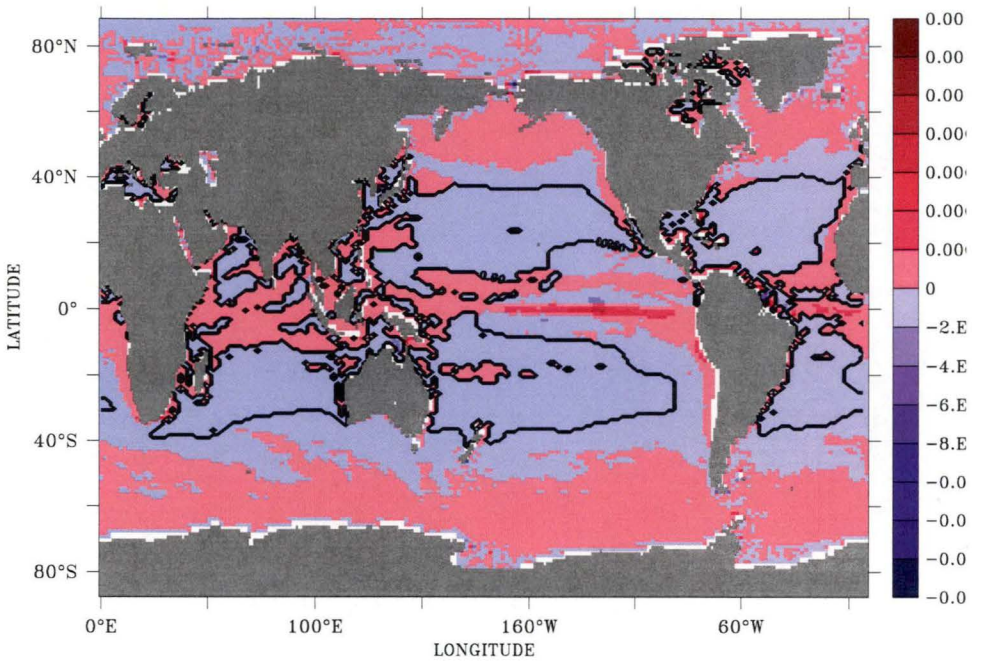

Figure 6-6: The annual mean distribution of vertical velocities (cm s^{-1}), at 50 m depth, for the control experiment. Downwelling occurs in the blue regions, while upwelling occurs in the red regions. The contour lines mark the oligotrophic regions, which are defined as regions with negative vertical velocities (i.e. downwelling) and phosphate concentrations that are lower than the half saturation constant (i.e. P_o = 0.1 M, Equation (10)).

a)

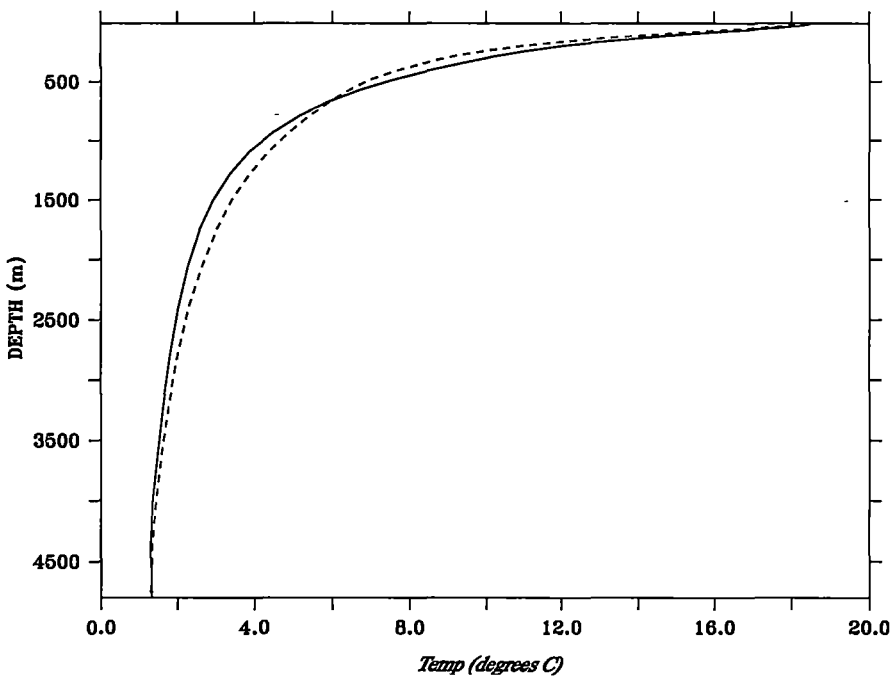
500
1500
2500
3500
4500
DEPTH (m)
0.0
4.0
8.0
12.0
16.0
20.0
Temp (degrees C)

b)

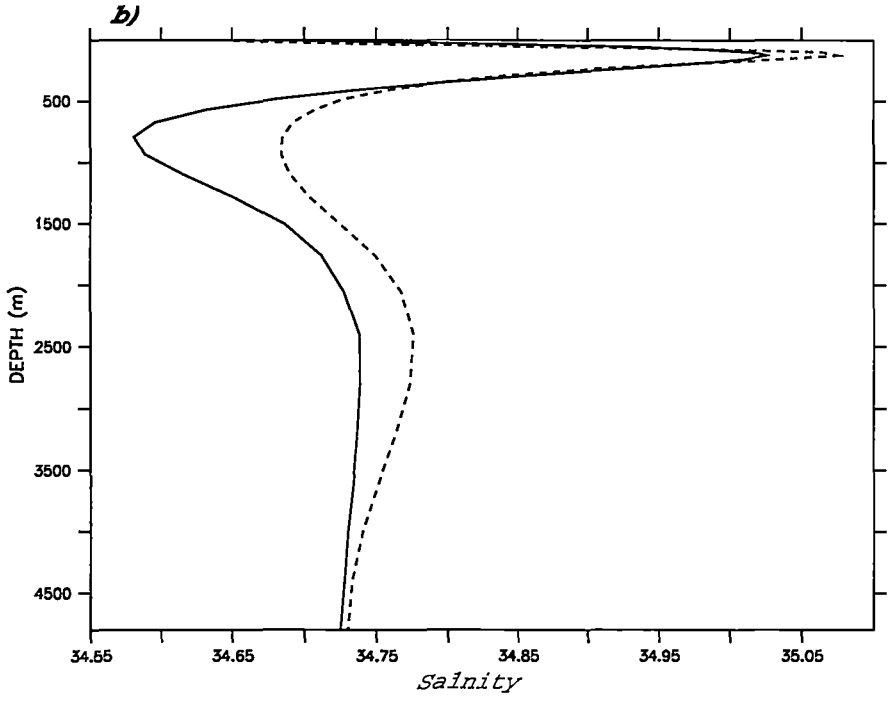
500
1500
2500
3500
4500
DEPTH (m)
34.55
34.65
34.75
34.85
34.95
35.05
Salinity

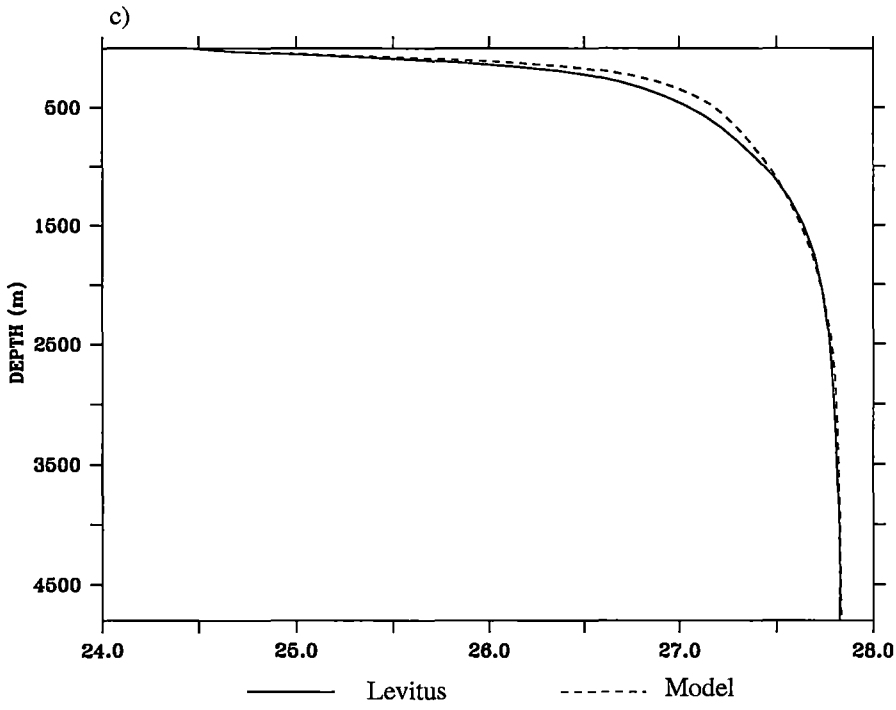

Figure 6-7: Vertical profiles of globally averaged a) temperature, b) salinity and c) density for observations [Conkright *et al.* (2002), solid lines] the control model experiment (dashed lines).

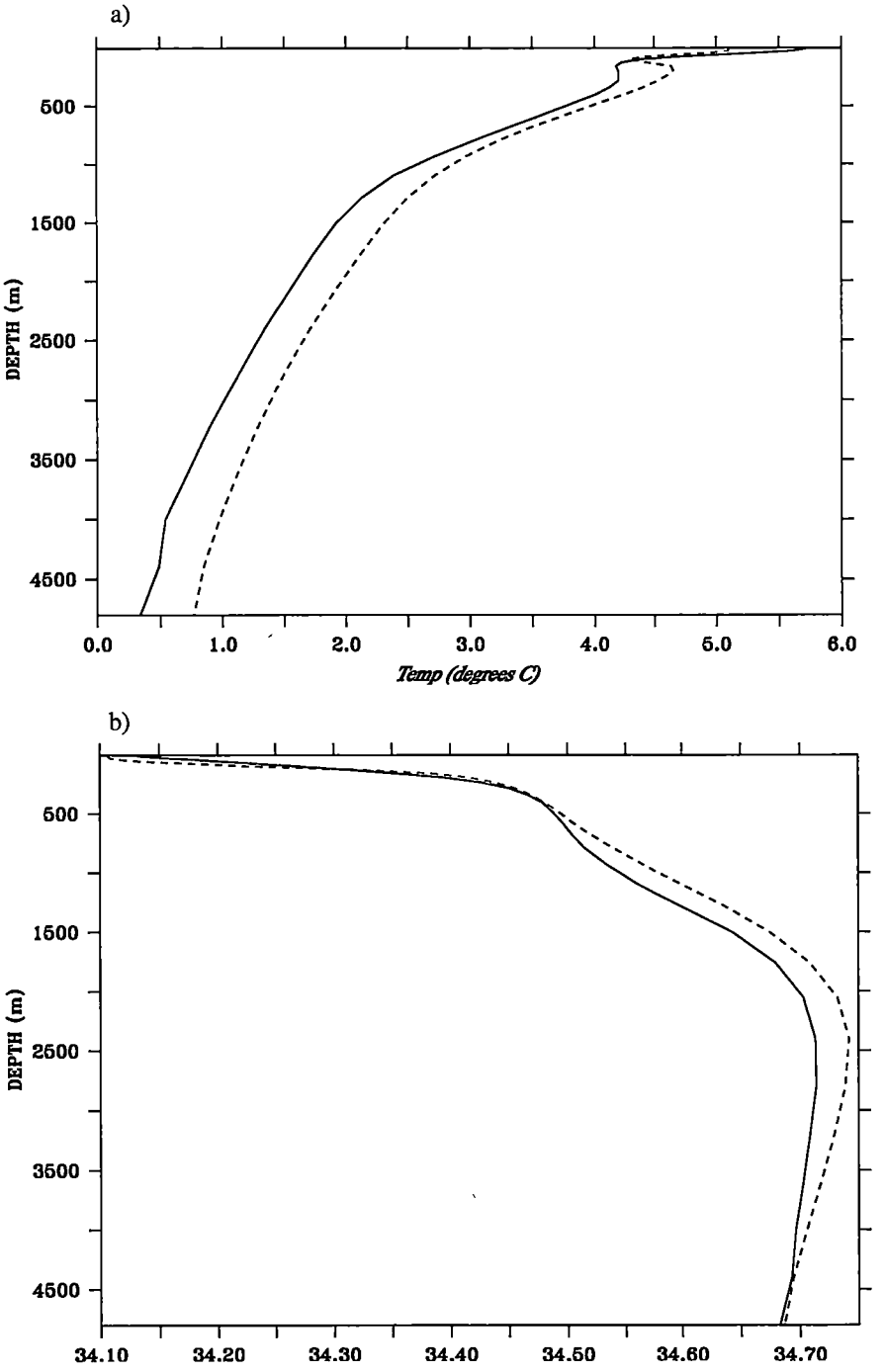
a)
500
1500
2500
3500
4500
DEPTH (m)
0.0
1.0
2.0
3.0
4.0
5.0
6.0
Temp (degrees C)
b)
500
1500
2500
3500
4500
DEPTH (m)
34.10
34.20
34.30
34.40
34.50
34.60
34.70

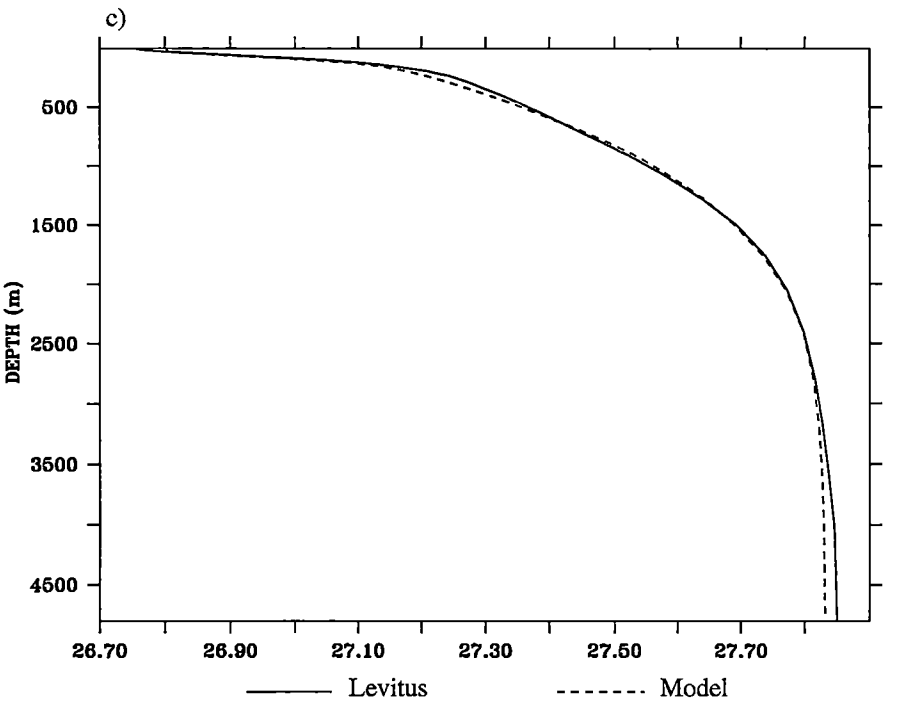

Figure 6-8: Vertical profiles a) temperature, b) salinity and c) density averaged over the southern hemisphere oceans (40°S – 90°S) for observations [Conkright *et al.* (2002), solid lines] the control model experiment (dashed lines).

a)

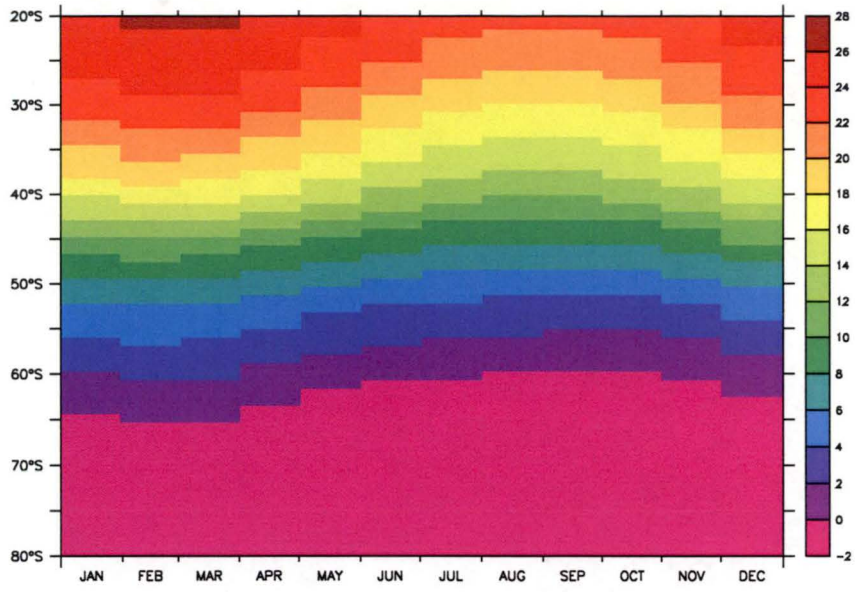

b)

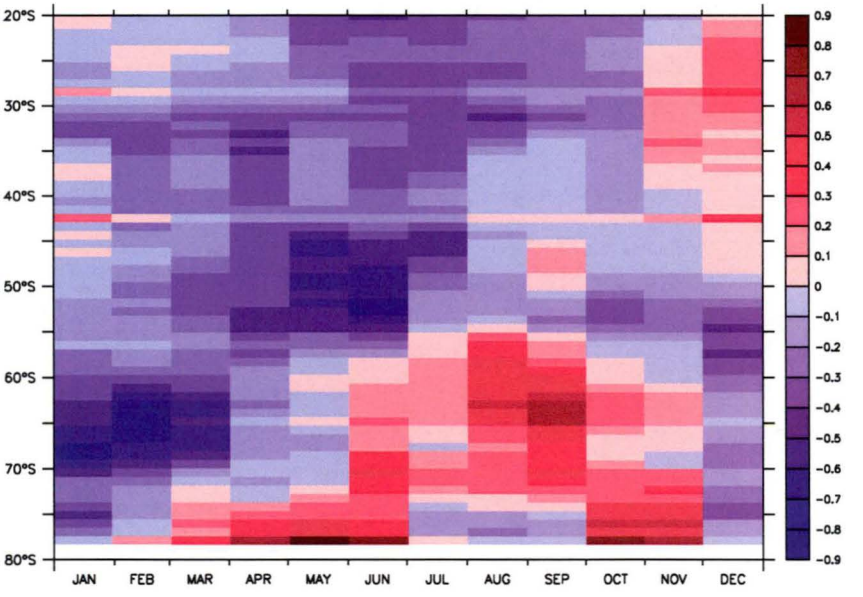

Figure 6-9: The zonally averaged annual cycle of sea-surface temperature (°C) for a) the control experiment, and b) for the difference between the control experiment and the climatology from Conkright *et al.* (2002) in the southern hemisphere oceans.

a)

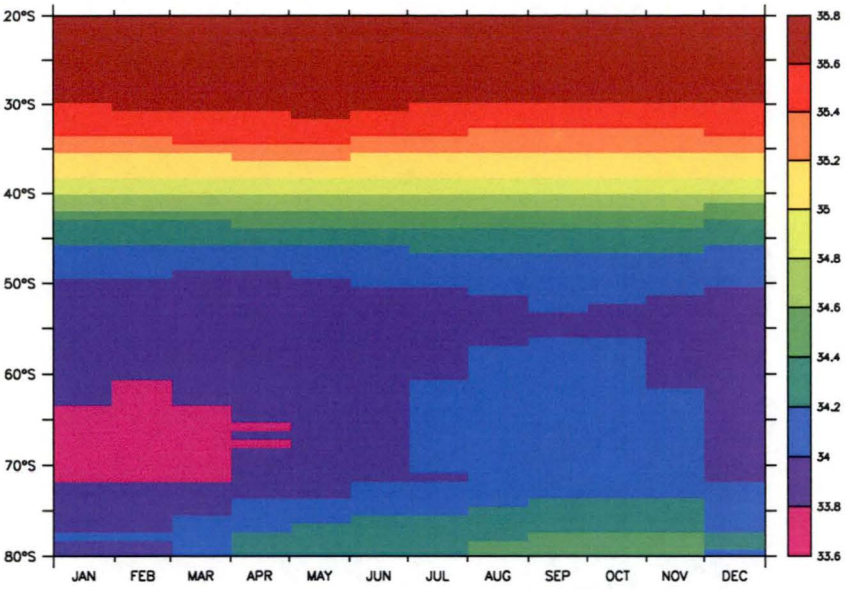

b)

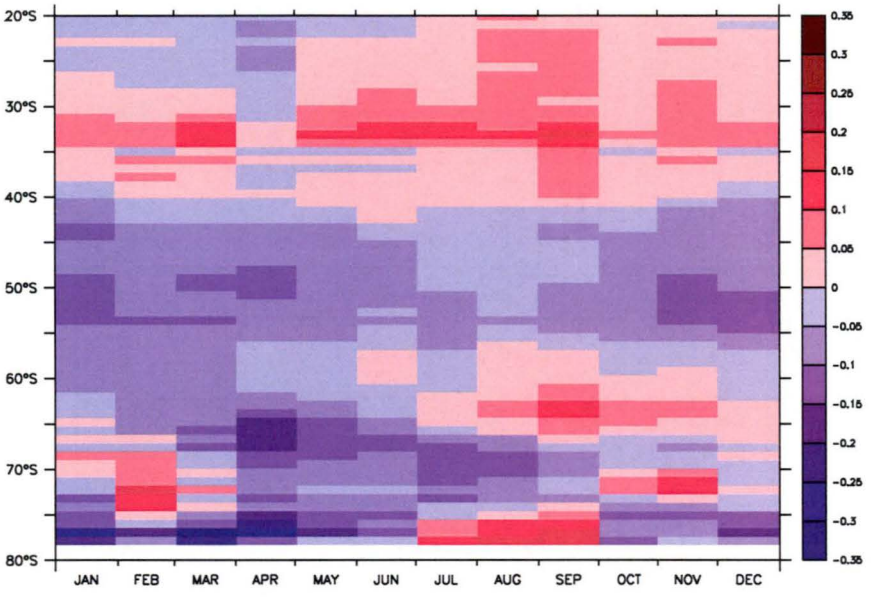

Figure 6-10: The zonally averaged annual cycle of salinity (psu) for a) the control experiment, and b) for the difference between the control experiment and the climatology from Conkright *et al.* (2002) in the southern hemisphere oceans.

a)

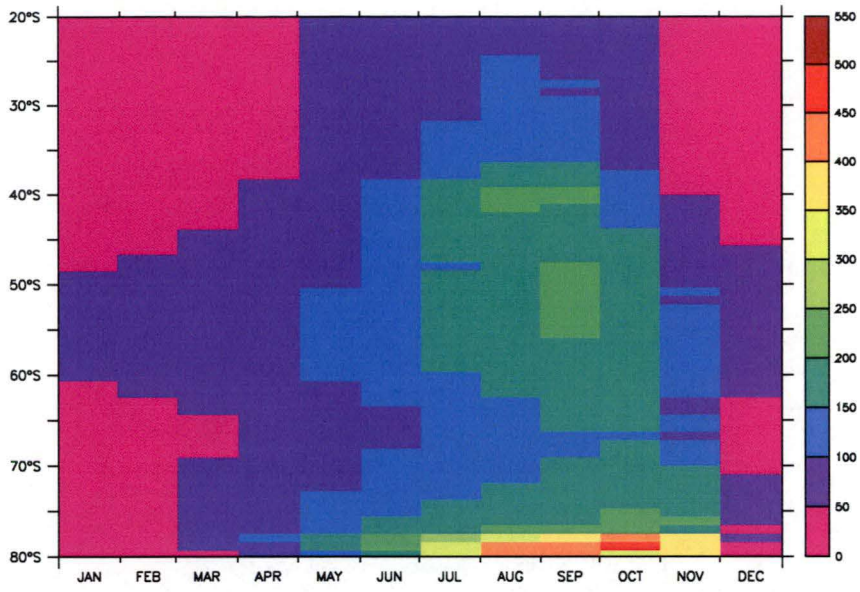

b)

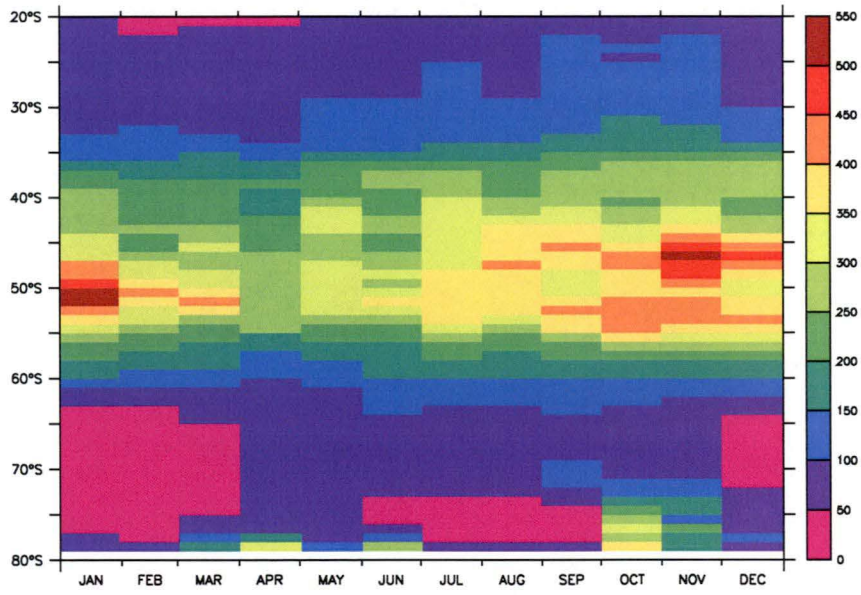

Figure 6-11: The annual cycle of the mixed layer depth (m) calculated using a density criterion (i.e. the mixed layer depth is defined by the depth where the density is greater than the sea-surface density by 0.05 psu) for a) the control experiment, and b) using the same criterion with the temperature and salinity observations of Conkright *et al.* (2002), in the southern hemisphere oceans.

a)

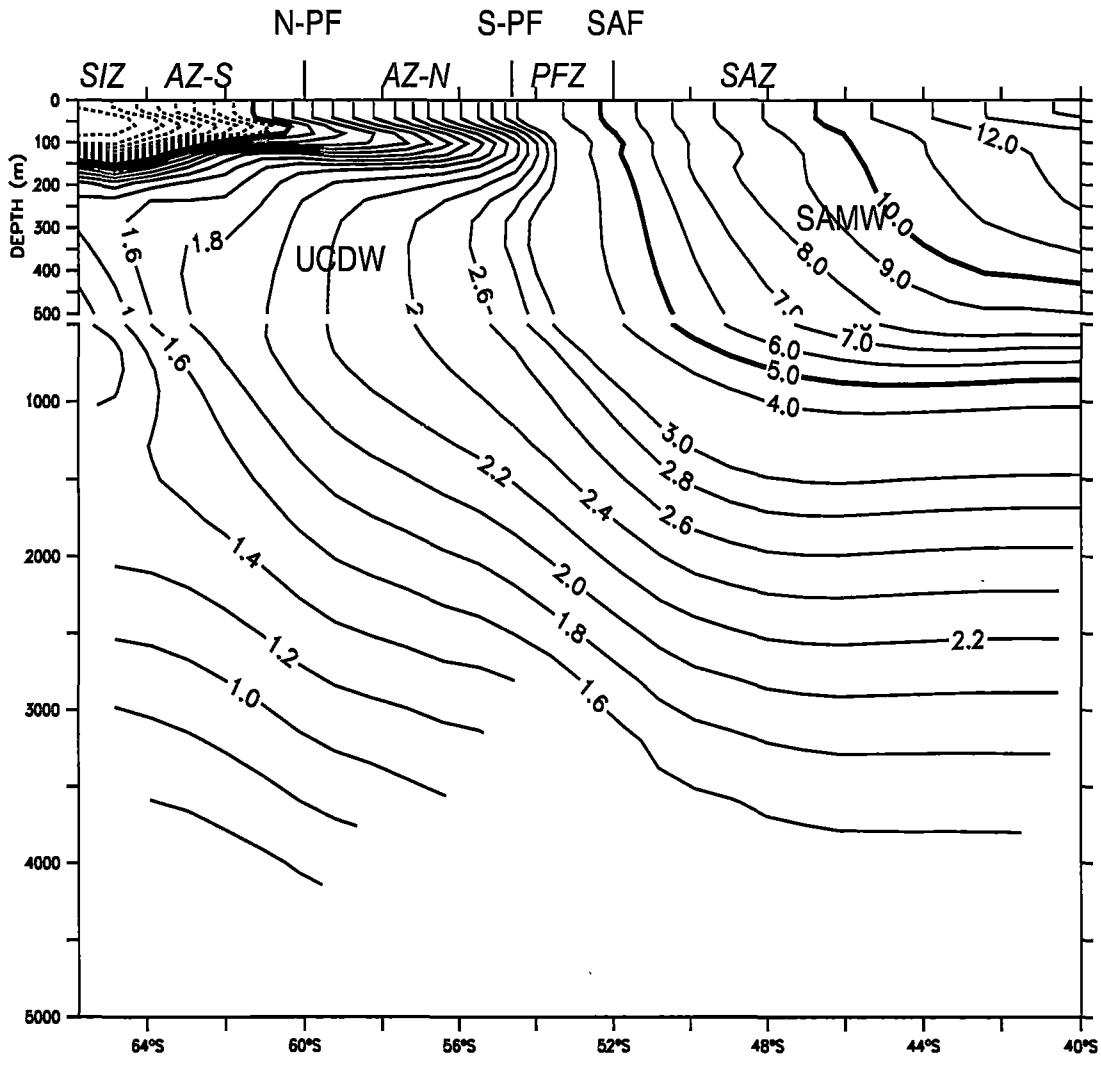
N-PF
S-PF
SAF
SIZ
AZ-S
AZ-N
PFZ
SAZ
DEPTH (m)
0
100
200
300
400
500
1000
2000
3000
4000
5000
64°S
60°S
56°S
52°S
48°S
44°S
40°S
UCDW
SAMW
1.6
1.8
2.6
2.2
1.4
1.2
1.0
2.0
2.4
2.8
3.0
12.0
10.0
9.0
8.0
7.0
6.0
5.0
4.0

b)

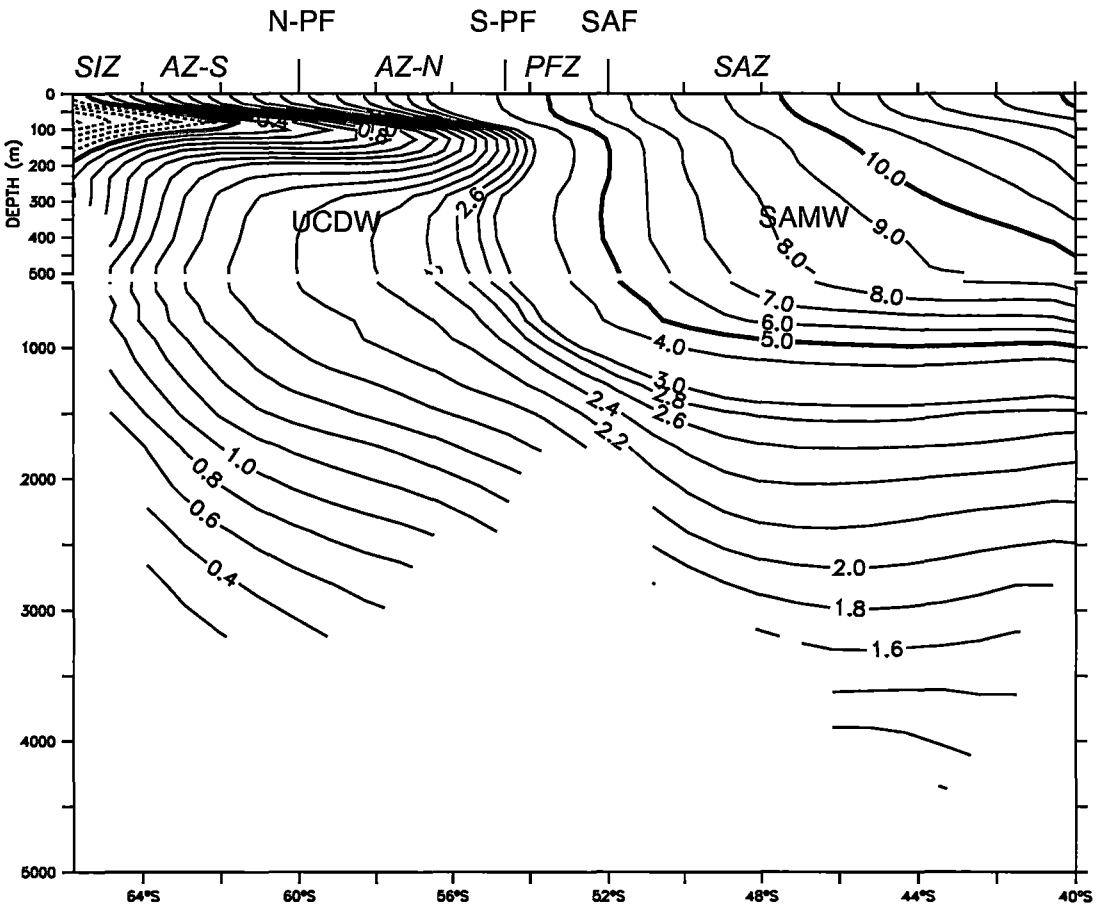

Figure 6-12: Zonal section along 144°E of annual mean temperature for a) the control experiment and b) Conkright *et al.* (2002). The oceanic zones are abbreviated as; SIZ - Seasonal Ice Zone, AZ-S Southern Antarctic Zone, AZ-N Northern Antarctic Zone, PFZ - Polar Frontal Zone, SAZ - Subantarctic Zone. The Fronts are abbreviated as; N-PF – the Northern Polar Front, S-PF -Southern Polar Front, SAF – Subantarctic Front. The water masses are abbreviated as; UCDW – Upper Circumpolar Deep Water, SAMW – Subantarctic Mode Water. *Note*: The positions of the zones and fronts are modelled.

a)

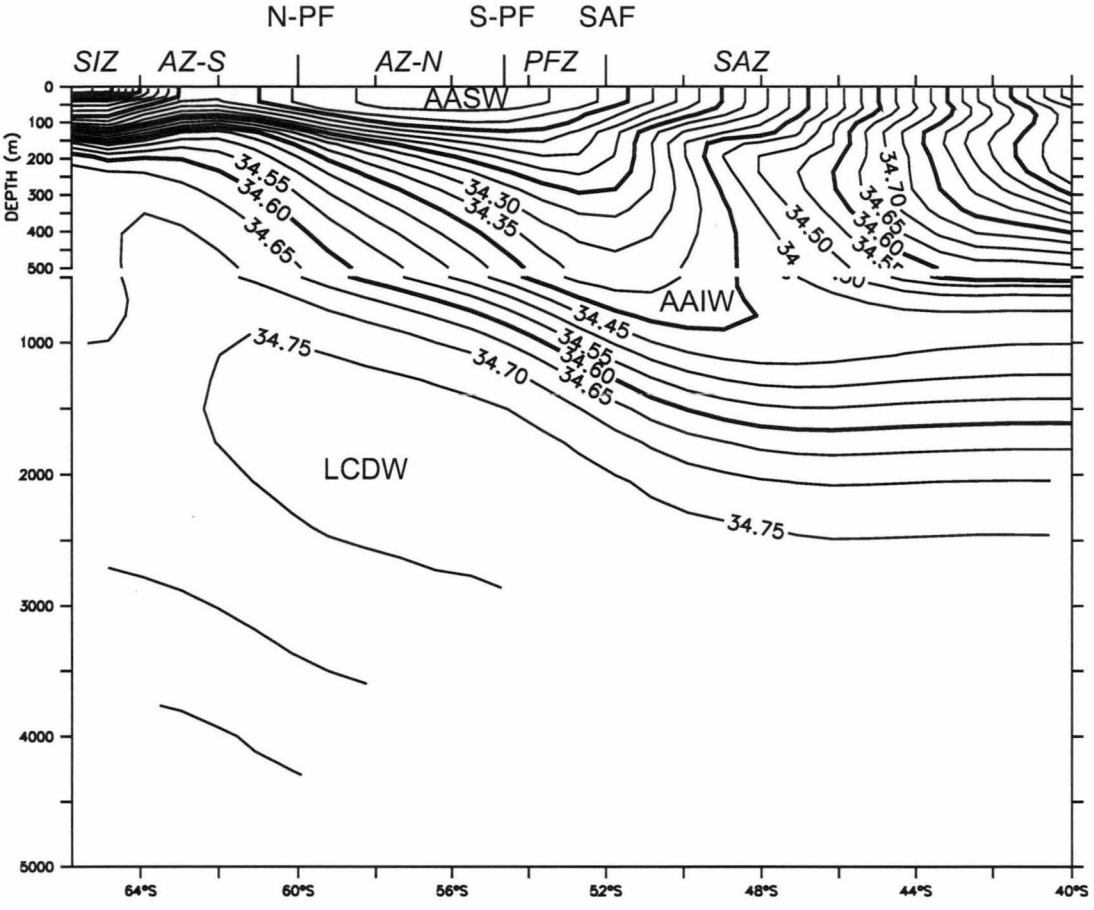
N-PF
S-PF
SAF
SIZ
AZ-S
AZ-N
PFZ
SAZ
AASW
AAIW
LCDW
DEPTH (m)
0
100
200
300
400
500
1000
2000
3000
4000
5000
34.55
34.60
34.65
34.30
34.35
34.50
34.70
34.45
34.75
64°S
60°S
56°S
52°S
48°S
44°S
40°S

b)

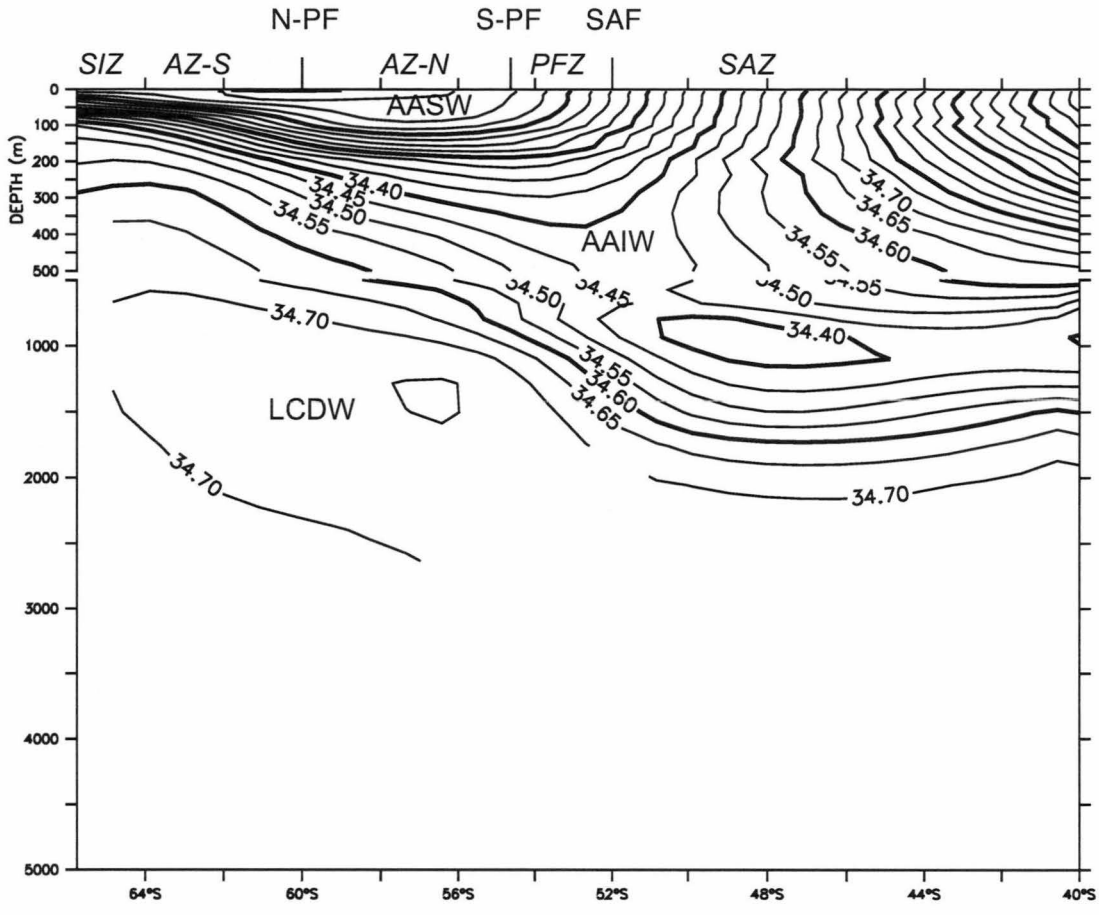

Figure 6-13: Zonal section along 144°E of annual mean salinity for a) the control experiment and b) Conkright *et al.* (2002). The oceanic zones are abbreviated as; SIZ - Seasonal Ice Zone, AZ-S Southern Antarctic Zone, AZ-N Northern Antarctic Zone, PFZ - Polar Frontal Zone and SAZ - Subantarctic Zone. The Fronts are abbreviated as; N-PF – the Northern Polar Front, S-PF - Southern Polar Front and SAF – Subantarctic Front. The water masses are abbreviated as; LCDW – Lower Circumpolar Deep Water, AAIW – Antarctic Intermediate Water and AASW – Antarctic Surface Water. *Note*: The positions of the zones and fronts are modelled.

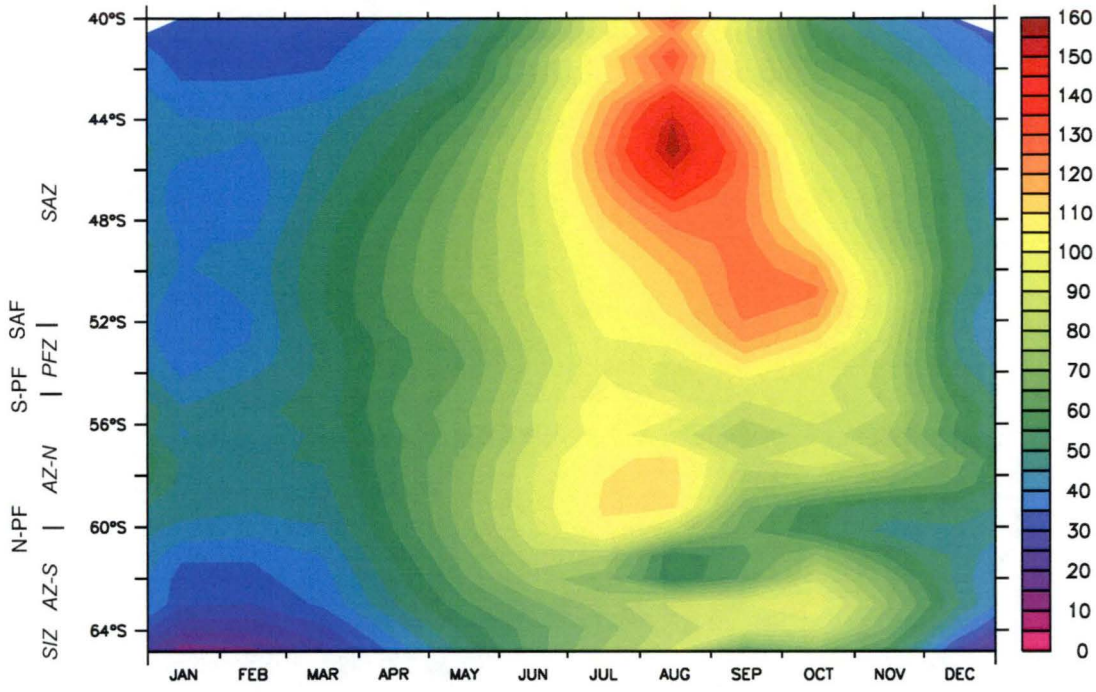

Figure 6-14: Modelled seasonal mixed layer depths (m) from the Chen *et al.* (1994) scheme along the approximate path (142°E) of the WOCE SR3 transect. The oceanic zones are abbreviated as; SIZ - Seasonal Ice Zone, AZ-S Southern Antarctic Zone, AZ-N Northern Antarctic Zone, PFZ - Polar Frontal Zone and SAZ - Subantarctic Zone. The Fronts are abbreviated as; N-PF – the Northern Polar Front, S-PF - Southern Polar Front and SAF – Subantarctic Front.

Table 6-1: Global new and export production estimates from model and observational studies.

Method	New production (GtC/yr)	Source
3D global biogeochemical circulation models	**3.6 - 25.5**	Najjar et al. (2002)
3D assimilation of tracers	**10**	Schlitzer (2002)
Atmospheric O_2/N_2	**19**	Keeling and Shertz (1992)
Seasonal tracers		
Seasonal oxygen variability	**3.7 - 5.1**	Najaar and Keeling (2000), Garcia and Keeling (2001)
Seasonal phosphate variability	**5.3 ± 0.8**	Lounachi and Najjar (2000)
Satellite chlorophyll	**10 - 20**	Falkowski et al. (1998), Laws et al. (2000)

Table 6-2: Comparison of various regional estimates of new (or export) production estimates in the southern hemisphere. The acronyms are SAZ, subantarctic zone; N-PFZ, northern polar frontal zone; and PFZ, polar frontal zone.

Method	Region	New/export production (GtC yr^{-1})	New/export production (molC m^{-2} yr^{-1})#	Source
3D Prognostic global biogeochemical cycle model	20°S – 90°S 50°S - 90°S	1.7 - 3.8 0.23 - 2.0	1.02 – 2.30 0.43 – 3.75	This study
"	30°S – 90°S	2.4 - 3.5	1.86 – 2.71	Gnanadesikan *et al.* (2004)
Air-sea oxygen fluxes	20°S -90°S	3.23	1.95	Najjar and Keeling (2000)
Atmospheric O_2/N_2	20°S – 90°S	11	6.62	Keeling and Shertz (1992)
3D assimilation of tracers	30°S - 90°S 50°S – 90°S	3 1.0 +/- 0.21	2.32 1.87	Schlitzer (2002a)
Global nutrient climatologies	40°S – 90°S	2.04	2.22	Louanchi and Najjar (2000)
"	40°S – 90°S 50°S - 90°S	2.0 +/- 1.7 0.9 - 2.2	2.22 1.68 – 4.12	MacCready and Quay (2001)

* Note: The following ocean areas (m^2) are used in calculating the local averages. Area of ocean (20°S – 90°S) = 1.38×10^{14}; area of ocean (30°S – 90°S) = 1.075×10^{14}; area of ocean (40°S – 90°S) = 7.497×10^{13}; area of ocean (50°S – 90°S) = $4,449 \times 10^{13}$.

Table 6-3: Comparison of various local estimates of new (or export) production estimates in the southern hemisphere. The acronyms are SAZ, subantarctic zone; N-PFZ, northern polar frontal zone; and PFZ, polar frontal zone.

Method	Region	New/export production (molC m^{-2} yr^{-1})	Source
3D Prognostic global biogeochemical cycle model	48°S – 52°S, 142°E (SAZ) 50°S – 52°S, 142°E (PFZ)	0.42 – 4.16 " (see Figure 6-15)	This study
1D biophysical model	47°S, 142°E (SAZ) 54°S, 140°E (PFZ)	6.30 – 7.20 8.60 – 10.10	Wang *et al.* (2001)
Nutrient depletion	46°S – 50°S (SAZ) 51.5°S - 54.5°S (PFZ)	3.40 1.40	Lourey and Trull (2001)
Nitrate isotopes, ^{15}N	50°S – 55°S (SAZ) 55°S - 59°S (N-PFZ)	5.80 3.70	Buesseler *et al.* (2003)
Dissolved inorganic carbon	41°S – 42°S, 55-75 (SAZ)	6.67 – 19.98	Metzl *et al.* (1999)

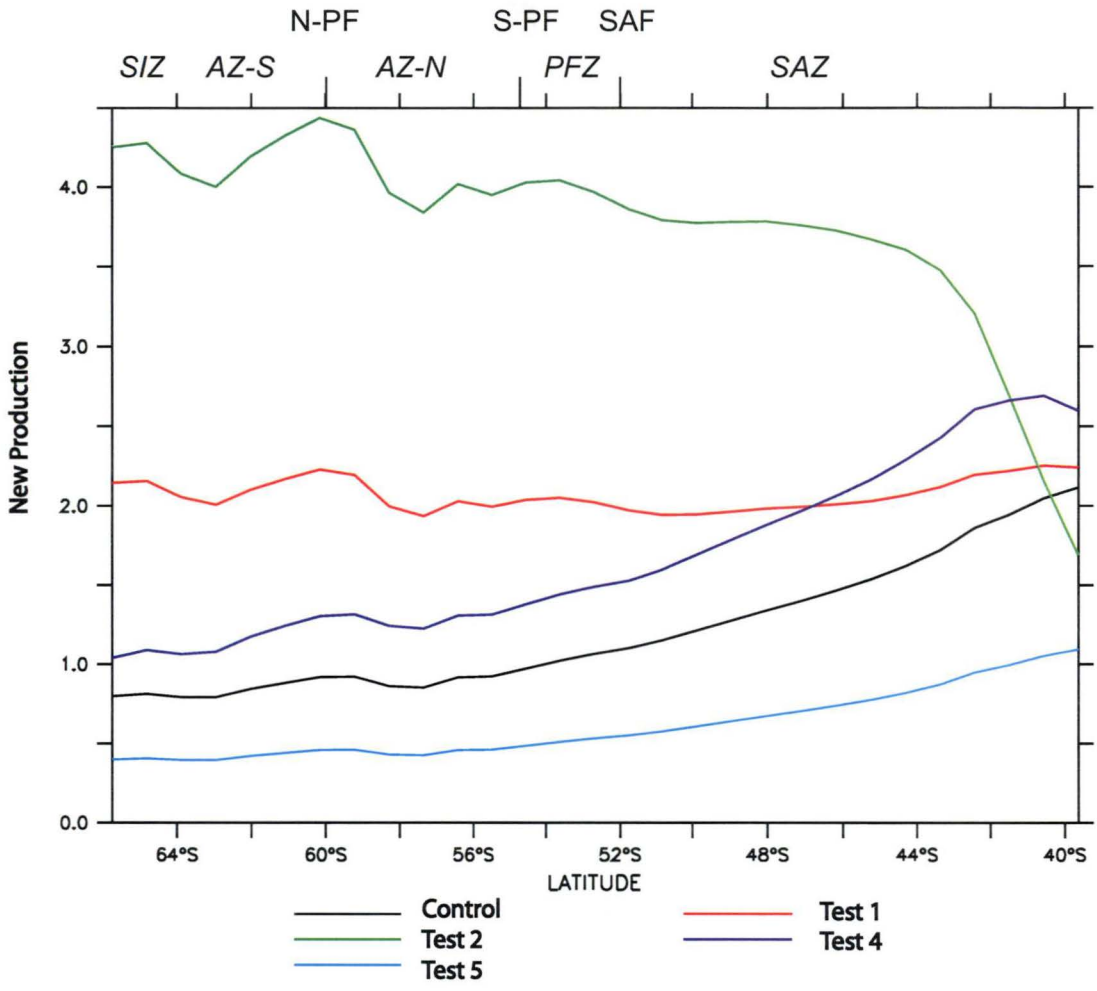

Figure 6-15: New production (molC m^{-2} yr^{-1}) along the WOCE SR3 line (~142°E) for a selection of the modelled new production perturbation experiments. The oceanic zones are abbreviated as; SIZ - Seasonal Ice Zone, AZ-S Southern Antarctic Zone, AZ-N Northern Antarctic Zone, PFZ - Polar Frontal Zone, SAZ - Subantarctic Zone. The Fronts are abbreviated as; N-PF – the Northern Polar Front, S-PF - Southern Polar Front, SAF – Subantarctic Front.

a)

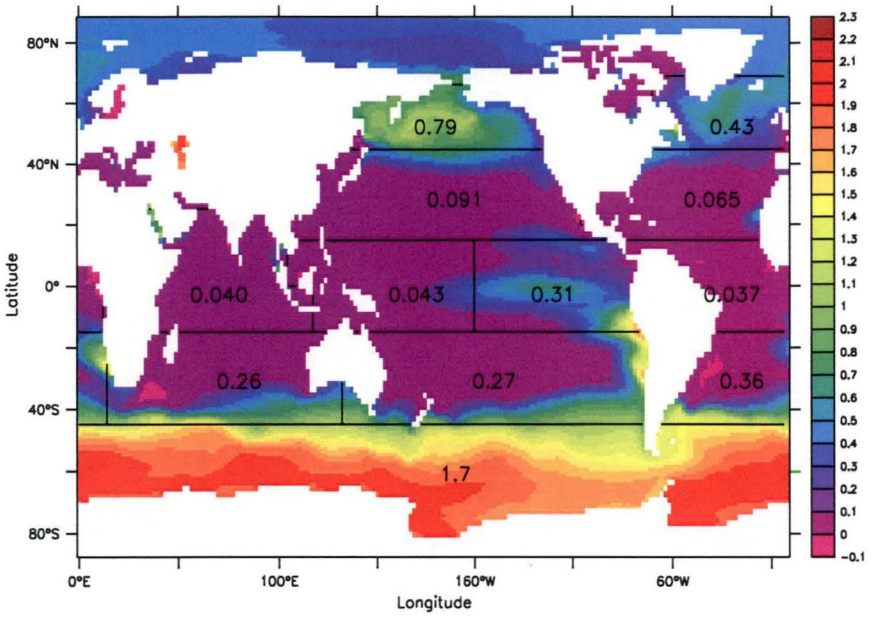

b)

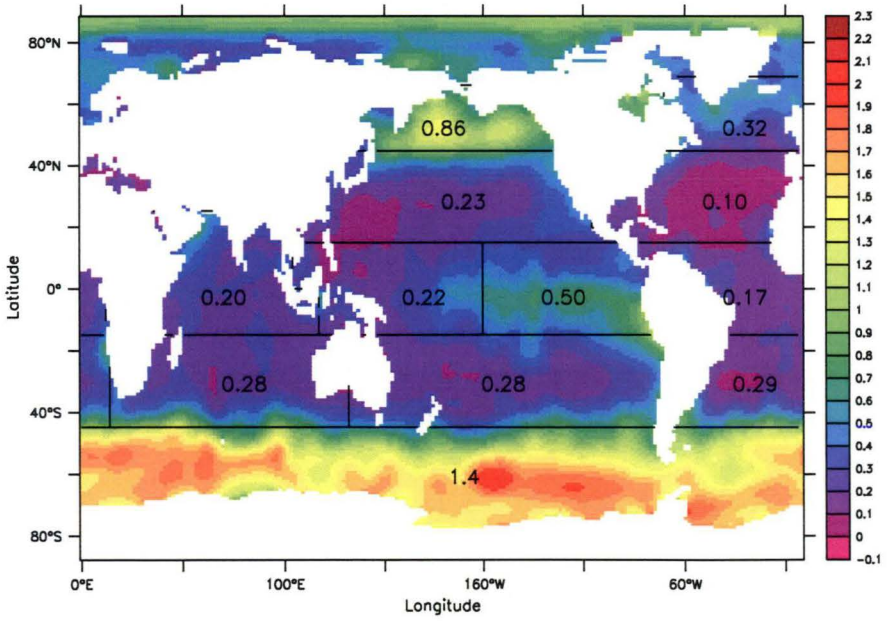

Figure 6-16; Surface phosphate distribution (mmol m^{-3}) for the a) control experiment and, b) Conkright *et al.* (2002). The number in each boxed region represents the regional average phosphate concentration (mmol m^{-3}).

a)

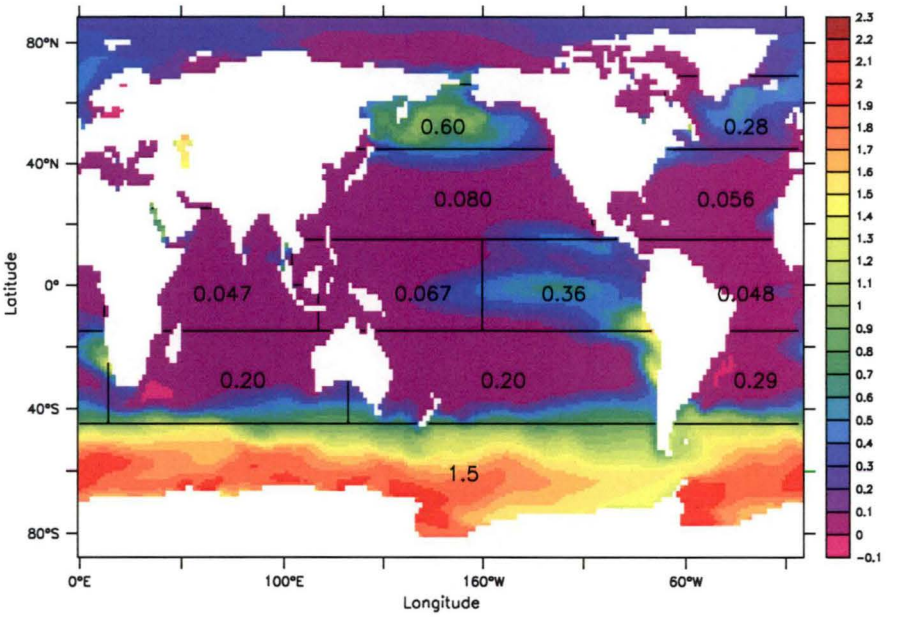
80°N
40°N
0°
40°S
80°S
Latitude
0°E
100°E
160°W
60°W
Longitude
0.60
0.28
0.080
0.056
0.047
0.067
0.36
0.048
0.20
0.20
0.29
1.5
2.3
2.2
2.1
2
1.9
1.8
1.7
1.6
1.5
1.4
1.3
1.2
1.1
1
0.9
0.8
0.7
0.6
0.5
0.4
0.3
0.2
0.1
0
-0.1

b)

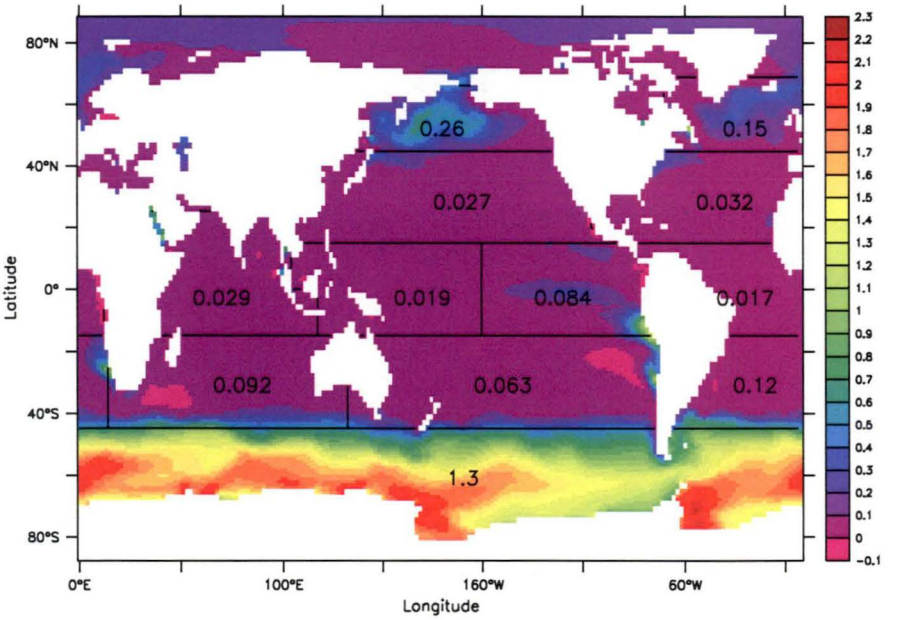
80°N
40°N
0°
40°S
80°S
Latitude
0°E
100°E
160°W
60°W
Longitude
0.26
0.15
0.027
0.032
0.029
0.019
0.084
0.017
0.092
0.063
0.12
1.3
2.3
2.2
2.1
2
1.9
1.8
1.7
1.6
1.5
1.4
1.3
1.2
1.1
1
0.9
0.8
0.7
0.6
0.5
0.4
0.3
0.2
0.1
0
-0.1

c)

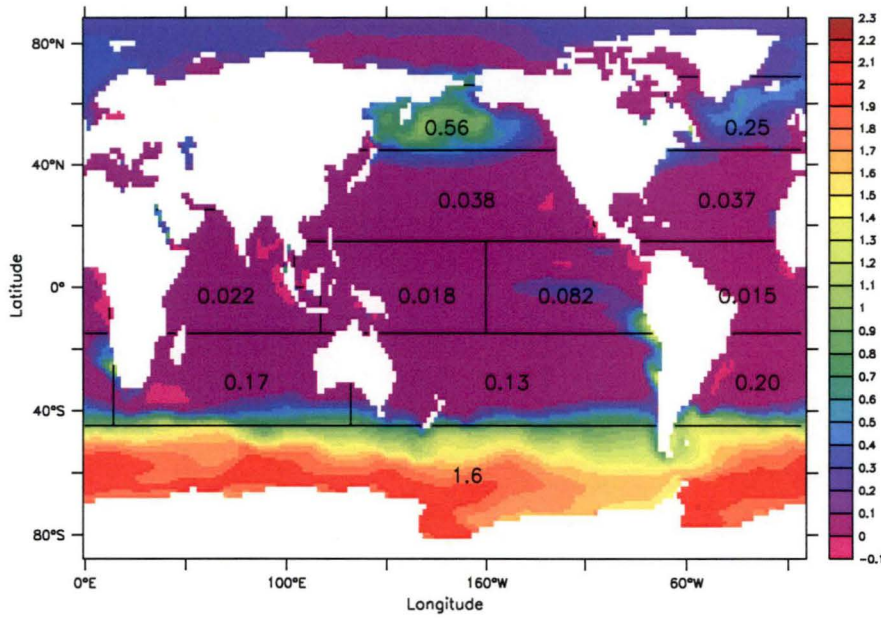

d)

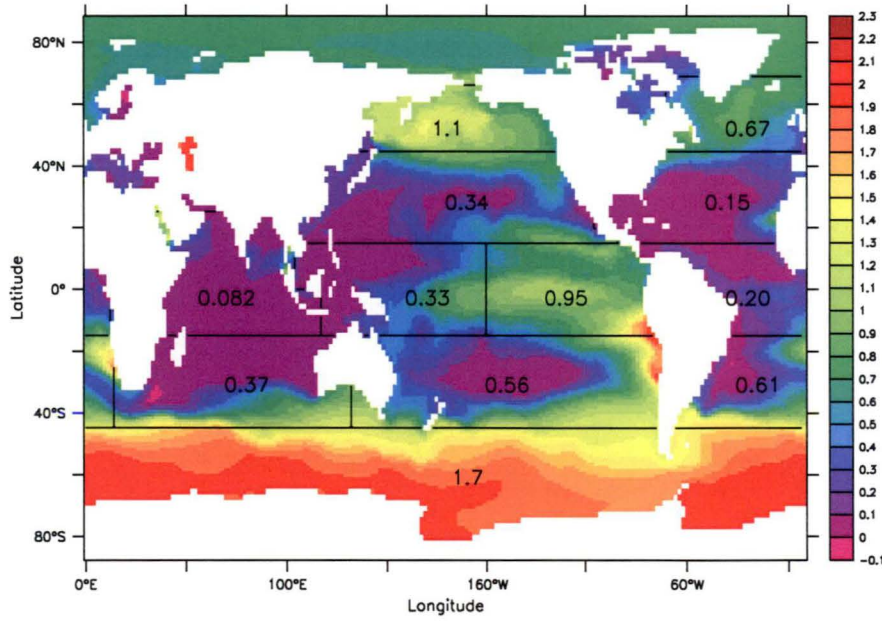

Figure 6-17: Surface phosphate distribution (mmol m^{-3}) for the new production perturbation experiments a) test 1, b) test 2, c) test 4 and d) test 5. The number in each boxed region represents the regional average phosphate concentration (mmol m^{-3}).

a)

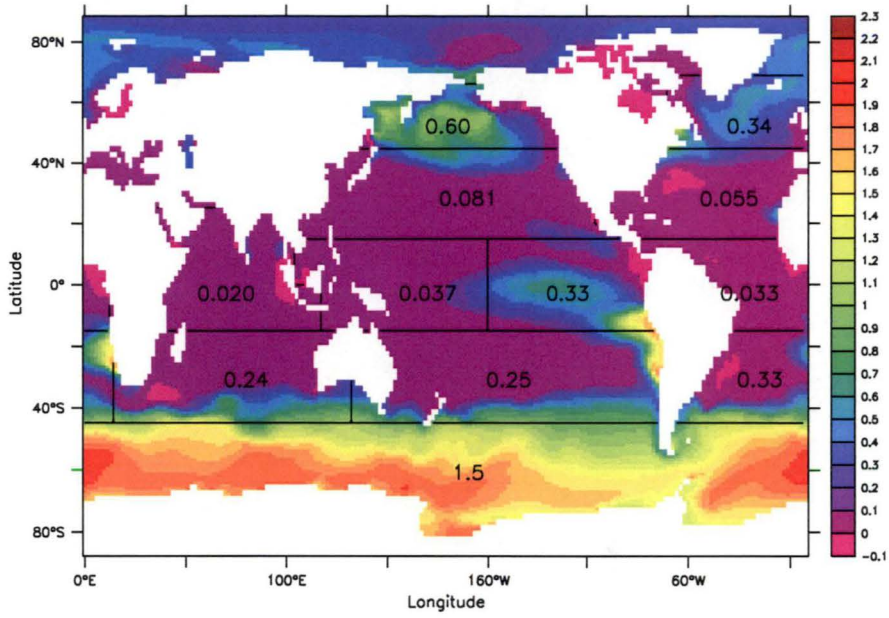

b)

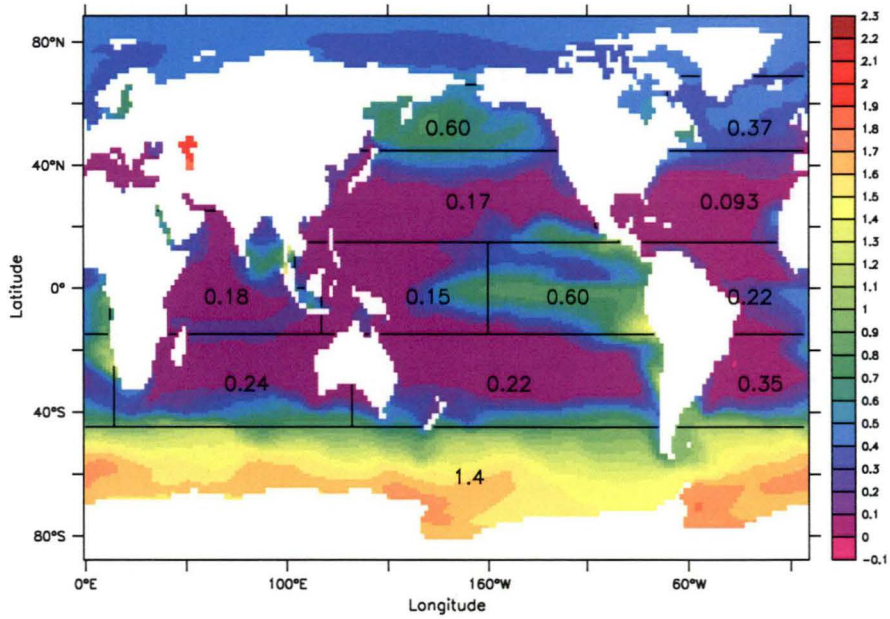

Figure 6-18: Surface phosphate distribution (mmol m^{-3}) for selected physical perturbation experiments a) test 9 and, b) test 15. The number in each boxed region represents the regional average phosphate concentration (mmol m^{-3}).

a)

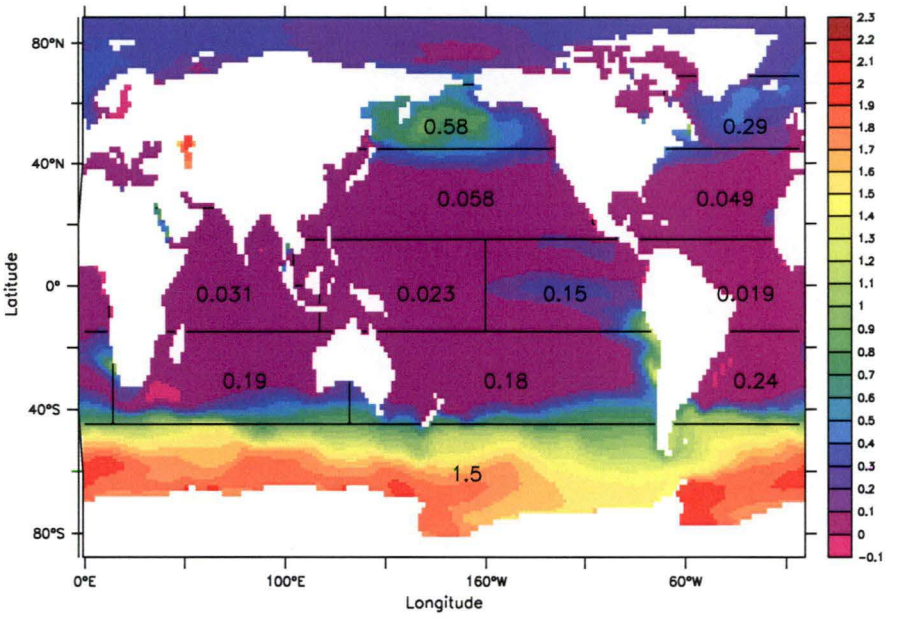

b)

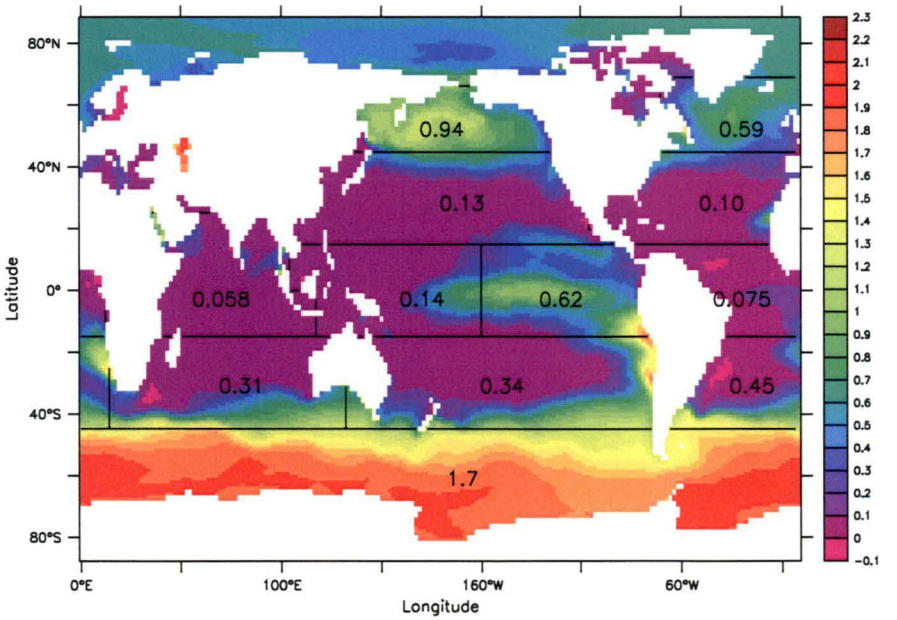

Figure 6-19: Surface phosphate distribution (mmol m^{-3}) for the biogeochemical perturbation experiments a) test 6 and, b) test 7. The number in each boxed region represents the regional average phosphate concentration (mmol m^{-3}).

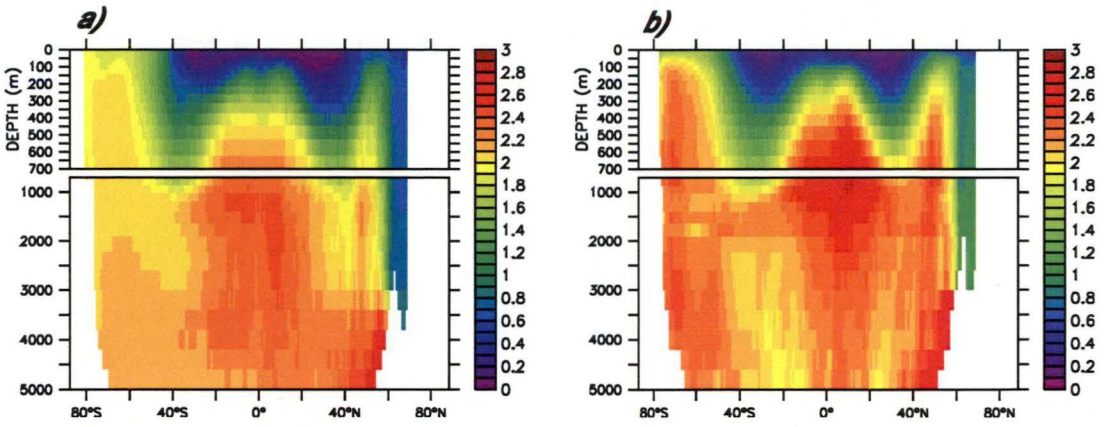

Figure 6-20: Zonally averaged annual mean section of phosphate (mmol m^{-3}) for a) the control experiment and, b) Conkright *et al.* (2002).

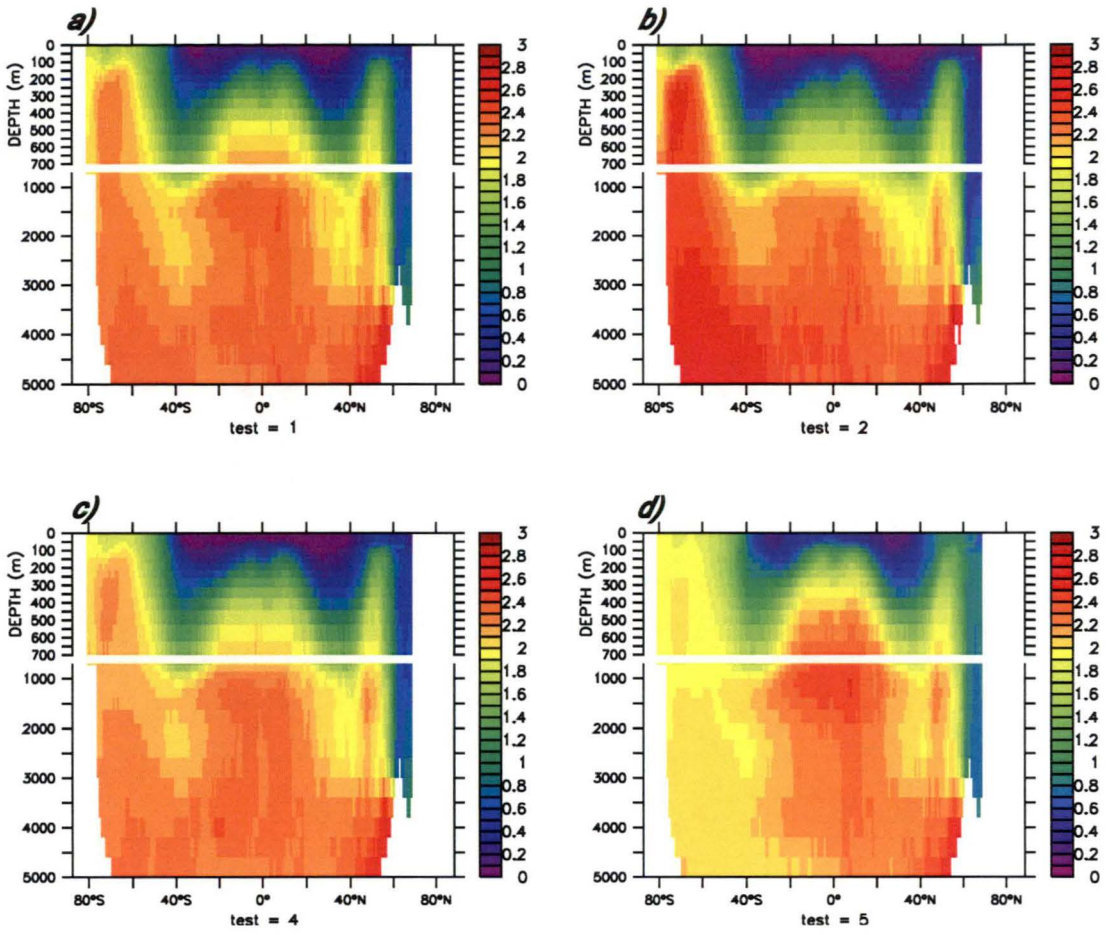

Figure 6-21: Zonally averaged annual mean section of phosphate (mmol m^{-3}) for a) test 1, b) test 2, c) test 4 and d) test 5.

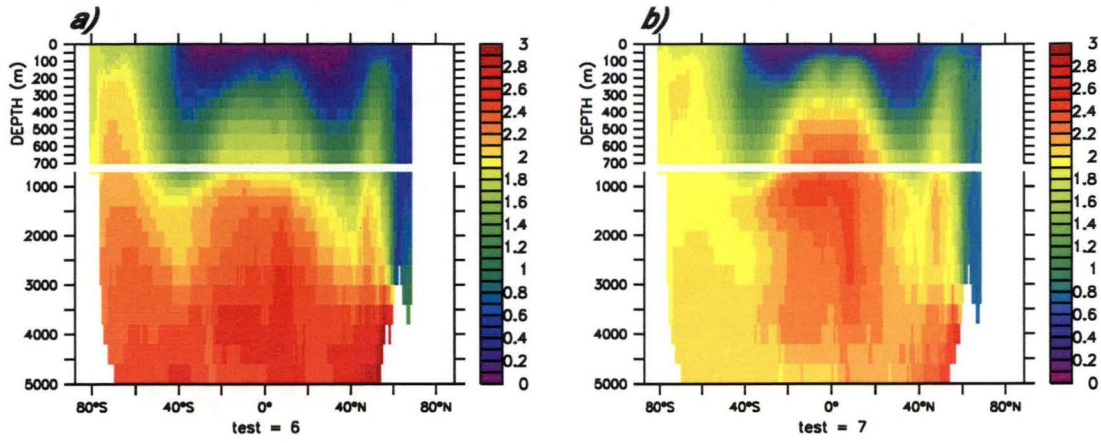

Figure 6-22: Zonally averaged annual mean section of phosphate (mmol m^{-3}) for a) test 6, b) test 7.

a)

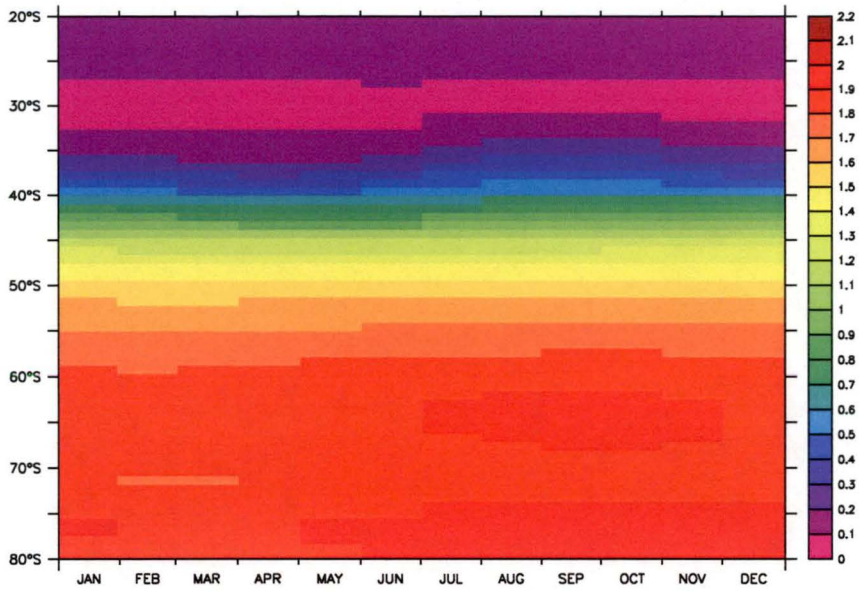
20°S
30°S
40°S
50°S
60°S
70°S
80°S
JAN
FEB
MAR
APR
MAY
JUN
JUL
AUG
SEP
OCT
NOV
DEC
2.2
2.1
2
1.9
1.8
1.7
1.6
1.5
1.4
1.3
1.2
1.1
1
0.9
0.8
0.7
0.6
0.5
0.4
0.3
0.2
0.1
0

b)

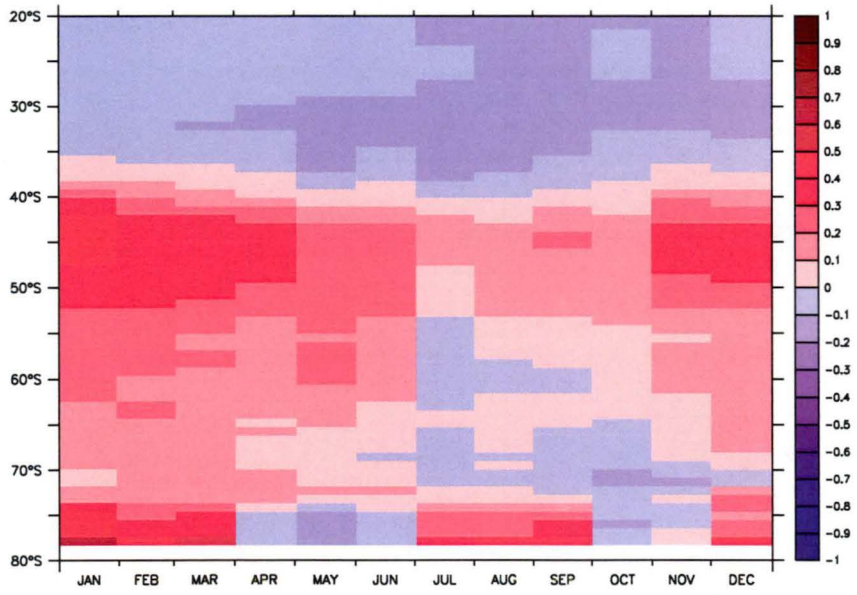
20°S
30°S
40°S
50°S
60°S
70°S
80°S
JAN
FEB
MAR
APR
MAY
JUN
JUL
AUG
SEP
OCT
NOV
DEC
1
0.9
0.8
0.7
0.6
0.5
0.4
0.3
0.2
0.1
0
−0.1
−0.2
−0.3
−0.4
−0.5
−0.6
−0.7
−0.8
−0.9
−1

c)

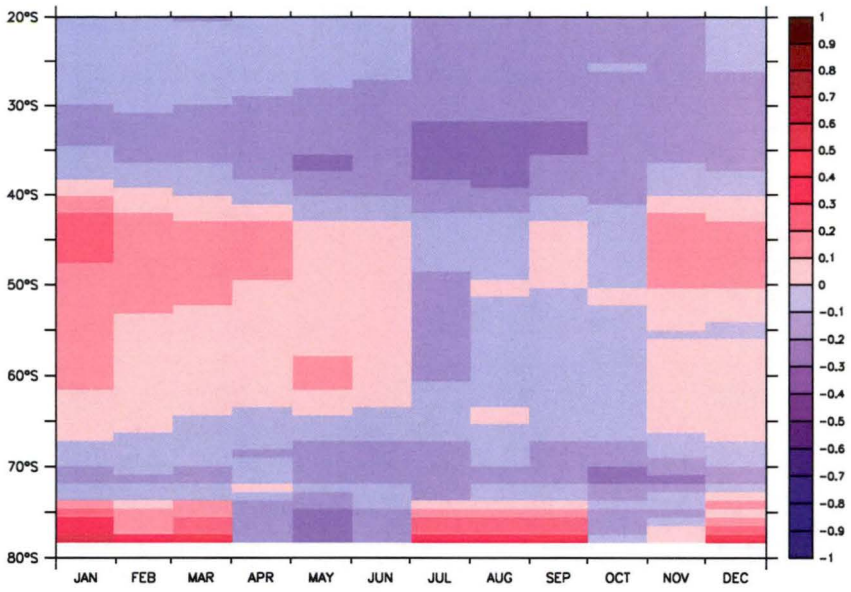

Figure 6-23: The zonally averaged annual cycle of phosphate (mmol m^{-3}) for a) the control experiment, b) the difference between the control experiment and the climatology from Conkright *et al.* (2002), and c) the difference between test 1 and the climatology from Conkright *et al.* (2002). Note that the perturbation experiment, test 1, produces twice the magnitude of new production than the control experiment.

a)

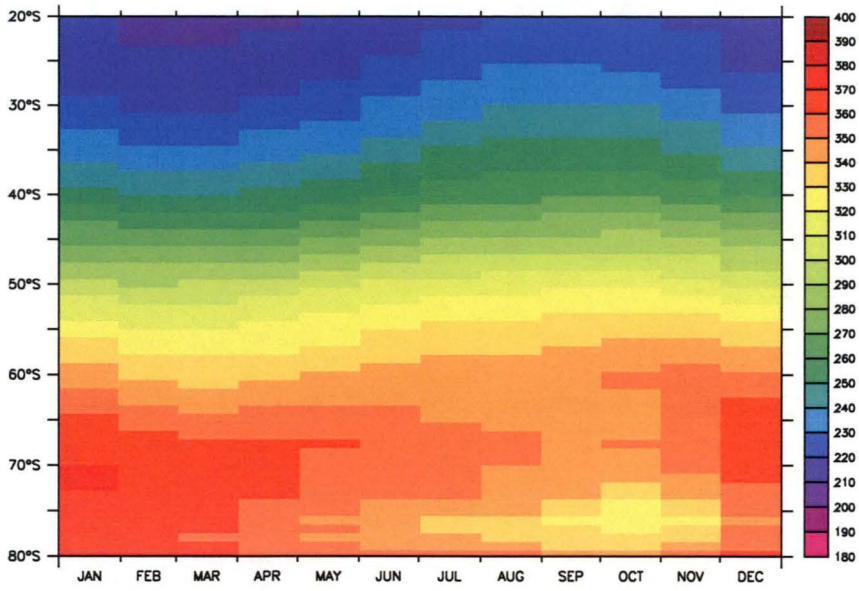

b)

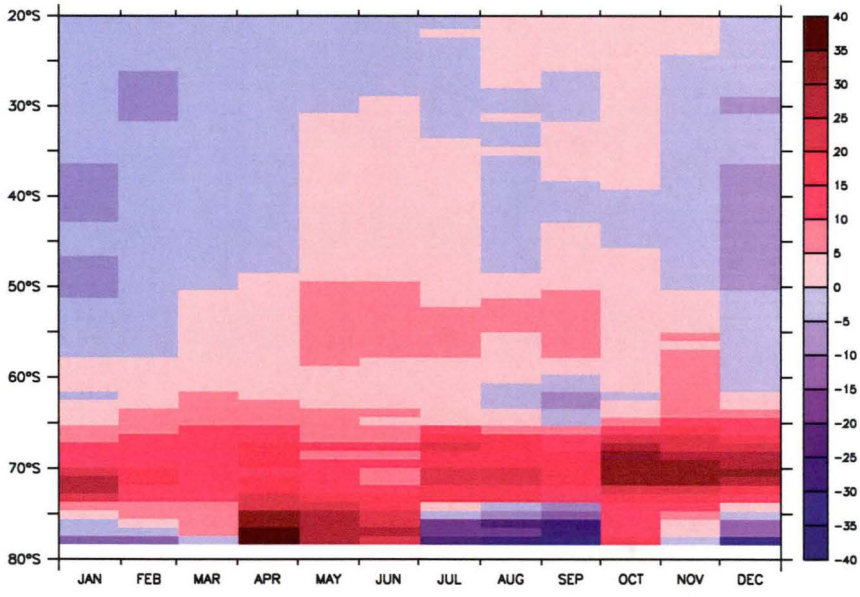

Figure 6-24: a) The zonally averaged oxygen concentrations (mmol m^{-3}) for the control case, b) the difference between the zonally averaged oxygen concentrations in the control case and the climatology of Conkright *et al.* (2002).

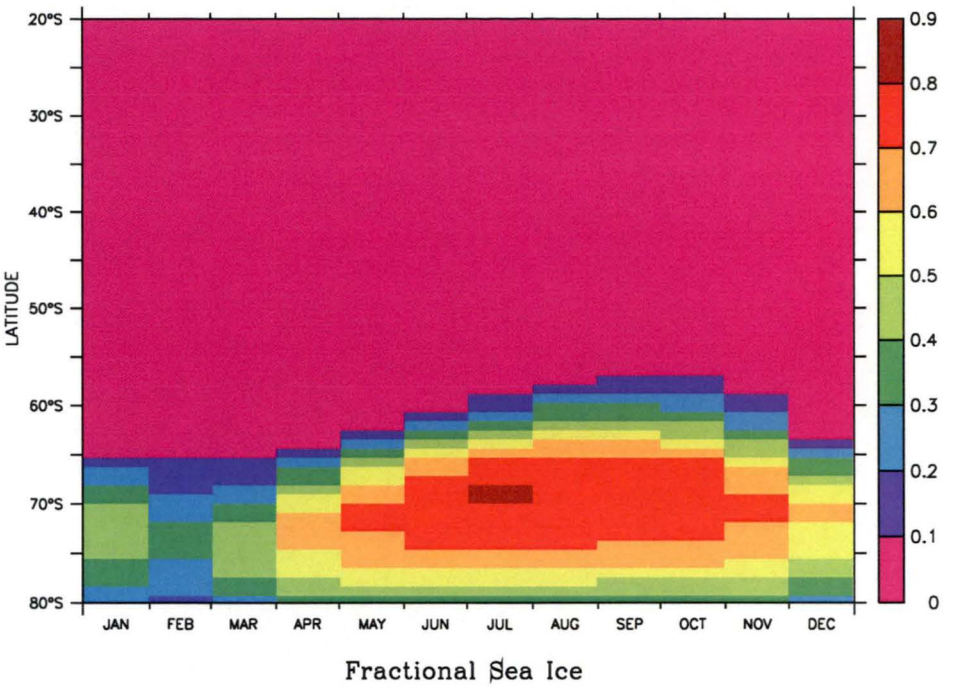

Figure 6-25: The annual cycle of the zonally averaged fraction of the sea-surface covered by sea-ice in the model.

a)

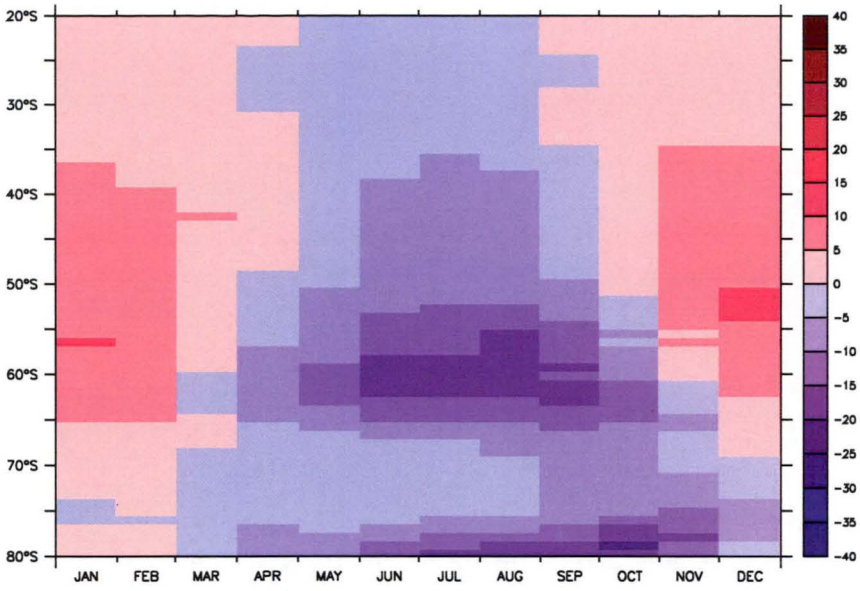
20°S
30°S
40°S
50°S
60°S
70°S
80°S
JAN
FEB
MAR
APR
MAY
JUN
JUL
AUG
SEP
OCT
NOV
DEC
40
35
30
25
20
15
10
5
0
-5
-10
-15
-20
-25
-30
-35
-40

b)

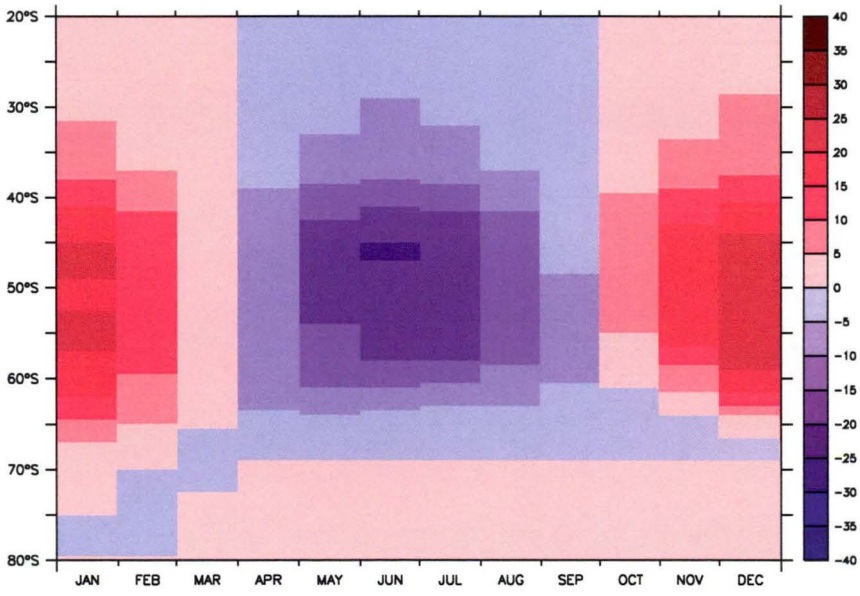
20°S
30°S
40°S
50°S
60°S
70°S
80°S
JAN
FEB
MAR
APR
MAY
JUN
JUL
AUG
SEP
OCT
NOV
DEC
40
35
30
25
20
15
10
5
0
-5
-10
-15
-20
-25
-30
-35
-40

c)

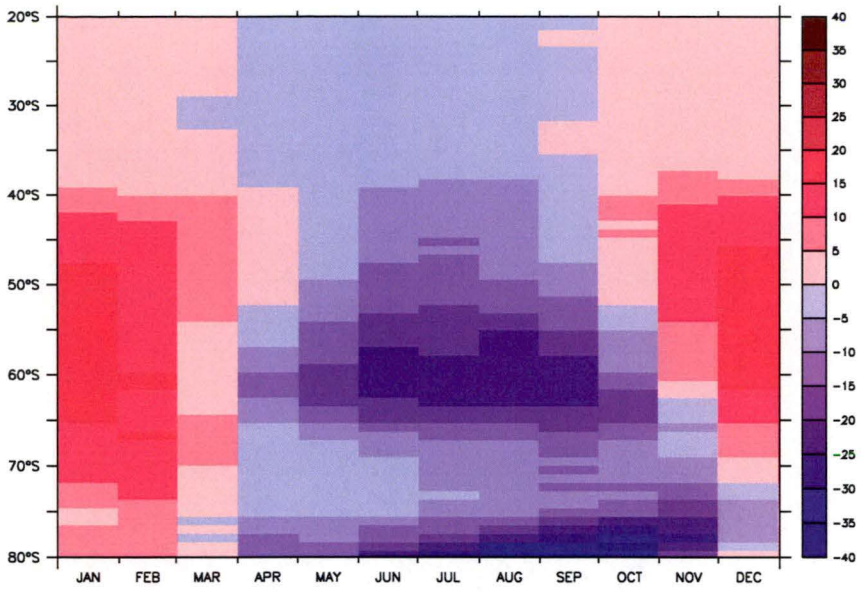

Figure 6-26: The zonally averaged annual cycle of oxygen fluxes (mol m^{-2} yr^{-1}) for a) the control experiment and b) Garcia and Keeling (2001), based on observations and c) test 2 (i.e. quadrupled new production).

7. Oceanic Oxygen: Is it a reliable tracer of new production

In this study, we test how effectively the air-sea oxygen flux technique of Najjar and Keeling (2000) retrieves new production in the southern hemisphere oceans and determine the relationship between SNO_{bio} and NP in the model. We identify the ocean processes that bias the air-sea oxygen flux approach of Najjar and Keeling (2000) and discuss whether improved estimates of new production can be made.

7.1. Estimating new production from air-sea O_2 fluxes

We apply the approach of Najjar and Keeling (2000) to tracer fields simulated using a global biogeochemical ocean model. We follow their method of estimating the hemispheric biological and thermal components of the SNO of oxygen described below. We use the oxygen fluxes from a global biogeochemical model. The Najjar and Keeling (2000) estimate is based on climatological oxygen fluxes [Najjar and Keeling (1997)] estimated from the seasonal surface oxygen anomalies of Najjar and Keeling (1997). The spatial and temporal coverage of the physical and biogeochemical fields, used by Najjar and Keeling (2000) to estimate the oxygen and heat fluxes, are not identical. Also, the oxygen climatology data set is a temporally and spatially smoothed field. The errors introduced as a result of these largely unavoidable inconsistencies are difficult to evaluate. This uncertainty is avoided in our study where oxygen and heat fluxes are produced from an internally consistent model, making it easier to isolate the impact of ocean processes on their method of estimating new production.

Najjar and Keeling (2000) calculated the biological flux of oxygen by subtracting the thermal flux from each of the monthly estimated O_2 fluxes. Following Keeling and Shertz (1992), the thermal components of the oxygen fluxes ($molO_2\ m^{-2}\ s^{-1}$), F_{therm}, are estimated from the annual

cycles of the modelled monthly-mean heat flux, sea surface temperature, and salinity fields according to

$$F_{therm} = -\frac{dC_{eq}}{dT}\frac{Q}{C_P}, \tag{16}$$

where Q is the heat flux (J m^{-2} s^{-1}), C_P is the heat capacity of seawater (J m^{-3} K^{-1}), and $\frac{dC_{eq}}{dT}$ is the temperature derivative of the oxygen solubility (molO_2 m^{-3} K^{-1}) [Weiss (1970)] with heat capacity set to a constant 3993 kJ m^{-1} °C.

We calculate the biological flux of oxygen, F_{bio}, at each grid point in the model by subtracting the thermal flux, calculated using Equation (16) from the total simulated O_2 fluxes, F_{total}

$$F_{bio}(i,j,t) = F_{total}(i,j,t) - F_{therm}(i,j,t). \tag{17}$$

Najjar and Keeling (2000) calculated the hemispheric biological SNO by subtracting the annual mean spatially integrated biological oxygen flux from the monthly mean spatially integrated biological oxygen fluxes, and then temporally integrating the monthly fluxes over the period where the flux is outgassing to the atmosphere – the SNO period. The biological SNO of oxygen in the southern hemisphere oceans (20°S - 90°S), SNO_{bio} (molO_2 yr^{-1}), is calculated from the simulated biological fluxes, F_{bio} (molO_2 m^{-2} $month^{-1}$), according to

$$SNO_{bio} = \sum_{t=1}^{12}\left[\iint F_{bio}(i,j,t)\,dA - \frac{\sum_{t=1}^{12}\iint F_{bio}(i,j,t)\,dA}{12}\right] \text{ for } [\ldots] > 0. \tag{18}$$

This equation implies a 'virtual' degassing of oxygen whenever the bracketed kernel is positive, even though this may occur when the surface O_2 concentration is less than the equilibrium solubility.

The SNO_{bio} can be converted into carbon units (GtC yr^{-1})

$$SNO_{bio}\left(GtC\ yr^{-1}\right)=\frac{SNO_{bio}\left(molO_2\ yr^{-1}\right)\times 12.01}{10^{15}\times 1.6}, \qquad (19)$$

using a C:O ratio of 106:170 - the photosynthetic quotient used in the biogeochemical model for the production of organic matter [Anderson and Sarmiento (1994)] - and multiplying by the molar ratio of carbon (12.01 g mol^{-1}).

7.2. The SNO_{bio} estimates from air-sea oxygen flux approach

We apply the method of Najjar and Keeling (2000), outlined in section 2, to the simulated oxygen fluxes from each of the perturbation experiments. Note that, unless superscripted, NP refers to new production estimated over the southern hemisphere (20°S – 90°S). Figure 7-1a (red line) shows the relationship between SNO_{bio} (Equation (18)) and NP in the southern hemisphere oceans for each of the new production pertrubation experiments (i.e. experiments 1-5, Table 4-1). A linear regression to the new production perturbation experiments gives the relationship

$$SNO_{bio}=0.39\,NP+0.44\ ,\ r^2=0.99\ , \qquad (20)$$

which rearranges to

$$NP=\frac{SNO_{bio}}{0.39}-1.1\ , \qquad (21)$$

from which we determine the model derived hemispheric g factor, $g_{hem}=0.39$, and the SNO offset , $k_{SNO}=1.1$ GtC yr^{-1}.

The two key results are:

i) the relationship between SNO_{bio} and NP is linear

ii) the linear relationship has a non-zero offset, k_{SNO}, when $SNO_{bio} = 0$.

The linear scaling between SNO_{bio} and NP suggests that g_{hem} is constant with variability in the magnitude and distribution of new production. Remember that the ocean circulation is identical in each of these experiments. The solid line in Figure 7-1a, represents where the experiments would lie if SNO_{bio} were a direct measure of NP (i.e. $g_{hem} = 1$ and $k_{SNO} = 0$). But, $g_{hem} < 1$ and the nonzero offset, k_{SNO}, indicates that factors other than the photosynthetic production of oxygen are producing a SNO of oxygen. If no correction is made for these factors, the technique will produce biased estimates of new production.

7.3. What factors produce biases in the estimates of New Production?

Using a series of model experiments, described in section 3, we identify and discuss what factors may cause the bias in the NP estimates. As biological matter forms through photosynthesis, oxygen is released into the water column, and this oxygen can escape to the atmosphere. If we can reliably estimate the proportion of the photosynthetically produced oxygen outgassed to the atmosphere, then we can expect that air-sea oxygen fluxes would be a reliable measure of NP. Najjar and Keeling (2000) argue that the photosynthetically produced oxygen within the mixed layer outgases to the atmosphere over the period during which the mixed layer shoals. Thus, they assume that the biological air-sea oxygen flux during the SNO period (i.e. the period where this flux is outgassing to the atmosphere), is equivalent to the photosynthetic production of oxygen, and therefore a direct measure of NP confined to the mixed layer. Also, they necessarily assume that all oxygen fluxes, other than the photosynthetic production of oxygen, are negligible during this period. Here we show, that these assumptions do not hold.

The biological oxygen flux, F_{bio}, does not track *NP* during the SNO period. Figure 7-2a shows the distribution of biological SNO, SNO_{bio}, calculated using Equation (18). Figure 7-2b shows the photosynthetic SNO, SNO_{photo}, which is photosynthetic oxygen flux, F_{photo}, integrated over the SNO period (December to May). F_{photo} is defined here as the maximum potential outgassing of oxygen due to photosynthesis. The amount of oxygen produced photosynthetically is known in the model and is calculated from new production (which is simulated in carbon units) using the Redfield ratio $O_2:C=1.6$, such that $F_{photo}=NP\times O_2:C$. A comparison of Figure 7-2a and Figure 7-2b, demonstrates that F_{bio} poorly tracks the spatial distribution of F_{photo} during the SNO period (i.e. November to March). There are several possible explanations for why, which include:

1. some new production occurs too deep to be outgassed,
2. not all the new production is seasonal,
3. the assumption of complete air-sea equilibration of oxygen is inadequate due to oxygen's finite gas exchange time with the atmosphere,
4. processes other than new production produce and modulate air-sea fluxes of oxygen.

Also, in both these studies, the annual mean flux is subtracted before calculating SNO_{bio} in an attempt to correct for the impact of the large-scale ventilation oxygen flux. The impact of subtracting the annual mean on estimates of *NP* will also be investigated.

For all months, including the months in the SNO period, F_{bio} is a complex combination of oxygen fluxes given by,

$$\begin{aligned} F_{bio} &= F_{total} - F_{therm} \\ &= F_{photo} + F_{diseq} + F_{vent} - F_{ice}\ , \end{aligned} \tag{22}$$

where F_{photo} is the potential outgassing of oxygen due to photosynthesis, F_{vent} is the oxygen flux due to the ventilation of subsurface and deep waters (i.e. the ventilation flux), F_{diseq} is disequilibrium flux, (i.e. the error introduced by assuming saturation in the computation of F_{therm}), and F_{ice} is the flux adjustment due to sea-ice (Equation (6)). Each of these fluxes will be discussed in more detail in the following sections. Accordingly, SNO_{bio} can also be produced by processes other than photosynthetic production of oxygen (i.e. $SNO_{bio} \neq SNO_{photo}$) and is given by:

$$SNO_{bio} = SNO_{photo} + SNO_{diseq} + SNO_{vent} - SNO_{ice} \ . \qquad (23)$$

In the real ocean, other factors including the subduction of bubbles into the subsurface ocean and atmospheric pressure variability may produce physical oxygen fluxes in the real ocean, but do not contribute to the simulated oxygen fluxes.

Current methods used to estimate new production rely on making critical assumptions about the influence of the factors listed above. As previously mentioned, Najjar and Keeling (2000) and Garcia and Keeling (2001) assume the impact of these factors is minimised by using the air-sea fluxes during the mixed layer shoaling period to estimate new production confined to the mixed layer. Note the assumption that mixed layers are shoaling everywhere in the Southern Ocean throughout the SNO period, does not hold in the model and may also not hold in the real ocean where mixed layers fluctuate a lot more than in the model.

The quantity we ultimately want to estimate from air-sea fluxes of oxygen is the total new production in the water column, NP. In the real ocean it is difficult, if not impossible, to quantify the bias introduced to new production estimates by the above factors. But, a global biogeochemical ocean model provides a consistent framework to test whether we expect these factors limit the effectiveness of this technique. In the following discussion, we will identify and quantify the processes and assumptions

that bias new production estimates calculated using the air-sea flux technique, and discuss whether they present a serious limitation to using the air-sea oxygen flux-based technique to estimate new production.

7.3.1. New production below the mixed layer and during autumn/winter

When the mixed layer is shallower than the euphotic zone, photosynthetically produced oxygen can accumulate and supersaturate waters throughout the euphotic zone and produce the well known subsurface oxygen maximum [Craig and Hayward (1987)]. Najjar and Keeling (2000) assumed that SNO_{bio} is equivalent to the mixed layer new production during the time period where the mixed layers are shoaling (i.e. $NP_{mld} \approx SNO_{bio}$ implying $g = 1$ for this particular relationship). They recognise that this estimate of new production is an underestimate of annual mean NP for several reasons - a proportion of total new production occurs in the euphotic zone below the mixed layer, occurs outside the SNO period and is not seasonal. Garcia and Keeling (2001) make the same assumption, arguing that this approximation has been shown to hold locally in the Sargasso Sea [Jenkins and Goldman (1985)] and the sub-arctic Pacific [Emerson (1987)], but recognize that SNO_{bio} could be both larger or smaller than photosynthetically produced oxygen in other regions of the ocean, depending on how much of the oxygen is trapped below the mixed layer. To estimate the effect shallow mixed layers may have on the outgassing of photosynthetically produced oxygen - and consequently new production estimates in the model - we calculate NP confined to the mixed layer, NP_{mld}, and see if consistency with the SNO_{bio} is improved.

Figure 7-3a shows the annual cycle of the photosynthetic oxygen flux assuming that all the photosynthetically produced oxygen is outgassed, F_{photo} (green line), and assuming that only the oxygen

produced in the mixed layer is outgassed, F_{photo_mld} (blue line). This mixed layer adjustment only reduces the SNO_{photo} by 28%.

Rather than plotting SNO_{bio} against annual mean new production, NP (red line, Figure 7-1b), SNO_{bio} is plotted against NP confined to the mixed layer (blue line). If SNO_{bio} were a perfect tracer of NP in the mixed layer, the simulated SNO_{bio} would lie along the solid black line. But, $SNO_{bio} \neq NP$. Next we test whether part of the mismatch is due to photosynthesis occurring outside the SNO period. But, plotting SNO_{bio} and NP confined to the SNO period as well as the mixed layer barely changes the relationship (aqua line).

Furthermore, Figure 7-2c shows the spatial distribution of the photosynthetic oxygen flux integrated over the SNO period (i.e. SNO_{photo_mld}), assuming that only the oxygen, produced from new production located within the mixed layer, F_{photo_mld}, escapes into the atmosphere. The spatial distribution of SNO_{photo_mld} is still very different from SNO_{bio}. The differences must be due to oxygen fluxes produced by processes other than photosynthesis. In the next sections, we discuss the processes that mask the photosynthetic oxygen flux.

7.3.2. Sea ice flux adjustment, F_{ice}

In the model the overall potential the total biological flux, F_{bio}^{total}, is reduced by the presence of sea ice by the proportion f_{ice} given by

$$F_{ice} = F_{bio}^{total} \times f_{ice} \,. \tag{24}$$

During the model simulation, this flux is subtracted from the total potential biological oxygen flux such that

$$F_{bio} = F_{bio}^{total} \times \left(1 - f_{ice}\right). \tag{25}$$

where F_{bio} is the simulated biological oxygen flux used in all the calculations above. To correct for the effect of ice we need to add on $F_{bio}^{total} \times f_{ice}$. But we do not know F_{bio}^{total}. The maximum possible correction to the biological outgassing flux could be estimated by multiplying the simulated new production in these regions by the fractional sea ice cover, f_{ice}. But we cannot use this correction without making the assumption that all the photosynthetically produced oxygen outgases (i.e. the the locally defined *g* is 1). Thus, without correcting for the effect of sea ice, we would expect the air-sea flux-based method to underestimate new production in ice-covered regions. Since the ice-covered regions are confined to small areas during the SNO period, we do not expect this correction to be very large and do not consider this term in the following discussion.

7.3.3. *Disequilibrium flux,* F_{diseq}

The disequilibrium flux, F_{diseq}, is the error produced by assuming complete equilibration in the calculation of the thermal oxygen flux using Equation (16). To quantify F_{diseq}, we run an experiment where biological productivity is set to zero throughout the global ocean, (i.e. $F_{photo} = 0$) and run to quasi-equilibrium (test 23, Table 4-1) such that $F_{vent} \simeq 0$. It takes the circulation a long time to bring the tracer fields to complete equilibrium – longer than the 2200 year run time of this experiment. Thus, there may be a small contribution from F_{vent} due to the ventilation of deep waters. Since, in this experiment, $F_{photo} = F_{vent} = 0$ (or small), any residual oxygen fluxes are due to the disequilibrium fluxes, F_{diseq}, Equation (22) reduces to

$$F_{diseq} \simeq F_{total} - F_{therm} \ . \tag{26}$$

Figure 7-4a shows a plot of the F_{diseq} versus the heat flux, *Q* (W m^{-2}), for each surface grid point between 20°S and 55°S. The thermal

oxygen flux approximation (Equation (16)) tends to overestimate the magnitude of F_{therm}. Therefore, we observe a negative correlation between F_{diseq} and Q. Several physical mechanisms may cause a disequilibrium flux. For example, although oxygen between the ocean and atmosphere equilibrates rapidly (order of a week), complete thermal equilibration may not occur in divergence zones and in deep convection regions, due to finite gas exchange times. Figure 7-4b of the percentage oxygen saturation (i.e. the percentage of the simulated oxygen content divided by the saturation oxygen content) in the surface ocean shows that waters remain undersaturated in deep convective regions of the Southern Ocean – a phenomenon also observed in the real ocean. But the contribution of finite gas exchange to F_{diseq} over the entire southern hemisphere is relatively small. The disequilibrium flux is predominately driven by the penetration of solar energy into the water column (Dietze and Oschlies (2005)), which produces an oversaturation of oxygen in regions where light penetrates below the mixed layer (Figure 7-4c,d). We would expect this effect to be even more pronounced if we used a more realistic solar penetration depth. Outgassing of this oxygen is delayed until the subsurface water becomes entrained in the mixed layer [Spitzer and Jenkins (1989)]. The temporal decoupling of oxygen saturation due to solar penetration below the mixed layer in the spring/summer period, and subsequent outgassing as the mixed layer deepens in the autumn/winter period, imposes a seasonal cycle on the disequilibrium flux (Figure 7-3b). The disequilibrium flux tends to attenuate the seasonal amplitude of the oxygen flux. We do not see an especially tight correlation between F_{diseq} and Q due to the spatial decoupling of oxygen supersaturation at depth and oxygen outgassing during the subsequent winter when mixed layers deepen. By this time, the water has been displaced with the Antarctic Circumpolar Current.

Figure 7-2b shows the distribution of the disequilibrium flux for the spring/summer (i.e. months of November to March). Surprisingly, there are regions where the disequilibrium flux is outgassing (shown in red).

These are regions where the heat flux is positive yet the disequilibrium flux is also positive. One explanation for the outgassing in these regions could be that the mixing of waters produces an oversaturation of oxygen due to the nonlinearity of oxygen solubility with temperature and salinity [Bieri *et al.* (1966)]. This effect was shown to produce an oxygen flux of a similar magnitude to the biological flux [Dietze and Oschlies (2005)]. Note that there are very few points that have both negative disequilibrium and heat fluxes, since mixing cannot produce an undersaturation of oxygen.

The integrated annual mean disequilibrium oxygen flux over the southern hemisphere oceans is small (i.e. 0.01 GtC yr^{-1}). But, the disequilibrium flux is highly seasonal (Figure 7-3). Consequently, the disequilibrium flux produces a SNO_{diseq} of 0.31 GtC yr^{-1} (Table 7-1) – which amounts to 22% of SNO_{photo}.

7.3.4. *Ventilation flux,* F_{vent}

The remineralisation of organic matter consumes oxygen and causes an undersaturation of oxygen in subsurface waters. The ocean circulation ventilates oxygen-depleted subsurface waters, resulting in an influx of atmospheric oxygen. We define this component of the biological oxygen flux, the ventilation oxygen flux, F_{vent}. In the real ocean, the biological oxygen fluxes due to photosynthesis, F_{photo}, and the remineralisation of organic matter, F_{vent}, are difficult to differentiate. Encouragingly, recently it has been shown that atmospheric N_2O observations may be used to differentiate between the observed photosynthetic and ventilation oxygen fluxes in future []. Fortunately, in the model we can run experiments that allow the two components to be isolated. F_{vent} can be approximated by

$$F_{vent} \simeq F_{vent\_loc} + F_{vent\_nonloc} \,, \tag{27}$$

where F_{vent_loc} is the local ventilation flux driven by remineralisation of organic matter formed by new production in the southern hemisphere

oceans (20°S – 90°S), NP_{loc}, and F_{vent_nonloc} is the non-local ventilation flux driven by the remineralisation of organic matter formed by new production outside the southern hemisphere oceans, NP_{nonloc} (Note: $NP_{global} = NP_{loc} + NP_{nonloc}$ and that NP without a subscript is identical to NP_{loc}).

To estimate F_{vent_nonloc}, we first perform an additional model experiment (test 22, Table 4-1) with new production is set to zero south of 20°S (i.e. since $NP = 0$, $F_{photo} = F_{vent\_nonloc} = 0$). Therefore, for test 22, Equation (22) reduces to

$$F_{bio} = F_{vent\_nonloc} + F_{diseq} \ . \tag{28}$$

To solve for F_{vent_nonloc}, we then subtract F_{diseq} calculated in section 5.1.3.

We can understand what drives F_{vent_nonloc}, from the relationship between NP_{global} and NP_{loc} (Figure 7-5), which rearranges to,

$$NP_{nonloc} = -0.4\ NP_{loc} + 3.53\ ,\ r^2 = 0.98\ . \tag{29}$$

From the relationship, we show that as NP_{loc} approaches zero, approximately 3.5 GtC/yr of new production persists outside the southern hemisphere. The organic matter formed outside the southern hemisphere oceans, NP_{nonloc}, is exported and remineralised at depth, depleting the oxygen content of the deep water. The undersaturated deep waters are upwelled in the divergence zone of the Southern Ocean, driving an ingassing of oxygen.

Figure 7-2c shows the spatial distribution of F_{vent_nonloc}. As expected, the non-local ventilation fluxes are restricted to the high latitudes where circumpolar deep waters upwell in the divergence zone. Deep convective overturning is more common in the wintertime and deep ventilation fluxes are relatively small during spring/summer when biological productivity is highest which imposes a strong seasonality on

the ventilation fluxes (Figure 7-3b). Although ventilation fluxes are smaller during the SNO period , the ventilation of deep waters during the SNO period produces a -0.17 GtC yr^{-1} SNO of oxygen (i.e. SNO_{vent_nonloc}, Table 7-1). The annual mean $\overline{F}_{vent\_nonloc}$ is -0.88 GtC yr^{-1} (Table 7-1).

The local component of the ventilation flux, F_{vent_loc}, for the control experiment, is assumed to be the oxygen flux remaining after subtracting each of the above processes. That is,

$$F_{vent\_loc} = F_{bio} - F_{vent\_nonloc} - F_{diseq} - F_{photo} \ . \qquad (30)$$

This flux is the most difficult flux to isolate. It may also incorporate fluxes due to other processes, such as new production below the mixed layer. But, the flux is dominated by ventilation processes. The regions where F_{vent_loc} ingasses, correlate spatially with where ventilation fluxes would be expected (i.e. the divergence zone in the Southern Ocean), as can be seen in Figure 7-2e of the spatial distributions of F_{vent_loc} for the control case. Also the seasonality has shows strong ingassing in the autumn/winter periods, as would be expected for a ventilation oxygen flux (Figure 7-3b). Together the ventilation fluxes produce a $SNO_{vent} = -0.51$ GtC yr^{-1} – that is almost 40% of the SNO_{photo} (Table 7-1).

7.3.5. *The annual mean biological oxygen flux, $\overline{F_{bio}}$.*

In the method of Najjar and Keeling (2000), the annual mean biological oxygen flux, $\overline{F_{bio}}$, is subtracted from the monthly fluxes before calculating SNO_{bio} (Equation (18)). In their study $\overline{F_{bio}}$ is small, so the overall effect on estimates of SNO_{bio} is negligible. It is not intuitive why the annual mean should be subtracted. If subtracting the annual mean is motivated by an attempt to separate the ventilation oxygen fluxes from the photosynthetic oxygen fluxes, then i) the ventilation flux, F_{vent} must be seasonally constant, and ii) the annual mean should remain constant with

changes in biological productivity. We demonstrate that both of these conditions do not hold. Firstly, Table 7-1 and Figure 7-3 show that in the model each of the processes discussed above, including ocean ventilation, has both a seasonal and annual mean component. We would also expect this in the real ocean, since most circulation processes that change oxygen concentrations in the surface ocean - including mixed layer deepening, convection and ventilation - are all highly seasonal. The ventilation flux occurs primarily in the winter months. By subtracting of $\overline{F_{bio}}$ we remove a component of the photosynthetic oxygen flux. Consequently, new production - which occurs primarily in the summertime – is overestimated by the annual mean (GtC month^{-1}) multiplied by the number of months over which oxygen is outgassing.

Secondly, Figure 7-6 shows that the annual mean biological oxygen flux, $\overline{F_{bio}}$, (GtC yr^{-1}) becomes less negative as new production increases in the southern hemisphere oceans, *NP* according to the following linear relationship

$$\overline{F_{bio}} = 0.24\,NP - 0.84\ ,\ r^2 = 0.99\ . \qquad (31)$$

This implies that the annual mean is not purely a reflection of the large-scale ventilation. Extrapolating this relationship to zero new production in the southern hemisphere oceans demonstrates that even without any local new production a 0.84 GtC yr^{-1} ingassing of atmospheric oxygen – as would be expected in an oceanic region where deep waters are ventilated. The intercept is approximately the sum of the annual mean non-local ventilation flux and the disequilibrium fluxes (Table 7-1). The increase in $\overline{F_{bio}}$ in the southern hemisphere oceans is driven by a combination of, i) non-local ventilation effects - where a reduction in the ventilation flux occurs in response to a decline in new production and subsequent subsurface oxygen consumption outside the region – as implied from the relationship between global and southern ocean new production (Equation (29)), and ii) local effects which change in the balance between the local oxygen production and

subsequent resupply of oxygen depleted waters as mixed layers deepen (Figure 7-7).

We advocate that the annual mean should not be subtracted. Clearly, from both the surface and zonal distributions (Figure 7-8), the distribution of simulated new production (Figure 7-8a) is better captured without (Figure 7-8c) than with (Figure 7-8b) subtracting the annual mean. Subtracting the mean causes a large overestimate of new production in the high latitudes and underestimates in the mid latitudes (Figure 7-8d).

Rather than calculating SNO_{bio} as in Equation (18), we recalculate the biological SNO without subtracting the annual mean, SNO'_{bio}, according to

$$SNO_{bio} = \sum_{t=1}^{12} \left[\iint F_{bio}(i,j,t)\, dA \right] \text{ for } [\ldots] > 0 \,. \tag{32}$$

The revised relationship between SNO_{bio} and NP for all the new production perturbation experiments is

$$NP = \frac{SNO_{bio}}{0.5} \,, \tag{33}$$

where $g_{hem} = 0.51$ and $k_{SNO} \simeq 0$ GtC yr^{-1}.

7.4. Can new production be estimated from air-sea oxygen fluxes?

To confidently estimate new production several criterion must be met. Firstly, the relationship between NP and SNO_{bio} must be linear. Secondly, the relationship must be robust. In other words, g_{hem} and k_{SNO} must remain constant with natural variability in ocean processes. Finally, the relationship between NP and SNO_{bio} must be determined – ideally from observations.

7.4.1. The linear relationship between biological SNO and new production.

Fortunately, the relationship between SNO_{bio} and NP is linear Figure 7-1). Experiments with very different spatial distributions (Figure 5-1a) and magnitudes of new production (Table 5-1) all fall on the same line. This is remarkable - a linear relationship is generally an assumption rather than a result. To test that this is not just a coincidence unique to the model, the relationship between NP and SNO_{bio} is determined using a set of new production perturbation experiments from a second global biogeochemical ocean model (i.e. MOM2, Table 7-1, Figure 7-1c – magenta line). Again, the relationship is linear. This model gives the following relationship between SNO_{bio} and NP.

$$SNO_{bio} = 0.25\ NP + 0.21\ ,\ r^2 = 0.94\ . \qquad (34)$$

It is conceivable that the relationship deviates from linearity when new production magnitudes in the southern hemisphere are low. To check this possibility, we use the experiment in which new production is set to zero in the Southern hemisphere oceans (test 22, Table 4-1 and marked in green in Figure 7-1c). When $NP = 0$, $SNO_{bio} = 0.08$, which is only slightly larger than the intercept of zero estimated by extrapolating the linear relationship to zero new production (Equation (32)). Differences between the two intercept estimates would be expected, since both the magnitudes and spatial distributions of new production outside the region differ between the two experiments, which influences the magnitude of SNO_{vent_nonloc}.

The relationship between SNO_{bio} and NP is given by the general equation

$$NP = \frac{SNO_{bio}}{g_{hem}} = \frac{SNO_{photo} + SNO_{diseq} + SNO_{vent\_loc} + SNO_{vent\_nonloc}}{g_{hem}}\ , \qquad (35)$$

such that when $NP = 0$ - and consequently $SNO_{photo} = SNO_{vent\_loc} = 0$ - the intercept, k_{SNO}, is given by

$$k_{SNO} = \frac{SNO_{diseq} + SNO_{vent\_noloc}}{g_{hem}} . \quad (36)$$

The fact $k_{SNO} = 0$, implies that $SNO_{diseq} \approx -SNO_{vent\_nonloc}$ in the MOM3 model. From Table 7-1 we know that $SNO_{diseq} = 0.31$ GtC yr^{-1} and $SNO_{vent\_nonloc} = -0.23$ GtC yr^{-1}. The same condition does not necessarily hold for air-sea oxygen flux based estimates of new production from other biogeochemical models. Rearranging the relationship between SNO_{bio} and NP to the second biogeochemical circulation model (i.e. MOM2) gives

$$NP = \frac{SNO_{bio}}{0.25} - 0.84 , \quad (37)$$

with $k_{SNO} = -0.84$ GtC yr^{-1} and $g_{hem} = 0.25$. We do not have the experiments to determine what drives k_{SNO} in this model, but given what we learned from MOM3, we would expect k_{SNO} to be large and negative if $SNO_{diseq} \ll SNO_{vent}$ during the SNO period.

Why is the relationship linear given the nonlinear nature of so many ocean processes? If we know what drives the gradient, g_{hem}, of the relationship between SNO_{bio} and NP, it may give some insight into why a linear relationship may be expected. The gradient in each model reflects the unique relationship between NP and F_{vent_nonloc}, which is set by the relationship between NP_{loc} and NP_{nonloc} (Equation (29)). In MOM3, as NP_{loc} decreases, NP_{nonloc} increases and F_{vent_nonloc} becomes more negative. That is, more organic matter remineralises in the deep water and more oxygen ingasses as these deep waters are ventilated in the divergence zone of the southern hemisphere oceans. The opposite

behaviour is observed in MOM2. Here, as NP_{loc} decreases, NP_{loc} increases (i.e. the gradient is positive) according to the following relationship,

$$NP_{nonloc} = 2.5\ NP_{loc} - 2.2\ , \tag{38}$$

and implies that F_{vent_nonloc} becomes less negative (i.e. less ingassing). The opposite responses observed between MOM3 an MOM2, reflect the difference in the depth of equatorial upwelling. In MOM3, the equatorial Pacific is more stratified (i.e. lower vertical diffusivity and more vertical levels). Thus, nutrients are upwelled from shallow in the water column. Nutrient supply is relatively inefficient leading to low equatorial new production. By contrast, in MOM2, the upwelled water is supplied from deeper in the water column where nutrient concentrations are high, nutrient supply to the ocean surface is efficient and new production is high.

We do not have enough information, as yet, to determine whether we might expect a linear relationship between F_{vent} and NP in the real ocean. Ideally, this would require applying the same analysis to interannual air-sea oxygen fluxes. But, the relationship between F_{vent_nonloc} and NP suggests that g_{hem} is driven by the large-scale ocean circulation and reflects the base state of the ocean. If so, we speculate that the relationship between F_{vent_nonloc} and NP should not vary on the time-scale of natural variability.

7.4.2. Is the relationship between biological SNO and new production robust?

A series of perturbation experiments were run as an indication of how robust we expect the relationship between NP and SNO_{bio} to be with natural variability in the remineralisation of biological matter and the physical circulation. The perturbations span the observed magnitude of variability in new production and biogeochemical properties in the real

oceans, and an acceptable range of physical circulation scenarios (See section 4). The physical circulation and remineralisation perturbation experiments are described in Table 4-3 and Table 4-2. The magnitude and spatial distribution of new production in both the perturbation experiments remain fairly constant. Therefore, changes in SNO_{bio} primarily reflect changes driven by the circulation and the remineralisation of biological matter.

Figure 7-1c plots both SNO_{bio} against NP for all the perturbation experiments - the red points represent the new production experiments, the green points the biogeochemical formulation perturbation experiments and the blue points the physical circulation perturbation experiments. Strikingly, both the physical and biogeochemical experiments cluster closely around the linear relationship estimated from the new production experiments (red line). Perturbations to the mixed layer dynamics, eddy and vertical diffusivity and meridional overturning change the SNO of oxygen by no more than 5%. Also, perturbations to the vertical distribution of new production and the remineralisation of organic matter do not produce appreciable changes in the magnitude of hemispheric SNO of oxygen.

The spread in SNO of oxygen can be interpreted as the expected change in SNO_{bio} from natural variability in the physical circulation and the remineralisation properties of the ocean. Given the small spread in SNO_{bio} due to the circulation and biogeochemistry, compared to the large spread due to acceptable perturbation to the magnitude of NP, suggests that the variability in SNO_{bio} is dominated by new production.

But, each perturbation experiment produces only a point estimate of SNO_{bio}, and the experiments could have potentially caused one or both of g_{hem} and k_{SNO} to change. As a first attempt to address this uncertainty, we run an additional couple of new production experiments (test 19 and test 20 in Table 4-3). These experiments have both a stronger overturning circulation than the control experiment and mixed layers which are deeper

by as much as a factor of two in the southern hemisphere oceans. Assuming a linear relationship between SNO_{bio} and NP, produces a g_{hem} value of 0.48 - only slightly less than for the new production perturbation experiments based on the physical circulation of the control experiment (i.e. $g_{hem} = 0.51$). It is encouraging that both g_{hem} and k_{SNO} barely change in response to such a change in ocean circulation. A more definitive assessment of the effect of the physical circulation on g_{hem} and k_{SNO} is needed. Again, applying the same analysis to oxygen fluxes from a simulation where both the circulation and new production vary interannually would increase confidence in this result.

7.4.3. Can the relationship between SNO_{bio} and NP be determined?

The success of the air-sea flux-based method for estimating new production relies on knowing the relationship between SNO_{bio} and NP in the real ocean. Which requires an estimation of both g_{hem} and k_{SNO}. How do we determine for these two unknowns? And, can they be determined observationally?

Figure 7-9a shows the distribution of locally defined g values, g_{local}, defined as

$$g_{local}(i,j) = \frac{SNO_{bio}(i,j)}{NP_{model}(i,j)} . \qquad (39)$$

Here, the spatial distribution of seasonal net outgassing of SNO_{bio} is calculated at each grid point according to

$$SNO_{bio}(i,j) = \sum_{t=1}^{12} \left[F_{bio}(i,j,t) \right] \quad \text{for } [\ldots] > 0 , \qquad (40)$$

where F_{bio} are the monthly biological oxygen fluxes. Note that at each grid point, g_{local}, is combination of a local slope, g and offset, k_{SNO}. There is

significant spatial variability in g_{local}. There are regions throughout the southern hemisphere oceans where the g_{local} is higher than 1 indicating that locally more oxygen is outgassed than is biologically produced through new production. In the subtropics, there is a narrow region of values greater than 1 that circles the blank regions where g_{local} is undefined. g_{local} is undefined in these regions since no new production occurs here. The high values may reflect the delay between production and release of oxygen. We speculate that the g_{local} values greater than 1 occur in this region because summer mixed layer depths are shallower than in the euphotic zone, and the oxygen produced is not released into the atmosphere until later in the season when the mixed layer deepens. By this time, the water has advected away from where it was produced and is outgassed in addition to the oxygen that was produced locally. Although estimating g_{local} in these particular locations may be complicated, these regions do not significantly influence hemispheric estimates since new production magnitudes here are low.

The dominant sources of spatial variability are SNO_{vent} and SNO_{diseq}. F_{vent}. That is, g_{local} can be expanded as follows

$$\begin{aligned} g_{local} &= \frac{SNO_{bio}}{NP} \\ &= \frac{SNO_{photo} + SNO_{vent} + SNO_{diseq}}{NP} \\ &= g + \frac{SNO_{vent} + SNO_{diseq}}{NP} . \end{aligned} \tag{41}$$

So, the greater the ventilation flux (ventilation fluxes are negative) the smaller the value of g_{local}. Figure 7-9b shows the spatial distribution of g_{local} for the control experiment, after correcting for F_{vent_nonloc} and F_{diseq}. The spatial distribution of g_{local} becomes much more uniform - particularly in the longitudinal direction - and g_{local} begins to converge towards the value of 1.

The zonal variability in g_{local} is largely driven by F_{vent}. The zonal distribution of g_{local} from two different global biogeochemical ocean models (i.e. MOM2 and MOM3, Figure 7-10) shows that in both models, the zonally averaged distribution of g_{local} in the southern hemisphere oceans decreases towards the high latitudes where deep waters are ventilated in the divergence zone. The smaller g_{local} in MOM2 suggests that F_{vent} is greater (i.e. more negative) in the MOM2 model than in MOM3.

Given the enormous spatial variability in g_{local} and the paucity of oxygen and new production measurements in the southern hemisphere oceans, it does not seem feasible to estimate g_{hem} observationally. Measuring at only several locations and extrapolating to data sparse regions would introduce significant levels of uncertainty to g_{hem} and subsequent estimates of new production in the southern hemisphere oceans. This motivates us to consider the atmospheric O_2/N_2 approach of Keeling and Shertz (1992). The atmosphere tends to integrate the spatial variability in the air-sea oxygen fluxes. From a sampling perspective, using the continuous records of atmospheric O_2/N_2 at a selection of atmospheric observing stations to monitor variability in new production is very attractive.

We propose one other approach for estimating g_{hem} and k_{SNO}. Without knowing the true values of g_{hem} and k_{SNO}, the two unknowns can be diagnosed from a series of global biogeochemical models and used to estimate NP from observed estimates of SNO_{bio}. As an initial estimate, here we use the two ocean models presented in this study to provide estimates of g_{hem} and k_{SNO} with associated uncertainties.

The relationships between SNO_{bio} and NP from the two models are

$$NP = \frac{SNO_{bio}}{0.5}, \tag{42}$$

for MOM3 with $g_{hem} = 0.51$ and a negligible k_{SNO}, and

$$NP = \frac{SNO_{bio}}{0.25} - 0.84, \tag{43}$$

for MOM2 with $g_{hem} = 0.25$ and a $k_{SNO} = -0.84$ GtC yr^{-1}.

We use the two different physical models to estimate an uncertainty of 0.35 ± 0.1 for g_{hem}. Based on the two models, we make a similar estimate of uncertainty for the SNO offset (i.e. k_{SNO} of 0.4 ± 0.4 GtC yr^{-1}). Using the southern hemisphere SNO_{bio} (i.e. 3.23 x 10^{14} mol O_2) from the air-sea flux climatology of Najjar and Keeling (2000) and a C:O_2 ratio of 106:-170, we estimate 6.9 ± 2 GtC yr^{-1} of annual mean new production. This estimate is much higher than the 3.8 GtC yr^{-1} estimate of Najjar and Keeling (2000) for new production confined to the mixed layer during the SNO period. Using the revised estimate of southern hemisphere SNO_{bio} of 2.62 x 10^{14} molO_2 yr^{-1} from Garcia and Keeling (2001) we estimate a 5.3 ± 1.5 GtC yr^{-1} of annual mean new production.

a)

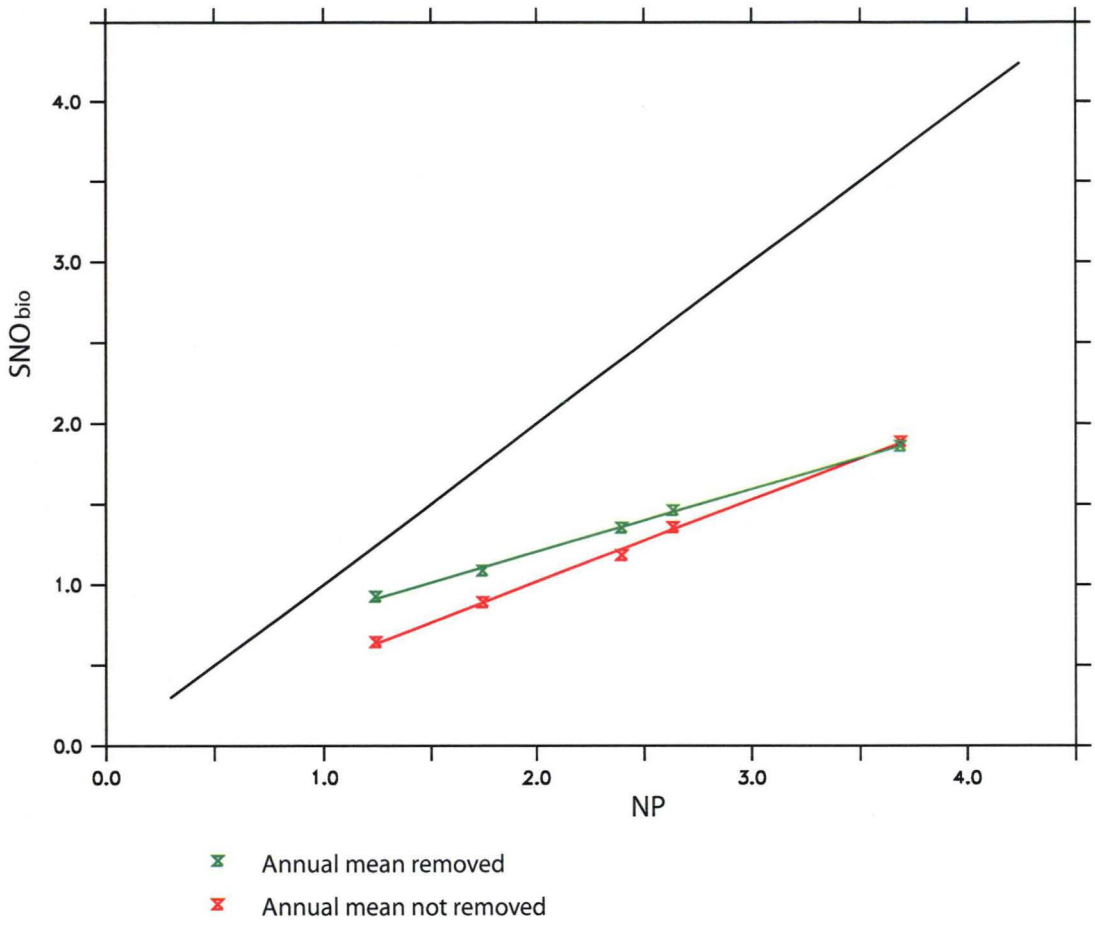
4.0
3.0
2.0
1.0
0.0
SNO bio
0.0
1.0
2.0
3.0
4.0
NP
Annual mean removed
Annual mean not removed

b)

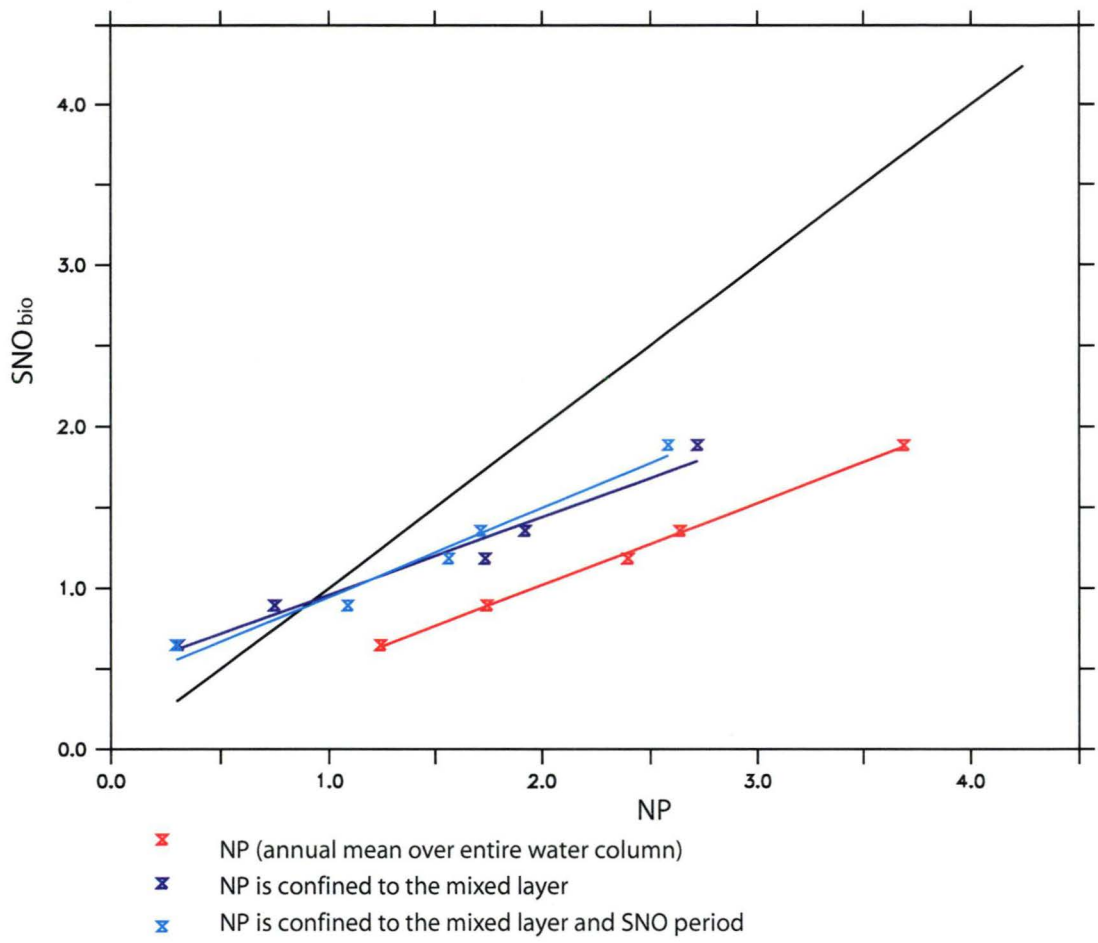
4.0
3.0
2.0
1.0
0.0
SNO bio
0.0
1.0
2.0
3.0
4.0
NP
NP (annual mean over entire water column)
NP is confined to the mixed layer
NP is confined to the mixed layer and SNO period

c)

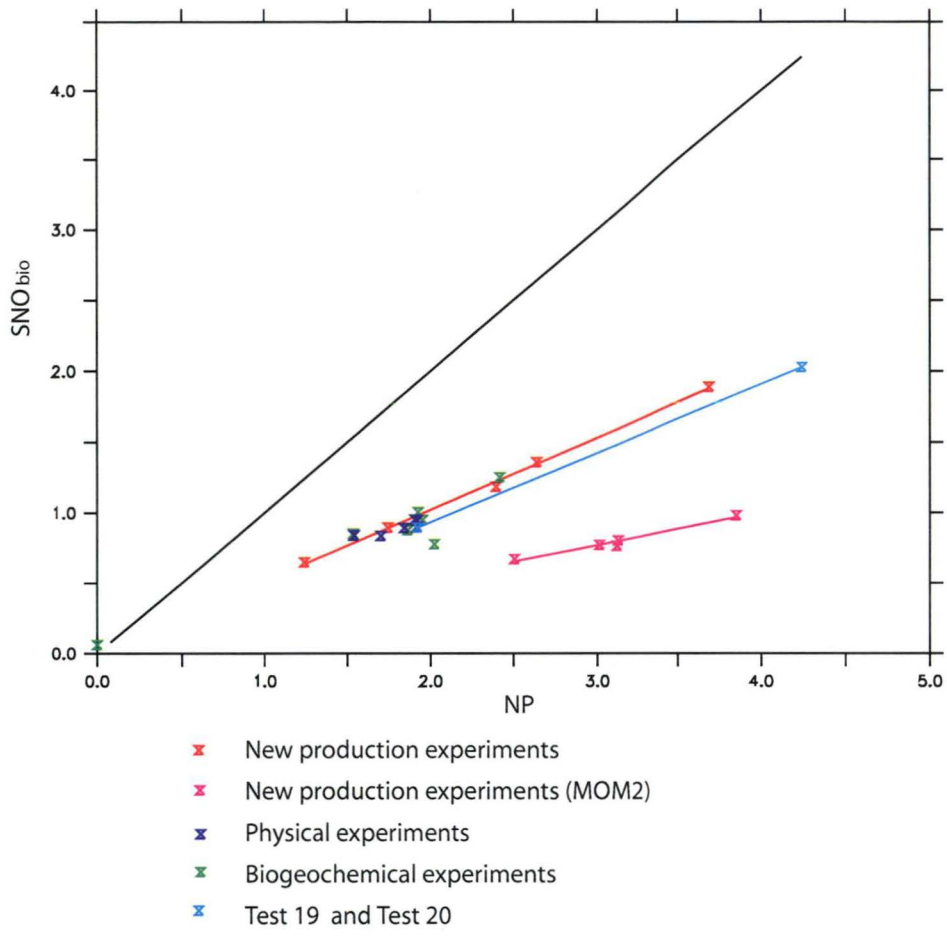

Figure 7-1: Estimates of southern hemisphere (20°S - 90°S) SNO_{bio} versus NP (GtC yr^{-1}), for a selection of model experiments, including a) the new production experiments with (Equation (18), green line) and without (Equation (32), red line) removing the annual mean biological oxygen flux, $\overline{F_{bio}}$, b) the SNO_{bio} from the new production experiments plotted against annual mean NP (red line), NP confined to the mixed layer (blue line) and NP confined to the mixed layer and the SNO period (aqua line), and c) the new production experiments from MOM3 (red line), the new production experiments from MOM2 (Equation (34), magenta line), the physical perturbation experiments (blue marks) the biogeochemical perturbation experiments (green marks) and finally, test 19 and test 20 (aqua line). The bold line marks the line where the experiments would fall if $SNO_{bio} = NP$.

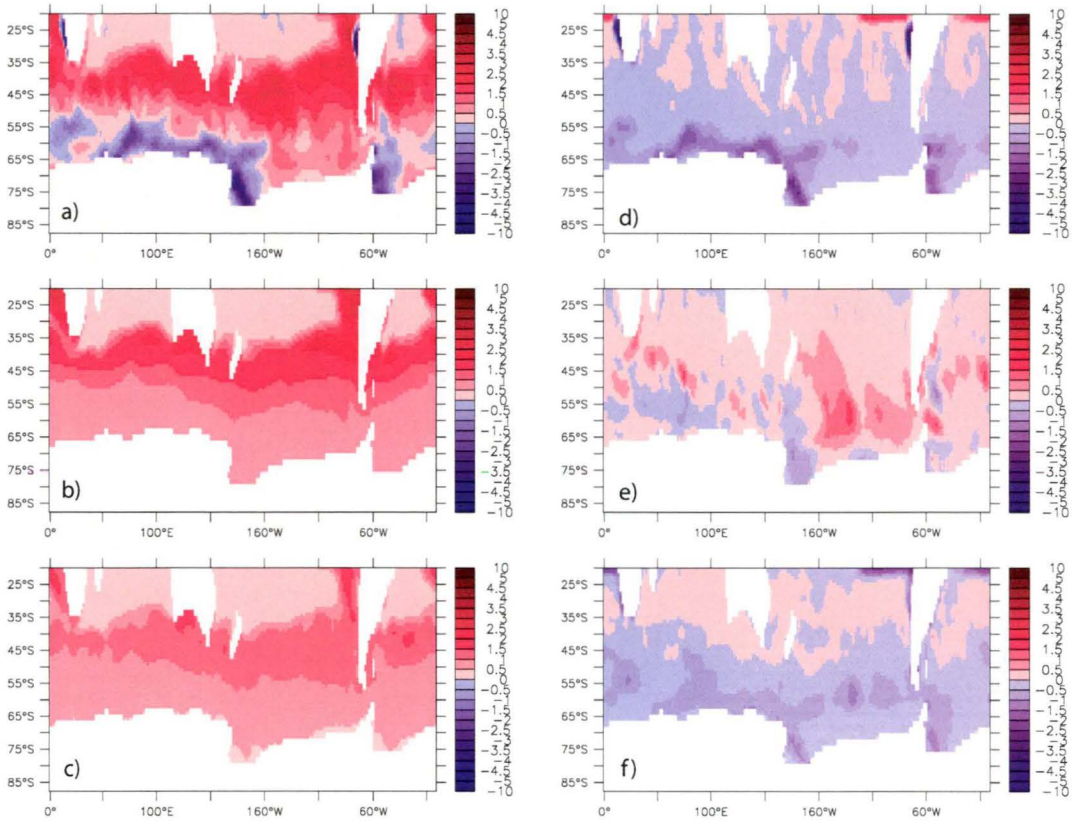

Figure 7-2: Spatial distribution of the a) biological SNO, SNO_{bio}, b) the potential SNO due to photosynthesis , SNO_{photo}, c) photosynthetic SNO integrated over the mixed layer, SNO_{photo_mld} , d) the SNO of the disequilibrium oxygen flux, SNO_{diseq}, e) the local ventilation oxygen flux, SNO_{vent_loc}, and f) the non-local ventilation flux, SNO_{vent_nonloc}. Positive values, shown in red, indicate an oceanic outgassing of oxygen. Units are in molO_2 m^{-2} integrated over the SNO period (i.e. December to May).

a)

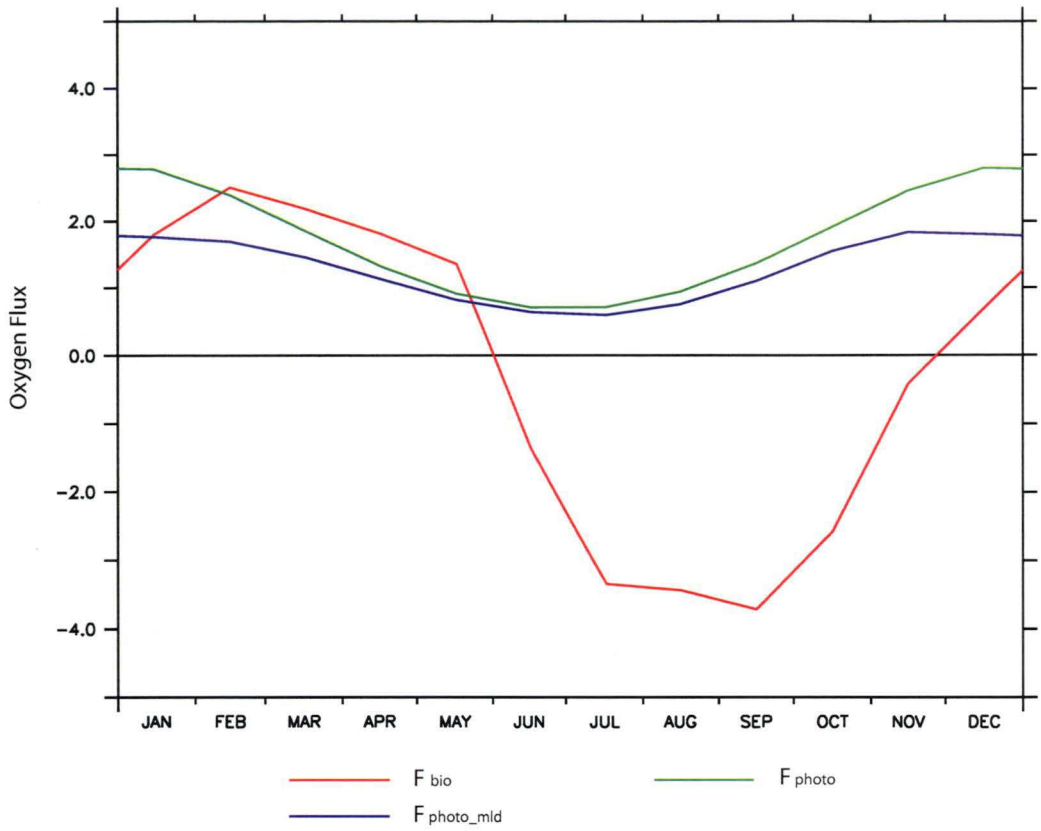
4.0
2.0
0.0
−2.0
−4.0
Oxygen Flux
JAN
FEB
MAR
APR
MAY
JUN
JUL
AUG
SEP
OCT
NOV
DEC
F bio
F photo
F photo_mld

b)

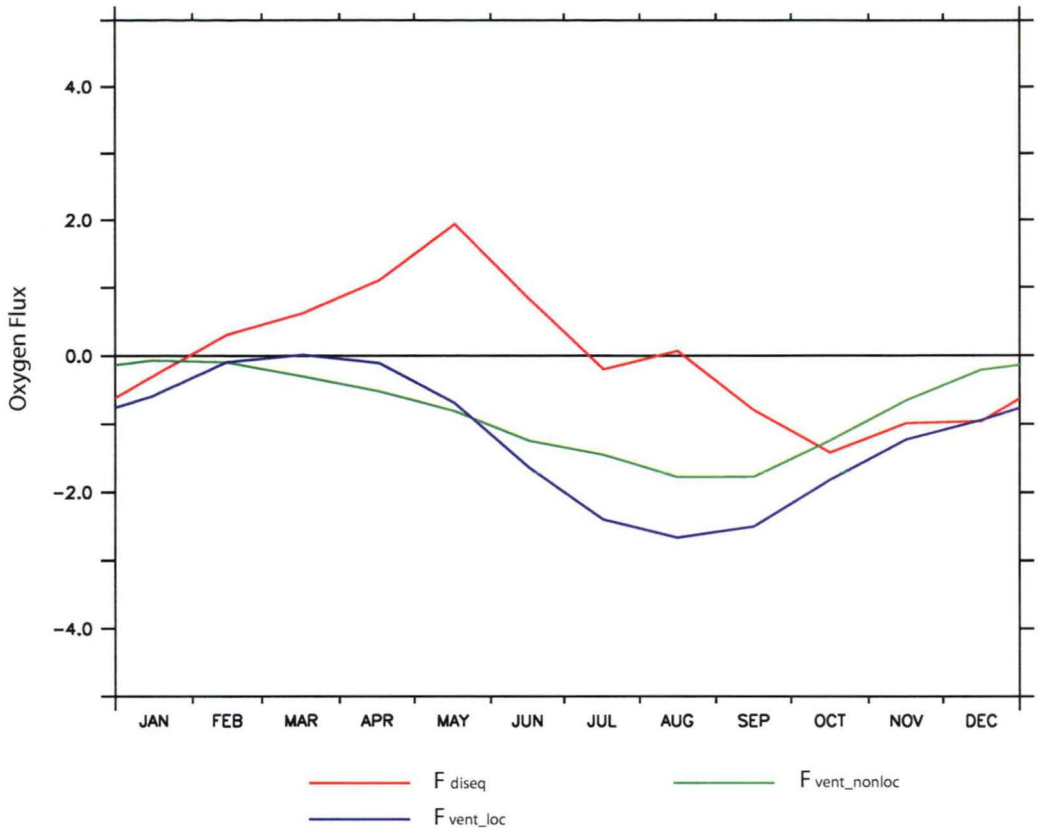

Figure 7-3: The seasonal cycles of the hemispherically integrated oxygen fluxes ($molO_2\ yr^{-1}$) for the main components of the biological oxygen flux, F_{bio} including a) the biological oxygen flux, F_{bio}, the potential oxygen outgassing due to photosynthesis, F_{photo}, and the potential outgassing due to photosynthesis confined to the mixed layer, F_{photo_mld}, and b) the disequilibrium flux, F_{diseq}, the nonlocal ventilation flux, F_{vent_nonloc} and the local ventilation flux F_{vent_loc}.

a)

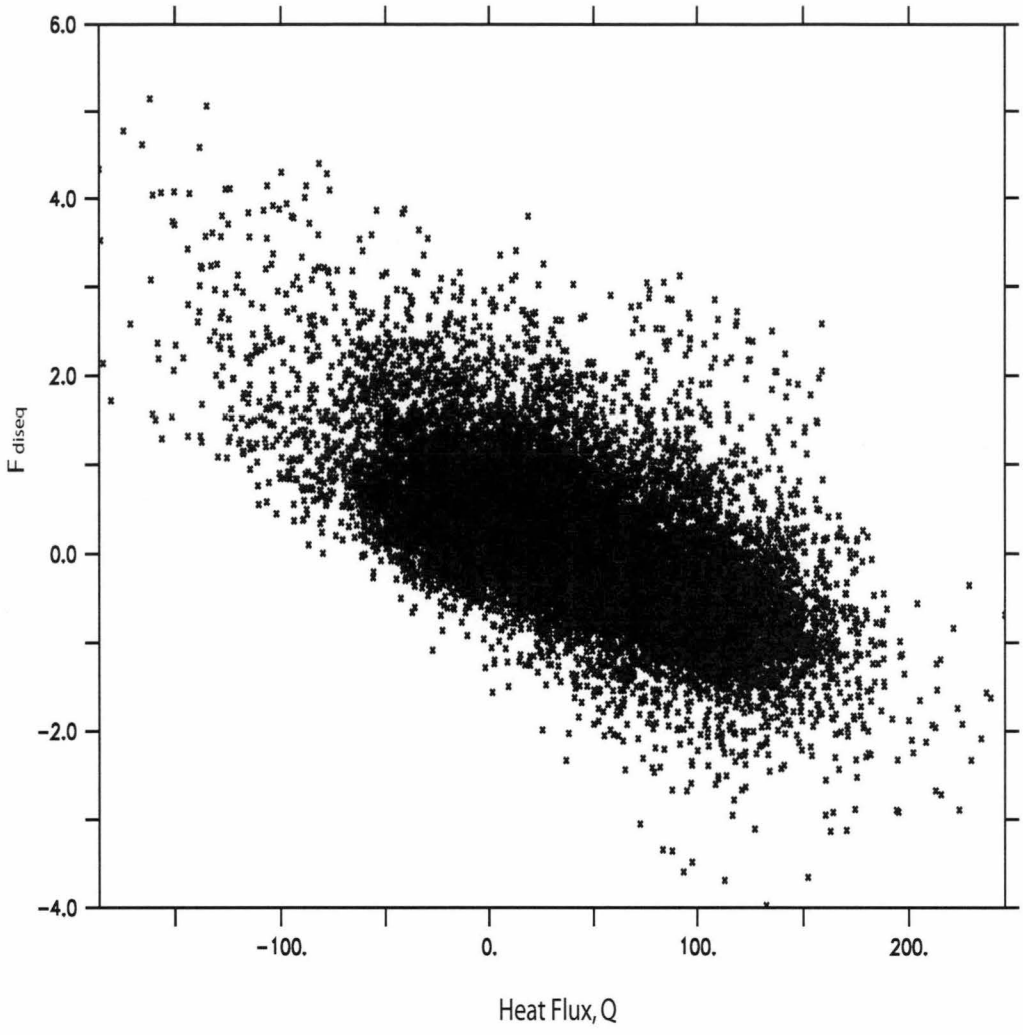

b)

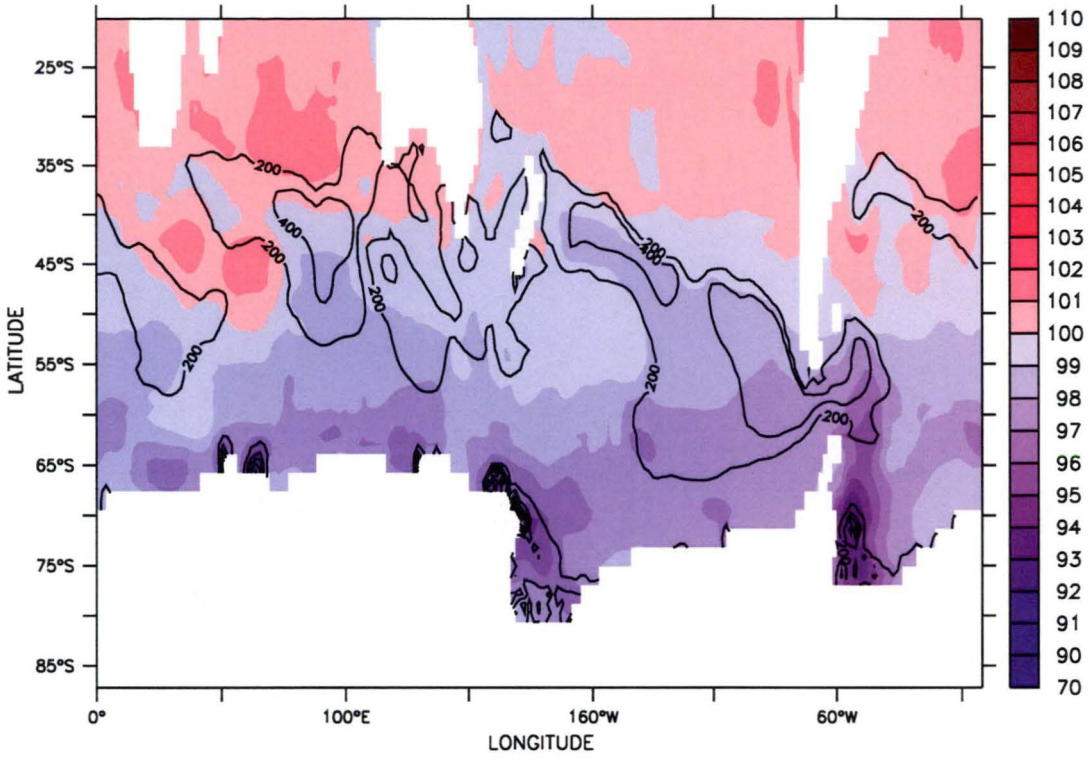
25°S
35°S
45°S
55°S
65°S
75°S
85°S
LATITUDE
0°
100°E
160°W
60°W
LONGITUDE
200
400
110
109
108
107
106
105
104
103
102
101
100
99
98
97
96
95
94
93
92
91
90
70

c)

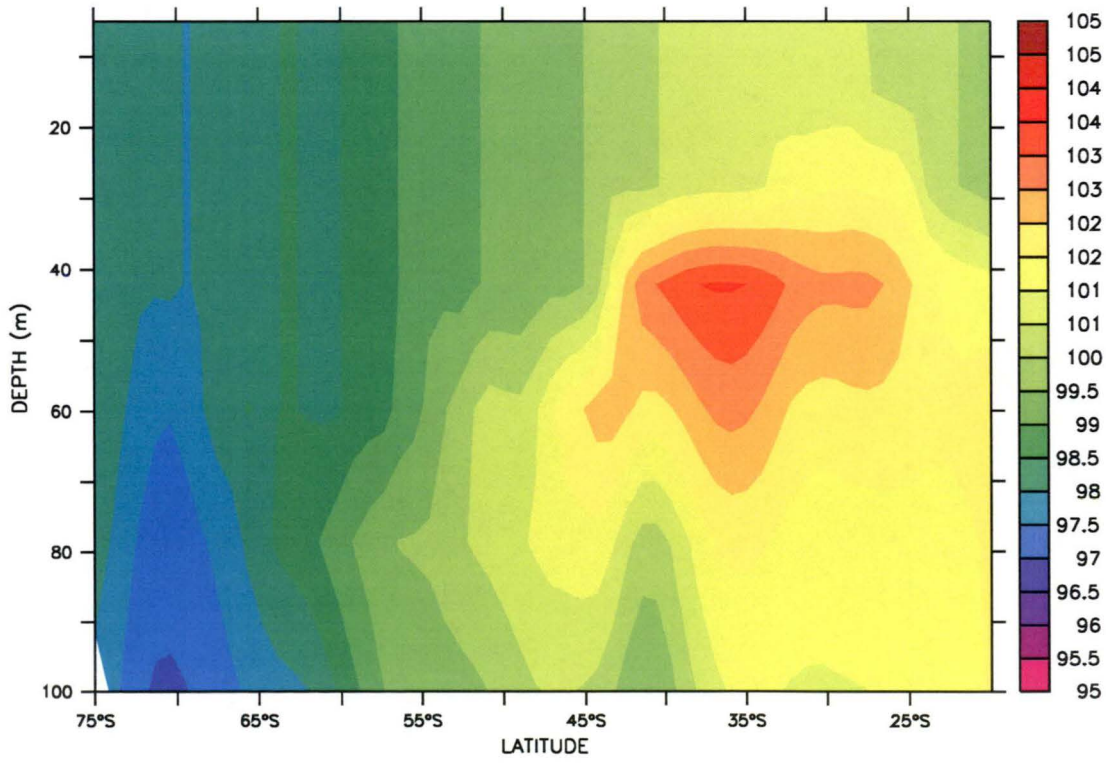
20
40
60
80
100
DEPTH (m)
75°S
65°S
55°S
45°S
35°S
25°S
LATITUDE
105
105
104
104
103
103
102
102
101
101
100
99.5
99
98.5
98
97.5
97
96.5
96
95.5
95

d)

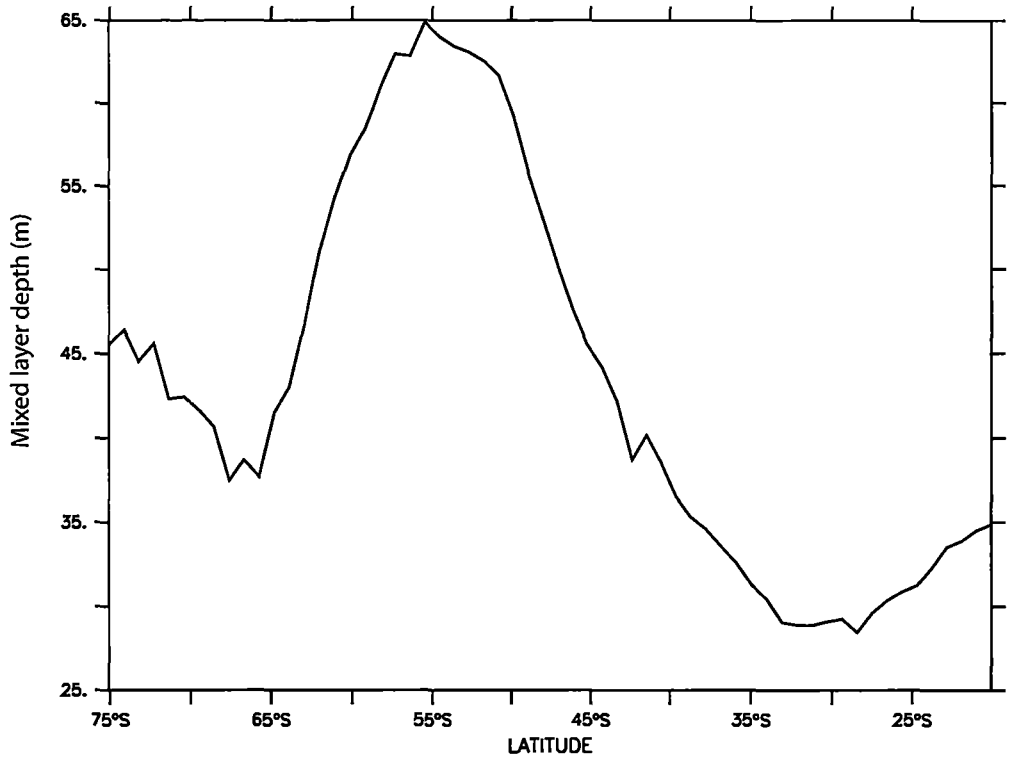

Figure 7-4: The disequilbrium flux. a) A plot of the F_{diseq} ($molO_2\ m^{-2}\ yr^{-1}$) vs Q ($W\ m^{-2}$) in the southern hemisphere oceans (20°S - 50°S). b) A surface plot of percent oxygen saturation (i.e. the percentage of the oxygen concentration divided by the saturation oxygen concentration) and the maximum seasonal mixed layer depth (m) (i.e. contours). c) A zonally averaged section of percent oxygen saturation. d) A zonally averaged section of mixed layer depth (m).

Table 7-1: The contribution of the processes (x), to the integrated (20°S - 90°S) annual mean air-sea oxygen flux, $\overline{F_{bio}}$, the biological SNO of oxygen, SNO_{bio}. The analysis is performed on the control case. Note that each process is integrated over the SNO period (i.e. December -May).

Ocean process (x)	Oxygen flux (F_x)	$\overline{F_x}$ (10^{14} molO_2 yr^{-1})	$\overline{F_x}$ (GtC yr^{-1})	SNO_x (10^{14} molO_2 yr^{-1})	SNO_x (GtC yr^{-1})
F_{photo}	Photosynthetic production	2.32	1.74	1.39	1.04
F_{diseq}	Disequilibrium	0.02	0.02	0.31	0.23
F_{vent_nonloc}	Nonlocal ventilation	-1.17	-0.88	-0.23	- 0.17
F_{vent_loc}	Local ventilation	-1.69	-1.27	-0.28	- 0.21
F_{bio}	Biological	-0.52	-0.39	1.19	0.89

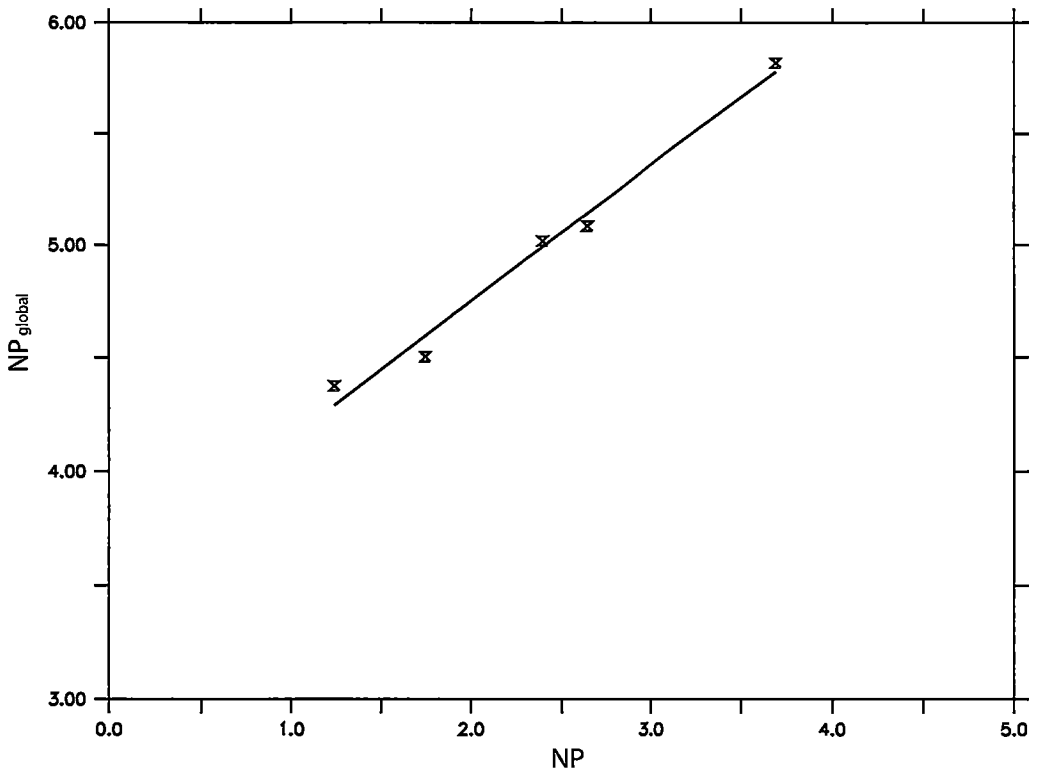

Figure 7-5: Global annual mean new production, NP_{global}, versus new production in the Southern hemisphere oceans, NP. A linear regression of the five new production perturbation experiments gives $NP_{global} = 0.6\,NP + 3.53$, $r^2 = 0.98$. The symbols are the same as for Figure 7-1.

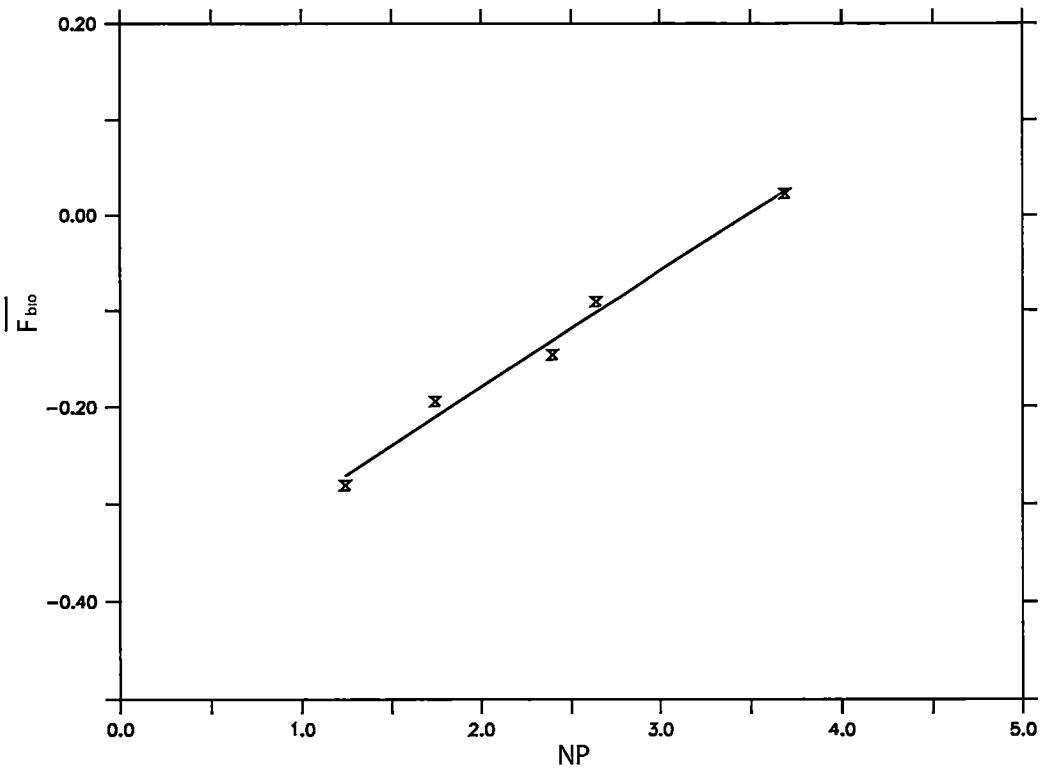

Figure 7-6: The annual mean biological oxygen flux, $\overline{F_{bio}}$ (GtC yr^{-1}), versus simulated new production in the southern hemisphere oceans, NP (GtC yr^{-1}). Linear regression to the five new production perturbation experiments gives the relationship ($\overline{F_{bio}} = 0.24\ SNO_{bio} - 0.84$, $r^2 = 0.99$).

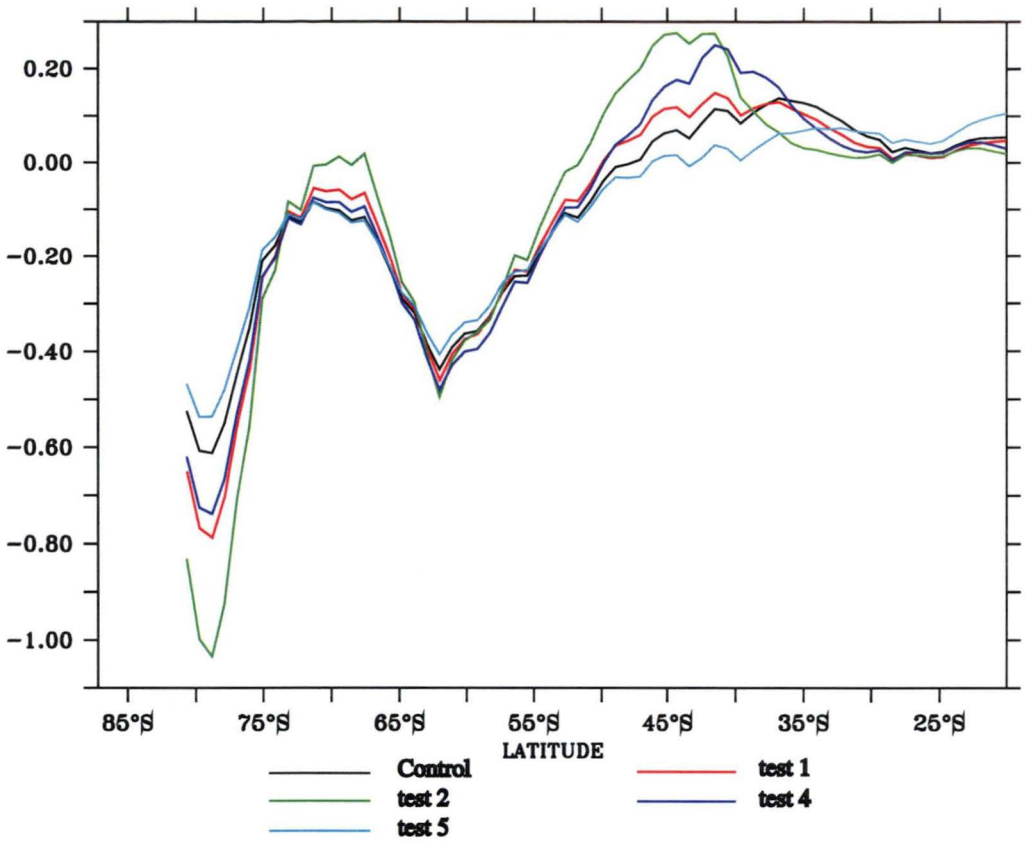

Figure 7-7: Zonal distribution of the annual mean biological oxygen flux $\overline{F_{bio}}$ ($molO_2\,m^{-2}\,month^{-1}$), for the new production perturbation experiments.

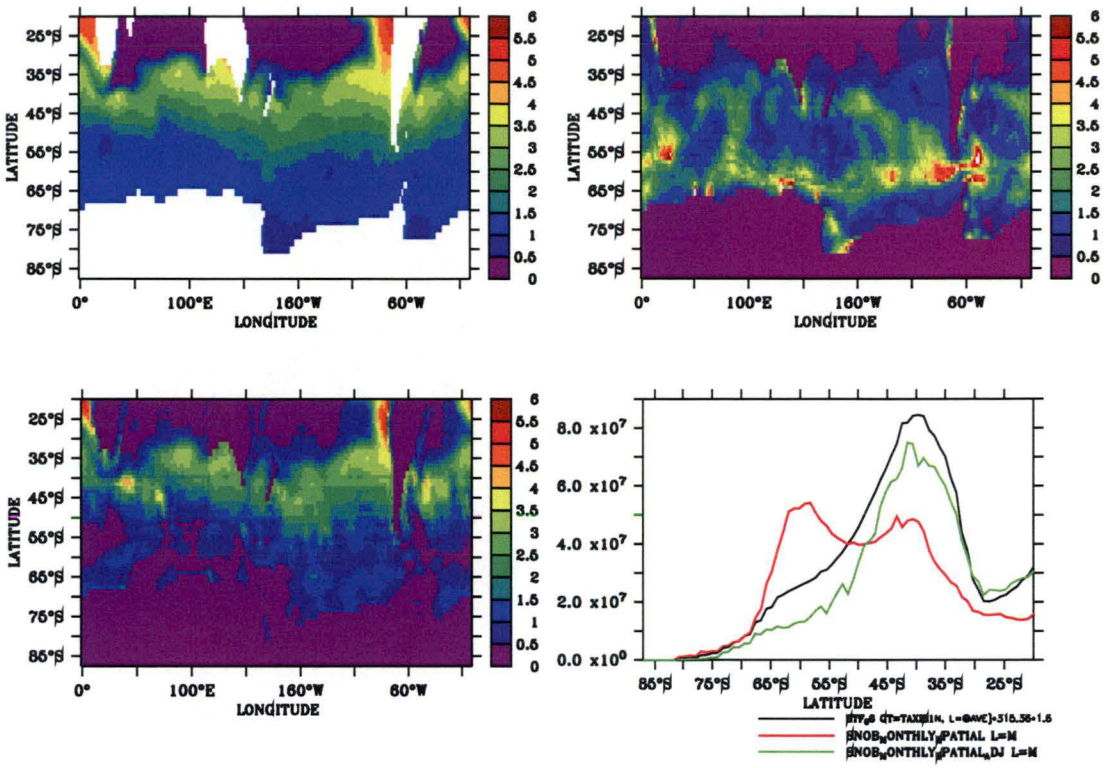

Figure 7-8: Distribution of a) the potential SNO due to photosynthesis, SNO_{photo} ($molO_2\ m^{-2}\ yr^{-1}$) b) SNO_{bio} calculated after removing the annual mean biological oxygen flux from the monthly biological oxygen fluxes (Equation (18)) and c) SNO_{bio} calculated from the monthly biological oxygen fluxes without removing the annual mean biological oxygen flux (Equation (32)). Figure d) plots the zonally integrated SNO_{bio} with subtracting the annual mean biological oxygen flux (red line) and without subtracting the annual mean biological oxygen flux (green line) and the potential SNO due to photosynthesis, SNO_{photo}.

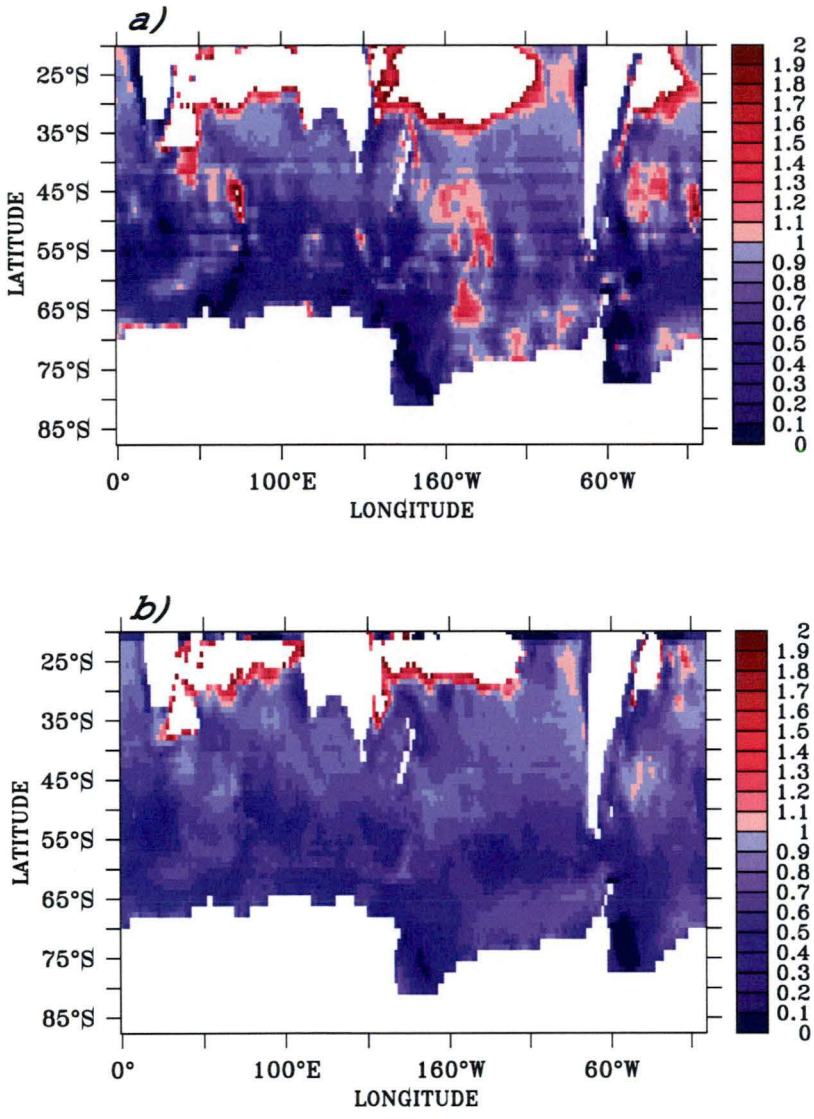

Figure 7-9: a) The distribution of the locally defined g factor, g_{local} (Equation (39)), b) the distribution of the locally defined g, g_{local}, after correcting for F_{vent} and F_{diseq}.

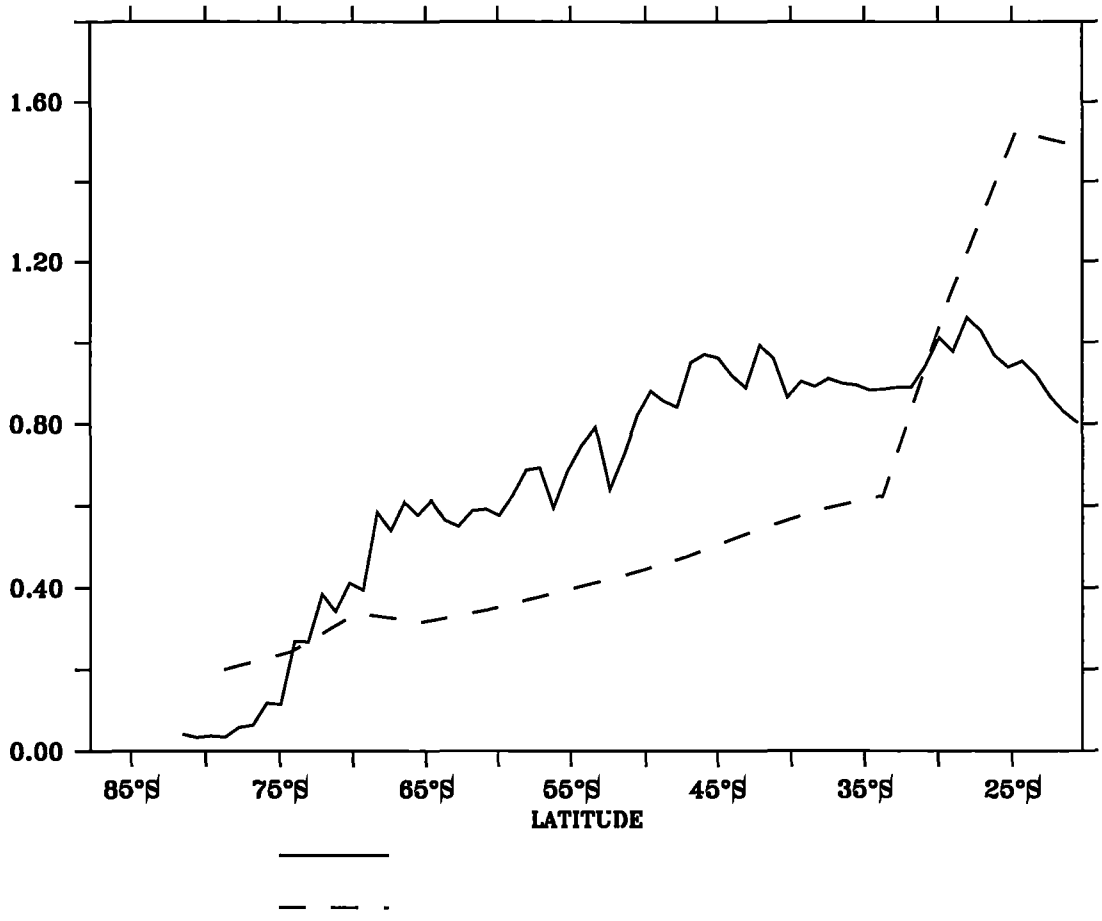

Figure 7-10: Zonally averaged distributions of g_{local} for two different global biogeochemical ocean models. The bold line represents MOM3. The dashed line represents MOM2 [Richard Matear, personal communication].

8. Atmospheric oxygen: Is it a reliable tracer of new production?

8.1. Estimating new production from atmospheric O_2/N_2

The appeal of using atmospheric oxygen to measure biological new production becomes clear when comparing the chemistry of O_2 to CO_2. There are several important differences between oxygen and CO_2 that have led to using seasonal atmospheric O_2 to estimate seasonal net biological production in the ocean. Firstly, oxygen equilibrates about 10 times faster than CO_2. This rapid response time makes atmospheric oxygen a potentially more sensitive tracer of biological productivity than CO_2. As already mentioned, unlike for the air-sea exchange of CO_2, the seasonal temperature and biological effects on oceanic air-sea oxygen exchange reinforce each other in the high latitude oceans, producing a large seasonal amplitude. Atmospheric O_2 is generally expressed in units of per meg, which is the difference in the observed O_2/N_2 ratio, $\left(O_2 / N_2\right)_{sample}$, from a reference sample, $\left(O_2 / N_2\right)_{reference}$

$$\delta\left(O_2 / N_2\right) = \left(\frac{\left(O_2 / N_2\right)_{sample}}{\left(O_2 / N_2\right)_{reference}} - 1 \right) \cdot 10^6 \ . \qquad (44)$$

The seasonal variability of oxygen is at least 10 times greater than that of CO_2. While the seasonal amplitude of pCO_2 at Cape Grim barely exceeds 1 ppm, the atmospheric seasonal amplitude can be as high as 120 per meg.

Keeling and Shertz (1992) first used atmospheric O_2/N_2 measurements to calculate hemisphere new production. Firstly the O_2/N_2 ratio was corrected for the terrestrial biospheric O_2/N_2 fluxes and the oceanic thermal effect [Keeling *et al.* (1993); Bender (1996)]. As for the air-sea O_2 flux approach, new production is calculated from the biological seasonal net outgassing, SNO_{bio}. Again, one of the largest uncertainties

arises from deducing how much of the oxygen, produced by biological productivity, is released to the atmosphere, that is the value used for g_{hem}. Note g_{hem} is generally considered to range from 0 to 1.

To test how effective atmospheric O_2/N_2 observations are at retrieving new production, we apply the technique of Keeling and Shertz (1992) to simulated atmospheric O_2/N_2 ratios. The simulated atmospheric O_2/N_2 ratios are produced by advecting the simulated air-sea fluxes of O_2 and N_2 in a global atmospheric transport model. The air-sea exchange of N_2 is not explicitly modelled. Here we estimate the air-sea N_2 flux (mol m^{-2} s^{-1}) from an annual cycle of the modelled monthly-mean heat flux, sea surface temperature and salinity fields according to Equation (16), except that c_{eq} is now the N_2 saturation concentration. Biological nitrogen fixation also produces a oceanic N_2 flux, which we do not include because most of the known nitrogen fixation occurs in the tropics and is a small part of the total N_2 flux. The Capone *et al.* (1998) estimate of global annual surface mixed layer N_2 fixation is very small (i.e. 80 x 10^{12} g) of relative to the thermal N_2 fluxes (i.e. of the order of 10^{15} g).

To estimate the total SNO of oxygen we first determine the change in O_2/N_2 ratio observed over the period when O_2 is outgassing using the peak-to-peak amplitude. We calculate the amplitude based on the average atmospheric O_2/N_2 concentration in the southern hemisphere (20°S – 90°S) from the monthly mean O_2/N_2 distribution in the lowest atmospheric model level.

The amplitude in O_2/N_2 in units of per meg is converted into the change in oxygen in parts per million, ppm, using the fact that a 1 ppm change in atmospheric O_2 produces a 4.76 per meg change in atmospheric O_2/N_2 given a background atmospheric concentration of 20% for O_2 and 78% for N_2. The total seasonal net outgassing of oxygen, SNO_{total}, is estimated by determining how much oxygen must be outgassed into the Southern Hemispheric atmosphere to produce the observed seasonal change in atmospheric O_2/N_2 concentration, and is calculated as in Keeling and Shertz (1992) where

$$SNO_{total} = \frac{amp}{10^6} \times N \times d_{KS} \ , \qquad (45)$$

and *amp* (ppm) is the seasonal amplitude of atmospheric O_2/N_2 recorded at an atmospheric observing station, $amp/10^6$ is the proportional change in atmospheric O_2/N_2 , N is the number of moles of dry air in the southern hemisphere atmosphere (i.e. $N = 8.8 \times 10^{19}$ moles) and d is dilution factor and is set to the same value used in the study of Keeling and Shertz (1992) (i.e. $d_{KS} = 0.5$).

To obtain the biological SNO the thermal component of the SNO is subtracted from the total SNO.

$$SNO_{bio} = SNO_{total} - SNO_{therm} \ . \qquad (46)$$

To calculate the thermal component of the SNO of oxygen that produces a change in the atmospheric O_2/N_2 ratio, we need to account for the thermal outgassing of both O_2 and N_2. Oxygen is more soluble than nitrogen, giving the seawater a higher O_2/N_2 ratio than the atmosphere. Since oxygen and nitrogen are outgassed in proportion to their oceanic concentrations, a flux of heat into the ocean increases the atmospheric O_2/N_2 ratio. The uncompensated component of the oxygen outgassing is approximately 48% of the thermal SNO. Most of the atmospheric variability of both O_2 and N_2 is driven by thermally driven air-sea fluxes, but the thermal fluxes contribute only a small percentage to the atmospheric O_2/N_2 variability since the fluxes of O_2 and N_2 are largely compensating.

The thermal component of the seasonal net outgassing (SNO_{therm}) over the southern hemisphere oceans (i.e. 20°S – 90°S) is calculated by subtracting the spatially integrated annual mean thermal oxygen from the spatially integrated seasonal fluxes in the same manner as for SNO_{bio} (Equation (18)).

Keeling and Shertz (1992) estimate new production, NP, from SNO_{bio} according to

$$NP = \frac{SNO_{bio}}{g_{ks}}, \tag{47}$$

where an arbitrary value of 0.5 is used for the proportionality factor, g_{ks}.

8.2. Atmospheric circulation model

The air-sea oxygen fluxes, simulated using a biogeochemical ocean model, are used as a lower boundary condition in an atmospheric transport model to simulate tracer distributions in the atmosphere. The atmospheric transport model used for the atmospheric simulations was a modified version the CSIRO Conformal-Cubic atmospheric model described in McGregor and Dix (2001). The oceanic air-sea fluxes of oxygen and nitrogen from the control run and selected perturbation experiments are run for 3 years in the atmospheric transport model. The 3rd year is used for the analysis. Hourly time series of atmospheric O_2 and N_2 concentrations in the model are retrieved at the locations of existing stations in the global atmospheric observing network. The monthly mean global atmospheric concentration fields are also recorded.

8.3. Evaluation of the atmospheric transport

The CSIRO Cubic Conformal atmospheric transport model (CCAM) is a relatively new model and work evaluating the transport of this model is in progress. An earlier version of the model was used in the (The Atmospheric Transport Model Intercomparison Project) project [Gurney *et al.* (2003)] and demonstrated slightly greater than average interhemispheric mixing across the range of models used in TransCom. Recently the latest version of the CCAM was evaluated using forward simulations of CO_2 emissions from fossil fuel burning and biospheric and air-sea exchange [Law *et al.* (2002)]. A comparison of simulated atmospheric CO_2 at specific grid cells with time-series, compiled by the World Data centre for Greenhouse Gases, demonstrated that several features of the CO_2 time series are modelled well. Here we focus on

assessing features of the atmospheric circulation most relevant to this study. This includes interhemispheric transports, atmospheric mixing and the seasonality of atmospheric O_2/N_2.

8.3.1. *Interhemispheric transport*

The TransCom experiments have been used to compare the atmospheric transport of gases of a large number of global atmospheric transport models. To assess the interhemispheric transport in CCAM, the model used in this study the same air-sea CO_2 flux fields used in the TransCom 3 experiment [Gurney *et al.* (2003)], were run in the atmospheric transport model to simulate the large-scale interhemispheric gradient in CO_2. The magnitude of the interhemispheric gradient is an indicator of the strength of the integrated vertical and meridional transports. Figure 8-1 shows the interhemispheric gradient produced by advecting the background air-sea CO_2 fluxes in CCAM. The background fluxes used were the two fossil fuel sources – the 1990 annual mean from Andres *et al.* (1996) and the 1995 annual mean from Brenkert (1998) - the biospheric exchange from the CASA (Carnegie Ames Standford Approach) model, Randerson *et al.* (1997) and the oceanic air-sea fluxes, T99, from Takahashi *et al.* (2002). See Gurney *et al.* (2003) for details.

The interhemispheric difference (IHD) in atmospheric CO_2 simulated by CCAM is 5.0 ppm, and was estimated by subtracting the annual mean CO_2 concentration from the southern hemisphere from that of the northern hemisphere. The IHDs simulated by the models participating in the TransCom 3 experiment [Gurney *et al.* (2003)], ranged from 4.5 to 7 ppm. Thus the IHD from CCAM is slightly lower than the median value of 5.6 ppm, but closer to the observed interhemispheric gradient (Figure 2-3). The studies of Keeling *et al.* (1998) and Garcia and Keeling (2001) both used the atmospheric transport model, TM2, to advect air-sea oxygen fluxes, produced from sea-surface oxygen climatologies. The TM2 model was found to have the lowest IHD of all the models participating in the TransCom 3 experiment (i.e. 4.5 ppm). Note that in the IHD's simulated from the models used in the TransCom 1

experiments had IHD's below the TransCom 3 range, indicating that earlier model studies tended to mix more vigorously.

Smaller simulated IHD's indicate more rapid mixing away from sites of surface exchange and a reduced tendency to vertically trap gases lower in the atmosphere. Consequently it would be expected that models with lower IHD's tend to produce smaller atmospheric O_2/N_2 amplitudes. Thus, it would be expected that the TM2 model would produce the lowest seasonal amplitudes of atmospheric tracers relative to other global atmospheric transport models, including CCAM.

8.3.2. *Atmospheric O_2/N_2*

The IHD is not always an accurate indicator of zonal and meridional mixing [Denning *et al.* (1999a)]. To further evaluate the models atmospheric transport, we advect the air-sea fluxes of Garcia and Keeling (2001) in CCAM. We determine how the atmospheric transport in CCAM performs relative to TM2, the global atmospheric transport model used in Garcia and Keeling (2001).

Figure 8-2 shows the annual cycles of atmospheric O_2/N_2 simulated by CCAM, at atmospheric O_2/N_2 observing stations in the southern hemisphere, using the air-sea fluxes from Garcia and Keeling (2001) (green line). The seasonal amplitude of atmospheric O_2/N_2 simulated at Samoa, Cape Grim, Macquarie and South pole using both CCAM and TM2 are shown in Table 8-1. As expected, given that the IHD suggests the interhemispheric transport in CCAM is less vigorous than TM2, the seasonal O_2/N_2 amplitudes simulated by CCAM at Cape Grim and South Pole are larger than those simulated by TM2 by approximately 10 - 20 per meg.

Figure 8-3 shows the spatial distributions of the seasonal amplitudes of atmospheric O_2/N_2 after advecting the air-sea fluxes of Garcia and Keeling (2001) in CCAM. There is an enormous amount of spatial structure in atmospheric O_2/N_2 amplitudes. This result is at odds with popular belief that strong zonal winds homogenise atmospheric O_2/N_2 concentrations in the southern hemisphere oceans.

Unfortunately, very few atmospheric O_2/N_2 modelling studies [e.g. Keeling *et al.* (1998)] have focused on the spatial distribution of the seasonal amplitude. Keeling *et al.* (1998) showed a figure of the seasonal amplitude of atmospheric O_2/N_2 produced by advecting the air-sea flux climatology in TM2. They found much less spatial variability in the magnitude of the seasonal O_2/N_2 amplitude (i.e. 40 – 90 per meg, see also Table 8-1) then produced here by advecting the air-sea fluxes of Garcia and Keeling (2001) in CCAM (i.e. 70 – 210 per meg). Perhaps this is not surprising considering; i) the increasing tendency for recent atmospheric transport models to mix less vigorously [Gurney *et al.* (2003)], which probably tends to enhance the seasonal amplitude of atmospheric O_2/N_2; ii) Keeling *et al.* (1998) note that they expect the amplitude of the seasonal anomalies to be underestimated as much as 50% in regions of sparse data coverage where they base their O_2 anomaly maps on 3-month or 5-month running means; iii) the seasonal O_2/N_2 amplitudes from both Keeling *et al.* (1998) and Najjar and Keeling (2000) were smaller than Garcia and Keeling (2001) because they both used oceanic temperature to fill in missing oceanic values rather than heat flux as in Garcia and Keeling (2001) [Hernan Garcia, personal communication] and iv) enhanced spatial structure in the spatial distribution of the seasonal amplitude of atmospheric O_2/N_2 from Keeling *et al.* (1998) is expected since the coarse sampling resolution of oxygen flux data smooths the spatial variability in the biological oxygen flux relative to biological productivity estimates based on satellite images.

To summarise, CCAM mixes less vigorously than TM2. Yet, compared to all the models used in the recent TransCom experiments, the model mixes more vigorously than the average. Thus, we would expect that CCAM would tend to underestimate observed O_2/N_2 amplitudes.

8.4. Comparison of seasonal O_2/N_2 amplitudes to observations

We compare the seasonal amplitudes of atmospheric O_2/N_2 simulated by CCAM using our biogeochemical ocean model to those simulated from the air-sea fluxes of Garcia and Keeling (2001) and to observations.

Figure 8-2 shows the annual cycles of atmospheric O_2/N_2 by advecting the air-sea oxygen fluxes, from the control experiment (black line) and test 2 (i.e. quadrupled new production in the southern hemisphere, red line) from the global biogeochemical circulation model, in CCAM. Interestingly, even though the seasonal amplitudes of zonally averaged air-sea fluxes from Garcia and Keeling (2001) and test 2 are similar (Figure 6-26), they produce very different amplitudes at atmospheric observing stations, particularly at Cape Grim. This reflects both the latitudinal and longitudinal differences in the spatial distributions of the air-sea oxygen fluxes, which produce different spatial distribution of atmospheric O_2/N_2.

Unfortunately, it is currently not possible to determine whether we would expect to see a similar degree of spatial variability in atmospheric O_2/N_2 amplitudes in the real atmosphere. Atmospheric oxygen is measured continuously at only a few stations in the southern hemisphere oceans. And, oxygen has only been measured at two stations between 45°S and 90°S – Macquarie Island and Palmer Station – where most of the spatial variability in atmospheric O_2/N_2 occurs. The short time series measured at these stations were made over different time periods so, it is not possible to say whether the differences in the seasonal amplitudes reflect interannual variability in large-scale ocean processes or spatial structure in the atmospheric O_2/N_2 distribution. The observed amplitude measured at Cape Grim varies interannually by at least $\pm$ 15 per meg [Bender (1996)].

Table 8-1 lists both the atmospheric O_2/N_2 amplitudes simulated by advecting the air-sea fluxes from the global biogeochemical ocean model (i.e control experiment and the perturbation experiment, test 2) in CCAM, and the observed seasonal amplitudes. The experiment with the highest new production in the southern hemisphere oceans (test 2) underestimates the seasonal amplitude of O_2/N_2 at Cape Grim. Given the observed interannual variability in the seasonal amplitude (i.e. 43 - 73 per meg, Bender (1996)), the seasonal amplitude simulated from test 2 (i.e. 60 per meg) is in agreement with the observations. The seasonal O_2/N_2 amplitude from the control experiment (i.e. 36 per meg) is on the low side. This may be because the maximum seasonal amplitude in the simulated air-sea fluxes occurs further south than in the observations (Figure 6-26).

Other possible explanations for the low seasonal amplitudes are that simulated new production is too low, oceanic ventilation is underestimated, or the atmospheric circulation is too vigorous. Given the comparison to other observational estimates of new production (

Table 6-2) and the simulated phosphate fields (Figure 6-23), the first possibility is unlikely.

The above comparison highlights the need for future studies to focus on the spatial variability of the seasonal amplitude of atmospheric O_2/N_2 and the need for more continuous oxygen measurements in the southern hemisphere. Later in the discussion, we will demonstrate how this spatial variability has important consequences on estimates of new production in the southern hemisphere oceans.

8.5. Atmospheric O_2/N_2 based estimates of new production

We apply the technique of Keeling and Shertz (1992) to the simulated atmospheric O_2/N_2 concentrations, from a selection of the perturbation experiments (listed in bold in Table 5-1). We eliminate any possibility of station bias by using the average atmospheric O_2/N_2 concentration in the southern hemisphere calculated from the monthly

mean O_2/N_2 distribution in the lowest atmospheric model level. Figure 8-4 plots atmospheric estimates of SNO_{bio} from each of the new production perturbation experiments (Table 4-1). The black line represents where estimates of SNO_{bio} would need to lie if the relationship of Keeling and Shertz (1992) were to hold (Equation (47)).The simulated SNO_{bio} in the southern hemisphere oceans is overestimated, relative the approach of Keeling and Shertz (1992), by as much as 270% (Figure 8-4). Fortunately however, like for the oceanic approach discussed in the previous chapter, SNO_{bio} scale linearly with NP

$$SNO_{bio} = 1.38\ NP - 0.10\ ,\ r^2 = 0.99 \tag{48}$$

and rearranges to

$$NP = \frac{SNO_{bio}}{1.38} + 0.07 \tag{49}$$

such that $g_{hem} = 1.38$ and $k_{SNO} = 0.07$ GtC yr^{-1}.

As for the oceanic approach, the relationship is linear and has a non-zero offset. But, the atmospheric g_{hem} is much larger than the g_{hem} from the oceanic approach and g_{ks} used in the study of Keeling and Shertz (1992) (i.e. in both cases $g_{hem} = 0.5$). g_{hem} is generally considered to range between 0 and 1. Also, k_{SNO} is very small.

8.6. The limitations of the atmospheric O_2/N_2 method for estimating new production

Most of the limitations of oceanic approach to estimating NP (discussed in the previous chapter) also apply to the atmospheric approach for estimating NP. Basically that is, estimates of SNO_{bio} are biased because the approach does not adequately account for oxygen fluxes driven by several oceanic processes (i.e. ventilation and

disequilibrium oxygen fluxes). The differences between simulated SNO_{bio} and the SNO_{bio} expected from the relationship proposed by Keeling and Shertz (1992) (Equation (47)), may also be driven by atmospheric processes.

8.6.1. Oceanic processes

One explanation for the overestimate of SNO_{bio} when applying the techniques of Keeling and Shertz (1992) to simulated atmospheric O_2/N_2 fields, is that $SNO_{atmos} > SNO_{ocean}$, where SNO_{atmos} is the SNO_{bio} the atmospheric approach and SNO_{ocean} is the SNO_{bio} fro the oceanic approach. Note SNO_{atmos} is calculated over a different time period to SNO_{ocean}. SNO_{ocean} is calculated over the time period when F_{bio} is outgassing to the atmosphere. In the oceanic approach the SNO period occurs between December and May (Figure 7-3a). SNO_{atmos} is calculated from the peak-to-peak amplitude of the atmospheric O_2/N_2 signal. In the atmospheric approach the SNO period occurs between March and September. From the seasonal cycles of the hemispherically integrated components of F_{bio} (Figure 7-3b), we see that the contribution of the ventilation and disequilibrium oxygen fluxes to SNO_{bio} is greater during the atmospheric SNO period than during the oceanic SNO period. The nonlocal ventilation and disequilibrium fluxes enhance the seasonal amplitude of $F_{photo} + F_{loc}$ by a factor of approximately 1.5. Almost 80% of the amplitude enhancement is solely due to the nonlocal ventilation oxygen flux. Thus, the large nonlocal ventilation oxygen flux is largely responsible for the fact that applying the atmospheric O_2/N_2 approach of Keeling and Shertz (1992) overestimates new production by a factor of approximately 2.7.

8.6.2. *Atmospheric processes*

It is conceivable that a factor of 2.7 overestimate of *NP* could be due to our initial estimate of the dilution factor (i.e. $d_{KS} = 0.5$) being a factor of 2.7 too large. Here we show this is not possible and that the 0.4 is lower limit for *d*. The general equation used by Keeling and Shertz (1992) to estimate *NP* using the atmospheric approach has two unknowns, *g* and *d*

$$NP = \left[\frac{amp \times N \times d}{10^6 g} - \frac{SNO_{therm}}{g} \right]. \tag{50}$$

The second term in Equation (50) is 2 orders of magnitude smaller that the first term and so to a first approximation $NP \propto \frac{d}{g} SNO_{atmos}$. Assuming the definition of *g* in the atmospheric approach is identical to the oceanic approach, then

$$NP = \frac{SNO_{atmos} d}{g} \simeq \frac{SNO_{ocean}}{g}. \tag{51}$$

Therefore

$$d = \frac{SNO_{ocean}}{SNO_{atmos}} = \frac{1}{2.7} = 0.4. \tag{52}$$

We know from section 8.6.1 above, that SNO_{atmos} at least too large by a factor of 1.5. To adjust for the contribution of the nonlocal ventilation and disequilibrium fluxes SNO_{atmos} must be divided by at least a factor of 1.5. such that $d = 0.7$. Thus, after adjusting for the influence of the nonlocal and disequilibrium oxygen fluxes, *d* must be greater than 0.4 and the fact that the atmospheric approach gives SNO_{bio} estimates that are a factor of 2.7 greater than the oceanic approach can not be explained by a dilution factor of that is a factor of 2.7 too low.

The fact that *d* in the model can not be low is further supported by; i) that the model probably mixes too vigorously, as implied by the fact that the IHD in CCAM is small compared to other atmospheric models (section 8.3.1), and, ii) the fact that the model underestimates the seasonal amplitude of O_2/N_2 (section 8.3.2).

8.6.3. The choice of atmospheric observing stations.

The atmospheric O_2/N_2 based estimates of SNO_{bio} from Figure 8-4 were based on the average atmospheric O_2/N_2 concentration in the southern hemisphere (20°S – 90°S) from the monthly mean O_2/N_2 distribution in the lowest atmospheric model level. Here we calculate the amplitude of O_2/N_2 from the 180 hour smoothed atmospheric O_2/N_2 hourly time series (per meg) at Cape Grim (cgo, Figure 8-2). The relationship between the estimates of SNO_{bio} based on O_2/N_2 concentrations at Cape Grim (Figure 8-5, red line) and *NP* is virtually identical to the hemispherically averaged estimates and *NP* (Figure 8-4, blue line). Cape Grim was chosen to estimate SNO_{bio} because a long time series of atmospheric oxygen has been recorded, and for consistency with the Keeling and Shertz (1992) study. The relationship is linear regardless of which atmospheric observing station is used in the southern hemisphere (not shown). The similarity between the cgo-based and the hemispherically averaged estimates of SNO_{bio} is a coincidence. The SNO_{bio} estimate is extremely station dependent. Figure 8-5 shows the SNO_{bio} estimates based on O_2/N_2 concentrations from a selection of station locations from the existing atmospheric observational network (blue points). The SNO_{bio} estimates from the different stations range between 5 to almost 15 times the expected SNO_{bio} estimates given the relationship proposed by Keeling and Shertz (1992). Cape Grim (cgo) and Baring head (bhd) produce the lowest estimates while Macquarie Island (mqa) and Palmer Station (psa) produce the highest.

What causes the spatial variability in the seasonal amplitude of the atmospheric O_2/N_2 signal? Figure 8-3a shows the spatial variability in the atmospheric O_2/N_2 seasonal amplitude across the Southern Ocean for the control experiment. The longitudinal variability suggests that, despite strong zonal winds, the southern hemisphere air is not mixed enough zonally to remove local effects. So what drives the spatial variability in the atmospheric O_2/N_2 seasonal amplitude? It cannot be the biological productivity because the simulated new production does not show much longitudinal structure (Figure 5-2a). The physical circulation of the atmosphere or ocean must produce these effects. The physical circulation in the atmospheric model could artificially enhance the degree of spatial structure in atmospheric O_2/N_2 if the model underestimates the strength of atmospheric mixing. But we have demonstrated in section 8.3 that the model mixes relatively vigorously. Thus we expect that the spatial structure in the atmospheric O_2/N_2 amplitudes is driven by spatial structure in the air-sea oxygen fluxes.

In the control experiment, the seasonal amplitude of the atmospheric O_2/N_2 signal ranges between 30 and 100 per meg and increases locally by almost 100% in response to a doubling of new production (test 4, Figure 8-3b). The spatial variability in the seasonal amplitude of atmospheric O_2/N_2 concentrations could be a reflection of the spatial variability in the oceanic circulation. We showed in section 7.3 that the ventilation and disequilibrium oxygen fluxes result in substantial spatial structure in the distribution of the biological oxygen flux. The spatial distribution of the seasonal amplitude of the biological oxygen flux is shown in Figure 8-6. The seasonal amplitude in the biological oxygen flux varies by more than a factor of 15 spatially. It tends to be larger where the mixed layers are deepest (contours) and in the upwelling divergence zone. A more realistic representation of the seasonal mixed layer produces more pronounced spatial variability in the seasonal amplitude of atmospheric O_2/N_2. The seasonal amplitude in atmospheric O_2/N_2 produced in test 9 (Table 4-3), without the Chen mixed layer scheme, the simulated mixed layers are much shallower and have less pronounced

spatial structure than the observed mixed layers (not shown) and therefore produce less spatial structure in atmospheric O_2/N_2.

Do we expect to see this degree of spatial variability in observed atmospheric oxygen concentrations? The common perception is that the strong zonal winds in the southern hemisphere homogenise atmospheric O_2/N_2 concentrations. One of the key findings of this study - that there is substantial zonal variability in atmospheric O_2/N_2 seasonal amplitudes - challenges this perception. But, it is not currently possible to make a thorough assessment of spatial variability in atmospheric O_2/N_2 seasonal amplitudes. No models have looked in detail at the spatial distribution of atmospheric O_2/N_2 fields, other than Keeling et al., 1998. But, they corrected their oxygen fluxes using temperature rather than heat fluxes which produced an underestimate of the seasonal O_2/N_2 amplitudes. Also, Garcia and Keeling (2001) only showed the seasonal amplitude of O_2/N_2 at selected observing stations, which are situated outside the zone with the most spatial variability in the simulated seasonal O_2/N_2 amplitudes.

If future observational and model studies confirm that there is substantial spatial variability in seasonal amplitudes of atmospheric O_2/N_2, then using atmospheric O_2/N_2 for monitoring new production and evaluating biogeochemical ocean models using one atmospheric observing station alone will be difficult. This study highlights the need for both more oxygen observations in the southern hemisphere and more inter-model comparisons focusing on the spatial variability in seasonal atmospheric O_2/N_2 concentrations.

8.7. A revised estimate of new production

Keeling and Shertz (1992) estimated a 11.6 GtC yr^{-1} of annual new production using their observational estimate of SNO_{bio} (i.e. 6.8 x 10^{14} mol) and their proposed relationship between NP and SNO_{bio}

$$NP = \frac{SNO_{bio}}{0.5} . \qquad (53)$$

We have demonstrated that this relationship does not hold because the ventilation and disequilibrium oxygen fluxes contribute to SNO_{bio} and contribute to the approximately 2.7 overestimate of NP. As in the previous chapter to correct for the bias introduced by the ventilation and disequilibrium fluxes, we apply the linear relationship between SNO_{bio} and NP determined from the model

$$NP = \frac{SNO_{bio}}{1.38} + 0.05 , \qquad (54)$$

to the observational estimate of southern hemispheric SNO_{bio} from Keeling and Shertz (1992). Using a $C:O_2$ ratio pf 106:-170 we obtain a much lower 3.7 GtC yr^{-1} estimate of southern hemisphere annual new production.

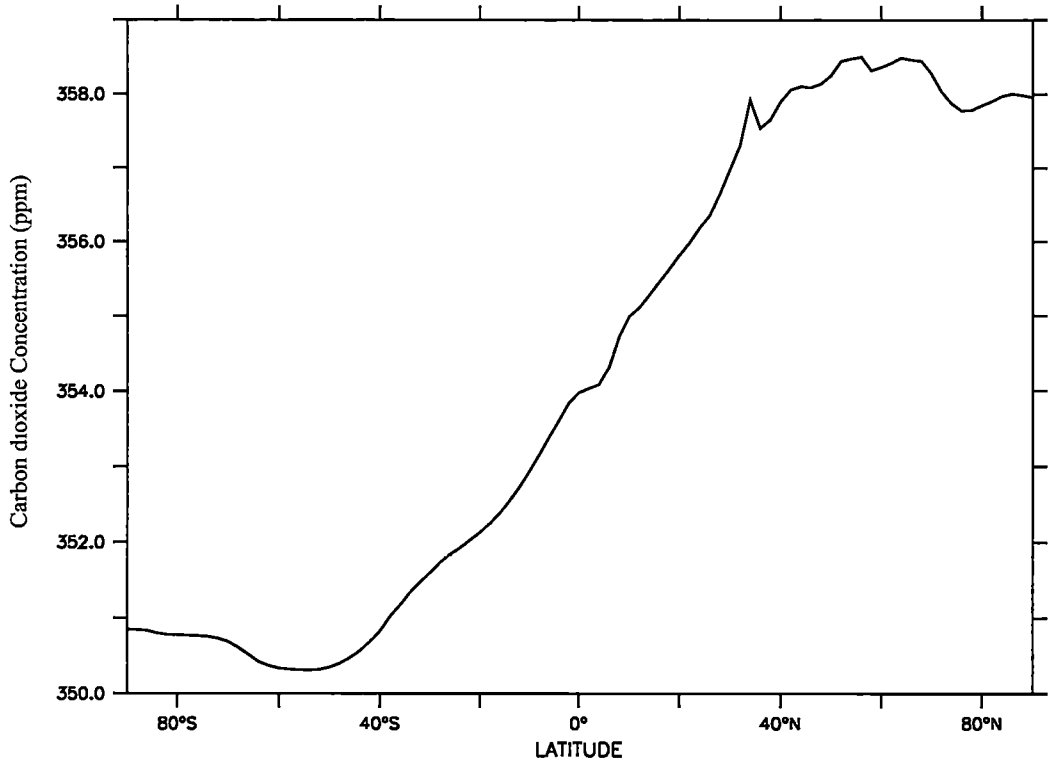

Figure 8-1: The annual mean, zonal mean surface CO_2 concentration (ppm) resulting from the same combined background fluxes used in the TRANSCOM 3 experiment [Gurney *et al.* (2003)]. The CO_2 fluxes used in the forward simulation are the two fossil fuel sources – the 1990 annual mean from Andres *et al.* (1996) and the 1995 annual mean from Brenkert (1998) - the biospheric exchange from the CASA (Carnegie Ames Standford Approach) model, Randerson *et al.* (1997) and the oceanic air-sea fluxes, T99, from Takahashi *et al.* (2002). See Gurney *et al.* (2003) for details. The concentrations are calculated relative to a background concentration of 350 ppm.

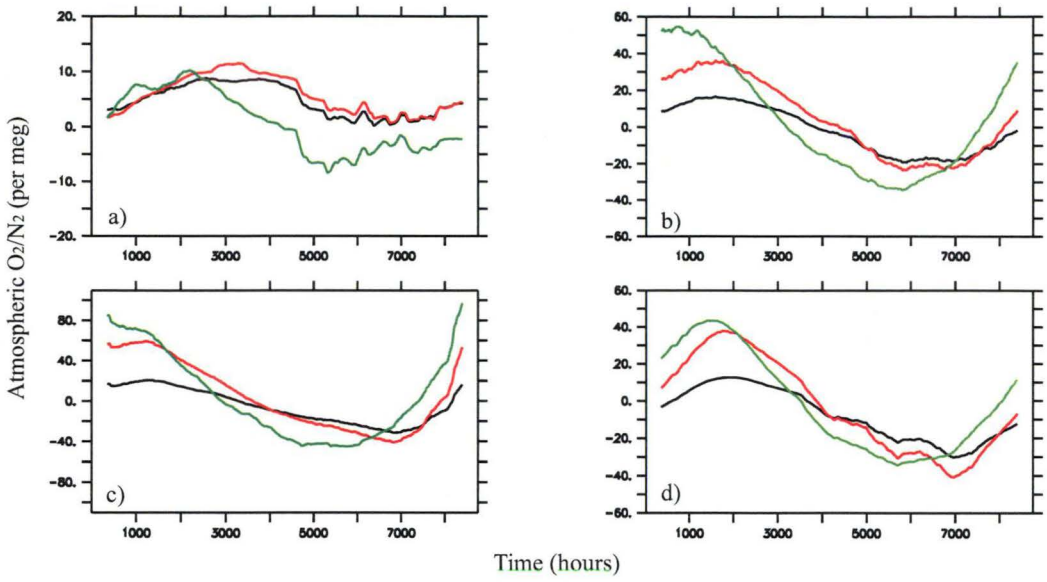

Figure 8-2: The 180-hour smoothed annual cycle of atmospheric O_2/N_2 (per meg), simulated at selected southern hemisphere observing stations, by advecting the air-sea O_2 fluxes from the control experiment (black line), the perturbation experiment, test2 (i.e. quadrupled new production in the southern hemisphere oceans, red line) and the climatology of Garcia and Keeling (2001) (green line), in the global atmospheric transport model CCAM. The atmospheric stations are a) Samoa (14°S, 170°W), b) Cape Grim (41°S, 150°E), c) Macquarie Island (54°S, 158°E), and d) South Pole (90°S).

Table 8-1: Observed and simulated seasonal amplitude (maximum - minimum) of 180-hourly smoothed atmospheric O_2/N_2 concentrations at selected atmospheric observing stations in the southern hemisphere.

Atmospheric Observing Station	O_2/N_2 amplitudes (per meg) Simulated in TM2 using the oxygen fluxes of Keeling *et al.* (1998)	Simulated in TM2 using the oxygen fluxes of Garcia and Keeling (2001)	Simulated in CCAM using the oxygen fluxes of Garcia and Keeling (2001)	Simulated in CCAM using the oxygen fluxes of CSIRO_MOM3 Control (test2)	Observed
Samoa (14°S, 170°W)	45	24	19	9 (11)	28
Cape Grim (41°S, 150°E)	45	67	89	36 (60)	71
South Pole (90°S)	47	58	78	43 (79)	62

a)

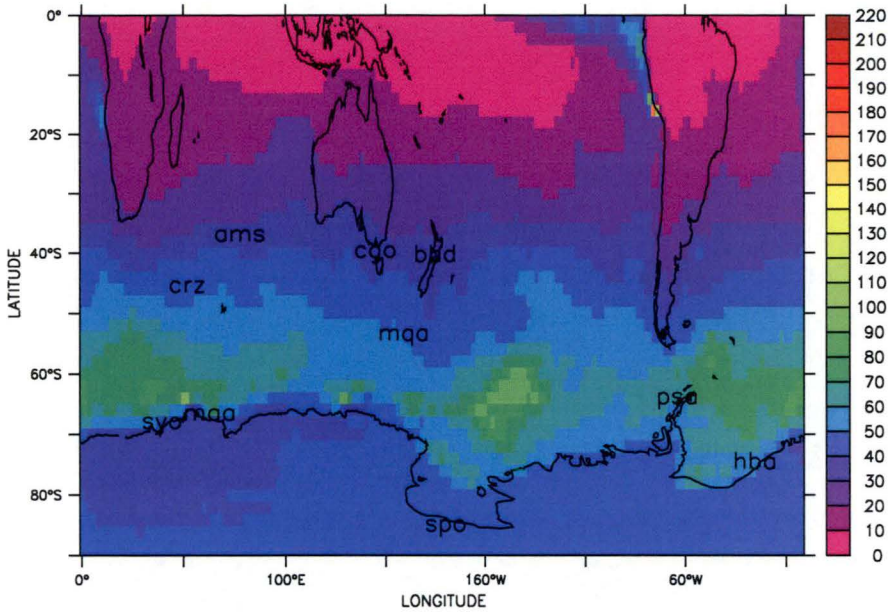
0°
20°S
40°S
60°S
80°S
LATITUDE
0°
100°E
160°W
60°W
LONGITUDE
ams
cgo
bhd
crz
mqa
syo
psa
hba
spo
220
210
200
190
180
170
160
150
140
130
120
110
100
90
80
70
60
50
40
30
20
10
0

b)

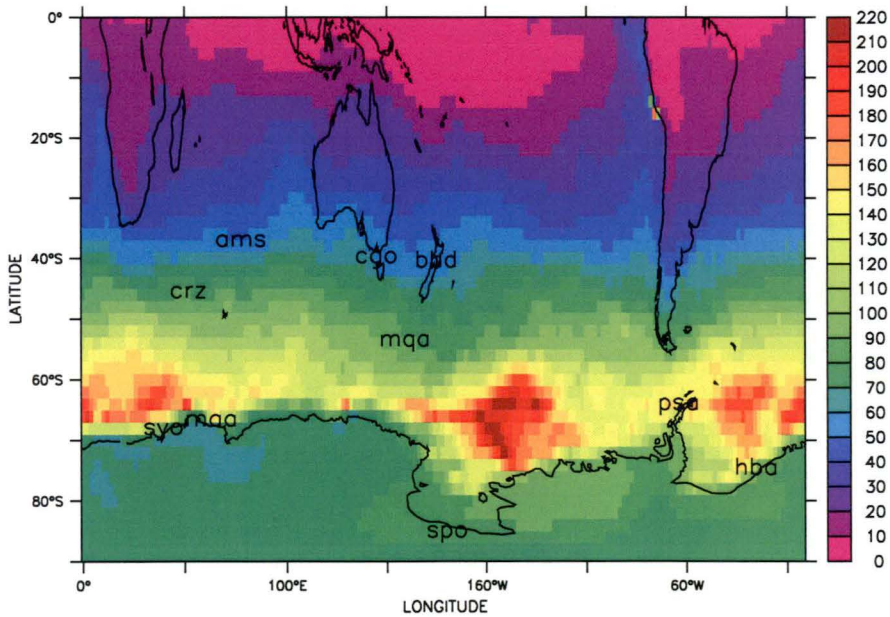
0°
20°S
40°S
60°S
80°S
LATITUDE
0°
100°E
160°W
60°W
LONGITUDE
ams
cgo
bhd
crz
mqa
syo
psa
hba
spo
220
210
200
190
180
170
160
150
140
130
120
110
100
90
80
70
60
50
40
30
20
10
0

c)

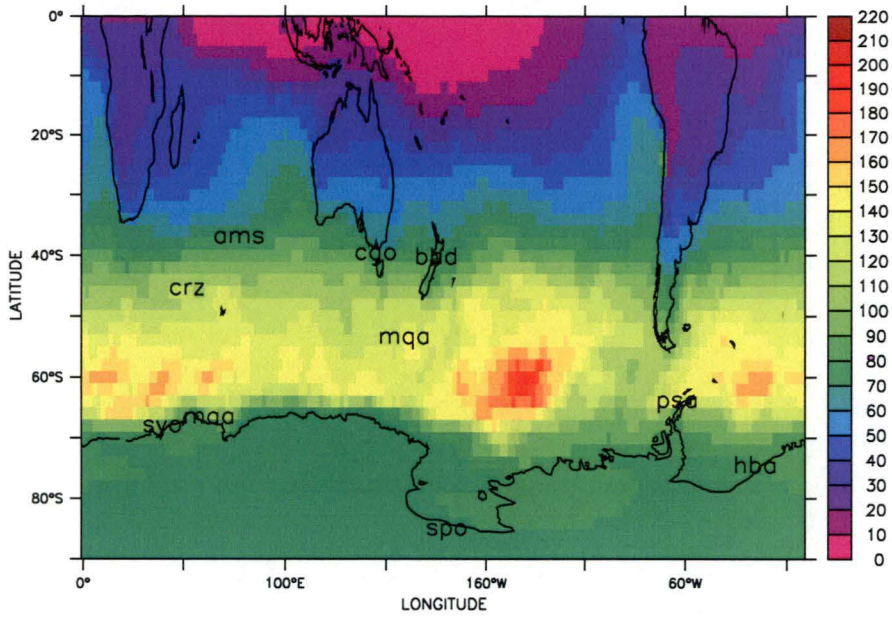

Figure 8-3: The seasonal amplitudes of atmospheric O_2/N_2 (per meg) (i.e. maximum minus minimum O_2/N_2) simulated by advecting the air-sea O_2 fluxes from a) the control experiment b) the perturbation experiment, test2 (i.e. quadrupled new production in the southern hemisphere oceans) and c) the climatology of Garcia and Keeling (2001), in the global atmospheric transport model CCAM. The labels correspond to the station names of the global atmospheric station network: cgo - Cape Grim, bhd – Baring Head, ams – Amsterdam Island, crz – Crozet Island, syo – Swoya, maa – Mawson, mqa – Macquarie Isalnd, psa – Palmer Station, hba, Halleys Bay, spo – South Pole.

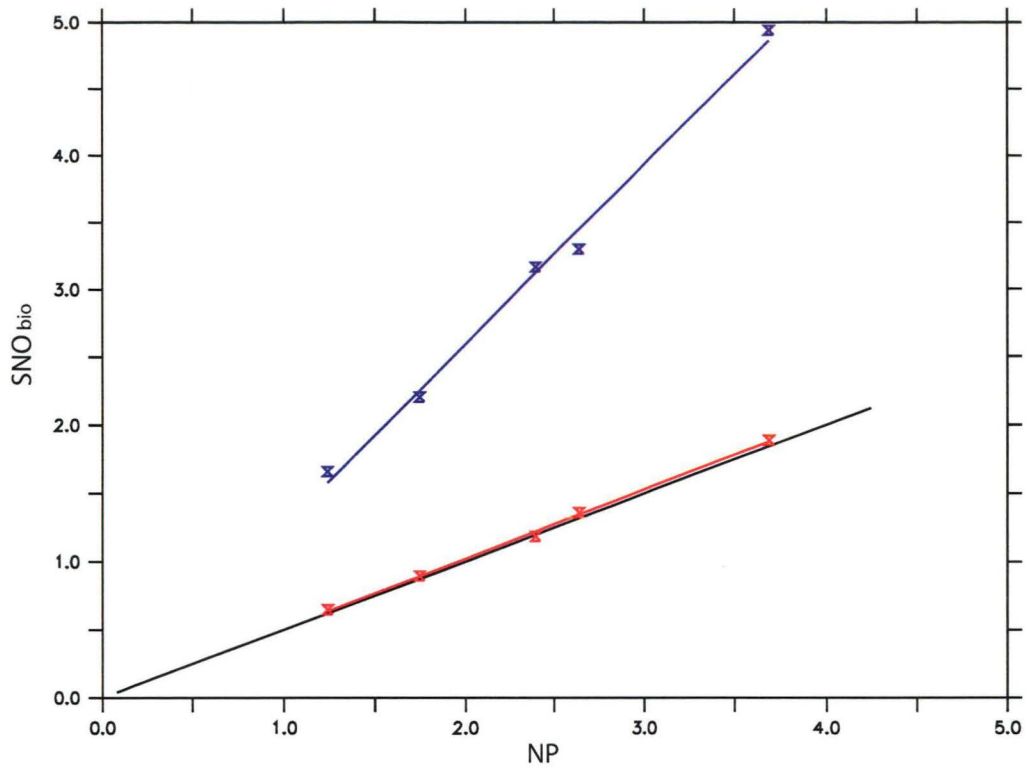

Figure 8-4: Atmospheric O_2/N_2 based estimates of SNO_{bio} (Equation (46)), versus simulated new production estimates, NP for the new production experiments. The bold line represents where the biological SNO estimates would lie according to the relationship of Keeling and Shertz (1992) (Equation (47)). The blue line is linear regression to the atmospheric SNO_{bio} estimates (blue points) ($SNO_{bio} = 1.38\ NP - 0.10$, $r^2 = 0.99$, Equation (48)) and the red line is the linear regression to the oceanic SNO_{bio} estimates (Equation (42)), from the new production perturbation experiments.

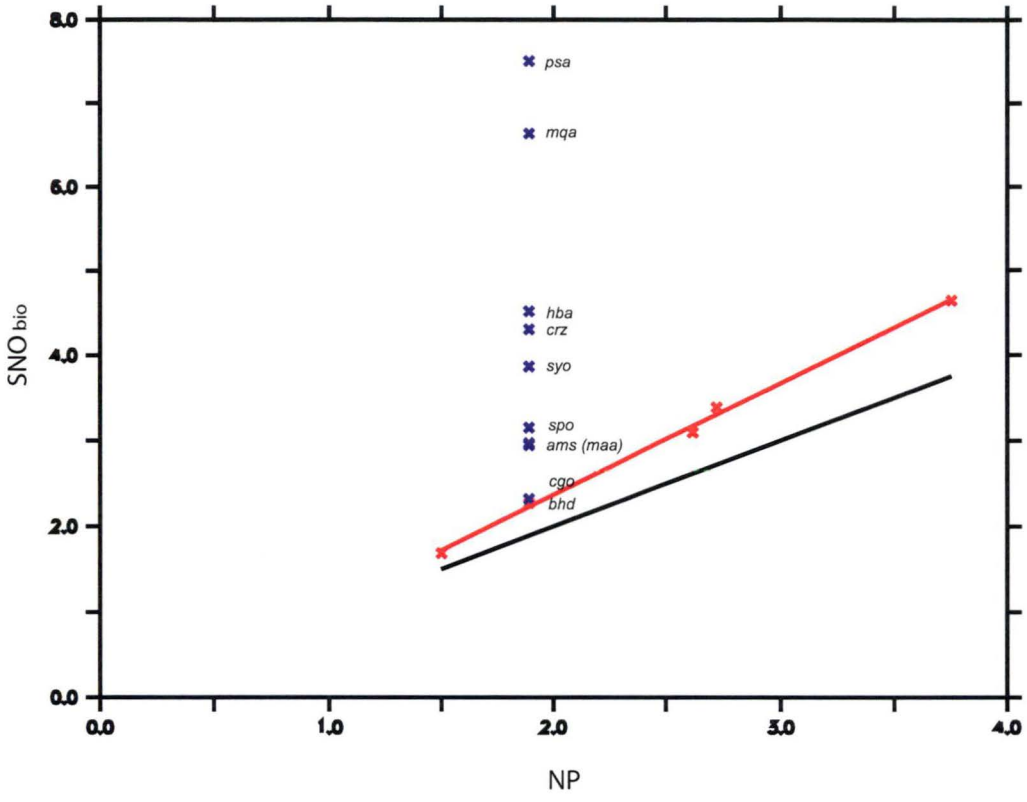

Figure 8-5: Atmospheric O_2/N_2 based estimates of biological SNO, SNO_{bio}, based on amplitude of atmospheric O_2/N_2 at Cape grim (cgo) versus simulated new production, NP. Overlayed are the new production estimates based on the amplitude of O_2/N_2 at a selection of atmospheric observing stations from the control case.

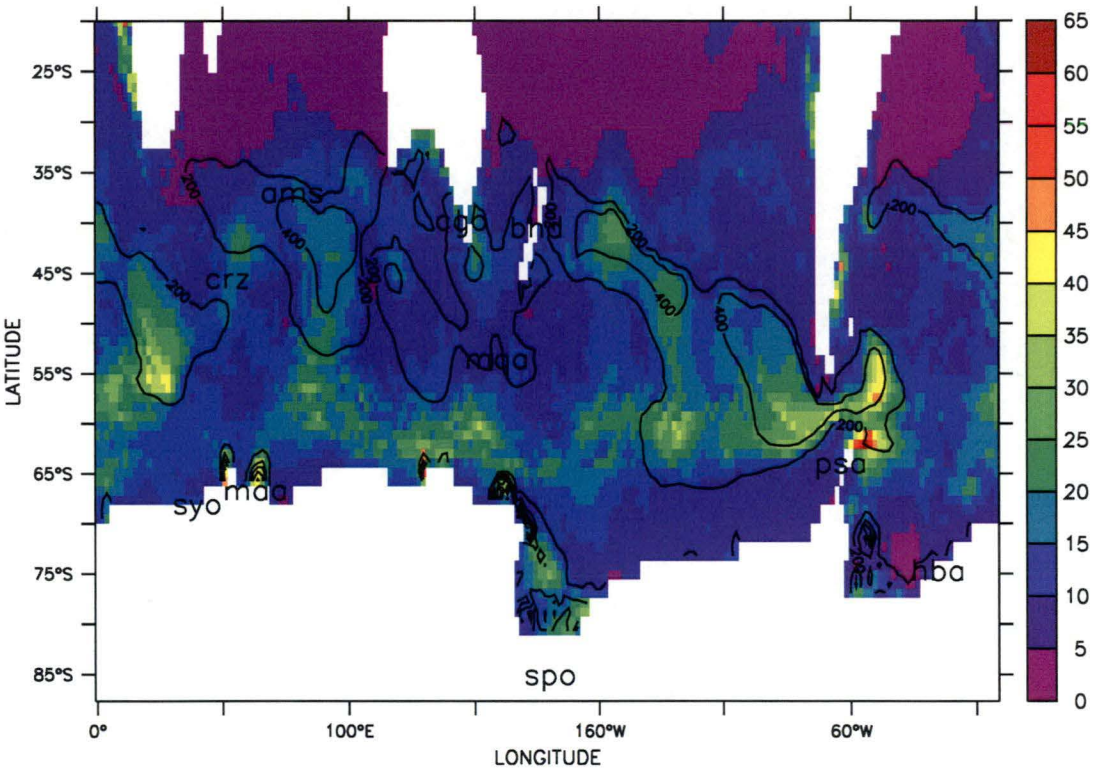

Figure 8-6: The seasonal amplitude of the biological oxygen flux, F_{bio}. The labels correspond to the station names of the global atmospheric station network as in previous figures. The contour lines are the maximum seasonal mixed layer depths (m).

9. Conclusions

Here we demonstrate that atmospheric observations can provide useful information on ocean processes. Firstly, we use atmospheric CO2 observations to estimate the magnitude of the southern hemisphere oceanic uptake of CO_2. Secondly, we investigate how well atmospheric O_2 observations constrain southern hemisphere new production.

9.1. CO_2 fluxes

Using an atmospheric inversion model we show that both the magnitude and the spatial distribution of the Takahashi *et al.* (2002) air-sea CO_2 flux distribution in the southern hemisphere can't be reconciled with observed large-scale atmospheric gradients of atmospheric CO_2. Takahashi *et al.* (2002) (T99) estimates a southern hemispheric CO_2 uptake of 1.8 GtC/yr based on air-sea CO_2 fluxes estimated from a compilation of ΔpCO_2 data. The atmospheric inversion study predicts a total (land and ocean) southern hemisphere CO_2 uptake of 1.65 to 1.90 GtC yr^{-1} for the 1990s (1991-1997). But constraining the ocean uptake to the estimate of T99 produces unrealistic CO_2 sources over southern hemisphere land regions. Constraining the southern hemispheric land sources to reasonable values, in addition to constraining the T99 flux, produces a negative bias in atmospheric CO_2 concentrations, indicating that less local oceanic CO_2 uptake is required for consistency with high latitude atmospheric CO_2 concentrations. The mid-latitude atmospheric CO_2 stations become positively biased, indicating that more local oceanic uptake of CO_2 is required. Consistency with the large-scale interhemispheric gradient can only be achieved by redistributing the oceanic CO_2 uptake from the high latitude oceans to the mid latitudes, suggesting that the T99 estimate of CO_2 uptake in the high latitudes is too high. The reduction in the high latitude southern ocean uptake from the T99 estimate is also one of the most robust findings from Gurney *et al.* (2002).

Interestingly, the magnitude of the latest revised observational estimate of CO_2 uptake in the southern hemisphere (http://www.ldeo.columbia.edu/res/pi/CO_2/carbondioxide/pages/air_sea_flux_rev1.html) is half the magnitude of the T99 estimate - in agreement with the conclusion that the T99 CO_2 uptake is too large. This latest finding demonstrates that atmospheric observations can be successfully used to improve oceanic estimates of oceanic CO_2 uptake.

Atmospheric CO_2 observations also constrain the seasonal air-sea fluxes. Contrary to the T99 estimate, the atmospheric inversion suggests that the high latitudes outgas CO_2 during the autumn-winter period, which is supported by direct observational evidence Metzl *et al.* (1999). The paucity of winter observations in the ΔpCO_2 compilation of Takahashi *et al.* (2002) suggests the compilation is biased by summer observations.

9.2. New production

A global biogeochemical circulation model was developed and applied to probe how effectively atmospheric and oceanic oxygen-based methods retrieve the magnitude of new production in the southern hemisphere oceans (20°S - 90°S). To tease apart the effects of the circulation and new production on the Seasonal Net Outgassing (SNO) of oxygen in the southern hemisphere oceans (section 7), a series of experiments are produced where the new production magnitudes are systematically perturbed without altering the circulation, and a series of experiments where the ocean circulation is perturbed without changing the distribution of new production. The model captures the key Southern Ocean water masses and frontal regions, and the suite of new production perturbation experiments spans a substantial range of the new production scenarios we might expect to observe in the true southern hemisphere oceans.

Two observational methods were applied to estimate biological new production, 1) based on the air-sea oxygen fluxes and 2) based on the seasonality in the atmospheric O_2/N_2 concentration. The air-sea fluxes

were simulated using the global biogeochemical circulation model, which were then used as a boundary condition in a global atmospheric transport model to simulate the O_2/N_2 concentrations in the atmosphere.

The air-sea flux approach, based on the study of Najjar and Keeling (2000), was applied to simulated air-sea oxygen fluxes to test how effectively the technique estimates new production in the southern hemisphere oceans. We isolate the processes that bias the new production estimates and demonstrate that current estimates of new production are biased by air-sea oxygen fluxes driven by ventilation and disequilibrium oxygen fluxes. We show that the bias is partly removed by not subtracting the annual mean biological oxygen flux before calculating SNO_{bio}, as has been done in previous studies. To further improve new production estimates, we must take the bias introduced by the ventilation and disequilibrium fluxes into account.

Fortunately, the air-sea flux based approach produced a linear relationship between the biological SNO of oxygen and new production in the southern hemisphere oceans. We propose the following general equation for estimating NP from SNO_{bio}

$$NP = \frac{SNO_{bio}}{g_{hem}} + k_{SNO}\ , \tag{55}$$

where the SNO offset, k_{SNO} reflects the relative contributions of F_{diseq} and F_{vent_nonloc} and g_{hem} is set by the large-scale relationships between F_{vent_nonloc}, NP_{loc} and NP_{nonloc}.

The challenge lies in the estimation of k_{SNO} and g_{hem} in the real ocean. Determining g_{hem} from local observations is not plausible due the enormous spatial variability in g, which is driven by spatial variability in the ventilation and disequilibrium fluxes. Instead we use the relationships between biological SNO and new production in two global biogeochemical ocean models to estimate an uncertainty in g_{hem} of 0.35 ± 0.15 and an uncertainty of 0.4 ± 0.4 GtC yr^{-1} in k_{SNO}.

From a sampling perspective, using atmospheric O_2/N_2 seems a more practical alternative for measuring variability new production, since the atmosphere acts to integrate the spatial variability in the oxygen fluxes. The Southern Ocean is a particularly attractive place to monitor atmospheric O_2/N_2. Due to the remoteness of the Southern Ocean from major terrestrial sources of O_2 variability the majority of the O_2/N_2 variability in the southern hemisphere is driven by O_2 exchange with the ocean. Keeling and Shertz (1992) estimated that almost 90% of the seasonal amplitude in atmospheric oxygen is driven by the ocean. Furthermore, the slow interhemispheric exchange of atmospheric oxygen on seasonal timescales means that seasonal variability of atmospheric O_2 primarily reflects air-sea exchange processes occurring within the southern hemisphere.

Applying the technique of Keeling and Shertz (1992) to the modelled atmospheric O_2/N_2 data to estimate new production, grossly overestimates simulated new production. Primarily the large ventilation flux causes the atmospheric method to overestimate new production. The seasonal amplitude of the ventilation oxygen flux reinforces the seasonal amplitude of the biological oxygen flux in the southern hemisphere oceans, which is subsequently reflected in the seasonal amplitudes of atmospheric O_2/N_2 concentrations.

The magnitude of the estimated new production is highly sensitive to which Southern Ocean station is used. We demonstrate the station sensitivity is due to the spatial variability in the atmospheric O_2/N_2 concentrations and challenges the previously held assumption that strong horizontal winds homogenise the southern hemisphere atmosphere. Interestingly, this contrasts with the conclusion from the first part of the thesis - that the southern hemisphere oceanic CO_2 uptake is relatively insensitive to the choice of stations within the southern hemisphere observing network. This difference is probably due to the relatively rapid air-sea exchange times of O_2/N_2 relative to CO_2. This study highlights the need for more continuous oxygen measurements in the southern hemisphere and for future studies to determine the spatially variability of

atmospheric O_2/N_2 in the atmosphere. We will then be in a better position to assess how many stations are needed to produce new production estimates that are not spatially biased.

The estimates of SNO_{bio} from the atmospheric and oceanic approaches are both biased by the ventilation and disequilibrium fluxes. But, the atmospheric O_2/N_2 approach produces an estimate of SNO_{bio} that is a factor of 2.7 greater than SNO_{bio} from the oceanic air-sea flux approach. Interestingly, a similar magnitude difference has been shown based on oxygen observations. Najjar and Keeling (2000) estimated 3.8 GtC yr^{-1} of mixed-layer new production for the southern hemisphere based on their observed estimate of SNO_{bio} (i.e. 3.23 x 10^{14} mol O_2) from an oxygen climatology. While Keeling and Shertz (1992) estimated 11.6 GtC yr^{-1} annual new production from their observed estimate of SNO_{bio} (i.e. 6.8 x 10^{14} mol) from atmospheric O_2/N_2 at Cape Grim, which is a factor of 3.0 great than the estimate from the oceanic approach.

We estimate new production by applying the simulated relationships between NP and SNO_{bio} from the two different global biogeochemical ocean circulation models to the *observed* SNO_{bio}. The two simulated relationships between SNO_{bio} and new production

$$NP = \frac{SNO_{bio}}{0.5}, \tag{56}$$

and

$$NP = \frac{SNO_{bio}}{0.25} - 0.84, \tag{57}$$

are used to define uncertainty bounds on new production. Based on the observed southern hemisphere SNO_{bio} from the air-sea flux climatology of Najjar and Keeling (2000) and a $C:O_2$ ratio of 106:-170, we estimate a new production magnitude of 6.9 ± 2 GtC yr^{-1}. For comparison, the

simulated relationship between NP and SNO_{bio} from the atmospheric approach

$$NP = \frac{SNO_{bio}}{1.38} + 0.07 \,, \tag{58}$$

is used to estimate NP from the observed atmospheric estimate of SNO_{bio} for southern hemisphere from Keeling and Shertz (1992), and a $C:O_2$ ratio of 106:-170 we obtain a new production estimate of 3.7 GtC yr^{-1}, a reduction of 7.9 GtC yr^{-1} from the original estimate of Keeling and Shertz (1992). After applying the simulated relationship the two estimates are much more consistent.

While Najjar and Keeling (2000) ascribe 25% of the discrepancy between their observed estimate of new production and the estimate of Keeling and Shertz (1992) to differences between the heat fluxes used to calculate the thermal SNO of oxygen, they suggested that the major cause was an error in the estimated dilution of the SNO of oxygen in the atmosphere. We demonstrate that in the model the dilution factor, d, can't explain the discrepancy between the atmospheric and oceanic approaches. The difference is due to SNO_{bio} from the atmospheric approach being much larger than SNO_{bio} from the oceanic approach. The estimates of SNO_{bio} from the two approaches are made over different time periods. Therefore, the ventilation fluxes bias the atmospheric estimate of SNO_{bio} more than the oceanic estimate of SNO_{bio}.

For the oxygen seasonality to be a valuable tool for monitoring new production the effect of variable ventilation on g_{hem} and k_{SNO} needs to be small. If both g_{hem} and k_{SNO} remain constant, despite variability in the ocean circulation, shifts in the magnitude of biological production and changes in the biogeochemical processes, we can be more confident that an observational g_{hem} can be estimated and we can retrieve a reliable new production from oxygen observations. If either or both g_{hem} and k_{SNO}

undergo large variations, then estimating new production from SNO_{bio} becomes more challenging. It then becomes extremely difficult to determine whether the SNO signal from any particular year is due to the changes in ventilation or changes in new production.

If we are optimistic and assume that variability in the ventilation flux on interannual time scales is small, realistically we will not be able to measure the air-sea fluxes of oxygen with enough spatial and temporal coverage on a yearly basis to monitor variability in new production. From a sampling perspective, using atmospheric O_2/N_2 is a more practical alternative for measuring variability new production, since the atmosphere acts to integrate the spatial variability in the oxygen fluxes. But, we need to determine how many atmospheric stations are required to remove the station bias.

As an interesting aside, note that the relationship between simulated NP (GtC yr^{-1}) and simulated integrated CO_2 uptake, F_{CO_2} (GtC yr^{-1}), in the southern hemisphere (20°S – 90°S) is also linear. It follows the relationship

$$F_{CO_2} = -0.2\ NP - 1.0\ ,\ r^2 = 1.0\ . \qquad (59)$$

Thus, for every 1 GtC yr^{-1} increase in NP, the CO_2 uptake by the southern hemisphere oceans increases by 0.2 GtC yr^{-1}. The atmospheric inversion model estimated a decrease in the southern hemisphere CO_2 uptake from 1.2 to 1.0 GtC yr^{-1} from the 1980's to the 1990's (Table 2-2). From Equation (59) this CO_2 uptake would equate to a reduction of 1 GtC yr^{-1} in new production.

10. References

Anderson, L. A. and J. L. Sarmiento (1994). "Redfield ratios of remineralization determined by nutrient data analysis." Global Biogeochemical Cycles **8**: 65-80.

Andres, R. J., G. Marland, I. Fung and E. Matthews (1996). "A 1 degrees x1 degrees distribution of carbon dioxide emissions from fossil fuel consumption and cement manufacture, 1950-1990." Global Biogeochemical Cycles **10**(3): 419-429.

Balkanski, Y., P. Monfray, M. Battle and M. Heimann (1999). "Ocean primary production derived from satellite data: An evaluation with atmospheric oxygen measurements." Global Biogeochemical Cycles **13**(2): 257-271.

Bender, M. (1996). "Variability in the O_2/N_2 ratio of southern hemisphere air, 1991-1994." Global Biogeochemical Cycles **10**: 9-22.

Berelson, W. M. (2001). "The flux of particulate organic carbon into the ocean interior: a comparison of four U.S. JGOFS regional studies." Oceanography **14**(4): 59-67.

Bieri, R. H., M. Koide and E. D. Goldberg (1966). "The noble gas contents of Pacific seawaters." Journal of Geophysical Research **71**: 5243-5265.

Bopp, L., P. Monfray, O. Aumont, J. L. Dufresne, H. Le Treut, G. Madec, L. Terray and J. C. Orr (2001). "Potential impact of climate change on marine export production." Global Biogeochemical Cycles **15**(1): 81-99.

Bousquet, P., P. Peylin, P. Ciais, C. Le Quere, P. Friedlingstein and P. P. Tans (2000). "Regional changes in carbon dioxide fluxes of land and oceans since 1980." Science **290**(5495): 1342-1346.

Bousquet, P., P. Peylin, P. Ciais, M. Ramonet and P. Monfray (1999). "Inverse modeling of annual atmospheric CO2 sources and sinks 2. Sensitivity study." Journal of Geophysical Research-Atmospheres **104**(D21): 26179-26193.

Boyd, P. W., A. J. Watson, C. S. Law, E. R. Abraham, T. Trull, R. Murdoch, D. C. E. Bakker, A. R. Bowie, K. O. Buesseler, H. Chang, M. Charette, P. Croot, K. Downing, R. Frew, M. Gall, M. Hadfield, J. Hall, M. Harvey, G. Jameson, J. LaRoche, M. Liddicoat, R. Ling, M. T. Maldonado, R. M. McKay, S. Nodder, S. Pickmere, R. Pridmore, S. Rintoul, K. Safi, P. Sutton, R. Strzepek, K. Tanneberger, S. Turner, A. Waite and J. Zeldis (2000). "A mesoscale phytoplankton bloom in the polar Southern Ocean stimulated by iron fertilization." Nature **407**(6805): 695-702.

Boyer, T., M. E. Conkright and S. Levitus (1999). "Seasonal variability of dissolved oxygen, percent oxygen saturation, and apparent oxygen utilization in the Atlantic and Pacific Oceans." Deep-Sea Research Part I-Oceanographic Research Papers **46**(9): 1593-1613.

Brenkert, A. L. (1998). Carbon dioxide emission estimates from fossil-fuel burning, hydraulic cement production, and gas flaring for 1995 on a one degree grid cell basis.

Bryan, K. and L. J. Lewis (1979). "A water mass model of the world ocean." Journal of Geophysical Research **84**: 347-376.

Buesseler, K. O., R. T. Barber, M. L. Dickson, M. R. Hiscock, J. K. Moore and R. Sambrotto (2003). "The effect of marginal ice-edge dynamics on production and export in the Southern Ocean along 170 degrees W." Deep-Sea Research Part Ii-Topical Studies In Oceanography **50**(3-4): 579-603.

Capone, D. G., A. Subramaniam, J. P. Montoya, M. Voss, C. Humborg, A. M. Johansen, R. L. Siefert and E. J. Carpenter (1998). "An extensive bloom of the N-2-fixing cyanobacterium Trichodesmium erythraeum in the central Arabian Sea." Marine Ecology-Progress Series **172**: 281-292.

Chen, D., L. M. Rothstein and A. J. Busalacchi (1994). "A Hybrid Vertical Mixing Scheme and Its Application to Tropical Ocean Models." Journal of Physical Oceanography **24**(10): 2156-2179.

Ciais, P., P. P. Tans, J. W. C. White, M. Trolier, R. J. Francey, J. A. Berry, D. R. Randall, P. J. Sellers, J. G. Collatz and D. S. Schimel (1995). "Partitioning of Ocean and Land Uptake of Co2 as Inferred by Delta-C-13 Measurements from the Noaa Climate Monitoring and Diagnostics Laboratory Global Air Sampling Network." Journal of Geophysical Research-Atmospheres **100**(D3): 5051-5070.

Conkright, M. E., R. A. Locarnini, H. E. Garcia, T. D. O'Brien, T. P. Boyer, B. B. Stephens and J. I. Antonov (2002). World OCEAN ATLAS 2001: Objective Analyses, Data, Statistics, and Figures, CD-ROM Documentation. Silver Spring, MD, National Oceanographic Data Center.

Cox, M. D. (1987). "Isopycnal diffusion in a z-coordinate ocean model." Ocean Modelling **74**: 1-5.

Craig, H. and T. Hayward (1987). "Oxygen supersaturation in the ocean: biological versus physical contributions." Science **235**: 199-201.

Danabasoglu, G., J. C. McWilliams and P. R. Gent (1994). "The Role of Mesoscale Tracer Transports in the Global Ocean Circulation." Science **264**(5162): 1123-1126.

Denning, A. S., M. Holzer, K. R. Gurney, M. Heimann, R. M. Law, P. J. Rayner, I. Y. Fung, S. M. Fan, S. Taguchi, P. Friedlingstein, Y. Balkanski, J. Taylor, M. Maiss and I. Levin (1999a). "Three-dimensional transport and concentration of SF6 - A model intercomparison study (TransCom 2)." Tellus Series B-Chemical and Physical Meteorology **51**(2): 266-297.

Denning, A. S., T. Takahashi and P. Friedlingstein (1999b). "Can a strong atmospheric CO2 rectifier effect be reconciled with a "reasonable" carbon budget?" Tellus Series B-Chemical and Physical Meteorology **51**(2): 249-253.

Denning, S. A., I. Y. Fung and D. Randall (1995). "Latitudinal gradient of atmospheric CO_2 due to seasonal exchange with land biota." Nature **376**: 240-243.

Dietze, H. and A. Oschlies (2005). "On the correlation between air-sea heat flux and abiotically induced oxygen gas exchange in a circulation model of the North Atlantic." Journal Of Geophysical Research-Oceans **110**(C9).

Doos, K. and D. J. Webb (1994). "The Deacon Cell and the Other Meridional Cells of the Southern-Ocean." Journal of Physical Oceanography **24**(2): 429-442.

Emerson, S. (1987). "Seasonal oxygen cycles and biological new production in surface waters of the subarctic Pacific Ocean." Journal of Geophysical Research **92**: 6535-6544.

England, M. H. and A. C. Hirst (1997). "Chlorofluorocarbons uptake in a world ocean model 2. Sensitivity to surface thermohaline forcing and subsurface mixing parameterisations." Journal of Geophysical Research **102**: 15,709-15,731.

Enting, I. G., C. M. Trudinger and R. J. Francey (1995). "A Synthesis Inversion of the Concentration and Delta-C-13 of Atmospheric Co2." Tellus Series B-Chemical and Physical Meteorology **47**(1-2): 35-52.

Eppley, R. W. (1972). " Temperature and phytoplankton growth in the sea." Fish. Bull. U.S. **70**: 1063-1085.

Falkowski, P. G., R. T. Barber and V. Smetacek (1998). "Biogeochemical controls and feedbacks on ocean primary production." Science **281**(5374): 200-206.

Francois, R., S. Honjo, R. Krishfield and S. Manganini (2002). "Factors controlling the flux of organic carbon to the bathypelagic zone of the ocean." Global Biogeochemical Cycles **16**(4).

Garcia, H. E. and L. I. Gordon (1992). "Oxygen Solubility in Seawater - Better Fitting Equations." Limnology and Oceanography **37**(6): 1307-1312.

Garcia, H. E. and R. F. Keeling (2001). "On the global oxygen anomaly and air-sea flux." Journal of Geophysical Research-Oceans **106**(C12): 31155-31166.

Gent, P. R. and J. C. McWilliams (1990). "Isopycnal mixing in ocean circulation models." Journal of Physical Oceanography **20**: 150-155.

Gerdes, R., C. Koeberle and J. Willebrandt (1991). "The influence of numerical advection schemes on the results of ocean general circulation models." Climate Dynamics **5**: 211-226.

Gloor, M., N. Gruber, J. Sarmiento, C. L. Sabine, R. A. Feely and C. Rodenbeck (2003). "A first estimate of present and preindustrial air-sea CO2 flux patterns based on ocean interior carbon measurements and models." Geophysical Research Letters **30**(1).

Gnanadesikan, A., J. P. Dunne, R. M. Key, K. Matsumoto, J. L. Sarmiento, R. D. Slater and P. S. Swathi (2004). "Oceanic ventilation and biogeochemical cycling: Understanding the physical mechanisms that produce realistic distributions of tracers and productivity." Global Biogeochemical Cycles **18**(4).

Gnanadesikan, A., R. D. Slater, N. Gruber and J. L. Sarmiento (2002). "Oceanic vertical exchange and new production: a comparison

between models and observations." Deep-Sea Research Part Ii-Topical Studies in Oceanography **49**(1-3): 363-401.
Godfrey, J. S. and A. Schiller (1997). Test of mixed-layer schemes and surface boundary conditions in an Ocean General Circulation Model, using IMET flux data set, CSIRO Australia: 39.
Griffies, S. M., A. Gnanadesikan, R. C. Pacanowski, V. D. Larichev, J. K. Dukowicz and R. D. Smith (1998). "Isoneutral diffusion in a z-coordinate ocean model." Journal of Physical Oceanography **28**(5): 805-830.
Gruber, N. (1998). "Anthropogenic CO_2 in the Atlantic Ocean." Global Biogeochemical Cycles **12**(1): 165-191.
Gruber, N., J. L. Sarmiento and T. F. Stocker (1996). "An improved method for detecting anthropogenic CO_2 in the oceans." Global Biogeochemical Cycles **10**: 809-837.
Gurney, K. R., R. M. Law, A. S. Denning, P. J. Rayner, D. Baker, P. Bousquet, L. Bruhwiler, Y. H. Chen, P. Ciais, S. Fan, I. Y. Fung, M. Gloor, M. Heimann, K. Higuchi, J. John, T. Maki, S. Maksyutov, K. Masarie, P. Peylin, M. Prather, B. C. Pak, J. Randerson, J. Sarmiento, S. Taguchi, T. Takahashi and C. W. Yuen (2002). "Towards robust regional estimates of CO2 sources and sinks using atmospheric transport models." Nature **415**(6872): 626-630.
Gurney, K. R., R. M. Law, A. S. Denning, P. J. Rayner, D. Baker, P. Bousquet, L. Bruhwiler, Y. H. Chen, P. Ciais, S. M. Fan, I. Y. Fung, M. Gloor, M. Heimann, K. Higuchi, J. John, E. Kowalczyk, T. Maki, S. Maksyutov, P. Peylin, M. Prather, B. C. Pak, J. Sarmiento, S. Taguchi, T. Takahashi and C. W. Yuen (2003). "TransCom 3 CO2 inversion intercomparison: 1. Annual mean control results and sensitivity to transport and prior flux information." Tellus Series B-Chemical and Physical Meteorology **55**(2): 555-579.
Hansell, D. A. and C. A. Carlson (1998). "Net community production of dissolved organic carbon." Global Biogeochemical Cycles **12**(3): 443-453.
Hirst, A. C., D. R. Jackett and T. J. McDougall (1996). "The meridional overturning cells of a world ocean model in neutral density coordinates." Journal of Physical Oceanography **26**: 776-791.
Honjo, S., R. Francois, S. Manganini, J. Dymond and R. Collier (2000). "Particle fluxes to the interior of the Southern Ocean in the Western Pacific sector along 170 degrees W." Deep-Sea Research Part Ii-Topical Studies in Oceanography **47**(15-16): 3521-3548.
Jenkins, W. J. and V. Goldman (1985). "Seasonal oxygen cycling and primary production in the Sargasso Sea." Journal of Marine Research **43**: 465-491.
Kara, A. B., P. A. Rochford and H. E. Hurlburt (2000). "An optimal definition for ocean mixed layer depth." Journal of Geophysical Research-Oceans **105**(C7): 16803-16821.
Keeling, C. D., S. C. Piper and M. Heimann (1989). A three dimensional model of atmospheric CO_2 transport based on observed winds, 4. Mean annual gradients and interannual variations. Aspects of Climate variability in the Pacific and Western Americas. D. H.

Peterson, AGU, Washington D.C. **Geophys. Monogr. Ser.:** 305-363.
Keeling, R. F., M. L. Bender and P. P. Tans (1993). "What atmospheric oxygen measurements can tell us about the global carbon cycle." Global Biogeochemical Cycles **7**: 37-67.
Keeling, R. F. and S. R. Shertz (1992). "Seasonal and Interannual Variations in Atmospheric Oxygen and Implications for the Global Carbon-Cycle." Nature **358**(6389): 723-727.
Keeling, R. F., B. B. Stephens, R. G. Najjar, S. C. Doney, D. Archer and M. Heimann (1998). "Seasonal variations in the atmospheric O-2/N-2 ratio in relation to the kinetics of air-sea gas exchange." Global Biogeochemical Cycles **12**(1): 141-163.
Kraus, E. B. and J. S. Turner (1967). "A one-dimensional model of the seasonal thermocline, II. The general theory and its consequences." Tellus **19**: 98-105.
Kumar, N. and a. more (1995). "Increased biological production and export production in the glacial Southern Ocean." Nature **378**: 675-680.
L.A., A. and S. J.L. (1995). "Global ocean phosphate and oxygen simulations." Global Biogeochemical Cycles **9**: 621-636.
Langenfelds, R. L., R. J. Francey, L. P. Steele, M. Battle, R. F. Keeling and W. F. Budd (1999). "Partitioning of the global fossil CO2 sink using a 19-year trend in atmospheric O-2." Geophysical Research Letters **26**(13): 1897-1900.
Large, W. G., G. Danabasoglu, S. C. Doney and J. C. McWilliams (1997). "Sensitivity to surface forcing and boundary layer mixing in a global ocean model: annual-mean climatology." Journal of Physical Oceanography **27**: 2418-2447.
Law, R. M., J. Li, E. Kowalczyk, J. L. McGregor and P. J. Rayner (2002). Comparison of observed and modelled CO_2 concentrations using the CSIRO cubic-conformal model nudged with NCEP winds. AGU 2002 Fall meeting, San Francisco.
Law, R. M. and P. J. Rayner (1999). "Impacts of seasonal covariance on CO2 inversions." Global Biogeochemical Cycles **13**(4): 845-856.
Law, R. M., P. J. Rayner, A. S. Denning, D. Erickson, I. Y. Fung, M. Heimann, S. C. Piper, M. Ramonet, S. Taguchi, J. A. Taylor, C. M. Trudinger and I. G. Watterson (1996). "Variations in modeled atmospheric transport of carbon dioxide and the consequences for CO2 inversions." Global Biogeochemical Cycles **10**(4): 783-796.
Laws, E. A., P. G. Falkowski, W. O. Smith, H. Ducklow and J. J. McCarthy (2000). "Temperature effects on export production in the open ocean." Global Biogeochemical Cycles **14**(4): 1231-1246.
Lehodey, P., F. Chai and J. Hampton (2003). "Modelling climate-related variability of tuna populations from a coupled ocean-biogeochemical-populations dynamics model." Fisheries Oceanography **12**(4-5): 483-494.
Louanchi, F. and R. G. Najjar (2000). "A global monthly climatology of phosphate, nitrate, and silicate in the upper ocean: Spring-summer export production and shallow remineralization." Global Biogeochemical Cycles **14**(3): 957-977.

Loukos, H., P. Monfray, L. Bopp and P. Lehodey (2003). "Potential changes in skipjack tuna (Katsuwonus pelamis) habitat from a global warming scenario: modelling approach and preliminary results." Fisheries Oceanography **12**(4-5): 474-482.

Lourey, M. J. and T. W. Trull (2001). "Seasonal nutrient depletion and carbon export in the Subantarctic and Polar Frontal Zones of the Southern Ocean south of Australia." Journal of Geophysical Research **106**(C12): 31463-31488.

MacCready, P. and P. Quay (2001). "Biological export flux in the Southern Ocean estimated from a climatological nitrate budget." Deep-Sea Research Part Ii-Topical Studies in Oceanography **48**(19-20): 4299-4322.

Maier-Reimer, E., U. Mikolajewicz and A. Winguth (1996). "Future ocean uptake of CO_2: interaction between ocean circulation and biology." Climate Dynamics **12**: 711-721.

Marchant, H. J., A. T. Davidson and S. W. Wright (1987). "The distribution and abundance of chroococcoid cyanobacteria in the Southern Ocean." Proceedings of the NIPR Symposium on Polar Biology **1**: 1-9.

Martin, J. H., G. A. Knauer, D. M. Karl and W. W. Broenkow (1987). "VERTEX: The carbon cycling in the northeast Pacific." Deep Sea Research **34**: 267-285.

Matear, R. J. (1995). "Parameter optimization and analysis of ecosystem models using simulated annealing: A case study at Station P." Journal of Marine Research **53**: 571-607.

Matear, R. J. and A. C. Hirst (1999). "Climate Change Feedback on the Future Oceanic CO_2 uptake." Tellus **51B**(3): 722-733.

McGregor, J. L. and M. R. Dix (2001). The CSIRO Conformal-Cubic Atmospheric GCM, IUTAM Symposium on Advances in Mathematical Modeling of Atmosphere and Ocean Dynamics. Dordrecht, Kluwer Academic Publishers.

McNeil, B. I., B. Tilbrook and R. J. Matear (2001). "Seasonal variations in DIC and $\delta^{13}C_{DIC}$ in the subantarctic zone, South of Australia." accepted by Deep Sea Research in August 2001.

Metzl, N., A. Poisson, F. Louanchi, C. Brunet, B. Schauer and B. Bres (1995). "Spatiotemporal Distributions of Air-Sea Fluxes of Co2 in the Indian and Antarctic Oceans - a First Step." Tellus Series B-Chemical and Physical Meteorology **47**(1-2): 56-69.

Metzl, N., B. Tilbrook and A. Poisson (1999). "The annual fCO(2) cycle and the air-sea CO2 flux in the sub- Antarctic Ocean." Tellus Series B-Chemical and Physical Meteorology **51**(4): 849-861.

Moore, J. K., M. R. Abbot, J. G. Richman, W. O. Smith, T. J. Cowles, K. H. Coale, G. W.D. and R. T. Barber (1999). "SeaWiFS satellite ocean color data from the Southern Ocean." Gephysical Research Letters **26**(10): 1465-1468.

Moore, J. K., S. C. Doney, D. M. Glover and I. Y. Fung (2002a). "Iron cycling and nutrient-limitation patterns in surface waters of the World Ocean." Deep-Sea Research Part Ii-Topical Studies in Oceanography **49**(1-3): 463-507.

Moore, J. K., S. C. Doney, J. A. Kleypas, D. M. Glover and I. Y. Fung (2002b). "An intermediate complexity marine ecosystem model for the global domain." Deep-Sea Research Part Ii-Topical Studies in Oceanography **49**(1-3): 403-462.

Najjar, R. G., X. Jin, F. Louanchi, O. Aumont, K. Caldeira, S. C. Doney, J. C. Dutay, M. Follows, G. M. Kay, E. Maier-Reimer, R. J. Matear, A. Mouchet, J. C. Orr, G. K. Plattner, J. L. Sarmiento, M. F. Weirig, Y. Yamanaka and A. Yool (2003). Export production simulated by the OCMIP-2 models. Poster at the Final JGOFS Open Science Conference. Washington, D.C.

Najjar, R. G. and R. F. Keeling (1997). "Analysis of the mean annual cycle of the dissolved oxygen anomaly in the World Ocean." Journal of Marine Research **55**(1): 117-151.

Najjar, R. G. and R. F. Keeling (2000). "Mean annual cycle of the air-sea oxygen flux: A global view." Global Biogeochemical Cycles **14**(2): 573-584.

Odate, T. and M. Fukuchi (1995). "Distribution and community structure of picophytoplankton in the Southern Ocean during the late austral summer of 1992." Proc. NIPR Symp. Polar Biology **8**: 86-100.

Orsi, A. H., W. M. Smethie and J. L. Bullister (2002). "On the total input of Antarctic waters to the deep ocean: A preliminary estimate from chlorofluorocarbon measurements." Journal of Geophysical Research-Oceans **107**(C8).

Palmer, J. R. and I. J. Totterdell (2001). "Production and export in a global ocean ecosystem model." Deep-Sea Research Part I-Oceanographic Research Papers **48**(5): 1169-1198.

Price, J. F., R. A. Weller and R. Pinkel (1986). "Diurnal Cycling - Observations and Models of the Upper Ocean Response to Diurnal Heating, Cooling, and Wind Mixing." Journal of Geophysical Research-Oceans **91**(C7): 8411-8427.

Randerson, J. T., M. V. Thompson, T. J. Conway, I. Y. Fung and C. B. Field (1997). "The contribution of terrestrial sources and sinks to trends in the seasonal cycle of atmospheric carbon dioxide." Global Biogeochemical Cycles **11**(4): 535-560.

Rayner, P. J., I. G. Enting, R. J. Francey and R. Langenfelds (1999). "Reconstructing the recent carbon cycle from atmospheric CO2, delta C-13 and O-2/N-2 observations." Tellus Series B-Chemical and Physical Meteorology **51**(2): 213-232.

Rintoul, S. R. and J. L. Bullister (1999). "A late winter hydrographic section from Tasmania to Antarctica." Deep-Sea Research Part I-Oceanographic Research Papers **46**(8): 1417-1454.

Rintoul, S. R. and T. W. Trull (2001). "Seasonal evolution of the mixed layer in the Subantarctic Zone south of Australia." Journal of Geophysical Research-Oceans **106**(C12): 31447-31462.

Sarmiento, J. L., N. Gruber, M. A. Brzezinski and J. P. Dunne (2004). "High-latitude controls of thermocline nutrients and low latitude biological productivity." Nature **427**(6969): 56-60.

Sarmiento, J. L. and C. Le Quéré (1996). "Oceanic carbon dioxide uptake in a model of century-scale global warming." Science **274**: 1346-1350.

Schlitzer, R. (2002a). "Carbon export fluxes in the Southern Ocean: results from inverse modeling and comparison with satellite based estimates." Deep Sea Research II **Special Volume on the Southern Ocean**: 1623-1644.

Schlitzer, R. (2002b). "Carbon export fluxes in the Southern Ocean: results from inverse modeling and comparison with satellite-based estimates." Deep-Sea Research Part Ii-Topical Studies in Oceanography **49**(9-10): 1623-1644.

Schmitz, W. J. (1995). "On the interbasin-scale thermohaline circulation." Reviews of Geophysics **33**: 151-173.

Schulenberger, R. and J. L. Reid (1981). "The Pacific shallow oxygen maximum, deep chlorophyll maximum, and primary productivity reconsidered." DEep Sea Research, Part A **28**: 901-919.

Sigman, D. M. and E. A. Boyle (2000). "Glacial/interglacial variations in atmospheric carbon dioxide." Nature **407**(6806): 859-869.

Six, K. D. and E. Maier-Reimer (1996). "Effects of plankton dynamics on seasonal carbon fluxes in an ocean general circulation model." Global Biogeochemical Cycles **10**: 559-583.

Spitzer, W. S. and W. J. Jenkins (1989). "Rates of vertical mixing, gas exchange and new production: Estimates from seasonal gas cycles in the upper ocean near Bermuda." Journal of Marine Research **47**: 169-196.

Stocker, T. F. and A. Schmittner (1997). "Influence of CO_2 emission rates on stability of the thermohaline circulation." Nature **388**: 862-865.

Takahashi, T., R. A. Feely, R. F. Weiss, R. H. Wanninkhof, D. W. Chipman, S. C. Sutherland and T. T. Takahashi (1997). "Global air-sea flux of CO2: An estimate based on measurements of sea-air pCO(2) difference." Proceedings of the National Academy of Sciences of the United States of America **94**(16): 8292-8299.

Takahashi, T., S. C. Sutherland, C. Sweeney, A. Poisson, N. Metzl, B. Tilbrook, N. Bates, R. Wanninkhof, R. A. Feely, C. Sabine, J. Olafsson and Y. Nojiri (2002). "Global sea-air CO2 flux based on climatological surface ocean pCO(2), and seasonal biological and temperature effects." Deep-Sea Research Part Ii-Topical Studies in Oceanography **49**(9-10): 1601-1622.

Tans, P. P., I. Y. Fung and T. Takahashi (1990). "Observational Constraints on the Global Atmospheric Co2 Budget." Science **247**(4949): 1431-1438.

Trull, T., S. R. Rintoul, M. Hadfield and E. R. Abraham (2001). "Circulation and seasonal evolution of polar waters south of Australia: Implications for iron fertilization of the Southern Ocean." Deep-Sea Research Part Ii-Topical Studies in Oceanography **48**(11-12): 2439-2466.

Visbeck, M., J. Marshall, T. Haine and M. Spall (1997). "Specification of eddy transfer coefficients in coarse- resolution ocean circulation models." Journal of Physical Oceanography **27**(3): 381-402.

Volk, T. and M. I. Hoffert (1985). Ocean carbon pumps: Analysis of relative strengths and efficiencies in Ocean driven atmospheric CO_2 changes. The carbon cycle and atmospheric CO_2: natural variations archean to present. E. T. Sundquist and W. S. Broecker,

American Geophysical Union. **Geophysical Mongraph 32:** 99-110.

Wang, X., R. J. Matear and T. W. Trull (2001). "Modeling seasonal phosphate export and resupply in the Subantarctic and Polar Frontal Zones in the Australian sector of the Southern Ocean." Journal of Geophysical Research **106**(C12): 31525-31542.

Wanninkhof (1992). "Relationship between wind speed and gas exchange over the ocean." Journal of Geophysical Research **97**: 7373-7382.

Weiss, R. F. (1970). "The solubility of nitrogen, oxygen and argon in water and seawater." Deep Sea Research **17**: 721-735.

Whitworth, T. I. (1983). "Monitoring the net transport of the Antractic Circumpolar Current at Drake Passage." Journal of Physical Oceanography **13**: 2045-2057.

Whitworth, T. I., W. D. Nowlin and S. J. Worley (1982). "The net transport of the Antarctic Circumpolar Current through Drake Passage." Journal of Physical Oceanography **12**: 960-971.

Wright, S. W., D. P. Thomas, H. J. Marchant, H. W. Higgins, M. D. Mackey and D. J. Mackey (1996). "Analysis of phytoplankton of the Australian sector of the Southern Ocean: comparisons of microscopy and size frequency data with interpretations of pigment HPLC data using the 'CHEMTAX' matrix factorisation program." Marine Ecology Progress Series **144**: 285-298.

Yamanaka, Y. and E. Tajika (1996). "The role of the vertical fluxes of particulate organic matter and calcite in the oceanic carbon cycle: Studies using a ocean biogeochemical general circulation model." Global Biogeochemical Cycles **10**: 361-382.